**University of Bath**

UNIVERSITY OF
**BATH**

**PHD**

**Investigations of Ion Migration in Organo-lead Halide Perovskites**

Ferdani, Dominic

*Award date:*
2019

*Awarding institution:*
University of Bath

[Link to publication](Link to publication)

**Alternative formats**

If you require this document in an alternative format, please contact:
openaccess@bath.ac.uk

# Investigations of Ion Migration in Organo-lead Halide Perovskites

## Dominic Ferdani

A thesis submitted for the degree of Doctor of Philosophy

## University of Bath

Chemistry

July 2019

# Abstract

Perovskite based photovoltaics have developed from a low performing offshoot of dye sensitized solar cells into its own field of solar cell research within a decade, with thousands of publications per year and record efficiencies greater than 23 %. Perovskite solar cell devices suffer from several important issues, toxicity and instability being the main two. Ion migration has been shown to cause material instability and hysteresis in devices. Substituting different cations and anions into the perovskite $ABX_3$ structure reduces hysteresis. Understanding the impact of substitution is important towards improved device design in the future.

In this thesis, muon spin relaxation ($\mu$SR) is presented as a novel probe for iodide diffusion. The migration of iodide is initially observed in methyl ammonium lead iodide and a deuterated analogue. The measured activation energy of $0.17\,\mathrm{eV}$ matches well with recent literature values for iodide migration showing, for the first time, that it is possible to detect iodide using $\mu$SR. The use of $\mu$SR to study iodide diffusion in perovskite was then taken further by investigating perovskites with 5 mol% cation substitution. The results here show that the substitution of 5% guanidinium causes complete inhibition of iodide diffusion due to small distortions of the perovskite lattice, making migration energetically expensive. A small decrease in diffusion coefficient was also observed for $Cs^+$ and formamidinium substitution.

The diffusion of bromide in pure methylammonium lead bromide and mixed anion perovskites was also investigated using $\mu$SR. Detecting bromide was not possible despite its similar properties to iodide. The diffusion of iodide in mixed anion perovskites was shown to be restricted as no iodide diffusion was detected in $MAPb(Br_{0.17}I_{0.83})_3$. Finally, the diffusion of iodide in 2D/3D hybrid perovskites was investigated using electrochemical impedance spectroscopy. It was shown that diffusion is once again strongly inhibited by the addition of larger A-site cations with just 1 mol% phenylethylammonium iodide causing inhibition of iodide diffusion in the measured temperature range. It was also shown that vertically aligned 2D/3D perovskites also show inhibited iodide diffusion.

i

# Acknowledgements

The time spent doing this PhD has been quite an adventure and without many key people the whole experience would have been completely different. The first group of people I would like to thank are my supervisory team. Simon Lewis and Andy Johnson were excellent secondary supervisors and have always been helpful when I have needed them. I was never worried about going to talk to them about a problem. Petra has been a fantastic supervisor throughout my PhD, not being too overbearing but always available when needed. She has helped provide excellent ideas and knowledge but probably most importantly guidance throughout the whole process.

The second group of people I would like to thank are the various PhD and postdoctoral researchers I have interacted with during my PhD experience. The other members of the Cameron group proved to be excellent companions over three years. Thanks to the more experienced PJC members, Ralf, Wentao and Xinging for all their help in the early perovskite stages and the Lewis group members for synthesis help. Special thanks must go to Sam and Pete who, beginning their PhDs at the same time, helped me through some of the struggles, especially on Wednesday afternoons, with well timed biscuits and jokes.

Thirdly, thanks to the various funding bodies who have provided me with several opportunities. The CSCT for the opportunity to pursue my PhD and the ISIS Neutron and Muon Source for their generous beam time allocations that allowed me to perform some of the key experiments in this thesis. With ISIS in mind I would like to thank all of the instrument scientists at the facility who helped me with my experiments, especially Peter Baker who introduced me to and guided me through all of the muon experiments.

Finally, thanks to my family and friends for all their support and encouragement.

# List of Publications

## Journal Articls

1. "Continuous low temperature synthesis of $MAPbX_3$ perovskite nanocrystals in a flow reactor" - Xinxing Liang, Robert W. Baker, Kejun Wu, Wentao Deng, <u>Dominic W. Ferdani</u>, Peter S. Kubiak, Frank Marken, Laura Torrente-Murciano and Petra J. Cameron, Reaction Chemistry & Engineering, 3, 640-644

2. "Partial cation substitution reduces iodide ion transport in lead iodide perovskite solar cells" - <u>Dominic W. Ferdani</u>, Samuel R. Pering, Djibajyoti Ghosh, Peter Kubiak, Alison B. Walker, Simone E. Lewis, Andrew L. Johnson, Peter J. Baker, M. Saiful Islam and Petra J. Cameron, Energy & Environmental Science, Advance Article, 2019

## International Conference Contributions

1. "Probing the Methyl Amine - Halogen Interaction in Methyl Ammonium Lead Iodide" - <u>Dominic W. Ferdani</u>, Petra J. Cameron, 8th International Conference on Hybrid and Organic Photovoltaics, Swansea, UK (Poster Presentation)

2. "Investigating Mixed Cation Perovskites with Muon Spin Relaxation" - <u>Dominic W. Ferdani</u>, Andrew L. Johnson, Simon E. Lewis, Peter J. Baker, Petra J. Cameron, 10th International Conference on Hybrid and Organic Photovoltaics, Benidrom, Spain (Poster Presentation)

# Contents

# List of Abbreviations

| | |
|---|---|
| μSR | Muon Spin Relaxation |
| ACN | Acetonitrile |
| AFM | Atomic Force Microscopy |
| AM | Air Mass |
| AVA | 5-aminovaleric acid |
| BA | Butylammonium |
| BCP | bathocuproine |
| CB | Conduction band |
| CdTe | Cadmium telluride |
| CIGS | Copper indium gallium selenide |
| CIS | Copper indium selenide |
| CZTS | Copper zinc tin sulphide |
| DFT | Density Functional Theory |
| DMF | Dimethylformamide |
| DMSO | Dimethyl Sulfoxide |
| DSSC | Dye-sensitised solar cells |
| $E_a$ | Activation Energy |
| $E_F$ | Fermi Level |

| | |
|---|---|
| $E_g$ | Band Gap |
| EIS | Electrochemical Impedance Spectroscopy |
| F-An | 4-fluoroanilinium Iodide |
| F-PrA | 2,2,3,3,3-pentafluoropropylammonium Iodide |
| FA | Formamidinium |
| FAPI | Formamidinium lead iodide |
| FWHM | Full Width at Half Maximum |
| GHG | Greenhouse gas |
| GIWAXS | Grazing Incidence Wide Angle X-ray Scattering |
| HOMO | Highest Occupied Molecular Orbital |
| IPA | Isopropanol |
| KT | Kubo-Toyabe |
| LF | Longitudinal Field |
| LUMO | Lowest Unoccupied Molecular Orbital |
| MA | Methylammonium |
| MAPBr | Methylammonium Lead Bromide |
| MAPI | Methylammonium lead iodide |
| Mu | Muonium |
| $PC_nBM$ | [6, 6]-Phenyl-$C_n$-butyric acid methyl ester |
| PCE | Power Conversion Efficiency |
| PEA | Phenyethylammonium |
| PEAPI | Phenylethylammonium lead iodide |
| PEDOT:PSS | poly(3,4-ethyl-enedioxythiophene)poly(styrene-sulfonate) |

PrA             Propylammonium

PV              Photovoltaic

pXRD            Powder X-ray Diffraction

QD              Quantum Dot Solar Cells

Spiro-OMeTAD  2,2,7,7-tetrakis (N,N-di-p-methoxyphenylamine)-9,9-spirobifluorene

SRH             Shockley-Read Hall

TCO             Transparent Conducting Oxide

VB              Valence band

# List of Figures

# List of Tables

# Chapter 1

# Introduction

## 1.1 Global Energy Situation

The world is approaching a global energy crisis caused by a rapidly increasing population, increased demand for energy per person, and a decline in the availability of fossil fuels.[1,2] The U.S. Environmental Information Administration estimates that global demand for energy will increase by 56 % by 2040, where this energy comes from will have a dramatic effect on the future.[3] Currently, approximately 82 % of global energy is generated from fossil fuel based sources, which produce greenhouse gas emissions (GHG).[4] GHG emissions have been heavily linked to the rising global temperature and there is a global initiative to try and lower their production.[5] The EU has laid out their aim to reduce GHG emissions by 80-95 % by the year 2050.[6] The UN initially set a goal to keep the global temperature rise below $2\,°C$, though more recent studies indicate $1.5\,°C$ is a better target.[7,8] For this target to be reached the percentage of energy generated by fossil fuels must be drastically reduced. Some of this power generation can be achieved through the use of nuclear power but this has its own drawbacks such as supply and safety issues.[9,10] The energy share from renewable sources needs to increase to 55 % if the EU 2050 climate goals are to be reached.[11]

The EU's short term goal is to see all countries generate 20 % of energy from renewable sources by 2020 and then 27 % by 2030 with other countries and regions having similar goals.[12] To achieve these goals the cost and efficiency of renewable energy must decrease to be competitive with current enery generation

technologies. Utility scale silicon solar power and wind are just reaching a point of grid parity.[13] Grid parity is the point where the cost of an electricity alternative source is less than or equal to the current standard power generation cost. Utility scale solar power refers to large area facilities specifically designated to energy generation. While the utility scale is competitive individual rooftop solar power is over three times the cost of coal.[13] At present there are four main sources of renewable energy; hydro electric, wind, solar PV and bio-power.[14] Hydro electric is the largest generator of renewable electricity but for many countries they do not have the appropriate water sources to produce power this way.

Solar energy is a very feasible method of generating much larger quantities of energy at low cost and on location. There is $1.4 \times 10^{17}\,\mathrm{W}$ $(1.4 \times 10^5\,\mathrm{TW})$ of power incident on the earth due to light from the sun.[15] This is over 7000 times larger than the 2017 estimated global energy consumption of $588\,\mathrm{EJ}$.[16] This energy can be used by certain types of material to generate electricity. The photovolataic (PV) effect is the physical phenomenon responsible for a materials ability to generate power from light.[17] Solar cells are a type of technology that make use of this effect, also known as the Becquerel effect after its discoverer, to generate electricity. Creating cheaper more efficient solar cells has been the focus of research over the last century.[18–21]

## 1.2    Solar Cell Technologies

### 1.2.1    First Generation PV

Silicon solar cells, the first generation of solar cells, were invented by Ohl in 1941.[22] Since then crystalline silicon cells have become the dominant force in the solar cell market accounting for approximately 90 % of sales.[23] Of this 90 % a third is made up of mono crystalline and two thirds is made up of multi crystalline silicon solar cells. Both mono and multi crystalline silicon cells operate using the same p-n junction system the difference is the materials from which the layers are made. The dominance of these first generation technologies is down to their advanced development cycle due to their early discovery, good efficiency and low toxicity when compared to other solar technologies.[24]
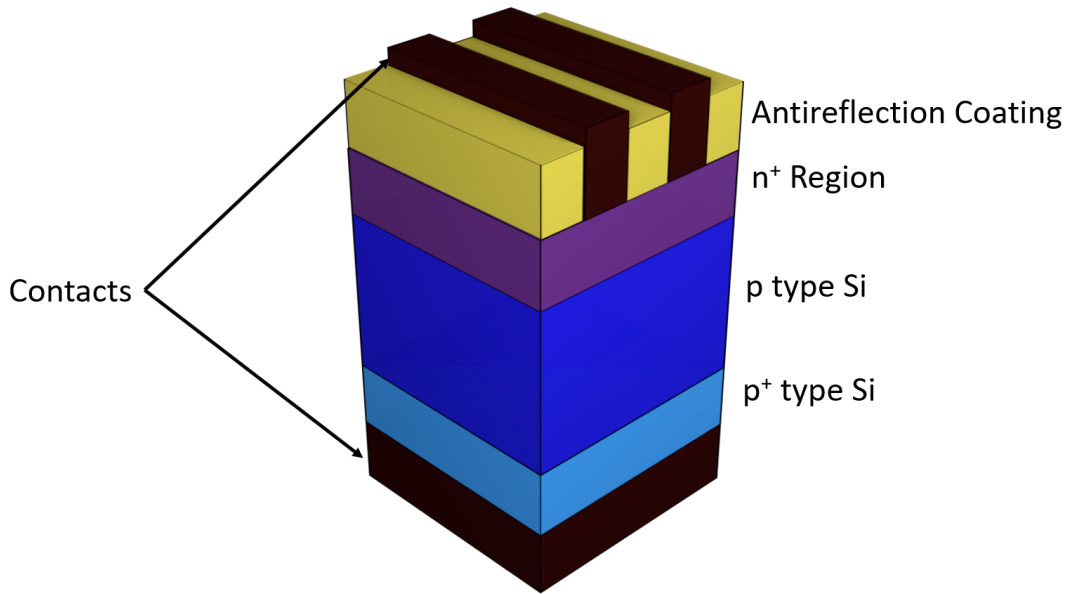
Figure 1-1: Diagram depicting the basic architecture of a first generation silicon solar cell

On a basic level a crystalline silicon solar cell has the structure shown in Figure 1-1. From the bottom up, the basic architecture is a contact with a $p^+$ type Si layer on top followed by a p-type Si layer which is in contact with an $n^+$ Si region, this is followed by antireflection coating and then the device is finished by front contacts. Semiconductor layers that are doped with extra electrons or extra holes are referred to as p or an n type layer. If 1 in every 10,000 atoms is a dopant then the layer is referred to as p+ or n+ (compared to 1 in every 100 million in regular p and n type). The contact between this p and n type material forms the p-n junction, the details of which will be discussed in more detail in Chapter 2.2 of this thesis.

The efficiency of lab based single junction and single crystal silicon cells have, in 2018, reached 26.1 % which is nearing the 29.43 % theoretical limit.[25] The efficiency of a solar cell is the percentage of the incident power on a device that is turned into usable power. While efficiencies have improved, Si cells, at present, struggle to make a big market breakthrough due to the cost of manufacturing large, highly crystalline silicon sheets. Since 2010 the levelized cost of silicon has fallen by 73% to $ 0.10 \, \mathrm{kW \, h^{-1}}$.[26] At these costs silicon solar power, on the utility

scale, is capable of competing directly with fossil fuels. This ability to compete is dependent on the location as countries with more annual sun can produce more solar power therefore lowering the cost of power generated by solar.[26]

## 1.2.2   Second Generation PV

Second generation solar cells were developed from the same principles as the first generation but they make use of thin films of absorber layer. The absorber layer is the part of the PV device that exhibits the photovoltaic effect and is responsible for the devices ability to generate power. The use of thin films can reduce the cost of both processing and raw materials as absorber layers from a few hundred nm to a few µm can be used, this is substantially less material than the hundreds of µm thick Si wafers needed for first generation PVs.[27] When it comes to market share, second generation cell accounts for the remaining 10 % not accounted for by first generation cells.[23] This 10 % is made up of cadmium telluride (CdTe), amorphous Si and copper indium gallium selenide (CIGS) .[23]

CdTe solar cells are a thin film solar cell with a CdTe p-type layer and a CdS n-type layer forming the p-n junction. CdTe makes up around half of the market share of thin film technologies.[23] A benefit of CdTe solar cells is that they have been shown to have the shortest energy payback time and lowest GHG emissions per kW h of all current commercial solar cells.[28] The efficiency record for CdTe PVs was, in 2016, pushed up to 22.1 % by First Solar.[24] This high efficiency has also translated well to module devices with the module record efficiency being 18.6 %.[24]

Despite these very promising properties CdTe cells have several different limitations to mass production.[29] The first is the use of a toxic cadmium chloride environment during the annealing process of the absorber layer.[30] As a result the manufacturing process requires a sealed environment which adds to the device cost. The second issue is brought about by the light p-type doping of the CdTe layer causing instability in the back contact and leading to increased resistance between the two layers.[31] The next issue is the use of toxic Cd in both the p and n type layers. The impact of Cd can be minimised with good device design and a robust recycling process but once again this adds to the cost. The final,

and probably most insurmountable issue, with CdTe is the use of Te. Tellurium is a scarce element and its low availability is predicted, in a best case scenario, to limit the energy production of CdTe solar cells to just 0.4 % of global energy demand in 2100.[32,33]

CIGS solar cells are also 2nd generation cells with thin absorber layers the same as CdTe cells except for the absorber layer being changed to a thin film of CIGS. Precursor materials to CIGS solar cells were first discovered in 1953 when Hahn *et al.* synthesised a copper indium selenide (CIS) material with a band gap of 1.04 eV. No solar cells were made with it until the 1970s when a 12 % efficiency single crystal solar cell was fabricated.[34,35] This led to more research into thin film CIS solar cells with slowly improving efficiencies. The incorporation of gallium into the absorber layer forming CIGS instead of CIS improved performance and since then efficiencies have risen up to a record of 22.6 %.[24]

Despite the impressive lab efficiencies, researchers have struggled to replicate them in larger modules, with those reaching only 16.1 %.[36] While there is no Cd in CIGS itself, the standard device architecture contains a CdS layer.[37] This CdS layer therefore causes the same toxicity issues that are prevalent in CdTe devices. Another problem for CIGS cells is the use of the rare metal indium limiting the maximum global power production.[32] Indium is not only rare but is also used heavily in other applications such as phone screens and LCD production. This, when linked with its low abundance, can lead to large fluctuations in price impacting on the dollar per Watt of CIGS PV modules.[38]

The final second generation PV technology is amorphous silicon. The difference between amorphous silicon and the first generation silicon solar cells is that in the absorber layer the silicon atoms are not in a strict lattice structure but are placed more randomly. The random arrangement of atoms alters the band gap of the material to 1.7 eV which is an increase of 0.6 eV over crystalline silicon.[18] Changing the band gap in this way, changes the wavelength of light that is absorbed from the near IR into more visible wavelengths. The first amorphous silicon solar cell was reported in 1976 when Carlson and Wronski fabricated a solar cell with an efficiency of 2 %.[39] Since then efficiency increases for amorphous silicon have been slow with the current record cell of just 14 % being fabricated

40 years after the first device.[40]

Despite the low lab efficiency the difference between lab scale amorphous Si and module scale efficiency is small, unlike other previously mentioned thin film PV technologies. Having a non-toxic, easily processable absorber layer, makes amorphous silicon an optimal material as it can help to lower device cost. Large levels of defect density, which increase upon illumination due to the Staebler-Wronski effect, fundamentally limit amorphous silicon's performance.[41,42] This low efficiency ceiling will likely limit the global uptake of amorphous Si cells as the dollar per Watt will not be low enough to compete with conventional power sources and other renewable technologies.[43]

### 1.2.3   Third Generation PV

The problems with second generation PV led researchers to continue investigating alternative means of solar energy generation. This research created several diverse technologies which are commonly referred to as third generation. They are mostly still being investigated on a lab scale but some small start-up companies are trying to bring them to market. There are five different types of third generation cells:

- Copper zinc tin sulphide solar cells

- Organic solar cells

- Quantum dot solar cells

- Dye-sensitized solar cells

- Perovskite solar cells

Copper zinc tin sulphide (CZTS) has recently become a material of focus for replacing CIGS due to its similar structure and properties, but with cheaper, more abundant and less toxic elements.[44] Unfortunately researchers have struggled to produce high efficiency solar cells using CZTS with the current record being 12.5 %.[45] Issues with absorber layer defects and challenging manufacturing processes are holding back progress with CZTS.[46]

Since the turn of the century organic solar cells have seen intense focus from the research community, this led to rapid efficiency developments from 2.5 % in

2001 to 11.5 % in 2016.[47,48] There are two different yet similar fields of organic PVs, these are small-molecule based and polymer based cells. The absorber layers in these two types of device are made from a donor and acceptor pair. The donor-acceptor pair can be comprised of a single molecule but is more commonly a pair of molecules[49] The donor molecule can give up an electron and the acceptor can receive an extra electron.[50] Commonly, both types of cell use a fullerene based acceptor such as [6, 6]-Phenyl-$C_n$-butyric acid methyl ester ($PC_nBM$) (where n = number of carbons in the fullerene) (Figure 1-2a) and then they differ in what is used as the donor.[51,52] In small molecule organic cells the donor is formed of low molecular weight, highly conjugated molecules with an example of a high performing thiophene based molecule shown in Figure 1-2b.[53] Polymer organic cells differ in that they use large (between 10 and 100 kDa) molecules also made up of conjugated carbon chains. At present the most common polymer solar cells are based around synthetically altered forms of polythiophene (Figure 1-2c).[54,55]

The large delocalised $\pi$ system in the polymer or small molecule forms the highest occupied molecular orbital (HOMO) and the lowest unoccupied molecular orbital (LUMO) . Organic materials are chosen to have a band gap that is suitable for PV applications. The role of the acceptor is to remove the excited electrons from the donor material as the photo generated excitons have a short lifetime. To create the maximum efficiency, the donor and acceptor materials of the organic solar cell are commonly blended together to create the absorber layer, this is sandwiched between contacts to create a full device as shown in Figure 1-2d.[56–58]

The main advantage of organic cells is that they are easy to process.[59] It is possible to screen print them at low temperatures which can lead to easy roll to roll printing.[60] This also leads to the ability to fabricate flexible organic solar cells increasing the number of applications for which they can be used.[61] Despite the benefits of organic cells they are still held back by several flaws beyond just their low efficiency. There are questions about the long term stability of the organic components due to the possibility of photolytic and photochemical reactions occurring and subsequently damaging the device performance.[62] A further issue is the development of increasingly complex absorber layers. More complex materials can help overcome stability and efficiency issues with the side effect

7
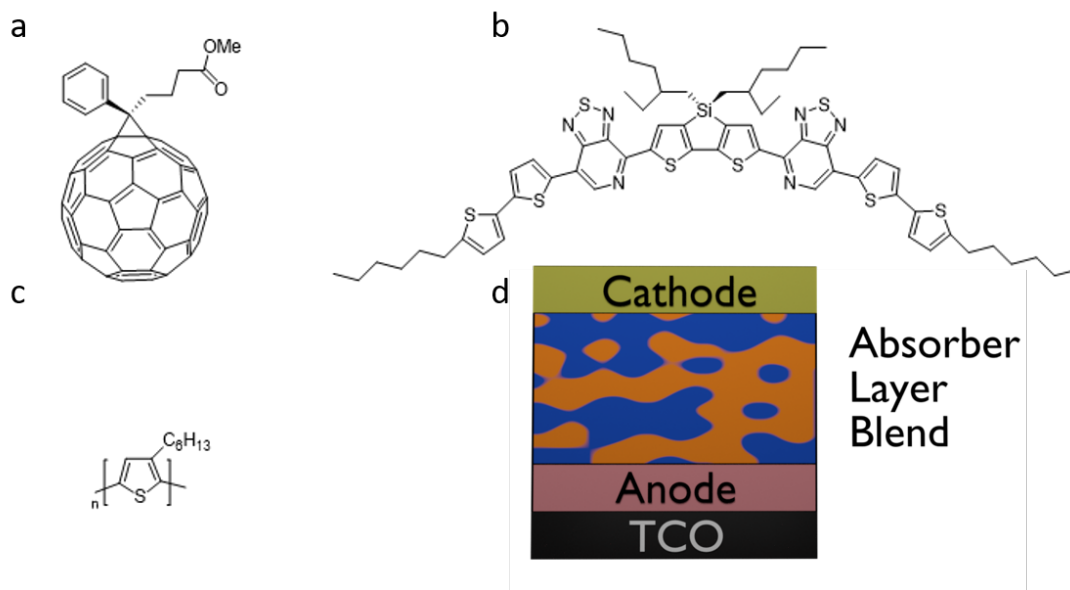
Figure 1-2: a) The structure of $PC_nBM$. b) An example of a high performing thiophene based electron donor group. c) The structure of a thiophene polymer used to make polymer solar cells. d) The device architecture of an organic solar cell with the orange and blue central section representing the blending of the acceptor and donor groups to make the bulk heterojunction.

of increased cost as the molecules become more synthetically challenging. This increased difficulty will therefore, make it more challenging to significantly lower the price of polymer cells. Despite these challenges, the ability to easily print low cost cells on flexible substrates could lead to the uptake of polymer cells in a few niche areas but it is unlikely to contribute significantly to meeting global energy demand.

Colloidal quantum dotsolar cells (QDS) were first fabricated in 2005 where a thin film of PbS quantum dots were used to absorb light.[63] The advantages of QDS are that they can be solution processed and their properties can be easily manipulated.[64] The size and shape of quantum dots can be altered by changing the synthetic procedure, these changes can then lead to different optical and electrical properties.[65] The efficiency of QDS are the second highest of the emerging PVs, with certified efficiencies of 13.4 %.[66] Despite the ease with which quantum dots can be manipulated, challenges in synthesising large quantities of perfect quantum dots is limiting progress, and prevents larger scale production.[67] The device architecture used for QDS is, at present, not optimised and further

developments could help QDS produce higher efficiencies.[64] Despite these flaws, QD solar cells have potential to be useful in multijunction solar cells where their easy processability and tunable band gap makes them promising candidates.

Dye-sensitised solar cells (DSSCs) were first developed by Michael Grätzel in 1991.[68] Power generation using organic dyes pre-dates this work, as researchers in the 1960s discovered that organic dyes attached to an oxide, where charge seperation can occur, generate electricity upon illumination.[69] This knowledge did not lead to successful solar cell integration due to the low coverage of dye that was being used. The problem was solved by Grätzel*et al.* who used a mesoporous layer of titania to increase the dye concentration in the device giving an efficiency of 7 %.[68]

This original DSSC used a ruthenium complex as the dye and subsequent research by the Grätzel group on the dye molecule as well as device structure pushed the performance up to 10 % before 2000.[70] The high cost and scarcity of ruthenium has led to research into alternative dyes such as earth abundant metal based dyes and organic dyes.[71,72] Dyes made with more abundant metals are still outperformed by ruthenium devices. In 2015, devices made using metal free organic dyes produced an efficiency of 14 %, comparable to the best performing ruthenium devices.[73] Dye cells have struggled to break into a commercial setting for multiple reasons. These include the high cost of ruthenium dyes, an inability to increase efficiencies beyond 15 %, the use of environmentally unfriendly $I^-/I_3$ redox couple and corrosive liquid solvents.[74]

## 1.3 Perovskites

### 1.3.1 The Emergence of Perovskites

In 2009, while researching DSSCs, Kojima *et al.* used an organometal halide perovskite as the dye and fabricated a solar cell with an efficiency of 3.8 %.[75] While not breaking any records for dye cells, the potential of the perovskite absorber layer has since led to the creation of its own field of solar research. Perovskite is the name given to the mineral $CaTiO_3$ that was first discovered in 1839 by Lev Perovski. The name is now used to describe the crystal structure

of $CaTiO_3$ and any other material with the same structure (Figure 1-3). The standard chemical formula of a perovskite is $ABX_3$, where A and B are cations and X is an anion. The valency of the three ions can either be $A^{2+}B^{4+}X^{2-}$ or $A^+B^{2+}X^-$ for example $CaTiO_3$ or $CsPbI_3$. Differences in size between A,B and X can lead to distortion of the crystal structure or the formation of different structures.[76] Structural distortion will be discussed in more detail in section 1.4.4.
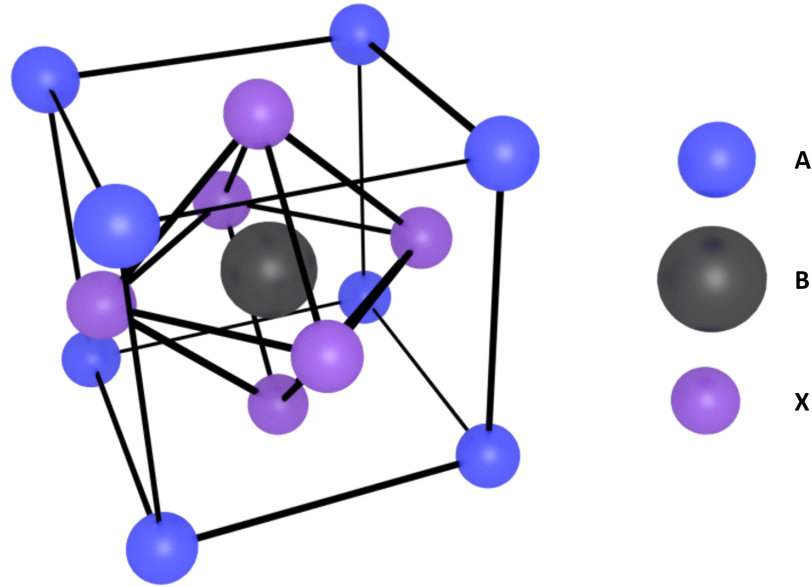


Figure 1-3: The $ABX_3$ structure commonly known as the perovskite structure where A and B are cations of different sizes and X is an anion to balance the charges.

Hybrid organic inorganic perovskites, where A is a methylammonium cation ($MA^+$), B is $Pb^{2+}$ and X is iodide were first characterised in 1978 by Weber.[77] After the initial characterisation, very little research was done on lead halide perovskites until the early 2000s when Mitzi and co-workers began to investigate their possible use in thin-film transistors and light emitting diodes.[78,79] Again, there was a period where very little hybrid lead halide perovskite research occurred until Kojima *et al.* prepared a perovskite DSSC in 2009. Shortly after that Im *et al.* fabricated hybrid perovskite quantum dots and used them to make a QD DSSC with 6.5 % efficiency.[80] These perovskite solar cells were extremely unstable as the liquid electrolyte, used as a redox couple, degraded the perovskite material.
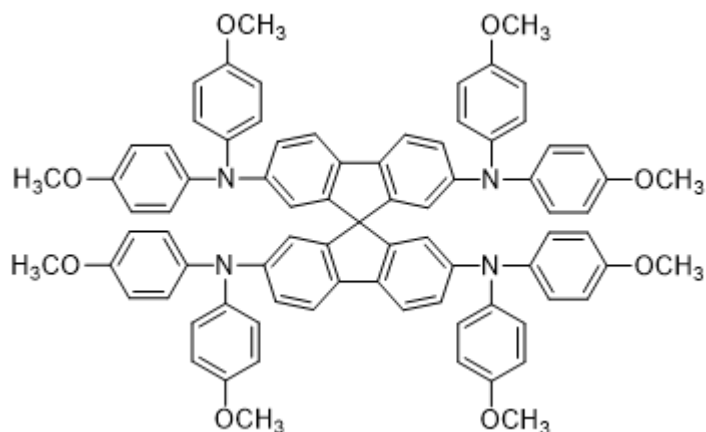
Figure 1-4: Chemical structure of Spiro-OMeTAD

The next step in PSC development came in 2012 when Kim *et al.* used a solid hole transport material to replace the liquid redox couple.[81] The material in question, 2,2,7,7-tetrakis (N,N-di-p-methoxyphenylamine)-9,9-spirobifluorene (Spiro-OMeTAD) (Figure 1-4), helped improve the efficiency of cells to over 9 % and simultaneously improved the stability of the devices.

Later in 2012, and within less than ten days of each other, Snaith and co-workers and Grätzel and co-workers published papers on perovskite solar cells. In the research by Snaith, mesoporous cells of up to 8 % were manufactured but, far more interestingly, a new device architecture was put forward that increased the efficiency of the cells to over 10 %.[82] The paper by Grätzel removed the hole transport layer while maintaining efficiencies of over 7 % therefore showing that perovskite could act not only as an absorber but as a hole transporter layer.[83]

Since 2012, the amount of research into the area of perovskite solar cells has increased dramatically with Figure 1-5 showing the number of perovskite papers being published each year. At present the highest power conversion efficiency (PCE) recorded for PSC is 23.7 %..[24] The device efficiencies are starting to challenge those of the top silicon cells.[24] This review will outline the key milestones in perovskite solar cell research as well as some of the key problems with the technology. This discussion is followed by a more focused look into the areas of perovskite research most relevant to this thesis.
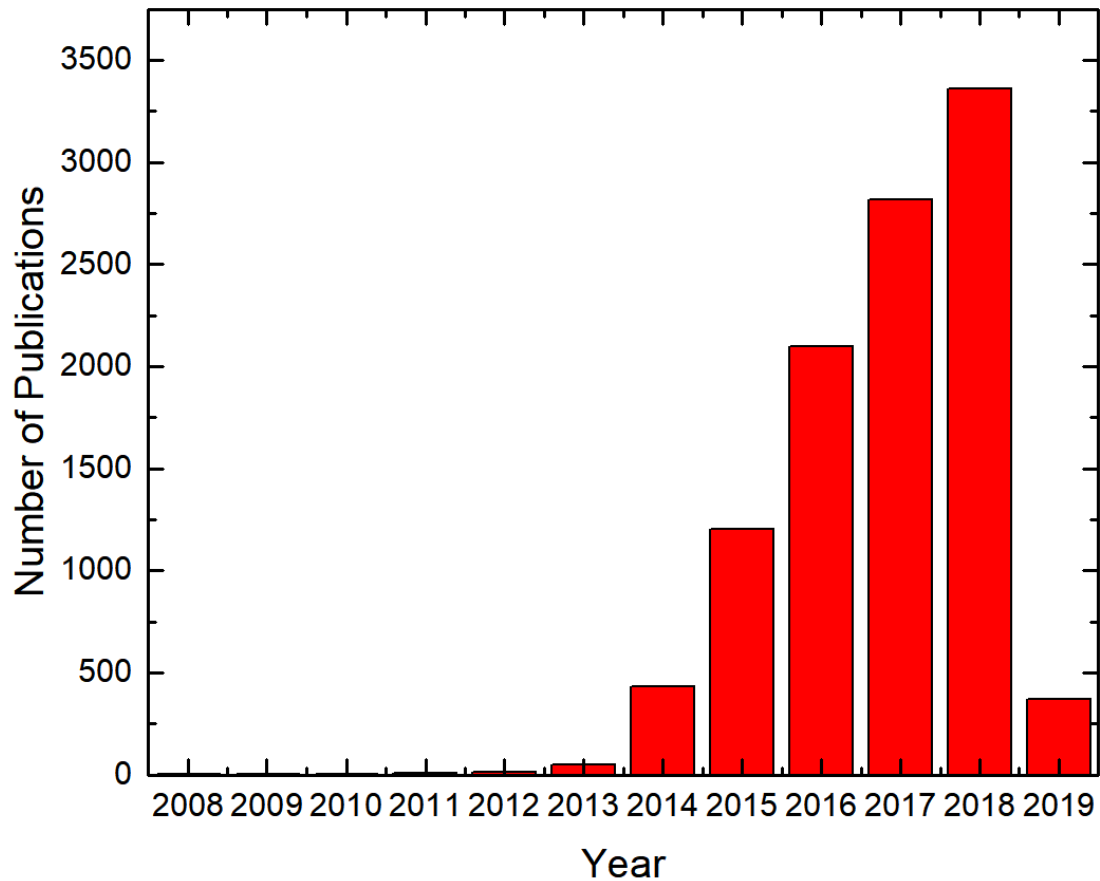
Figure 1-5: The number of perovskite solar cell publications per year. The data was sourced by searching Web of Science for articles with the topic 'Perovskite Solar Cells' on the 1st of February 2019.

## 1.4 Key Developments in Perovskite Research

### 1.4.1 Different Perovskite Architectures

When constructing a perovskite solar cell device a perovskite absorber layer is sandwiched between two extraction transport layers, one for holes and one for electrons. PSCs can come in a variety of different architectures. The two most common architectures are planar heterojunction and mesoscopic. Within those two classes are different subclasses. Planar cells can be 'inverted' or 'conventional'. Mesoscopic cells include titanium oxide based, aluminium oxide based and carbon based architectures (Figure 1-6). As PSCs were first discovered by researchers investigating dye cells, the initial PSCs were commonly made with a mesoporous $TiO_2$ layer as was the standard with dye cells. The mesoporous ar-

chitecture consists of a transparent conducting oxide substrate (TCO) substrate, a compact TiO$_2$ layer, a mesoporous oxide layer with perovskite deposited into it, a hole transport layer and finally an electrical contact (Figure 1-6b).
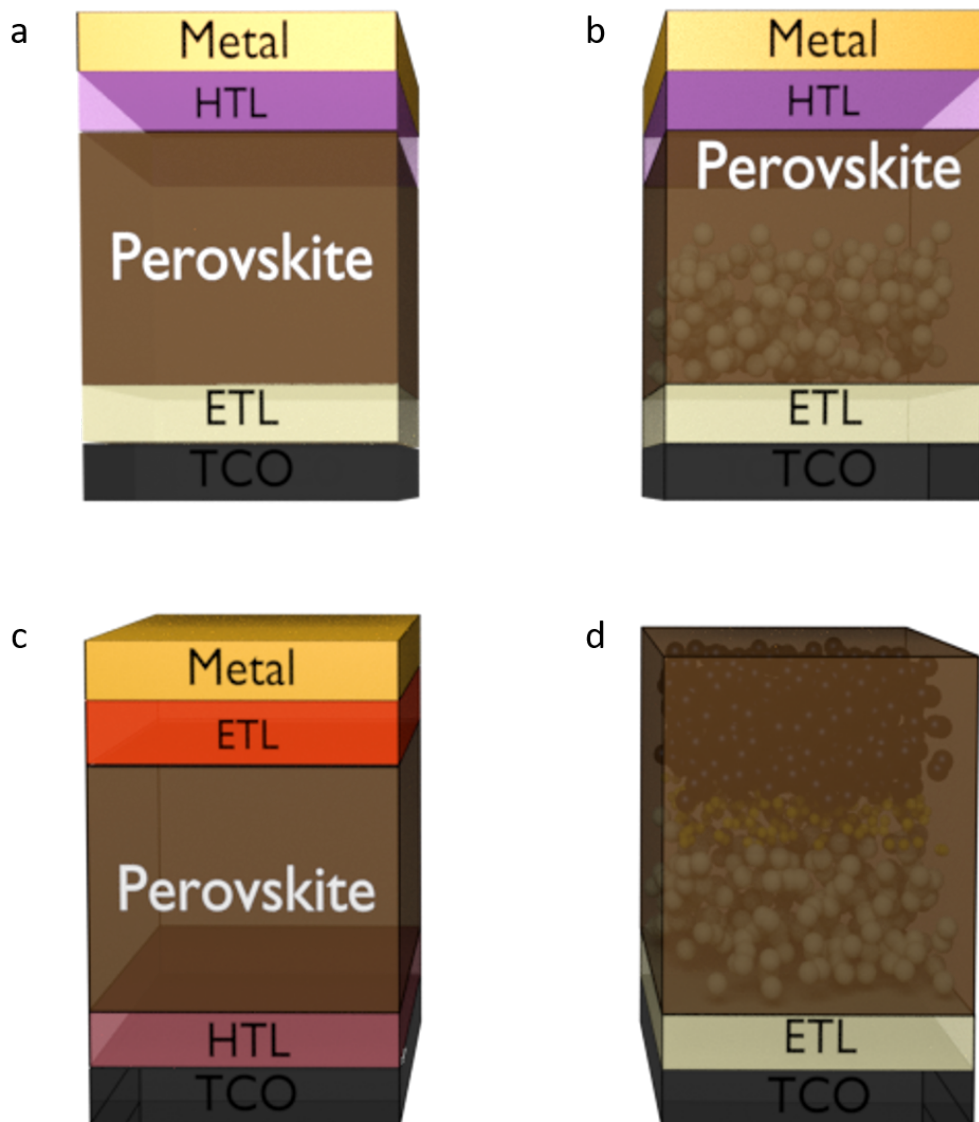


Figure 1-6: The four most common PSC architectures, a) planar cell, b) mesoporous cell, c) planar inverted cell and d) mesoporous carbon cell. The white spheres represent mesoporous titania, the small yellow spheres represent a mesoporous zirconia layer and the black spheres are mesoporous carbon.

The benefits of a mesoscopic scaffold are still unclear, there is still debate on whether the layer improves cell performance.[84] What has been shown, is that the thickness of the mesoporous layer can have an affect on the efficiency of the solar

cell. Thinner mesoporous titania layers of 300 nm have been shown to produce superior cells.[85] Snaith and co-workers presented a novel mesoscopic solar cell structure using the insulating material $Al_2O_3$ as the mesoscopic layer.[82] The cells containing insulator were more efficient than those containing $TiO_2$, showing that the perovskite could generate carriers and also transport them.

Liu *et al.* then showed that the mesoscopic layer was not needed at all. They produced the first example of a planar perovskite solar cell removing the mesoporous layer and depositing perovskite straight onto the compact $TiO_2$ layer (Figure 1-6a).[86] Planar cells are easy to fabricate and have produced high efficiency solar cells but the top performing devices still use a mesoporous layer.[87,88]

The next type of standard cell architecture was developed in 2013 by Jeng *et al.*[89] In this work they inverted the device to transform the cell from a n-i-p architecture to a p-i-n architecture. This initial work used poly(3,4-ethylenedioxythiophene)poly(styrene-sulfonate) (PEDOT:PSS) as the hole transport layer and then bathocuproine (BCP) as the electron transport layer, subsequent work replaced BCP with $PC_nBM$ giving rise to the standard inverted perovskite architecture (Figure 1-6c).[90] Inverted cells can be fabricated at low temperature (<150 °C) meaning that flexible cells can be produced easily giving inverted cells a wider range of possible applications.[91]

The final standard architecture seen in literature is the carbon based design shown in Figure 1-6d. The design was first published by Mei *et al.* who fabricated a device with three different printed mesoscopic layers on a $TiO_2$ compact layer.[92] The first mesoscopic layer was the standard mesoporous titania layer, followed by a thin mesoporous zirconia layer and finally a much thicker layer of porous carbon. Perovskite was then infiltrated into these stacked layers leaving a finished device which did not require an additional hole transporting layer. This type of cell can have very good efficiency and long term stability.[93] The ability of the carbon electrode to protect the perovskite from water has been shown to be the main reason for the observed stability improvements.[94]

## 1.4.2 Tandem Cells

The efficiency of a single junction solar cell is fundamentally limited to an efficiency between 31 % and 33 %. This efficiency limit is known as the Shockley-Queisser limit.[95] As the record efficiencies of perovskites, silicon and other thin films have begun to approach this limit, multi-junction cells are the only way to make devices that perform beyond the Shockley-Queisser limit. This is why tandem cells have become an area of increased interest in the PV research community.
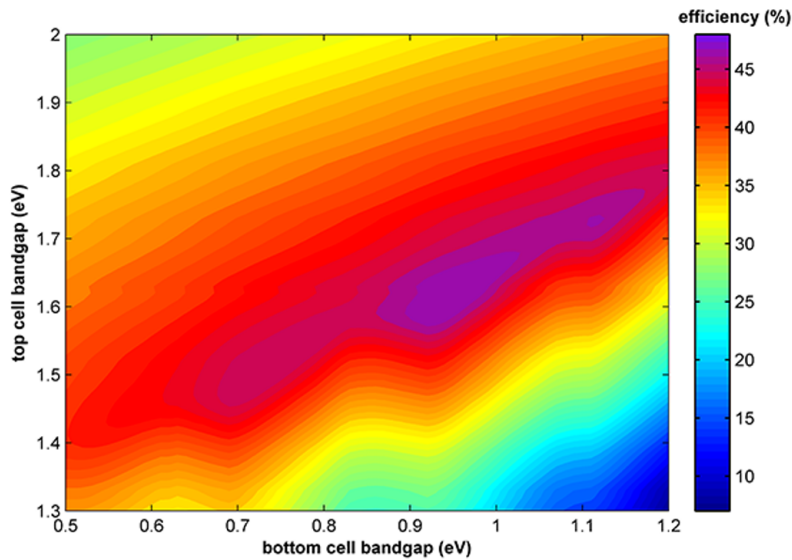


Figure 1-7: The theoretical maximum efficiency of a two junction tandem cell under standard conditions based on different band gaps of the top and bottom cell.[96]

A simple tandem device contains two different absorber layers connected in series. The top absorber layer often has a larger band gap which allows it to absorb high energy photons while the lower energy photons pass through. The lower energy photons are then absorbed by the bottom absorber layer which has a narrower band gap. The theoretical efficiency that is possible with a double junction tandem device varies over a 2D space depending on the band gap of the top and bottom cells (Figure 1-7).[96] The appeal of perovskites as a top cell is the tunable nature of the band gap. If silicon ($E_g$ 1.1 eV) is used as the bottom cell then a perovskite band gap of approximately 1.7 eV could theoretically lead to the highest efficiency. With respect to the published literature, there have been

15

many different tandem cells made with various different peroskites.[97] At present the highest efficiency perovskite/c-Si tandem is 26.6 %.[98]

## 1.4.3 Different Processing Methods for Perovskite Layers

The use of different cell architectures is only one way in which PSCs have changed over the last few years. The perovskite layers in the first devices were fabricated with a simple spin coating step followed by a 45 minute anneal at 100 °C.[82] This processing method, while simple and effective, was not the optimal process for making high quality films. It was realised early on that high quality films were an integral part of making high efficiency devices and therefore an optimised processing methodology was needed. Another important consideration is that layer production should be scalable so as to be commercially viable. Spin coating is not a scalable technique and is not commercially viable. Due to these important factors, much research has focused on processing methods in an attempt to maximise both efficiency and commercial viability.

PSCs are still mostly solution processed in either a one or two step process. The one step process involves a precursor ink containing the lead source, cation and anion whereas in the two step processes a thin film of the chosen lead source is deposited and then the perovskite is formed using a separate solution containing the cation.

**One-Step Spin Coating Deposition Methods**

Simple one step spin coating is still one of the most commonly used methods for depositing the absorber layer. Research has shown the optimum sample annealing temperature is 100 °C for at least 60 minutes.[99] Also important to producing high quality PSCs is the humidity of the environment in which the material is deposited and annealed. Relative humidity of between 30% and 40% produce the highest efficiency cells when the cells are made in ambient atmosphere.[100] The performance of these cells however, is substantially below the best cells produced in inert atmosphere glove boxes.

A newer, highly popular method of fabrication that reduces anneal time and also gives rise to high quality films, is the use of an anti-solvent deposited onto the

16
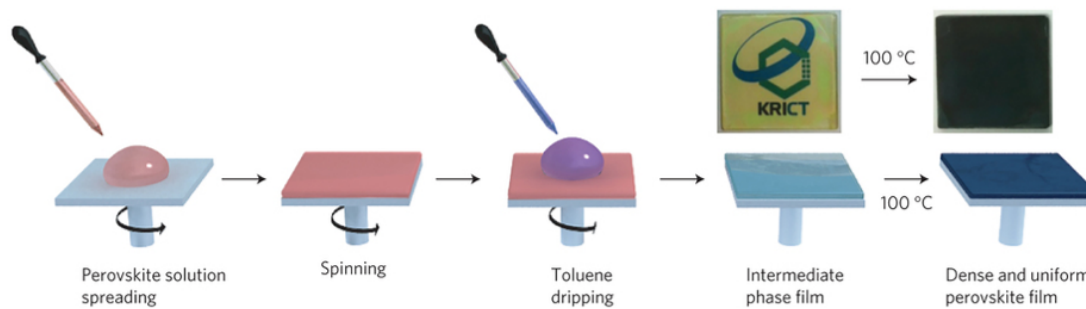
Figure 1-8: Schematic showing the toluene dripping process for manufacturing high quality perovskite thin films reproduced with permission from.[101]

perovskite during spin coating.[101] During spin coating the addition of the anti-solvent replaces the initial solvent causing rapid formation of a densely packed uniform perovskite layer with just a short annealing time of 10 minutes needed to remove any remaining solvent.[102] This method was first reported by Jeon *et al.* when they used toluene as the anti-solvent producing cells with efficiencies equivalent to the standards at the time (Figure 1-8).[101] Since this publication diethyl ether, chlorobenzene and ethyl acetate have been presented as promising anti-solvents for perovskite processing.[103–105] All of these have been used to produce high efficiency solar cells in inert atmospheres but ethyl acetate has proven to be affective in making high quality films up to humidities of 75 %. The water affinity of ethyl acetate preferentially sequesters the water from the nearby atmosphere preventing it from reacting with the perovskite film.[106]

High quality thin films were fabricated by Li *et al.* by spin coating perovskite and removing the solvent at a pressure of 20 Pa.[107] Devices with an efficiency of 19.6 % were made using this vacuum assisted solvent removal method. This method produces comparable devices to the anti-solvent deposition methods but with less wasted solvent. Other solution based one step deposition methods have been presented that efficiently crystallise the perovskite and remove the solvent from the film. These include flash annealing, where an short high energy burst of light is used to almost immediately anneal the substrate, this method reduced the annealing time to 1 ms with only a small drop in overall device efficiency.[108]

17

## Two-Step Spin Coating Deposition Methods

Two step deposition of hybrid perovskites was presented well before their use in solar cells by Mitzi *et al.*.[109] Two step deposition for perovskite solar cells was first reported by Burschka *et al.* in 2013.[110] In their work, they prepared a $TiO_2$ mesoporous layer which was infiltrated with $PbI_2$ deposited by spin coating from a solution of dimethylformamide (DMF). This substrate was then dipped into an isopropanol (IPA) solution containing $CH_3NH_3^+I^-$. An immediate colour change from yellow to dark brown was observed. This method produced high quality, compact and pinhole free films leading to cells with an efficiency of 15 % which was the highest reported efficiency at the time.

The two-step deposition method was first used by Liu *et al.* to fabricate planar solar cells.[111] The efficiency of planar two-step cells was pushed above 15 % by Docampo *et al.*.[112] In their work they used a mixed cation solution of methylammonium iodide and methylammonium chloride to produce high quality films. Further research into the deposition of the $PbI_2$ layer investigated the use of dimethyl sulfoxide (DMSO) as the solvent, as it retarded the crystalisation of the $PbI_2$ layer by coordinating strongly to $PbI_2$. This delay in crystallisation lead to more complete conversion of $PbI_2$ to MAPI with a smaller variation in particle sizes giving more reproducible higher performance films.[113] Ching *et al.* showed that small percentages of water in the precursor mixture can help to improve performance pushing the efficiencies above 20 %.[114]

Improving the quality of the $PbI_2$ film has proved to be an important part of producing good quality films from two step deposition. Treating the film with an organic solvent vapor of either toluene and chlorobenzene is one possible way to improve film quality.[115] The solvent vapour treatment increased the $PbI_2$ grain size and also the porosity which led to improved penetration of the MAI producing more complete transformation of the $PbI_2$ to methylammonium lead iodide (MAPI). This method of treatment produced devices with almost double the efficiency of control cells.[115] A method without thermal annealing in ambient air has been presented by Yang *et al.*.[116] They spin coated the initial $PbI_2$ layer then subsequently spin coated an MAI layer before leaving the $PbI_2$/MAI bilayer to mix under ambient conditions. This method produced good quality films and

efficient cells at a humidity of up to 30 % in just 30 minutes.

A two step deposition method free of hazardous solvents has also been shown to produce good performance devices while removing the need for DMF or DMSO. Using $Pb(NO_3)_2$ instead of a halide based lead precursor the initial lead layer can be deposited from an aqueous solution and then the cation and anion are added by dipping the perovskite in an IPA solution of MAI.[117] PbO has also been used instead of $PbI_2$ with the PbO layer electrodeposited and then converted to MAPI in a second step. Cells made this way were highly reproducible with good efficiencies and the waste from spin coating is minimized.[118]

$PbI_2$ films can be converted to MAPI using MAI vapour and a low vacuum. This technique produces PSCs with similar efficiency to those fabricated using a standard two step deposition.[119] The $PbI_2$ film was deposited then a small amount of MAI was placed on a hot plate and then covered by a desiccator lid to provide a small vacuum. This produced highly crystalline films in just 30 minutes.

**Other Deposition Methods**

Spin coating as a deposition method is restricted to small substrate sizes. To become competitive with silicon PV it must be possible to deposit PSCs on a larger scale. To solve this scalability issue other deposition methods have been presented as possible solutions. One method of making smooth large area films is through vacuum deposition. This can be achieved by thermal evaporation of either two separate precursors or a single precursor source under a high vacuum.[86,120] The films made using high vacuum deposition are often high quality leading to high performance cells but the equipment cost can be prohibitive for lab research.[121]

Doctor blading is a method of deposition commonly used in the solar research community to deposit mesoporous $TiO_2$ layers in DSSCs and is a proven method of perovskite deposition on larger scales. Initially MAPI devices with an efficiency up to 16 % were made using doctor blading[122] and since then efficiencies over 19 % have been achieved with mixed perovskite systems.[123] The previously mentioned cells were all small area cells but when the area is increased to $1\,cm^2$ the resulting efficiencies are 7 %.[124]

Another method that can be adapted to roll to roll is spray coating. In 2014,

Barrows *et al.* used ultra sonic spray coating in ambient conditions to produce mixed halide devices with an efficiency of 11 %.[125] Das *et al.* also used a similar method to fabricate devices with efficiencies up to 13 %.[126] In this method the precursor solution is fed into a high frequency ultrasonic nozzle which turns the solution into micrometer size droplets that are then sprayed onto the hot substrate. A systematic study into ultrasonic spray coating showed the importance of film morphology and how precursor stoichiometry and solvent can impact it.[127] A simple spray coating method using just an airbrush was used to produce small area cells with an efficiency of 18 %.[128] More impressively in this work was the $10\,cm \times 10\,cm$ sized substrate with an active area of $40\,cm^2$ that was fabricated. This large area device had a top efficiency of 15 %.

The method of choice for deposition has a big impact on device efficiency mainly through altering the quality of the the thin perovskite film. The early methods of spin coating still prove to be very effective for lab scale devices especially when an anti-solvent is used. Scaling up presents different fabrication issues but several methods look promising for further development of large scale devices.

## 1.4.4   Changing the Perovskite Material

The perovskite composition has a lot of flexibility in its possible components and there being hundreds of perovskites with different compositions already discovered. Altering the components of the material has been an important area of research due to the ability to control material properties, such as band gap, using only slight modifications of the material. As long as the charges balance, there is only one limiting factor when it comes to selecting what to alter in the $ABX_3$ composition. In order to keep the 3D perovskite structure of MAPI, ions within a fixed size range need to be used. V. M. Goldschmidt developed a tolerance factor apporach and used the ionic sizes of the different perovskite components to produce a single value, $\alpha$.[129]

$$\alpha = \frac{r_A + r_X}{\sqrt{2}(r_B + r_X)} \tag{1.1}$$

Equation 1.1 is used to calculate $\alpha$ where $r_A$, $r_B$ and $r_X$ are the ionic radii

3D                                    2D
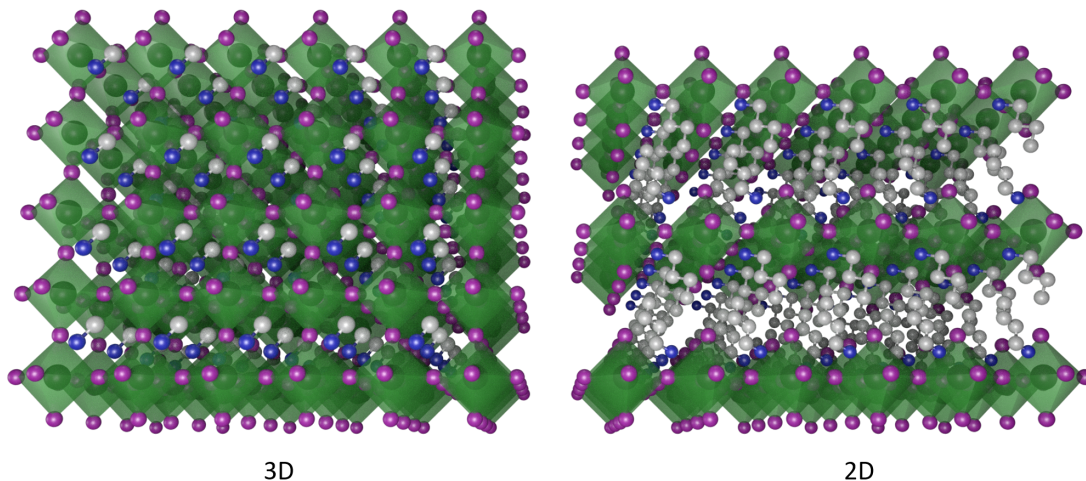
Figure 1-9: The structure of 3D and 2D perovskites.

of their respective components. If the value of $\alpha$ is greater than 1 then it is likely that a 2D perovskite will be formed (Figure 1-9); if it is between 0.8 and 1 then the resulting structure will be a 3D perovskite (Figure 1-9). Finally, if $\alpha$ is less than 0.8 then it is unlikely that a perovskite structure will form due to the difference between the size of the two cations. In this section the different ways the basic MAPI structure has been altered and how this affects its properties will be discussed. The discussion will initially focus on 3D perovskites but 2D and 2D/3D hybrid perovskites will be touched on at the end of the section.

**Changing the A-site Cation**

The original PSCs all contained methyl ammonium as the organic cation but since then several others have been shown as possible replacements improving the perovskite performance or stability. As previously stated the tolerance factor is an important metric when it comes to determining if a certain sized cation will form a 3D perovskite or not. With this in mind Kieslich *et al.* produced a wide ranging tolerance factor study investigating 13 different cations varying in size from tropylium (a seven membered aromatic ring with the formula $[C_7H_7]^+$) to ammonium.[76,130] Their calculations showed that, for lead iodide based per- ovskites, there were six amine based cations that gave a tolerance factor between 0.8 and 1. The structures of these 6 cations is shown in Figure 1-10.

At the time the predictions were made (2015) methylammonium and for-
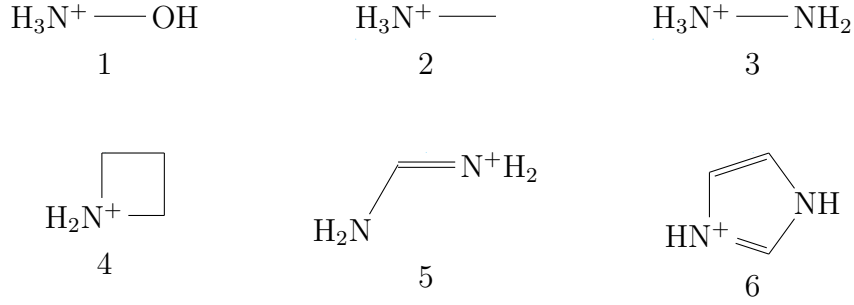
Figure 1-10: The six organic cations predicted by Kieslich *et al.* to form 3D perovskites with Pb and iodide. 1) Hydroxylammonium, 2) methylammonium, 3) hydrazinium, 4) azetidinium, 5) formamidinium and 6) imidiazolium.

mamidinium (FA) perovskites had already been fabricated and used in PSCs. MA were the first cations used and then FA PSCs were fabricated by Eperon *et al.* in 2014.[131] Eperon *et al.* investigated $FAPbI_xBr_{3-x}$ perovskites and how altering the Br percentage helped to tune the bandgap. As a part of this study, it was shown that films of $FAPbI_3$ (FAPI) had a band gap 1.48 eV which is lower than MAPI ($\approx 1.55$ eV) and closer to the optimal band gap for PV devices (between 1.1 and 1.4 eV). Devices fabricated with pure FAPI had an average efficiency of 9.7 %.

FAPI solar cells can suffer from low fill factors caused by the existance of two polymorphs at room temperature, the first is black $\alpha$-$FAPbI_3$ and the second is yellow $\delta$-$FAPbI_3$. These two phases were first observed by Stoumpos *et al.* who performed an in depth crystallographic analysis of several different perovskite structures.[132] They showed that the $\alpha$ phase is the standard 3D perovskite structure but the $\delta$ phase is made up of face sharing $PbI_6$ octahedra. Incomplete formation of the $\alpha$ phase or degradation to the $\delta$ phase have both been shown to restrict the performance of pure FAPI PSCs.[133]

Mixing of MA and FA has proved to be an excellent strategy to improve performance of perovskite solar cells with the first example by Pellet *et al.* producing films with a better optical band gap by two step deposition. Using a variety of compositions they showed that $MA_{0.6}FA_{0.4}PbI_3$ produced the highest efficiency cells of 13.4 %.[134] Improvements in film quality, investigation of different depositon methods and device architectures has led to an increase in the efficiency of mixed MA/FA perovskites up to 18.3 %, with $MA_{0.6}FA_{0.4}$ being the

best performing stoichiometry.[135–138]

Of the other cations predicted by Kieslich *et al.* hydrazinium and azetidinium have both been used to either partially or fully substitute MA in PSCs. In the case of Hz, fully substituting MA led to a complete a loss of performance caused by the apparent formation of a non-perovskite phase. The best stoichiometry for Hz/MA mixtures was 10 % Hz which gave a very small increase in device performance driven by a small increase in $J_{sc}$ that was attributed to an improvement in light absorbance and enhanced crystallinity.[139] For $AzPbI_3$, an orange material is formed with a unique structure giving the material increased water resistance.[140] Doping MAPI films with small amounts of Az (1 mol%) decreased the device hysteresis without sacrificing overall performance.

The remaining two cations, imidazolium and hyroxylammonium, have not yet been used in PSCs. Hyroxylammonium has been used as the cation to fabricate hydroxylammonium lead chloride perovskites for photocatalysis but its band gap, 3.8 eV, is not applicable for use in PV devices.[141] There is just one example of an imidazolium lead iodide perovskite that was synthesised by Weber *et al.* with the structure of the material being 1D face-sharing chains surrounded by imidazolium cations.[142] This 1D structure is not conducive to PV applications due to restricted charge transfer and poor light absorbtion.

The final organic cation used to fabricate PSCs was included in the Kieslich study but its tolerance factor fell slightly above 1 meaning the predicted structure is some form of 2D perovskite. This cation, guanidinium, was shown to form a 3D perovskite by Dimesso *et al.* who subsequently manufactured PSC devices using 100 % GA perovskites resulting in efficiencies of 0.3 %.[143] Using a 6:1 ratio of MA to GA it is possible to slightly improve overall device efficiency when compared to a pure MAPI device.[144] This increase in efficiency is caused by an increase in $V_{oc}$ that was attributed to improved carrier lifetime.[145] It was suggested by De Marco *et al.* that increased bonding from the three amine head groups of GA passivates under-coordinated iodide ions located in the material. Since the Dimesso paper, GA has been used to make mixed cation $MA_{1-x}GA_xPbI_3$ cells.[145] The optimised cation ratio of 14 % GA led to cells with efficiencies above 20 % and a longer lifetime than MAPI control cells.

Fully inorganic PSCs have also been investigated, with caesium as a replacement for MA. Thin films of $CsPbI_3$ form a yellow non-perovskite structure at room temperature known as $\delta$-$CsPbI_3$. The band gap of $\delta$-$CsPbI_3$ is approximately 2.8 eV which is higher than the ideal value for PV applications.[146] It is possible to cause this yellow phase to undergo a transition into a cubic black phase ($\alpha$-$CsPbI_3$) with a band gap of 1.73 eV by heating the film above 100 °C in the presence of hydroiodic acid.[147] $\alpha$-$CsPbI_3$ is unstable in ambient conditions and degrades back to $\delta$-$CsPbI_3$ via an orthorhombic $\gamma$-$CsPbI_3$ structure.[148] Encapsulated devices fabricated in an inert atmosphere and tested under vacuum have produced efficiencies of 1.3 %, far below that of MAPI.[147]

While not being a success as the only counter ion in the system, Cs has been used in mixed cation perovskites. Doping of a MAPI film with 10 % Cs causes an increase in $V_{oc}$ and $J_{sc}$ due to an improvement in film morphology giving an overall 20 % increase in efficiency when compared to a MAPI reference.[149] The first study used an inverted cell architecture and a subsequent study using a mesoporous architecture and 9 % Cs doping produced devices with a 15 % improvement in efficiency compared to MAPI reference cells as well as improved thermal stability.[150]

Another mixture of A-site cations that has been shown to produce high quality cells is Cs and FA. Lee *et al.* mixed Cs and FA in a perovskite device for the first time showing that just 10 % Cs helped gave a modest increase in efficiency when compared to pure FAPI devices.[151] As well as the efficiency improvement, the moisture and photo stability of the perovskite films is increased. They hypothesised that the $Cs^+$ causes a contraction of the perovskite lattice increasing the interactions strength between the FA and the surrounding iodide ions. The mixing of Cs and FA helps to stabilise the desirable $\alpha$ phase by tuning the tolerance factor by mixing a low tolerance factor perovskite with a high tolerance factor perovskite.[152]

**Changing the X-site Anion**

The ability to tune the properties by altering the anion in PSCs has proven to be a very useful way of helping to develop the current optimum devices. The

most obvious alternatives to iodide are the other halogens; bromide, chloride and fluoride. The most investigated halogens apart from iodide are bromide and chloride. Fluoride is too small to allow most cations in the lattice and precursors containing $F^-$ anions can be extremely hazardous. Incorporating fluoride ions into perovskites has not been successful. Nagane *et al.* did manage to incorporate fluorine into a PSC in the form of the pseudohalide $[BF_4]^-$.[153] They showed a small increase in wavelength of photoluminescence but did not make any functioning PSCs so its affect on performance is unknown.

In 2013, Noh *et al.* showed the effect of different stoichiometric ratios of iodide and bromide in MAPI.[154] They varied the amount of bromide between 0 % and 100 % showing a quadratic relationship between band gap derived from absorption edge and Br composition (Equation 1.2) where $x$ is the composition of Br in a perovskite with the formula $MAPb(I_{1-x}Br_x)$ (Figure 1-11a).

$$E_g(x) = 1.57 + 0.39x + 0.33x^2 \qquad (1.2)$$

The most important conclusion from this work, was showing that the efficiency of devices made with I/Br did not decrease a lot up to 30 % Br, but extra bromide massively increased the long term stability of the devices. They showed that the optimum ratio was 4:1 I:Br, with this giving the best efficiency to stability trade off (Figure 1-11b).

A second equation has also been published that used Tauc plots instead of absorption onset (Equation 1.3) to predict band gaps..[155]

$$E_g(x) = E_{I3} + (E_{Br3} - E_{I3} - b)\frac{x}{3} + b(\frac{x}{3})^2 \qquad (1.3)$$

In Equation 1.3 $E_{I3}$ is the band gap of MAPI, $E_{Br3}$ is the band gap of MAPBr, $b$ is the bowing parameter and $x$ is the amount of bromide in the material. The bowing parameter is needed as the composition disorder of the material causes the valence and conduction band edges to change. The use of the Tauc method gave band gap values that were a few meV different to that from absorbance edge analysis.

Hoke *et al.* have observed photoinstability in mixed iodide:bromide per-ovskites.[156] They performed photoluminescence experiments and the response of the perovskite changed with respect to the time under illumination. A new
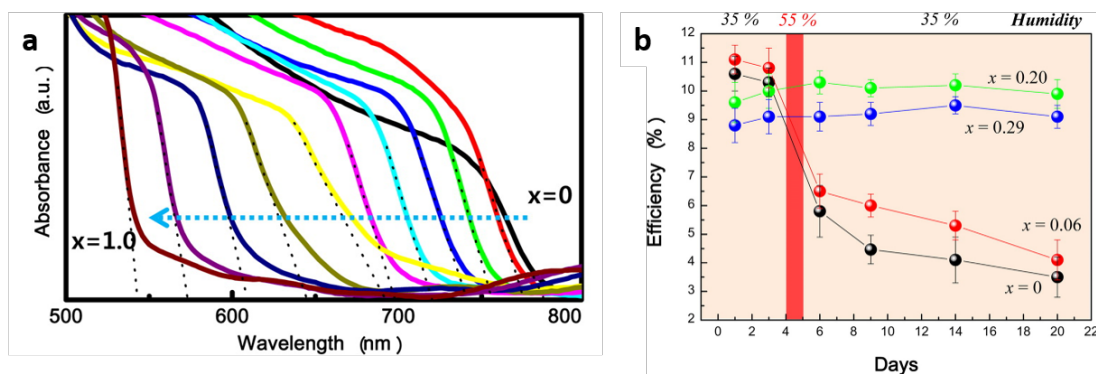
Figure 1-11: Iodide Bromide mixed anion study UV and performance results. Reprinted with permission from.[154] Copyright 2018 American Chemical Society.

peak appeared at $1.68\,\text{eV}$ and if the light soaking lasted over a minute the intensity of the new peak was orders of magnitude larger than that of the usual peak.[156] It was hypothesised that this response was caused by halide segregation into iodide or bromide rich regions. An *in silico* study investigated this further, showing that the phase seperation is a thermodynamic process where the incident light provides the needed energy to cause the material to phase separate. They also proposed a phase diagram where, at $300\,\text{K}$, iodide:bromide perovskites are unstable with a stoichiometry between 30 and 60 % bromide.[157]

Methylammonium lead chloride is not commonly seen in PV research as it forms white films with a band gap of $3.06\,\text{eV}$. Incremental mixing of the quantity of bromide and chloride can lead to a similar trend in band gap as seen with bromide iodide. Covering the full range of mixtures between 100 % iodide to 100 % chloride can give band gaps spanning between $1.5\,\text{eV}$ and $3.06\,\text{eV}$ with the films being coloured from black to red through yellow until they become white.[158]

The incorporation of chloride into MAPI is very common making the mixed anion $MAPI_{3-x}Cl_x$. The first time this perovskite was fabricated was back in 2012 by Lee *et al.* who used a $PbCl_2$ precursor and 3 equivalent of MAI to deposit their perovskite films.[82] They claimed to have formed the perovskite $MAPI_2Cl$ based on X-Ray analysis but subsequently there have been many conflicting reports about whether the Cl is actually present in the final perovskite film.[159] In summary, some researchers have used X-ray diffraction, energy dispersive X-ray spectroscopy, X-ray photoelectron spectroscopy and time of flight single ion mass spectrometry to show Cl is present, but others, using the same techniques, have been unable

to detect Cl.[160–167]

The final option explored for the X-site is the pseudohalide thiocyanate $SCN^-$. $SCN^-$ substitution was first presented in 2015 by Jiang *et al.* who substituted two iodide ions with two $SCN^-$; this substitution enhanced the stability and slightly decreased the performance when compared to MAPI cells.[168] Deposition of a $Pb(SCN)_2$ layer instead of a $PbI_2$ layer in a two step method deposition also led to increased stability despite their being only a small amount of $SCN^-$ remaining in the final film.[169] A similar affect was seen with one step deposition where 5 % of $Pb(SCN)_2$ in the precursor solution produced 19.5 % efficient devices with reduced hysteresis.[170] Mixed cation and anion perovskites with FA, Cs, Iodide and $SCN^-$ have been fabricated with improved stability and moisture resistance when compared to MAPI.[171]

## More Complex Systems

The possibility of combining the different cations and anions in different ways has led to the creation of triple cation mixed anion systems. The first of these was $Cs_x(FA_{0.83}MA_{0.17})_{1-x}Pb(I_{0.83}Br_{0.17})_3$, Saliba *et al.* used this perovskite with 5 % Cs to fabricate mesoporous devices with an average efficiency of 19 % with the best device having an efficiency of 21.1 %.[87] These devices were also stable for at least 250 hours.[87] Another triple cation mixed anion system was studied by Duong *et al.* and Zhang *et al.* who used Rb instead of the Cs used by Saliba *et al.*. Once again 5 % of Rb was the optimum amount to use and devices made with $Rb_{0.05}FA_{0.80}MA_{0.15}Pb(I_{0.85}Br_{0.15})_3$ were comparable in performance to the triple cation containing Cs.[172,173]

It is possible to remove the MA entirely. Saliba *et al.* fabricated devices containing three different ratios of Rb, Cs and FA with $Rb_{0.05}Cs_{0.10}FA_{0.85}Pb(I_{0.83}Br_{0.17})_3$ producing the highest efficiency (19.3 %) devices.[174] The only limiting factor when incorporating Rb into perovskites is that, at Rb ratios over 10 mol% Rb, a Rb rich phase forms which reduces cell performance.[172] There is also some dispute about whether $Rb^+$ is incorporated into the lattice. Uchida *et al.* used XRD analysis to show that $Rb^+$ is not incorporated into the lattice.[175]

Saliba *et al.* continued their work into cation substitution by being the first

group to show that it is possible to fabricate perovskite containing four cations Rb, Cs, MA and FA. The perovskite that produced the highest efficiency cells was $Rb_{0.05}Cs_{0.05}(FA_{0.83}MA_{0.17})_{0.90}Pb(I_{0.83}Br_{0.17})_3$ with an average efficiency of 20.2 %.[174] These quad cation perovskites were also used in tandem solar cells by Duong *et al.* who showed that incorporating Rb decreased hysteresis and increased the light stability.[98]

**Reduced Dimensionality Perovskites**

So far, all of the perovskites discussed are 3D perovskites but it is possible to make perovskites with 2D, 1D and 0D. 3D perovskites consist of corner-sharing $PbI_6$ octahedra in all dimensions. This long range order is very important for charge transport and band gaps making the 3D nature important for PV applications. 2D perovskites are made from separate sheets of $PbI_6$ with cations spacers in between the layers (Figure 1-9). 2D and 3D perovskite structures can be merged together to make 2D and 3D hybrid structures, sometimes referred to as Ruddlesden-Popper perovskites. They have the chemical structure $A_{n-1}A'_2B_nX_{3n+1}$ where A is a smaller cation (e.g. MA), A' is a larger organic cation that forms the 2D layered structure (e.g. Butylammonium), B is the metal cation and X is a halide. The most important parameter in 2D/3D hybrid structures is the n value which can range anywhere between 1 and $\infty$. If $n = 1$ then the resulting perovskite will be 2D with single sheets separated by organic spacers. Conversely if $n = \infty$ then it is a 3D perovskite. By varying n, the number of interconnected layers of octahedra there are before an organic spacer layer changes (Figure 1-12).

For 1D perovskites, the octahedra link together forming nanowires that are surrounded by organic cations. One dimensional perovskites have excellent exiton self-trapping properties.[176] Exciton self-trapping is the process where a neutral exciton species has it's lifetime extended as it strongly couples with the lattice vibrations. These interesting self-trapping properties make 1D perovskites an interesting material for possible use in white light emitting materials, the discovery of which could revolutionise light generation.[177] Finally, in 0D perovskites the octahedara are not connected to each other and each one is fully surrounded by

n=3                               n=2
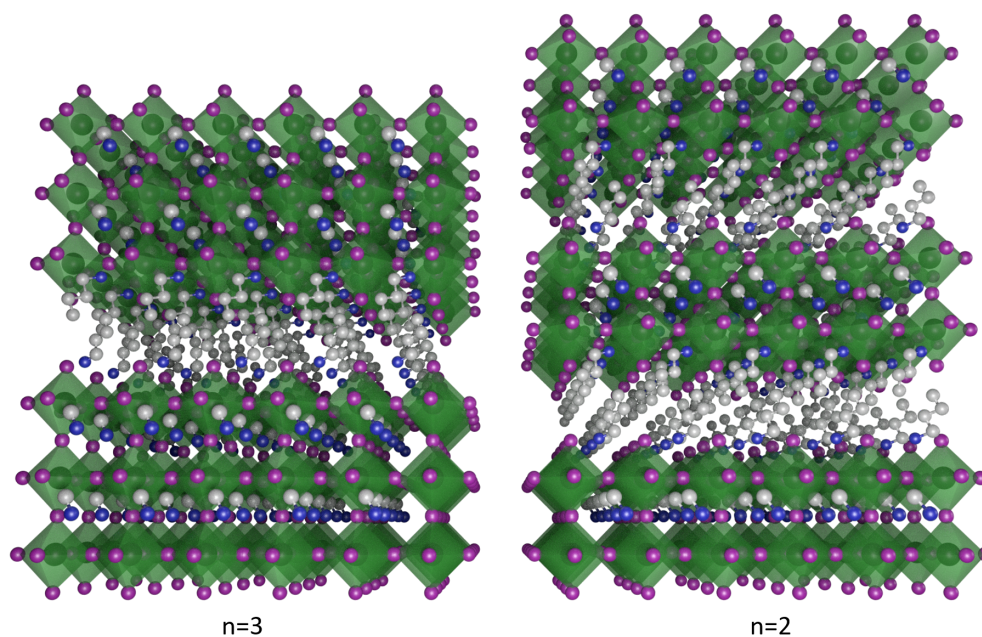
Figure 1-12: Diagram showing the changes in 2D/3D hybrid perovskites based on changing the n value.

organic cations (Figure 1-13). When it comes to zero dimensional perovskites, the most famous material is $Cs_4PbBr_6$.[178] The most interesting property of this material is its efficient and stable green luminescence which is of most interest in LED production. Another interesting feature of $Cs_4PbBr_5$ is that has been shown to emit $Pb^{2+}$ ions in the UV-Vis region.[178] While 1D and 0D perovskites have their own interesting properties, 2D, 3D and mixtures of 2D/3D perovskites are at present the most interesting for PV applications and will be the focus of this section.

The first 2D/3D hybrid perovskite used in PSC was made with phenyethylammonium (PEA) as the organic cation.[179] The research focused on $n = 3$ perovskite giving $(PEA)_2(MA)_2Pb_3I_{10}$, and a $E_g$ of 1.61 eV. The group fabricated PSC with their material and observed an increased $V_{oc}$ (1.18 V) when compared to MAPI ($\approx$1 V) as well as a PCE of 7.02 % when using a high scan rate. The stability of films of the PEA based perovskites was shown to be superior to MAPI films. The authors showed there was no increase in the $PbI_2$ peak in the XRD pattern of the material after being stored in a humidity controlled environment for 40 days.

Further investigation of PEA based perovskites was performed by Quan *et al.* who investigated a range of n values between 1 and $\infty$.[180] They showed the
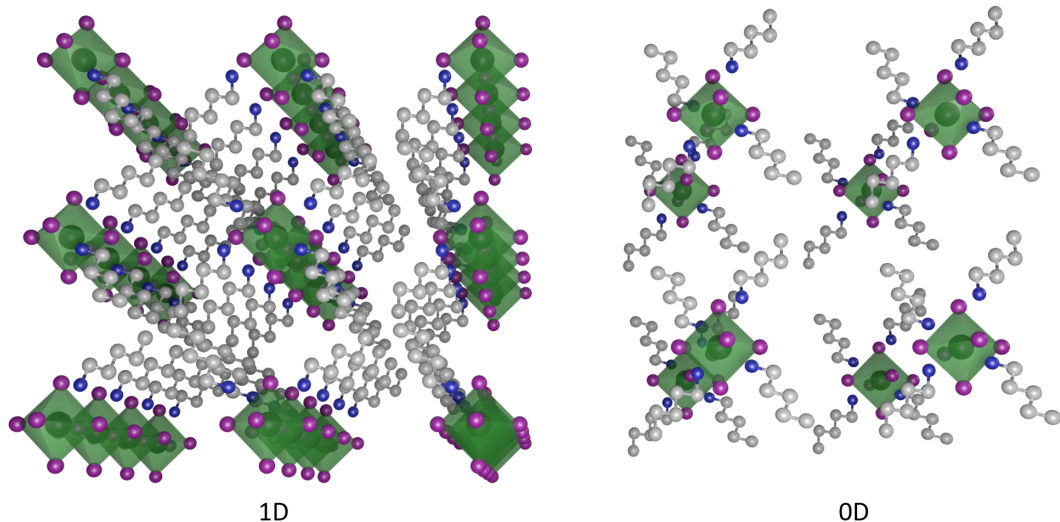
Figure 1-13: Standard structure of 1D and 0D perovskites.

relationship between performance and stability imparted by the 2D/3D hybrid structures. Changing the n value led to a trade-off between performance and stability, where materials with lower n values have increased stability but lower performance in PSC. As n was increased the device performance increased and the stability decreased. Efficient PSC were fabricated with $n = 40$ (17.10 %), $n = 60$ (17.21 %) and MAPI (16.47 %). After 8 weeks the MAPI efficiency had dropped to 0.72 % while the $n = 40$ and $n = 60$ perovskite devices were 13.14 % and 12.80 % efficiency respectively.

Cao *et al.* were the first to use butylammonium (BA) as the organic cation in 2D/3D perovskites.[181] They observed that the bandgap of the material decreased from 2.24 eV to 1.60 eV when n was increased from 1 to 4. They were also the first group to observe the 2θ peak at 8° that corresponds to the (002) plane. This plane cuts through the horizontal centre of the $PbI_6$ octahedra and is indicative of the presence of 2D perovskites (Figure 1-14). Of the devices fabricated in this work, the champion 2D/3D device produced a PCE of 4.02 % a $V_{oc}$ of 929 mV and a $J_{sc}$ of 9.43 mA cm$^{-2}$. The poor performance, especially the low $J_{sc}$, was attributed to poor charge transfer through the perovskite due to the directionality of the $PbI_6$ octahedra. The $PbI_6$ sheets ran parallel to the two transport layers which limited charge transfer.

Yao *et al.* showed the stability of larger devices made using 2D/3D per-
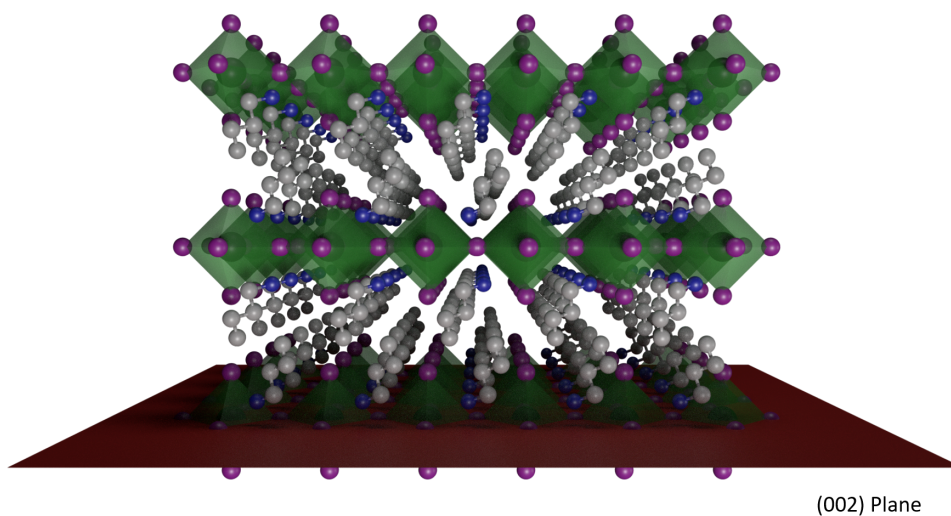
(002) Plane

Figure 1-14: An image showing the (002) plane in a 2D perovskite.

ovskites.[182] They fabricated standard sized devices and larger $2.32\,cm^2$ cells showing that 2D/3D perovskites could give higher performance than 3D MAPI in large scale devices. They also tested the stability of the devices by light soaking them for 500 hours. The 2D devices retained 90 % of their initial efficiency after 500 hours. In contrast the MAPI cells were completely degraded under the same conditions.

A wider range of organic spacers, 1,4-diaminobutane, 1,6-diaminohexane and 1,8-diaminooctane was investigated by Safdari *et al.*[183] These were the first cations with two amine groups to be investigated. The group investigated the optoelectronic properties and the device performance of solar cells containing $n = 1$ perovskites made with the three cations. The band gaps for the perovskites, in ascending order of alkyl chain length of the cation, were $2.37\,eV$, $2.44\,eV$ and $2.55\,eV$. Unsurprisingly, given the band gaps, the performance of devices was inferior to 3D MAPI perovskites. The effect of varying the n value to make MA containing 2D/3D hybrids was not investigated. At present it is not known how the di-ammonium cations affect higher n value perovskites.

Overcoming the low performance of 2D/3D hybrid perovskites was an important challenge and Wang *et al.* took a big step towards having 2D/3D hybrid perovskite compete with their fully 3D counterparts when they fabricated devices

with a champion efficiency of 19.5 %.[184] They used a previously reported FA/Cs cation mixture with small quantities of BA (9 and 5 mol%). Non-encapsulated devices of the 5 mol% BA perovskite retained 80 % of their efficiency after 1000 hours of full spectrum illumination. Encapsulated devices retained 80 % of their efficiency for almost 4000 hours.

Grancini *et al.* used 3 mol% 5-aminovaleric acid mixed into MAPI to produce a 2D/3D hybrid perovskite.[185] An interesting aspect of this work was that the acid group on the larger cation interacted with the mesoporous $TiO_2$ layer creating an area of 2D perovskite on the surface of the $TiO_2$ and mostly 3D perovskite capping the titania. Carbon based devices fabricated in this work were shown to be stable for 10000 hours under illumination.

As previously mentioned, the charge transporting properties of 2D materials are not conducive to high efficiency devices due to the orientation of the network of $PbI_6$ octahedra. It is possible to orient the sheets to improve the properties. Spin coating an $n = 4$ perovskite film of PEA and MA at $150\,°C$ causes the sheets of octahedra to align in a vertical manner, therefore allowing easier transfer of charges between contacts.[186] Non-encapsulated devices of perovskites processed like this produce a PCE of 12.52 % and retain over 60 % of said efficiency for over 2250 hours.

**Changing the Metal**

Finding a replacement for lead, or at least minimising the amount used in a device, is seen as an important step towards large scale PSC adoption. The first metal that was looked into was tin, owing to it having many properties that are analogous to Pb. In 2014 a tin based perovskite $MASnI_3$ was synthesised and tested in PV devices producing a PCE of 6.4 %.[187] The perovskite had to be synthesised and sealed in an inert atmosphere before testing because any contact with air caused almost instantaneous degradation of the material. This degradation was caused by the $Sn_2^+$ oxidising to $Sn_4^+$. A lack of stability in air has been the biggest issue facing tin based perovskites.

Since 2014 the overall performance of tin perovskites has not increased but the stability has been improved by altering the cation from MA to FA. With $FASnI_3$ it

is possible to make devices that are stable for 100 days.[188] Low stability, combined with low efficiency, makes Sn unlikely to replace Pb unless there are some major advances in performance.

A different type of perovskite, known as the double perovskite, has also been predicted as a replacement for lead based perovskites. Double perovskites have the standard formula $A_2BB'X_6$ where A is a cation, X is an anion, B is a +1 cation and B' is a +3 cation. The two different charged cations give an overall charge balanced structure. Splitting the desired charge over two different metals opens up a much larger range of possible materials. Eleven double perovskites were predicted by a computational study to have good properties for PV devices.[189] As of yet only a few of these have been synthesised and only one has been used in a full solar device.[190–193] The best PCE generated by a double perovskite device is only 1.44 %.[193]

## 1.5 Issues with Perovskites

Despite their high efficiencies there are a few keys issues that are preventing commercialisation of PSC, these are toxicity, stability and hysteresis.

### 1.5.1 Toxicity

Perhaps the most obvious issue to people outside the field of perovskite research is the presence of $Pb^{2+}$ as a major component of the absorber layer. MAPI can also be converted into the water soluble compound $PbI_2$ by polar solvents. $PbI_2$ is known carcinogen that is banned in many countries.[194] Throughout history lead has found many uses in bullets, radiation shields, leaded petrol and lead-acid batteries. In the mid 20th century the toxicity of lead was becoming better understood and its use, especially in uncontrolled environments, began to be phased out with the United States of America banning the sale of leaded petrol in 1996. Some of the symptoms of lead poisoning include, neurological damage, central nervous system damage and gastrointestinal issues. Damage is also greater in children than in adults due to accumulation in the body.[195,196]

While removing lead would be highly beneficial to commercialisation of PSC,

there is not a large amount of lead present in a device as the absorber layer is only a few hundred nanometres thick. The low quantity of lead combined with effective encapsulation techniques to prevent leakage into the environment could mitigate environmental toxicity during use.[197] At the end of their life cycle, appropriate disposal and recycling of devices could help to further reduce the issues surrounding lead.[198,199]

## 1.5.2 Stability

Arguably the most important challenge to the commercialisation of PSC is their long term stability. The standard perovskite material, $MAPbI_3$, degrades when exposed to oxygen, moisture, light and elevated temperature.[150,200–202] Degradation by moisture and light is caused by chemical reactions of the perovskite layer, with studies showing that $PbI_2$ and $I_2$ are formed during hydrolytic degradation. A possible reaction scheme is outlined in equations 1.4-1.7, it can be seen that both water and light are needed to cause degradation.[203]

$$CH_3NH_3PbI_{3(s)} \xrightleftharpoons{H_2O} CH_3NH_3I_{(aq)} + PbI_{2(s)} \tag{1.4}$$

$$CH_3NH_3I_{(aq)} \xrightleftharpoons{} CH_3NH_{2(aq)} + HI_{(aq)} \tag{1.5}$$

$$4\,HI_{(aq)} + O_2 \xrightleftharpoons{} 2\,I_{2(s)} + H_2O \tag{1.6}$$

$$2\,HI_{(aq)} \xrightleftharpoons{h\nu} H_2 + I_{2(s)} \tag{1.7}$$
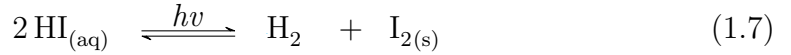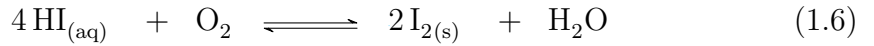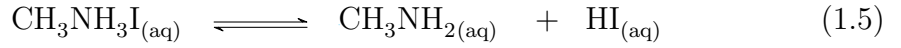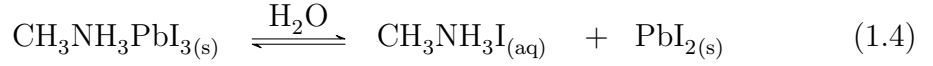
The degradation of MAPI by oxygen is caused by the superoxide $O_2^-$ species. This superoxide deprotonates the organic cation leading to the formation of water, $PbI_2$, methylamine and iodide.[204] Superoxide species are formed more easily in iodide vacancies within the material and therefore removing these vacancies, especially on the surface of crystallites, can improve device stability.[205] MAPI powder is thermally stable to over $300\,^\circ\text{C}$ with degradation being caused by release of HI and methylamine as gases followed by degradation of the lead precursor at an even higher temperature.[206]

Long term stability is the biggest problem for commercialisation of PSC as they cannot compete with first generation PV if they can only function for a short length of time. Encapsulation of devices is a common method to increase stability.[198] The selection of sealing method is important and can add further cost to finished devices.[207] Encapsulation is also necessary to minimise the risk of lead leakage into the environment.[197] Improvements to the intrinsic stability of the perovskite are still needed to reach the levels required for applications.

### 1.5.3 Hysteresis

Hysteresis is the changing of the output of a system based on its past and present inputs. As a phenomenon, it is prevalent in many systems with the simplest, and most commonly known, being rubber band deformation. In relation to perovskites the phenomena was first reported in 2013 by Dualeh *et al.*[208] It was observed that altering the scan velocity and scan direction, from open circuit to short circuit or vice versa, during JV testing had an effect on the current density, fill factor and efficiency. In general for PSC a faster scan rate can give higher efficiencies due to an increase in $J_{sc}$.[209] Scanning backwards from open circuit to short circuit also gives a higher efficiency than the forward scan due to an improvement in fill factor.[209]

There are several theories as to the cause of hysteresis with the most common three being ferroelectric effects, trapping and detrapping of electrons at interfaces and finally ion migration.[210] In principle any cation with a dipole, such as methylammonium, can generate a ferroelectric effect. Theoretical studies have suggested that spontaneous electric polarisation in perovskites can lead to the formation of ferroelectric domains that could contribute to hysteresis.[211] It has been shown experimentally by Fan *et al.* that there is no ferroelectric behaviour at room temperature.[212] A further argument against ferroelectrics causing hysteresis is that the timescale of $MA^+$ rotation is not in the range required to cause hysteresis.[213]

Trap states in both the bulk and the perovskite/transport layer interface can cause trapping of charge carriers.[214] These trap states are generated either through non-stoichiometric precursor solutions or thermal decomposition of the

deposited layer. When a device is under forward bias the trap states are filled, and can then be emptied under short circuit conditions.[215] It has been suggested that this charging and discharging of traps is partially to blame for hysteresis. Passifying trap states is an effective way of minimising hysteresis caused by trapping. Passifying trap states can be effectively accomplished with fullerenes and a lewis acid.[216,217]

The severity of hysteresis is highly dependent on the scan rate and the device architecture used (Chapter 1.6.1).[209,218] For mesoporous cells, faster scan rates give an increased hysteresis but planar cells give the opposite response.[209] Inverted cells tend to show minimal hysteresis.[219,220] The choice of blocking layer can have a big effect with spiro-OMeTAD and $TiO_2$ giving high hysteresis and PEDOT:PSS and NiO devices having minimal hysteresis.[221] While this is strong evidence that the hysteresis is only caused by the nature of the contacts, work by Calado *et al.* showed that this is not the case. Using a combination of experiment and simulation work they showed that hysteresis requires both mobile ions and recombination near interfaces.[222] As ion migration is an important part of this thesis, its origin, detection and impact on perovskites will be discussed in more detail in Chapter 1.6.

## 1.6 Ion Migration

### 1.6.1 Observing Ion Migration

Ion migration in perovskites is a phenomena that has sparked interest in the research community due to its impact on both performance and stability. The first question when it comes to ion migration in perovskites is what is actually moving. The three different ions $Pb^{2+}$, $I^-$ and $MA^+$ could all be mobile with different activation energies and diffusion rates. A mixed computational and experimental study by Eames *et al.* calculated activation energies ($E_a$) for migration of all three ions. The resulting $E_a$ values were $0.58\,eV$ for $I^-$, $2.31\,eV$ for $Pb^{2+}$ and $0.84\,eV$ for $MA^+$.[223] They also proposed a migration path for iodide migration (Figure 1-15). Their model showed that migration was along a slightly curved path on the outside of the octahedra. First principles calculations investigating diffusion
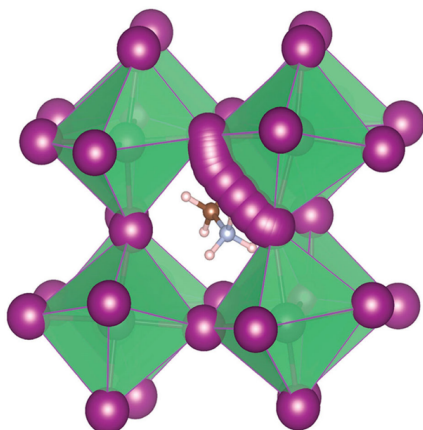
Figure 1-15: The migration pathway of iodide diffusion predicted by DFT. Reproduced with permission from ref.[223] Copyright 2018 Nature Publishing Group

along different pathways in both MAPI and FAPI gave a range of activation energies.[224] In MAPI the $E_A$ for $I^-$ was either $0.32\,\text{eV}$ or $0.44\,\text{eV}$ depending on the path. The $E_a$ for iodide migration in FAPI was higher for both paths.

A different set of density functional theory (DFT) calculations published at a similar time gave a significantly different value for the $E_a$ of iodide diffusion. In the Azpiroz *et al.* paper they calculated an activation energy of $0.08\,\text{eV}$.[225] While the two papers disagree on the $E_a$ of the migration they do agree that iodide is the most mobile ion in perovskite.

As well as computational models predicting ion migration, there have also been several experimental studies that show ion diffusion in perovskites. Ion migration was observed using an electric field and optical imaging.[226] At elevated temperature an electric field was applied to a perovskite layer and a thin strip of $PbI_2$ was formed. The $PbI_2$ layer then moved through the material as the ions from the neighbouring regions converted it to MAPI leaving behind $PbI_2$. This was easily observed visually as well as using energy-dispersive X-ray spectroscopy.

Temperature dependent current measurements on planar perovskite devices have yielded an $E_a$ of $0.23\,\text{eV}$ for iodide motion. In this method a voltage was applied to the device and increased step wise with the change in the current density being measured. From this information the electrical current decay rate was calculated and an Arrhenius plot gave an activation energy.[227]

Light exposure has a big impact on ion diffusion as shown by Xing *et al.*[228]

Using temperature dependent conductivity measurements as well as tracking a PbI$_2$ layer through the material they were able to show that increased light exposure lowered the E$_A$ of iodide diffusion in perovskites. The activation energies that they measured changed from 0.50 eV in the dark to 0.14 eV under illumination at 0.25 sun. The size of the grains also caused shifts in the activation energy with a small grain film (0.27 eV), a large grain film (0.50 eV) and a single crystal (1.05 eV) all having very different values. These results show the impact of grain boundary size on the experimental activation energy.

Electrochemical impedance spectroscopy (EIS) was first used in PSC in 2013 to observe charge accumulation in mesoporous cells.[229] Dualeh *et al.* compared PSCs with dye-sensitized solar cells to produce an impedance model and hinted at the possibility of detecting iodide diffusion using EIS.[208]

An activation energy for ion diffusion calculated from EIS and also the link between ion movement and degradation was shown by Bag *et al.* By fitting temperature dependent impedance they were able to produce an Arrhenius plot with an activation energy of 0.58 eV. Further studies using intensity modulated voltage sweep and EIS have produced activation energies of 0.43 eV and 0.55 eV for iodide.[230,231]

All of the previous measurements of diffusion involve the construction of a device and applying an external stimulus such as a current or light. Investigating one specific part of the device is not trivial as the interfaces and choice of contact can all impact the measurement. In 2017, using various different NMR techniques an activation energy of 0.17 eV for iodide was measured.[232] This value is lower than those previously measured by impedance and other device based measurements. While this section may not have covered all of the different methods and results that have generated activation energies for iodide diffusion it is clear that there is substantial disagreement between different methodologies.

One final type of ion migration to mention is that of extrinsic ions. There are several ions (Li$^+$, H$^+$ and NA$^+$) that have been observed to migrate through PSC devices.[233] These extrinsic ions are introduced through the contact layers (e.g. lithium doping in Spiro-OMeTAD).

## 1.6.2 The Impact of Ion Migration

One impact of ion migration is that it is partially responsible for hysteresis in PSC JV curves (see section 1.5.3).[209] Another performance related issue caused by ion migration is reversible performance loss over a day/night cycle. Domanski *et al.* showed that under illumination for 5 hours devices lost 10 % of their efficiency.[234] This loss was regained when the devices were left in the dark. Using time of flight mass spectrometry the authors showed that the elemental distribution of ions in the perovskite was changing under operating conditions.

The migration of iodide through the perovskite can also limit the long term stability of devices made with silver contacts. Previous studies have shown that iodide ions can migrate through the hole transport layers and react with the metal electrode. This is especially problematic with silver as silver iodide is readily formed.[235,236]

Given the impact that ion migration has on performance, restricting it via device or material design is important for the long term outlook of perovskites. It has been demonstrated that a nanocarbon layer can suppress the diffusion of ions as it can block ions but does not block charges.[237] Another method for blocking ion motion is with a $Zr(Ac)_4$ interlayer between the electron transport layer and the perovskite.[238] This layer effectively blocks the ions but not the charges. There are not many other studies showing blocking of ion migration. The use of interlayers is partially studied but there is scope for a lot more investigation. Altering the perovskite stoichiometry has been thoroughly investigated but never with the intention of limiting iodide diffusion.

# 1.7 Muon Spin Relaxation μSR

## 1.7.1 Measuring Ion Diffusion with Muons

A recent development in measuring ion diffusion is to use muon spin relaxation. Muon experiments were first carried out in 1937. Initially, μSR was a niche technique for measuring magnetism but it is becoming a more popular tool for probing a variety of processes such as ion diffusion or superconductivity.[239,240]

With respect to ion migration, the first successful muon study on ion migration was reported in 2009 when Sugiyama *et al.* observed the diffusion of lithium ions through $LiCoO_2$.[241] This was quickly followed by another study on lithium from Powell *et al.* this time in various $Li_3N$ battery materials.[242] Since then there have been a few studies on different lithium containing materials.[243–246]

With modern batteries looking to replace lithium with the more sustainable sodium, detection of sodium has also been shown to be possible with muons. Månsson *et al.* studied the diffusion of both $Li^+$ and $Na^+$ in cobalt oxide materials.[247] They were able to successfully observe the diffusion of the two different cations with good agreement to other measurement methods.

The previously discussed μSR experiments use muons with an energy of 4 MeV that stop in approximately 0.1 to 1 mm depending on the samples density.[240] A sufficient amount of solid sample is therefore required to allow the muon to be implanted into the sample. The requirement of a large quantity of solid sample meant that initially, μSR studies into ion migration were performed on solid powders.[241,242,247] It is possible to measure diffusion of ions in thin films at certain depths in the films by lowering the energy of the incident muons to a range of 1-10 eV.[248] The energy of these muons can be adjusted to implant them at a chosen point between 2-300 nm in the film.[249] Experiments like this have shown the difference in diffusion properties when you move from a bulk powder into a thin film environment.[250] The advantages of muon spin relaxation (μSR) over other techniques is that it measures the intrinsic diffusion properties of the material without visible light, current or voltage stimulus. A second benefit of μSR is that a full device is not needed so there is no impact on the material properties from contacts and interfaces.

# References

(1) Population Division, *World Population Prospects: The 2017 Revision, Key Findings and Advance Tables*, tech. rep., United Nations, Department of Economic and Social Affairs.

(2) British Petroleum Company, *BP Statistical Review of World Energy 2018*, tech. rep., 2018.

(3) J. Conti, *International Energy Outlook 2014*, tech. rep., 2014.

(4) World Energy Council, *World Energy Resources*, tech. rep., World Energy Council, 2013.

(5) T. R. Anderson, E. Hawkins and P. D. Jones, *Endeavour*, 2016, **40**, 178–187.

(6) ECF, *Power Perspectives 2030: On the road to a Decarbonised Power Sector*, tech. rep., European Climate Foundation, 2011, pp. 1–85.

(7) UN General Assembly, *United Nations Framework Convention on Climate Change*, tech. rep., 1994.

(8) R. J. Millar, J. S. Fuglestvedt, P. Friedlingstein, J. Rogelj, M. J. Grubb, H. Matthews, R. B. Skeie, P. M. Forster, D. J. Frame and M. R. Allen, *Nature Geoscience*, 2017, **10**, 741.

(9) J. M. Pearce, *Sustainability*, 2012, **4**, 1173–1187.

(10) M. Dittmar, *Energy*, 2012, **37**, 35–40.

(11) European Union, *Energy Roadmap 2050*, tech. rep., 2012.

(12) European Union, *2030 Energy Strategy*, tech. rep., 2014.

(13) Lazard, *Lazard's Levelized Cost of Energy Analysis*, tech. rep., 2017.

(14) REN21, *Renewables 2017 Global Status Report*, tech. rep., REN21 Secretariat, Paris, 2017.

(15) L. M. Peter, *Philosophical transactions. Series A, Mathematical, physical, and engineering sciences*, 2011, **369**, 1840–1856.

(16) International Energy Agency, *Global Energy & $CO_2$ Status Report*, tech. rep. March, 2018.

(17)   A. E. Becquerel, *Comptes Rendus de L'Academie des Sciences*, 1839, **9**, 145–149.

(18)   L. El Chaar, L. A. Lamont and N. El Zein, *Renewable and Sustainable Energy Reviews*, 2011, **15**, 2165–2175.

(19)   T. Saga, *NPG Asia Materials*, 2010, **2**, 96–102.

(20)   B. Parida, S. Iniyan and R. Goic, *Renewable and Sustainable Energy Reviews*, 2011, **15**, 1625–1636.

(21)   E. Kabir, P. Kumar, S. Kumar, A. A. Adelodun and K. H. Kim, *Renewable and Sustainable Energy Reviews*, 2018, **82**, 894–900.

(22)   R. S. Ohl, *Light-sensitive electric device including silicon*, 1948.

(23)   Fraunhofer Institute for Solar Energy Systems, *Photovolataics Report*, tech. rep., 2017.

(24)   NREL, *Solar Efficiency Chart*.

(25)   F. Haase, C. Hollemann, S. Schäfer, A. Merkle, M. Rienäcker, J. Krügener, R. Brendel and R. Peibst, *Solar Energy Materials and Solar Cells*, 2018, **186**, 184–193.

(26)   IRENA, *Renewable Power Generation Costs in 2017*, tech. rep., Abu Dhabi, 2018.

(27)   A. Acevedo-Luna, R. Bernal-Correa, J. Montes-Monsalve and A. Morales-Acevedo, *Journal of Applied Research and Technology*, 2017, **15**, 599–608.

(28)   J. Peng, L. Lu and H. Yang, *Renewable and Sustainable Energy Reviews*, 2013, **19**, 255–274.

(29)   M. Powalla and D. Bonnet, *Advances in OptoElectronics*, 2007, **2007**, 1–6.

(30)   B. M. Basol and B. McCandless, *Journal of Photonics for Energy*, 2014, **4**, 040996.

(31)   A. G. Aberle, *Thin Solid Films*, 2009, **517**, 4706–4710.

(32)   V. Fthenakis, *Renewable and Sustainable Energy Reviews*, 2009, **13**, 2746–2750.

(33) C. Tao, J. Jiang and M. Tao, *ECS Trans.* 2011, vol. 33, pp. 3–11.

(34) H. Hahn, G. Frank, W. Klingler, A.-D. Meyer and G. Stürger, *Zeitschrift für anorganische und allgemeine Chemie*, 1953, **271**, 153–170.

(35) S. Wagner, J. L. Shay, P. Migliorato and H. M. Kasper, *Applied Physics Letters*, 1974, **25**, 434–435.

(36) J. Ramanujam, U. P. Singh, M. Tomassini, N. Barreau, H. Steijvers, J. van Berkumd, Z. Vroon, M. Zeman, U. Zimmermann, A. F. da Cunha, M. Edoff, S. Nishiwaki, Y. E. Romanyuk, G. Bilger, A. N. Tiwari, C. P. Bjorkman, S. Spiering, A. N. Tiwari, T. Torndahl and G. E. Cirlin, *Energy Environ. Sci.*, 2017, **361/362**, 540–546.

(37) P. Jackson, D. Hariskos, E. Lotter, S. Paetel, R. Wuerz, R. Menner, W. Wischmann and M. Powalla, *Progress in Photovoltaics: Research and Applications*, 2011, **19**, 894–897.

(38) C. Candelise, M. Winskel and R. Gross, *Progress in Photovoltaics: Research and Applications*, 2012, **20**, 816–831.

(39) D. E. Carlson and C. R. Wronski, *Applied Physics Letters*, 1976, **28**, 671–673.

(40) H. Sai, T. Matsui and K. Matsubara, *Applied Physics Letters*, 2016, **109**, 183506.

(41) D. L. Staebler and C. R. Wronski, *Applied Physics Letters*, 1977, **31**, 292–294.

(42) M. Stuckelberger, R. Biron, N. Wyrsch, F.-J. Haug and C. Ballif, *Renewable and Sustainable Energy Reviews*, 2017, **76**, 1497–1523.

(43) R. E. Schropp, R. Carius and G. Beaucarne, *MRS Bulletin*, 2007, **32**, 219–224.

(44) M. P. Suryawanshi, G. L. Agawane, S. M. Bhosale, S. W. Shin, P. S. Patil, J. H. Kim and a. V. Moholkar, *Materials Technology*, 2013, **28**, 98–109.

(45) W. Wang, M. T. Winkler, O. Gunawan, T. Gokmen, T. K. Todorov, Y. Zhu and D. B. Mitzi, *Advanced Energy Materials*, 2014, **4**, 1301465.

(46) X. Song, X. Ji, M. Li, W. Lin, X. Luo and H. Zhang, *International Journal of Photoenergy*, 2014, **2014**, 1–11.

(47) S. E. Shaheen, C. J. Brabec, N. S. Sariciftci, F. Padinger, T. Fromherz and J. C. Hummelen, *Applied Physics Letters*, 2001, **78**, 841–843.

(48) J. Liu, S. Chen, D. Qian, B. Gautam, G. Yang, J. Zhao, J. Bergqvist, F. Zhang, W. Ma, H. Ade, O. Inganäs, K. Gundogdu, F. Gao and H. Yan, *Nature Energy*, 2016, **1**, 16089.

(49) T. Meier, R. Pawlak, S. Kawai, Y. Geng, X. Liu, S. Decurtins, P. Hapala, A. Baratoff, S.-X. Liu, P. Jelínek, E. Meyer and T. Glatzel, *ACS Nano*, 2017, **11**, 8413–8420.

(50) S. Rafique, S. M. Abdullah, K. Sulaiman and M. Iwamoto, *Renewable and Sustainable Energy Reviews*, 2018, **84**, 43–53.

(51) G. Dennler, M. C. Scharber and C. J. Brabec, *Advanced Materials*, 2009, **21**, 1323–1338.

(52) C. Yan, S. Barlow, Z. Wang, H. Yan, A. K.-Y. Jen, S. R. Marder and X. Zhan, *Nature Reviews Materials*, 2018, **3**, 18003.

(53) Y. Sun, G. C. Welch, W. L. Leong, C. J. Takacs, G. C. Bazan and A. J. Heeger, *Nature Materials*, 2011, **11**, 44–48.

(54) S. Yanagida, G. Senadeera, K. Nakamura, T. Kitamura and Y. Wada, *Journal of Photochemistry and Photobiology A: Chemistry*, 2004, **166**, 75–80.

(55) H.-J. Wang, C.-P. Chen and R.-J. Jeng, *Materials*, 2014, **7**, 2411–2439.

(56) J. Nelson, *Materials Today*, 2011, **14**, 462–470.

(57) L. Lu, T. Zheng, Q. Wu, A. M. Schneider, D. Zhao and L. Yu, *Chemical Reviews*, 2015, **115**, 12666–12731.

(58) L. Meng, Y. Zhang, X. Wan, C. Li, X. Zhang, Y. Wang, X. Ke, Z. Xiao, L. Ding, R. Xia, H.-L. Yip, Y. Cao and Y. Chen, *Science*, 2018, **361**, 1094–1098.

(59) F. C. Krebs, *Solar Energy Materials and Solar Cells*, 2009, **93**, 394–412.

(60)  R. Søndergaard, M. Hösel, D. Angmo, T. T. Larsen-Olsen and F. C. Krebs, *Materials Today*, 2012, **15**, 36–49.

(61)  F. C. Krebs, M. Jørgensen, K. Norrman, O. Hagemann, J. Alstrup, T. D. Nielsen, J. Fyenbo, K. Larsen and J. Kristensen, *Solar Energy Materials and Solar Cells*, 2009, **93**, 422–441.

(62)  M. Jørgensen, K. Norrman, S. A. Gevorgyan, T. Tromholt, B. Andreasen and F. C. Krebs, *Advanced Materials*, 2012, **24**, 580–612.

(63)  S. A. McDonald, G. Konstantatos, S. Zhang, P. W. Cyr, E. J. D. Klem, L. Levina and E. H. Sargent, *Nature Materials*, 2005, **4**, 138–142.

(64)  M. R. Kim and D. Ma, *The Journal of Physical Chemistry Letters*, 2015, **6**, 85–99.

(65)  J. Tang and E. H. Sargent, *Advanced Materials*, 2011, **23**, 12–29.

(66)  E. M. Sanehira, A. R. Marshall, J. A. Christians, S. P. Harvey, P. N. Ciesielski, L. M. Wheeler, P. Schulz, L. Y. Lin, M. C. Beard and J. M. Luther, *Science Advances*, 2017, **3**, eaao4204.

(67)  G. H. Carey, A. L. Abdelhady, Z. Ning, S. M. Thon, O. M. Bakr and E. H. Sargent, *Chemical Reviews*, 2015, **115**, 12732–12763.

(68)  B. O'Regan and M. Grätzel, *Nature*, 1991, **353**, 737–740.

(69)  H. Gerischer, M. Michel-Beyerle, F. Rebentrost and H. Tributsch, *Electrochimica Acta*, 1968, **13**, 1509–1515.

(70)  C. J. C. Barbe, F. Arendse, P. Comte, M. Jirousek, F. Lenzmann, V. Shklover, M. Gra and M. Gratzel, *Journal of the American Ceramic Society*, 1997, **80**, 3157–3171.

(71)  B. Bozic-Weber, E. C. Constable and C. E. Housecroft, *Coordination Chemistry Reviews*, 2013, **257**, 3089–3106.

(72)  C.-P. Lee, R. Y.-Y. Lin, L.-Y. Lin, C.-T. Li, T.-C. Chu, S.-S. Sun, J. T. Lin and K.-C. Ho, *RSC Adv.*, 2015, **5**, 23810–23825.

(73)  K. Kakiage, Y. Aoyama, T. Yano, K. Oya, J.-i. Fujisawa and M. Hanaya, *Chemical Communications*, 2015, **51**, 15894–15897.

(74) S. Mathew, A. Yella, P. Gao, R. Humphry-Baker, B. F. E. Curchod, N. Ashari-Astani, I. Tavernelli, U. Rothlisberger, M. K. Nazeeruddin and M. Grätzel, *Nature Chemistry*, 2014, **6**, 242–247.

(75) A. Kojima, K. Teshima, Y. Shirai and T. Miyasaka, *Journal of the American Chemical Society*, 2009, **131**, 6050–1.

(76) G. Kieslich, S. Sun and A. K. Cheetham, *Chem. Sci.*, 2014, **5**, 4712–4715.

(77) D. Weber, *Zeitschrift für Naturforschung*, 1978, **33b**, 1443–1445.

(78) D. B. Mitzi, K. Chondroudis and C. R. Kagan, *IBM Journal of Research and Development*, 2001, **45**, 29–45.

(79) C. R. Kagan, D. B. Mitzi and C. D. Dimitrakopoulos, *Science*, 1999, **286**, 945–947.

(80) J.-H. Im, C.-R. Lee, J.-W. Lee, S.-W. Park and N.-G. Park, *Nanoscale*, 2011, **3**, 4088–93.

(81) H.-S. Kim, C.-R. Lee, J.-H. Im, K.-B. Lee, T. Moehl, A. Marchioro, S.-J. Moon, R. Humphry-Baker, J.-H. Yum, J. E. Moser, M. Grätzel and N.-G. Park, *Scientific Reports*, 2012, **2**, 591.

(82) M. M. Lee, J. Teuscher, T. Miyasaka, T. N. Murakami and H. J. Snaith, *Science*, 2012, **338**, 643–647.

(83) L. Etgar, P. Gao, Z. Xue, Q. Peng, A. K. Chandiran, B. Liu, M. K. Nazeeruddin and M. Grätzel, *Journal of the American Chemical Society*, 2012, **134**, 17396–17399.

(84) T. Salim, S. Sun, Y. Abe, A. Krishna, A. C. Grimsdale and Y. M. Lam, *J. Mater. Chem. A*, 2015, **3**, 8943–8969.

(85) T. C. Sum and N. Mathews, *Energy Environ. Sci.*, 2014, **7**, 2518–2534.

(86) M. Liu, M. B. Johnston and H. J. Snaith, *Nature*, 2013, **501**, 395–8.

(87) M. Saliba, T. Matsui, J.-Y. Seo, K. Domanski, J.-P. Correa-Baena, M. K. Nazeeruddin, S. M. Zakeeruddin, W. Tress, A. Abate, A. Hagfeldt, M. Grätzel, N. Mohammad K., S. M. Zakeeruddin, W. Tress, A. Abate, A. Hagfeldt and M. Grätzel, *Energy Environ. Sci.*, 2016, **9**, 1989–1997.

(88)  K. T. Cho, S. Paek, G. Grancini, C. Roldán-Carmona, P. Gao, Y. Lee and M. K. Nazeeruddin, *Energy Environ. Sci.*, 2017, **10**, 621–627.

(89)  J.-Y. Jeng, Y.-F. Chiang, M.-H. Lee, S.-R. Peng, T.-F. Guo, P. Chen and T.-C. Wen, *Advanced Materials*, 2013, **25**, 3727–3732.

(90)  P. Docampo, J. M. Ball, M. Darwich, G. E. Eperon and H. J. Snaith, *Nature Communications*, 2013, **4**, 1–6.

(91)  S. S. Reddy, S. Shin, U. K. Aryal, R. Nishikubo, A. Saeki, M. Song and S.-H. Jin, *Nano Energy*, 2017, **41**, 10–17.

(92)  M. Hu, L. Liu, A. Mei, Y. Yang, T. Liu and H. Han, *J. Mater. Chem. A*, 2014, **2**, 17115–17121.

(93)  Y. Cai, L. Liang and P. Gao, *Chinese Physics B*, 2018, **27**, 018805.

(94)  S. Ito, G. Mizuta, S. Kanaya, H. Kanda, T. Nishina, S. Nakashima, H. Fujisawa, M. Shimizu, Y. Haruyama and H. Nishino, *Phys. Chem. Chem. Phys.*, 2016, **18**, 27102–27108.

(95)  W. Shockley and H. J. Queisser, *Journal of Applied Physics*, 1961, **32**, 510–519.

(96)  C. Honsberg and S. Bowden, *Tandem Cells*.

(97)  T. Leijtens, K. A. Bush, R. Prasanna and M. D. McGehee, *Nature Energy*, 2018, 1–11.

(98)  T. Duong, Y. L. Wu, H. Shen, J. Peng, X. Fu, D. Jacobs, E. C. Wang, T. C. Kho, K. C. Fong, M. Stocks, E. Franklin, A. Blakers, N. Zin, K. McIntosh, W. Li, Y. B. Cheng, T. P. White, K. Weber and K. Catchpole, *Advanced Energy Materials*, 2017, **7**, 1–11.

(99)  A. Dualeh, N. Tétreault, T. Moehl, P. Gao, M. K. Nazeeruddin and M. Grätzel, *Advanced Functional Materials*, 2014, **24**, 3250–3258.

(100)  M. K. Gangishetty, R. W. J. Scott and T. L. Kelly, *Nanoscale*, 2016, **8**, 6300–6307.

(101)  N. J. Jeon, J. H. Noh, Y. C. Kim, W. S. Yang, S. Ryu and S. I. Seok, *Nature materials*, 2014, **13**, 1–7.

(102) S. Paek, P. Schouwink, E. N. Athanasopoulou, K. T. Cho, G. Grancini, Y. Lee, Y. Zhang, F. Stellacci, M. K. Nazeeruddin and P. Gao, *Chemistry of Materials*, 2017, **29**, 3490–3498.

(103) J.-W. Lee, H.-S. Kim and N.-G. Park, *Accounts of Chemical Research*, 2016, **49**, 311–319.

(104) M. Xiao, F. Huang, W. Huang, Y. Dkhissi, Y. Zhu, J. Etheridge, A. Gray-Weale, U. Bach, Y.-B. Cheng and L. Spiccia, *Angewandte Chemie International Edition*, 2014, **53**, 9898–9903.

(105) M. Yin, F. Xie, H. Chen, X. Yang, F. Ye, E. Bi, Y. Wu, M. Cai and L. Han, *J. Mater. Chem. A*, 2016, **4**, 8548–8553.

(106) J. Troughton, K. Hooper and T. M. Watson, *Nano Energy*, 2017, **39**, 60–68.

(107) X. Li, D. Bi, C. Yi, J.-D. Décoppet, J. Luo, S. M. Zakeeruddin, A. Hagfeldt and M. Grätzel, *Science*, 2016, **353**, 58–62.

(108) J. Troughton, M. J. Carnie, M. L. Davies, C. Charbonneau, E. H. Jewell, D. A. Worsley and T. M. Watson, *J. Mater. Chem. A*, 2016, **4**, 3471–3476.

(109) K. Liang, D. B. Mitzi and M. T. Prikas, *Chemistry of Materials*, 1998, **10**, 403–411.

(110) J. Burschka, N. Pellet, S.-J. Moon, R. Humphry-Baker, P. Gao, M. K. Nazeeruddin and M. Grätzel, *Nature*, 2013, **499**, 316–319.

(111) D. Liu and T. L. Kelly, *Nature Photonics*, 2013, **8**, 133–138.

(112) P. Docampo, F. C. Hanusch, S. D. Stranks, M. Döblinger, J. M. Feckl, M. Ehrensperger, N. K. Minar, M. B. Johnston, H. J. Snaith and T. Bein, *Advanced Energy Materials*, 2014, **4**, 1400355.

(113) Y. Wu, A. Islam, X. Yang, C. Qin, J. Liu, K. Zhang, W. Peng and L. Han, *Energy Environ. Sci.*, 2014, **7**, 2934–2938.

(114) C.-H. Chiang, M. K. Nazeeruddin, M. Grätzel and C.-G. Wu, *Energy Environ. Sci.*, 2017, **10**, 808–817.

(115) M. I. El-Henawey, R. S. Gebhardt, M. M. El-Tonsy and S. Chaudhary, *J. Mater. Chem. A*, 2016, **4**, 1947–1952.

(116) B. Yang, O. Dyck, J. Poplawsky, J. Keum, S. Das, A. Puretzky, T. Aytug, P. C. Joshi, C. M. Rouleau, G. Duscher, D. B. Geohegan and K. Xiao, *Angewandte Chemie - International Edition*, 2015, **54**, 14862–14865.

(117) T.-Y. Hsieh, T.-C. Wei, K.-L. Wu, M. Ikegami and T. Miyasaka, *Chem. Commun.*, 2015, **51**, 13294–13297.

(118) J.-h. Huang, K.-j. Jiang, X.-p. Cui, Q.-q. Zhang, M. Gao, M.-j. Su, L.-m. Yang and Y. Song, *Scientific Reports*, 2015, **5**, 15889.

(119) S. Casaluci, L. Cinà, A. Pockett, P. S. Kubiak, R. G. Niemann, A. Reale, A. Di Carlo and P. Cameron, *Journal of Power Sources*, 2015, **297**, 504–510.

(120) H. Xu, Y. Wu, F. Xu, J. Zhu, C. Ni, W. Wang, F. Hong, R. Xu, F. Xu, J. Huang and L. Wang, *RSC Adv.*, 2016, **6**, 48851–48857.

(121) J. Ávila, C. Momblona, P. P. Boix, M. Sessolo and H. J. Bolink, *Joule*, 2017, **1**, 431–442.

(122) Y. Deng, E. Peng, Y. Shao, Z. Xiao, Q. Dong and J. Huang, *Energy Environ. Sci.*, 2015, **8**, 1544–1550.

(123) S. Tang, Y. Deng, X. Zheng, Y. Bai, Y. Fang, Q. Dong, H. Wei and J. Huang, *Advanced Energy Materials*, 2017, **7**, 1–7.

(124) A. T. Mallajosyula, K. Fernando, S. Bhatt, A. Singh, B. W. Alphenaar, J.-C. Blancon, W. Nie, G. Gupta and A. D. Mohite, *Applied Materials Today*, 2016, **3**, 96–102.

(125) A. T. Barrows, A. J. Pearson, C. K. Kwak, A. D. F. Dunbar, A. R. Buckley and D. G. Lidzey, *Energy Environ. Sci.*, 2014, **7**, 2944–2950.

(126) S. Das, B. Yang, G. Gu, P. C. Joshi, I. N. Ivanov, C. M. Rouleau, T. Aytug, D. B. Geohegan and K. Xiao, *ACS Photonics*, 2015, **2**, 680–686.

(127) W. C. Chang, D. H. Lan, K. M. Lee, X. F. Wang and C. L. Liu, *ChemSusChem*, 2017, **10**, 1405–1412.

(128) J. H. Heo, M. H. Lee, M. H. Jang and S. H. Im, *J. Mater. Chem. A*, 2016, **4**, 17636–17642.

(129) V. M. Goldschmidt, *Die Naturwissenschaften*, 1926, **14**, 477–485.

(130) G. Kieslich, S. Sun and T. Cheetham, *Chem. Sci.*, 2015, **6**, 3430–3433.

(131) G. E. Eperon, S. D. Stranks, C. Menelaou, M. B. Johnston, L. M. Herz and H. J. Snaith, *Energy Environ. Sci.*, 2014, **7**, 982.

(132) C. C. Stoumpos, C. D. Malliakas and M. G. Kanatzidis, *Inorganic Chemistry*, 2013, **52**, 9019–9038.

(133) Y. Zhou, M. Yang, A. L. Vasiliev, H. F. Garces, Y. Zhao, D. Wang, S. Pang, K. Zhu and N. P. Padture, *J. Mater. Chem. A*, 2015, **3**, 9249–9256.

(134) N. Pellet, P. Gao, G. Gregori, T. Y. Yang, M. K. Nazeeruddin, J. Maier and M. Graetzel, *Angewandte Chemie - International Edition*, 2014, **53**, 3151–3157.

(135) J. Kim, H. P. Kim, M. A. M. Teridi, A. R. b. M. Yusoff and J. Jang, *Scientific Reports*, 2016, **6**, 37378.

(136) C. C. Chen, S. H. Chang, L. C. Chen, F. S. Kao, H. M. Cheng, S. C. Yeh, C. T. Chen, W. T. Wu, Z. L. Tseng, C. L. Chuang and C. G. Wu, *Solar Energy*, 2016, **134**, 445–451.

(137) M. Salado, L. Calio, R. Berger, S. Kazim and S. Ahmad, *Phys. Chem. Chem. Phys.*, 2016, **18**, 27148–27157.

(138) Y. Deng, Q. Dong, C. Bi, Y. Yuan and J. Huang, *Advanced Energy Materials*, 2016, **6**, 1–6.

(139) A. F. Akbulatov, L. A. Frolova, D. V. Anokhin, K. L. Gerasimov, N. N. Dremova and P. A. Troshin, *J. Mater. Chem. A*, 2016, **4**, 18378–18382.

(140) S. R. Pering, W. Deng, J. R. Troughton, P. S. Kubiak, D. Ghosh, R. G. Niemann, F. Brivio, F. E. Jeffrey, A. B. Walker, M. S. Islam, T. M. Watson, P. R. Raithby, A. L. Johnson, S. E. Lewis and P. J. Cameron, *J. Mater. Chem. A*, 2017, **5**, 20658–20665.

(141) M. Aamir, Z. H. Shah, M. Sher, A. Iqbal, N. Revaprasadu, M. A. Malik and J. Akhtar, *Materials Science in Semiconductor Processing*, 2017, **63**, 6–11.

(142) O. J. Weber, K. L. Marshall, L. M. Dyson and M. T. Weller, *Acta Crystallographica Section B Structural Science, Crystal Engineering and Materials*, 2015, **71**, 668–678.

(143) L. Dimesso, A. Quintilla, Y.-M. Kim, U. Lemmer and W. Jaegermann, *Materials Science and Engineering: B*, 2016, **204**, 27–33.

(144) N. D. Marco, H. Zhou, Q. Chen, P. Sun, Z. Liu, L. Meng, E.-P. Yao, Y. Liu, A. Schiffer and Y. Yang, *Nano Letters*, 2016, **16**, 1009–1016.

(145) A. D. Jodlowski, C. Roldán-Carmona, G. Grancini, M. Salado, M. Ralaiarisoa, S. Ahmad, N. Koch, L. Camacho, G. De Miguel and M. K. Nazeeruddin, *Nature Energy*, 2017, **2**, 972–979.

(146) L. Protesescu, S. Yakunin, M. I. Bodnarchuk, F. Krieg, R. Caputo, C. H. Hendon, R. X. Yang, A. Walsh and M. V. Kovalenko, *Nano Letters*, 2015, **15**, 3692–3696.

(147) G. E. Eperon, G. M. Paterno, R. J. Sutton, A. Zampetti, A. A. Haghighirad, F. Cacialli, H. J. Snaith, G. M. Paterno', R. J. Sutton, A. Zampetti, A. A. Haghighirad, F. Cacialli and H. J. Snaith, *J. Mater. Chem. A*, 2015, **3**, 19688–19695.

(148) R. J. Sutton, M. R. Filip, A. A. Haghighirad, N. Sakai, B. Wenger, F. Giustino and H. J. Snaith, *ACS Energy Letters*, 2018, **3**, 1787–1794.

(149) H. Choi, J. Jeong, H.-B. Kim, S. Kim, B. Walker, G.-H. Kim and J. Y. Kim, *Nano Energy*, 2014, **7**, 80–85.

(150) G. Niu, W. Li, J. Li, X. Liang and L. Wang, *RSC Adv.*, 2017, **7**, 17473–17479.

(151) J.-W. Lee, D.-H. Kim, H.-S. Kim, S.-W. Seo, S. M. Cho and N.-G. Park, *Advanced Energy Materials*, 2015, **5**, 1501310.

(152) Z. Li, M. Yang, J. S. Park, S. H. Wei, J. J. Berry and K. Zhu, *Chemistry of Materials*, 2016, **28**, 284–292.

(153) S. Nagane, U. Bansode, O. Game, S. Chhatre and S. Ogale, *Chemical Communications*, 2014, **50**, 9741–9744.

(154) J. H. Noh, S. H. Im, J. H. Heo, T. N. Mandal and S. I. Seok, *Nano Letters*, 2013, **13**, 1764–1769.

(155) P. Fedeli, F. Gazza, D. Calestani, P. Ferro, T. Besagni, A. Zappettini, G. Calestani, E. Marchi, P. Ceroni and R. Mosca, *The Journal of Physical Chemistry C*, 2015, **119**, 21304–21313.

(156) E. T. Hoke, D. J. Slotcavage, E. R. Dohner, A. R. Bowring, H. I. Karunadasa and M. D. McGehee, *Chemical Science*, 2015, **6**, 613–617.

(157) F. Brivio, C. Caetano and A. Walsh, *Journal of Physical Chemistry Letters*, 2016, **7**, 1083–1087.

(158) R. G. Niemann, A. G. Kontos, D. Palles, E. I. Kamitsos, A. Kaltzoglou, F. Brivio, P. Falaras and P. J. Cameron, *The Journal of Physical Chemistry C*, 2016, **120**, 2509–2519.

(159) L. K. Ono, E. J. Juarez-Perez and Y. Qi, *ACS Applied Materials and Interfaces*, 2017, **9**, 30197–30246.

(160) M. Ralaiarisoa, Y. Busby, J. Frisch, I. Salzmann, J.-J. Pireaux and N. Koch, *Phys. Chem. Chem. Phys.*, 2017, **19**, 828–836.

(161) H. Zhang, Q. Liao, X. Wang, K. Hu, J. Yao and H. Fu, *Small*, 2016, **12**, 3780–3787.

(162) D. Luo, L. Yu, H. Wang, T. Zou, L. Luo, Z. Liu and Z. Lu, *RSC Adv.*, 2015, **5**, 85480–85485.

(163) Y. Chen, T. Chen and L. Dai, *Advanced Materials*, 2015, **27**, 1053–1059.

(164) B. Yang, J. Keum, O. S. Ovchinnikova, A. Belianinov, S. Chen, M.-H. Du, I. N. Ivanov, C. M. Rouleau, D. B. Geohegan and K. Xiao, *Journal of the American Chemical Society*, 2016, **138**, 5028–5035.

(165) A. Binek, I. Grill, N. Huber, K. Peters, A. G. Hufnagel, M. Handloser, P. Docampo, A. Hartschuh and T. Bein, *Chemistry - An Asian Journal*, 2016, **11**, 1199–1204.

(166) T.-W. Ng, C.-Y. Chan, M.-F. Lo, Z. Q. Guan and C.-S. Lee, *J. Mater. Chem. A*, 2015, **3**, 9081–9085.

(167)  Y. Tidhar, E. Edri, H. Weissman, D. Zohar, G. Hodes, D. Cahen, B. Rybtchinski and S. Kirmayer, *Journal of the American Chemical Society*, 2014, **136**, 13249–13256.

(168)  Q. Jiang, D. Rebollar, J. Gong, E. L. Piacentino, C. Zheng and T. Xu, *Angewandte Chemie - International Edition*, 2015, **54**, 7617–7620.

(169)  Q. Tai, P. You, H. Sang, Z. Liu, C. Hu, H. L. Chan and F. Yan, *Nature Communications*, 2016, **7**, 1–8.

(170)  W. Ke, C. Xiao, C. Wang, B. Saparov, H. S. Duan, D. Zhao, Z. Xiao, P. Schulz, S. P. Harvey, W. Liao, W. Meng, Y. Yu, A. J. Cimaroli, C. S. Jiang, K. Zhu, M. Al-Jassim, G. Fang, D. B. Mitzi and Y. Yan, *Advanced Materials*, 2016, **28**, 5214–5221.

(171)  Y.-H. Chiang, M.-H. Li, H.-M. Cheng, P.-S. Shen and P. Chen, *ACS Applied Materials & Interfaces*, 2017, **9**, 2403–2409.

(172)  T. Duong, H. K. Mulmudi, H. Shen, Y. L. Wu, C. Barugkin, Y. O. Mayon, H. T. Nguyen, D. Macdonald, J. Peng, M. Lockrey, W. Li, Y. B. Cheng, T. P. White, K. Weber and K. Catchpole, *Nano Energy*, 2016, **30**, 330–340.

(173)  M. Zhang, J. S. Yun, Q. Ma, J. Zheng, C. F. J. Lau, X. Deng, J. Kim, D. Kim, J. Seidel, M. A. Green, S. Huang and A. W. Y. Ho-Baillie, *ACS Energy Letters*, 2017, **2**, 438–444.

(174)  M. Saliba, T. Matsui, K. Domanski, J.-Y. Seo, A. Ummadisingu, S. M. Zakeeruddin, J.-P. Correa-Baena, W. R. Tress, A. Abate, A. Hagfeldt and M. Gratzel, *Science*, 2016, **354**, 206–209.

(175)  R. Uchida, S. Binet, N. Arora, G. Jacopin, M. H. Alotaibi, A. Taubert, S. M. Zakeeruddin, M. I. Dar and M. Graetzel, *Small*, 2018, **14**, 1–7.

(176)  Z. Yuan, C. Zhou, Y. Tian, Y. Shu, J. Messier, J. C. Wang, L. J. van de Burgt, K. Kountouriotis, Y. Xin, E. Holt, K. Schanze, R. Clark, T. Siegrist and B. Ma, *Nature Communications*, 2017, **8**, 14051.

(177)  S. Li, J. Luo, J. Liu and J. Tang, *The Journal of Physical Chemistry Letters*, 2019, **10**, 1999–2007.

(178) J. Almutlaq, J. Yin, O. F. Mohammed and O. M. Bakr, *The Journal of Physical Chemistry Letters*, 2018, **9**, 4131–4138.

(179) I. C. Smith, E. T. Hoke, D. Solis-Ibarra, M. D. McGehee and H. I. Karunadasa, *Angewandte Chemie-International Edition*, 2014, **53**, 11232–11235.

(180) L. N. Quan, M. Yuan, R. Comin, O. Voznyy, E. M. Beauregard, S. Hoogland, A. Buin, A. R. Kirmani, K. Zhao, A. Amassian, D. H. Kim and E. H. Sargent, *Journal of the American Chemical Society*, 2016, **138**, 2649–2655.

(181) D. H. Cao, C. C. Stoumpos, O. K. Farha, J. T. Hupp and M. G. Kanatzidis, *Journal of the American Chemical Society*, 2015, **137**, 7843–7850.

(182) K. Yao, X. Wang, Y. X. Xu, F. Li and L. Zhou, *Chemistry of Materials*, 2016, **28**, 3131–3138.

(183) M. Safdari, P. H. Svensson, M. T. Hoang, I. Oh, L. Kloo and J. M. Gardner, *J. Mater. Chem. A*, 2016, **4**, 15638–15646.

(184) Z. Wang, Q. Lin, F. P. Chmiel, N. Sakai, L. M. Herz and H. J. Snaith, *Nature Energy*, 2017, **2**, 1–10.

(185) G. Grancini, C. Roldán-Carmona, I. Zimmermann, E. Mosconi, X. Lee, D. Martineau, S. Narbey, F. Oswald, F. De Angelis, M. Graetzel and M. K. Nazeeruddin, *Nature Communications*, 2017, **8**, 15684.

(186) H. Tsai, W. Nie, J.-C. Blancon, C. C. Stoumpos, R. Asadpour, B. Harutyunyan, A. J. Neukirch, R. Verduzco, J. J. Crochet, S. Tretiak, L. Pedesseau, J. Even, M. A. Alam, G. Gupta, J. Lou, P. M. Ajayan, M. J. Bedzyk, M. G. Kanatzidis and A. D. Mohite, *Nature*, 2016, **536**, 312–316.

(187) N. K. Noel, S. D. Stranks, A. Abate, C. Wehrenfennig, S. Guarnera, A.-A. Haghighirad, A. Sadhanala, G. E. Eperon, S. K. Pathak, M. B. Johnston, A. Petrozza, L. M. Herz and H. J. Snaith, *Energy Environ. Sci.*, 2014, **7**, 3061–3068.

(188) S. J. Lee, S. S. Shin, Y. C. Kim, D. Kim, T. K. Ahn, J. H. Noh, J. Seo and S. I. Seok, *Journal of the American Chemical Society*, 2016, **138**, 3974–3977.

(189) X. G. Zhao, J. H. Yang, Y. Fu, D. Yang, Q. Xu, L. Yu, S. H. Wei and L. Zhang, *Journal of the American Chemical Society*, 2017, **139**, 2630–2638.

(190) A. H. Slavney, T. Hu, A. M. Lindenberg and H. I. Karunadasa, *Journal of the American Chemical Society*, 2016, **138**, 2138–2141.

(191) E. T. McClure, M. R. Ball, W. Windl and P. M. Woodward, *Chemistry of Materials*, 2016, **28**, 1348–1354.

(192) F. Wei, Z. Deng, S. Sun, F. Zhang, D. M. Evans, G. Kieslich, S. Tominaka, M. A. Carpenter, J. Zhang, P. D. Bristowe and A. K. Cheetham, *Chemistry of Materials*, 2017, **29**, 1089–1094.

(193) C. Wu, Q. Zhang, Y. Liu, W. Luo, X. Guo, Z. Huang, H. Ting, W. Sun, X. Zhong, S. Wei, S. Wang, Z. Chen and L. Xiao, *Advanced Science*, 2018, **5**, 1700759.

(194) M. Grätzel, *Nature Materials*, 2014, **13**, 838–842.

(195) E. van der Voet, R. Salminen, M. Eckelman, G. Mudd, T. Norgate and R. Hischier, *Environmental Risks and Challenges of Anthropogenic Metals Flows and Cycles*, tech. rep., 2013.

(196) I. R. Benmessaoud, A. L. Mahul-Mellier, E. Horváth, B. Maco, M. Spina, H. A. Lashuel and L. Forró, *Toxicology Research*, 2016, **5**, 407–419.

(197) A. Babayigit, A. Ethirajan, M. Muller and B. Conings, *Nature Materials*, 2016, **15**, 247–251.

(198) B. J. Kim, D. H. Kim, S. L. Kwon, S. Y. Park, Z. Li, K. Zhu and H. S. Jung, *Nature Communications*, 2016, **7**, 11735.

(199) A. Binek, M. L. Petrus, N. Huber, H. Bristow, Y. Hu, T. Bein and P. Docampo, *ACS Applied Materials & Interfaces*, 2016, **8**, 12881–12886.

(200) T. Leijtens, G. E. Eperon, N. K. Noel, S. N. Habisreutinger, A. Petrozza and H. J. Snaith, *Advanced Energy Materials*, 2015, **5**, 1500963.

(201) M. Shahbazi and H. Wang, *Solar Energy*, 2016, **123**, 74–87.

(202) B. Philippe, B.-W. Park, R. Lindblad, J. Oscarsson, S. Ahmadi, E. M. J. Johansson and H. Rensmo, *Chemistry of Materials*, 2015, **27**, 1720–1731.

(203)  G. Niu, W. Li, F. Meng, L. Wang, H. Dong and Y. Qiu, *Journal of Materials Chemistry A*, 2014, **2**, 705–710.

(204)  N. Aristidou, I. Sanchez-Molina, T. Chotchuangchutchaval, M. Brown, L. Martinez, T. Rath and S. A. Haque, *Angewandte Chemie - International Edition*, 2015, **54**, 8208–8212.

(205)  N. Aristidou, C. Eames, I. Sanchez-Molina, X. Bu, J. Kosco, M. Saiful Islam and S. A. Haque, *Nature Communications*, 2017, **8**, 1–10.

(206)  A. Dualeh, P. Gao, S. I. Seok, M. K. Nazeeruddin and M. Grätzel, *Chemistry of Materials*, 2014, **26**, 6160–6164.

(207)  F. Matteocci, L. Cinà, E. Lamanna, S. Cacovich, G. Divitini, P. A. Midgley, C. Ducati and A. Di Carlo, *Nano Energy*, 2016, **30**, 162–172.

(208)  A. Dualeh, T. Moehl, N. Tetreault, J. Teuscher, P. Gao, M. K. Nazeeruddin and M. Gratzel, *Acs Nano*, 2014, **8**, 362–373.

(209)  H. J. Snaith, A. Abate, J. M. Ball, G. E. Eperon, T. Leijtens, N. K. Noel, S. D. Stranks, J. T. W. Wang, K. Wojciechowski and W. Zhang, *Journal of Physical Chemistry Letters*, 2014, **5**, 1511–1515.

(210)  D. H. Song, M. H. Jang, M. H. Lee, J. H. Heo, J. K. Park, S.-J. Sung, D.-H. Kim, K.-H. Hong and S. H. Im, *Journal of Physics D: Applied Physics*, 2016, **49**, 473001.

(211)  J. M. Frost, K. T. Butler and A. Walsh, *APL Materials*, 2014, **2**, 081506.

(212)  Z. Fan, J. Xiao, K. Sun, L. Chen, Y. Hu, J. Ouyang, K. P. Ong, K. Zeng and J. Wang, *The Journal of Physical Chemistry Letters*, 2015, **6**, 1155–1161.

(213)  S. Meloni, T. Moehl, W. Tress, M. Franckevičius, M. Saliba, Y. H. Lee, P. Gao, M. K. Nazeeruddin, S. M. Zakeeruddin, U. Rothlisberger and M. Graetzel, *Nature Communications*, 2016, **7**, 10334.

(214)  C. Li, A. Guerrero, Y. Zhong and S. Huettner, *Journal of Physics: Condensed Matter*, 2017, **29**, 193001.

(215)  B. Chen, M. Yang, S. Priya and K. Zhu, *Journal of Physical Chemistry Letters*, 2016, **7**, 905–917.

(216) Y. Shao, Z. Xiao, C. Bi, Y. Yuan and J. Huang, *Nature Communications*, 2014, **5**, 1–7.

(217) N. K. Noel, A. Abate, S. D. Stranks, E. S. Parrott, V. M. Burlakov, A. Goriely and H. J. Snaith, *ACS Nano*, 2014, **8**, 9815–9821.

(218) H. S. Kim and N. G. Park, *Journal of Physical Chemistry Letters*, 2014, **5**, 2927–2934.

(219) J. H. Heo, H. J. Han, D. Kim, T. K. Ahn and S. H. Im, *Energy Environ. Sci.*, 2015, **8**, 1602–1608.

(220) D. Forgács, M. Sessolo and H. J. Bolink, *J. Mater. Chem. A*, 2015, **3**, 14121–14125.

(221) H.-S. Kim, I.-H. Jang, N. Ahn, M. Choi, A. Guerrero, J. Bisquert and N.-G. Park, *The Journal of Physical Chemistry Letters*, 2015, **6**, 4633–4639.

(222) P. Calado, A. M. Telford, D. Bryant, X. Li, J. Nelson, B. C. O'Regan and P. R. Barnes, *Nature Communications*, 2016, **7**, 13831.

(223) C. Eames, J. M. Frost, P. R. F. Barnes, B. C. O'Regan, A. Walsh and M. S. Islam, *Nature Communications*, 2015, **6**, 7497.

(224) J. Haruyama, K. Sodeyama, L. Han and Y. Tateyama, *Journal of the American Chemical Society*, 2015, **137**, 10048–10051.

(225) J. M. Azpiroz, E. Mosconi, J. Bisquert and F. De Angelis, *Energy Environ. Sci.*, 2015, **8**, 2118–2127.

(226) Y. Yuan, Q. Wang, Y. Shao, H. Lu, T. Li, A. Gruverman and J. Huang, *Advanced Energy Materials*, 2016, **6**, 1–7.

(227) C. Li, S. Tscheuschner, F. Paulus, P. E. Hopkinson, J. Kießling, A. Köhler, Y. Vaynzof and S. Huettner, *Advanced Materials*, 2016, **28**, 2446–2454.

(228) J. Xing, Q. Wang, Q. Dong, Y. Yuan, Y. Fang and J. Huang, *Phys. Chem. Chem. Phys.*, 2016, **18**, 30484–30490.

(229) H. S. Kim, I. Mora-Sero, V. Gonzalez-Pedro, F. Fabregat-Santiago, E. J. Juarez-Perez, N. G. Park and J. Bisquert, *Nature Communications*, 2013, **4**, 1–7.

(230) T.-Y. Yang, G. Gregori, N. Pellet, M. Grätzel and J. Maier, *Angewandte Chemie International Edition*, 2015, **54**, 7905–7910.

(231) A. Pockett, G. E. Eperon, N. Sakai, H. J. Snaith, L. M. Peter and P. J. Cameron, *Phys. Chem. Chem. Phys.*, 2017, **19**, 5959–5970.

(232) A. Senocrate, I. Moudrakovski, G. Y. Kim, T.-Y. Yang, G. Gregori, M. Grätzel and J. Maier, *Angewandte Chemie International Edition*, 2017, **56**, 7755–7759.

(233) Z. Li, C. Xiao, Y. Yang, S. P. Harvey, D. H. Kim, J. A. Christians, M. Yang, P. Schulz, S. U. Nanayakkara, C.-S. Jiang, J. M. Luther, J. J. Berry, M. C. Beard, M. M. Al-Jassim and K. Zhu, *Energy Environ. Sci.*, 2017, **10**, 1234–1242.

(234) K. Domanski, B. Roose, T. Matsui, M. Saliba, S. H. Turren-Cruz, J. P. Correa-Baena, C. R. Carmona, G. Richardson, J. M. Foster, F. De Angelis, J. M. Ball, A. Petrozza, N. Mine, M. K. Nazeeruddin, W. Tress, M. Grätzel, U. Steiner, A. Hagfeldt and A. Abate, *Energy Environ. Sci.*, 2017, **10**, 604–613.

(235) Y. Kato, L. K. Ono, M. V. Lee, S. Wang, S. R. Raga and Y. Qi, *Advanced Materials Interfaces*, 2015, **2**, 1500195.

(236) C. Besleaga, L. E. Abramiuc, V. Stancu, A. G. Tomulescu, M. Sima, L. Trinca, N. Plugaru, L. Pintilie, G. A. Nemnes, M. Iliescu, H. G. Svavarsson, A. Manolescu and I. Pintilie, *Journal of Physical Chemistry Letters*, 2016, **7**, 5168–5175.

(237) E. Bi, H. Chen, F. Xie, Y. Wu, W. Chen, Y. Su, A. Islam, M. Grätzel, X. Yang and L. Han, *Nature Communications*, 2017, **8**, 1–7.

(238) X. Zhang, C. Liang, M. Sun, H. Zhang, C. Ji, Z. Guo, Y. Xu, F. Sun, Q. Song and Z. He, *Phys. Chem. Chem. Phys.*, 2018, **20**, 7395–7400.

(239) A. Hillier and R. Cywinski, *The classification of superconductors using muon spin rotation*, 1997, vol. 13.

(240) S. J. Blundell, *Chemical Reviews*, 2004, **104**, 5717–5735.

(241) J. Sugiyama, K. Mukai, Y. Ikedo, H. Nozaki, M. Månsson and I. Watanabe, *Physical Review Letters*, 2009, **103**, 147601.

(242) A. S. Powell, J. S. Lord, D. H. Gregory and J. J. Titman, *The Journal of Physical Chemistry C*, 2009, **113**, 20758–20763.

(243) J. Sugiyama, K. Mukai, H. Nozaki, M. Harada, K. Kamazawa, Yutakaikedo, M. Månsson, O. Ofer, E. J. Ansaldo, J. H. Brewer, K. H. Chow, Isaowatanabe, Y. Miyake and T. Ohzuku, *Physics Procedia*, 2012, **30**, 105–108.

(244) T. E. Ashton, J. V. Laveda, D. A. MacLaren, P. J. Baker, A. Porch, M. O. Jones and S. A. Corr, *Journal of Materials Chemistry A*, 2014, **2**, 6238.

(245) J. Sugiyama, *Journal of the Physical Society of Japan*, 2013, **82**, SA023.

(246) M. Amores, T. E. Ashton, P. J. Baker, E. J. Cussen and S. A. Corr, *J. Mater. Chem. A*, 2016, **4**, 1729–1736.

(247) M. Månsson and J. Sugiyama, *Physica Scripta*, 2013, **88**, 068509.

(248) H. V. Alberto, R. C. Vilão, R. B. L. Vieira, J. M. Gil, A. Weidinger, M. G. Sousa, J. P. Teixeira, A. F. da Cunha, J. P. Leitão, P. M. P. Salomé, P. A. Fernandes, T. Törndahl, T. Prokscha, A. Suter and Z. Salman, *Physical Review Materials*, 2018, **2**, 025402.

(249) E. Morenzoni, H. Glückler, T. Prokscha, R. Khasanov, H. Luetkens, M. Birke, E. M. Forgan, C. Niedermayer and M. Pleines, *Nuclear Instruments and Methods in Physics Research, Section B: Beam Interactions with Materials and Atoms*, 2002, **192**, 254–266.

(250) J. Sugiyama, H. Nozaki, I. Umegaki, K. Mukai, K. Miwa, S. Shiraki, T. Hitosugi, A. Suter, T. Prokscha, Z. Salman, J. S. Lord and M. Månsson, *Physical Review B*, 2015, **92**, 014417.

# Chapter 2

# Theory

## 2.1  Solar Spectrum

With an approximate volume of $1.41 \times 10^{18}\,\text{km}^3$ the sun dominates the landscape of our solar system, producing light and heat that allow life to prosper on Earth.[1] The sun emits light with the spectrum shown in Figure 2-1, at the edge of the Earth's atmosphere the spectrum is comparable to a black body emitter at $5760\,\text{K}$.[2,3] A black body emits radiation of a specific distribution of wavelengths based on its temperature. At room temperature a black body appears black due to it emitting mostly infra-red radiation which is not visible to the human eye, giving rise to its name.[4]

The radiation incident on the atmosphere differs from that on the surface of Earth due to several factors. The absorption of light by $H_2O$, $O_3$, $CO_2$ and $O_2$ is the cause of the large missing sections (e.g. $1800\,\text{nm}$) in the terrestrial spectrum when compared to the extra terrestrial spectrum.[2] Another factor impacting the spectrum incident on Earth is absorption and scattering caused by air and dust, causing a loss of power over the whole solar spectrum.[2] This loss is dependent on the incident angle of the sun to the point of detection. This angle dependence is accounted for using Air Mass (AM), defined by Equation 2.1 where L is the optical path length, $L_0$ is the optical path length when the sun is directly overhead and $\theta$ is the angle between the two different paths.[5]

$$AM = \frac{L}{L_0} = \frac{1}{cos(\theta)} \tag{2.1}$$

When the sun is directly overhead the observer the Air Mass is 1. AM 1.5, which
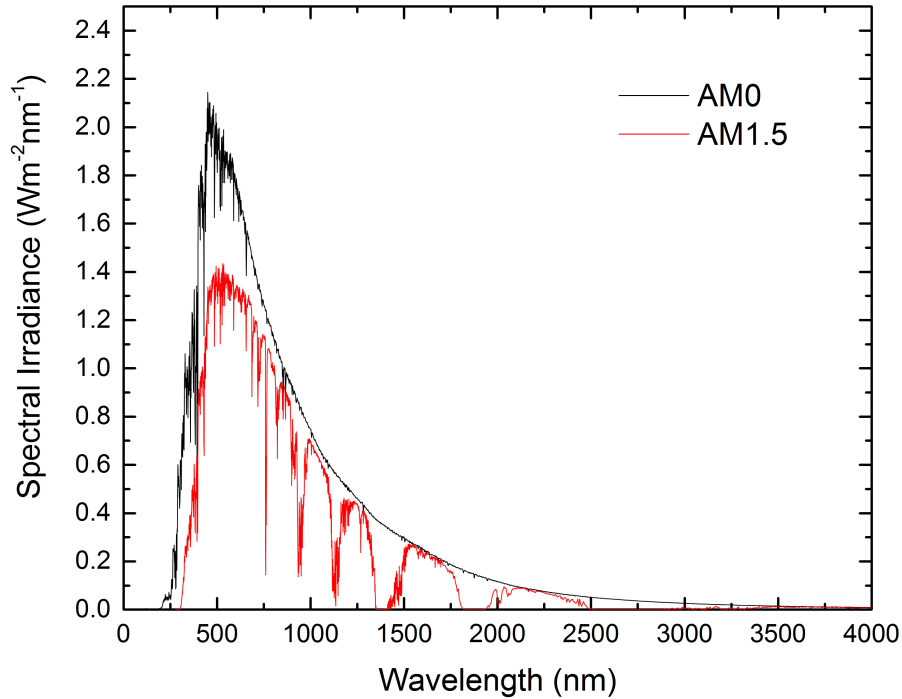
Figure 2-1: Extra terrestrial solar spectrum (Black) and solar spectrum at Air Mass 1.5 (Red).

is shown in Figure 2-1, is the standard spectrum used in solar research which corresponds to an angle of 42°. AM 1.5 is also used to normalise the integrated irradiance to $1000\,\mathrm{Wm^{-2}}$.[5]

## 2.2 Semiconductors

### 2.2.1 Semiconductor Band Structure

Semiconductors act as a conducting material at higher temperatures but act as an insulator at lower temperatures. These unique properties are a product of the alignment of the electron bands within the material. When two atoms join together their atomic orbitals combine and split into pairs of molecular orbitals of different energy. If a large group of molecules is brought together their molecular orbitals overlap at slightly different energies. The combining of enough molecular orbitals leads to a continuum of orbitals and the formation of large bands. The

highest occupied orbital in this case is referred to as the valence band (VB) and the lowest unoccupied orbital is the conduction band (CB). Figure 2-2 shows this combining of orbitals and how the band structures differ with different numbers of molecules. The difference between the bands of a metal and semiconductor is also shown. An insulator and semiconductor have the same orbital structure except with an increased gap between the VB and CB, this gap is the band gap ($E_g$) of the semiconductor or insulator.
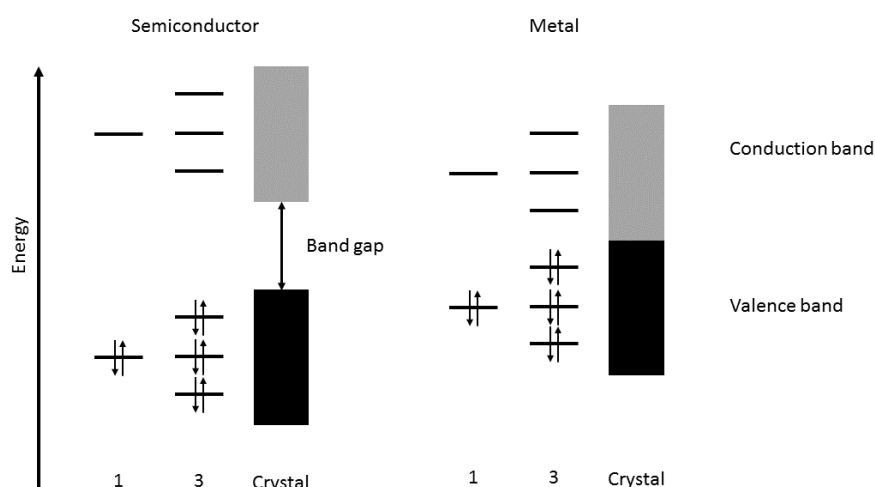


Figure 2-2: Representation of the formation of a band gap in a semiconductor (left) and no band gap formed in a metal (right). The number represents the number of molecules involved in the formation of each the different band diagrams.

At absolute zero an intrinsic semiconductor will have a fully populated VB and no electrons in the CB. As the temperature is increased electrons acquire energy and some are excited from the VB to the CB leaving behind a hole. At higher temperature more electrons will have the energy needed to cross the band gap. Once an electron is in the CB it is free to move through the lattice. The hole in the VB can also move through the lattice by having an adjacent electron move in to fill the hole creating a new hole in its previous location. This process is repeated with multiple electrons giving the impression of the hole moving through the lattice.

An important value with respect to semiconductors is the Fermi level ($E_F$). The $E_F$ is the energy level where the probability of finding an electron is 0.5, for an intrinsic semiconductor this will be half way between the VB and the CB as shown in Figure 2-3. As previously mentioned, a semiconductor at $0\,K$ will have a fully populated VB and an empty CB. As a semiconductor's temperature increases the electrons can be excited up to the CB. In an intrinsic semiconductor this does not change the $E_F$. The probability of finding an electron at a certain energy level at a certain temperature can be calculated using the Fermi-Dirac equation (Equation 2.2), where $f(E)$ is the Fermi Dirac distribution, E is the energy, $E_F$ is the Fermi level and $k_BT$ is the Boltzmann constant multiplied by the temperature.

$$f(E) = \frac{1}{e^{\left(\frac{E-E_F}{k_BT}\right)} + 1} \qquad (2.2)$$

The previously discussed theory of semiconductors has been based on an intrinsic semiconductor but it is impossible to make a completely pure intrinsic semiconductor experimentally. All semiconductors contain a small amount of defects and doping depending on how precisely they have been manufactured. Doping, is the accidental or deliberate addition of different elements to the semiconductor. There are two different types of doping, P and N, these gives rise to differing band properties. Taking a semiconductor made from group IV silicon as an example, N doping would involve the replacement of some amount of Si atoms with a group V element, usually phosphorous. The phosphorous atom provides an electron to the lattice. These electrons, if at the right energy level, populate a new band between the original CB and VB as shown in Figure 2-3. At $0\,K$, N-doping causes the $E_F$ to shift to the midpoint between the donor level and the CB.

The reverse effect can be achieved by doping the silicon semiconductor with a group III element, usually boron. This group III element provides one less electron to the lattice creating an extra band of holes giving the band structure shown in Figure 2-3. Semiconductors contain minority and majority carriers, these are the holes and electrons, which one is the majority is dependent on the doping of the semiconductor. In an N-doped semiconductor the majority carrier would be electrons due to the extra electrons coming from the dopant and for P-doped semiconductors the majority carrier is holes.
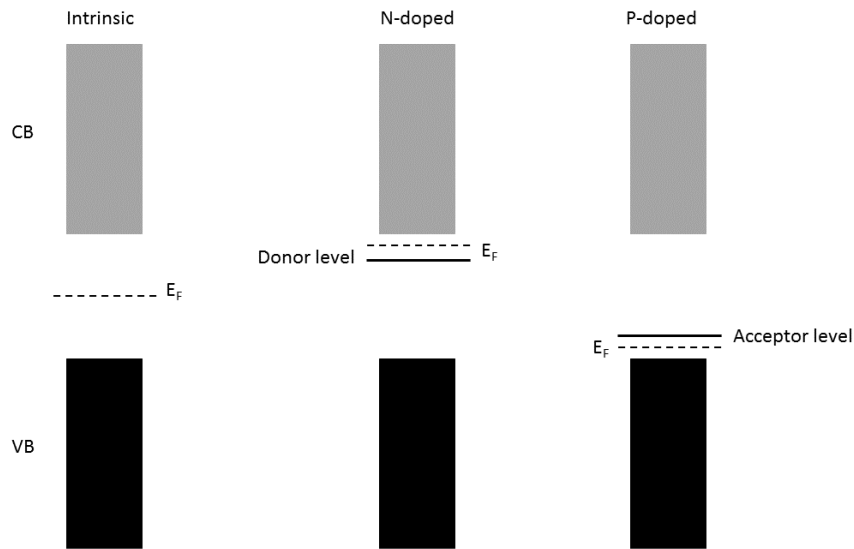
Figure 2-3: Simplified band structure diagrams of an intrinsic semiconductor, an N doped semiconductor and a P doped semiconductor at 0K.

## 2.2.2 Charge Generation and Recombination

The generation of free charge carriers in a semiconductor can occur by two different methods. The first is through thermal excitation, the second, and the one most relevant to solar cell, is photogeneration (Figure 2-4a). This type of generation occurs when a photon of energy greater than the $E_g$ of the semiconductor is absorbed by the material. The energy of the incident photon is transferred to an electron and excites it into the CB leaving behind a hole in the VB.[6] If the energy of the photon exceeds that of the $E_g$ then the electron is excited further into the CB, any excess energy is quickly lost through collisions with the lattice. This process is known as thermalisation and is responsible for limiting the maximum efficiency of single junction solar cells to 33 %.[7]

Once an electron is excited to the CB it will remain there for a short time before it returns to the VB via recombination. There are several different types of recombination that are all relevant to PV devices. Radiative recombination is the process by which an excited electron recombines directly with a hole in the VB. This recombination causes the emission of a photon and is the basis for light emitting diodes (Figure 2-4b).[8]

Auger recombination is another form of recombination and occurs when two
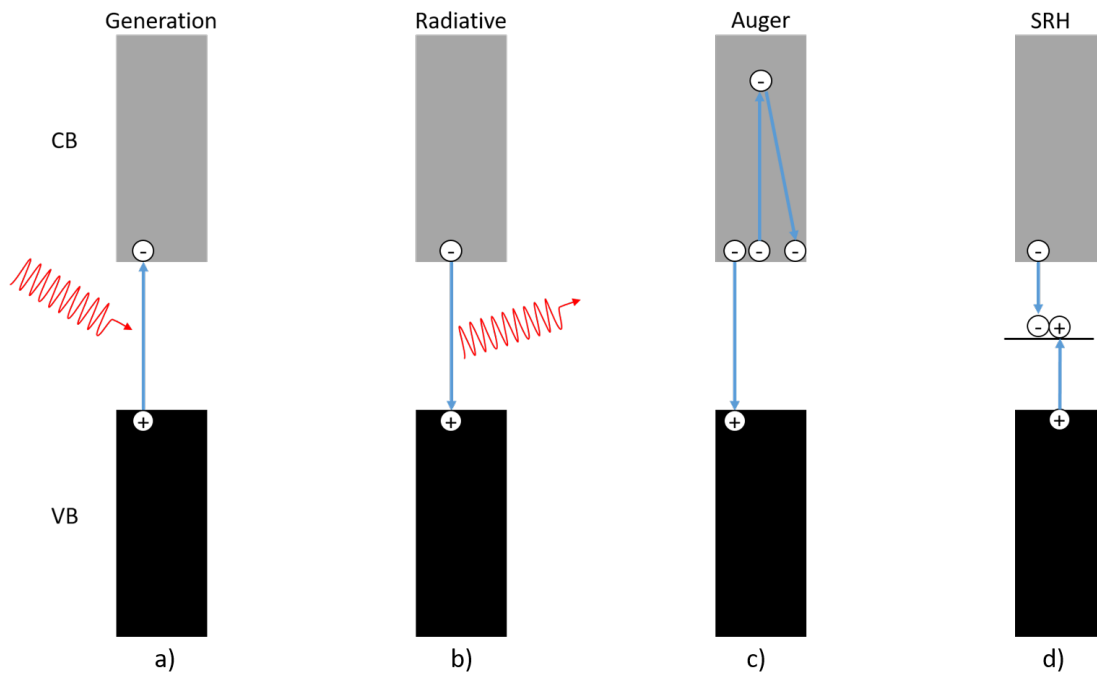
Figure 2-4: Graphic representations of a) photogeneration and the three main types of recombination a) radiative b) Auger and c) Shockley-Read-Hall (SRH).

excited electrons interact with each other in the CB. When the two electrons interact the energy of one is transferred to the other causing one to return to the VB and recombine with a hole while the other electron is excited further into the CB (Figure 2-4c). The over excited electron subsequently returns to the band edge via thermalisation.[8]

The third type of recombination is Shockley-Read Hall (SRH) recombination and involves trap states in the forbidden region of the semiconductor band gap (Figure 2-4d).[9] An electron in the CB can move down into a trap state in the space between the CB and VB. Once the electron is in this trap state two different processes can occur and the relative rates of these two processes will dictate what process is dominant. The first option is for the electron to be thermally excited back to the CB, the second is for a hole to move up to the same trap state and recombine with the electron. The rate of thermal excitation or recombination for the electron in the trap state varies depending on the position of the trap state. Trap states closest to the centre of the $E_g$ cause the most SRH recombinations as they have the best balance between electron trapping and retention as well as attracting the hole to recombine. Trap states too close to the CB would be

65

unable to bring holes in to recombine fast enough as the electron would only need a small amount of thermal energy to return to the CB.[10]

## 2.3   The P-N junction

A P-N junction is formed by the joining of an N-type semiconductor with a P-type semiconductor and it has the band structure shown in Figure 2-5. The two semiconductors have different $E_F$ and carrier concentrations. The formation of an interface between the high electron concentration N-type and the high hole concentration P-type material leads to diffusion of carriers between the two materials. The diffusion of carriers continues until an equilibrium is reached where the drift and diffusion of the carriers is equal and the two $E_F$s become equal.[11]
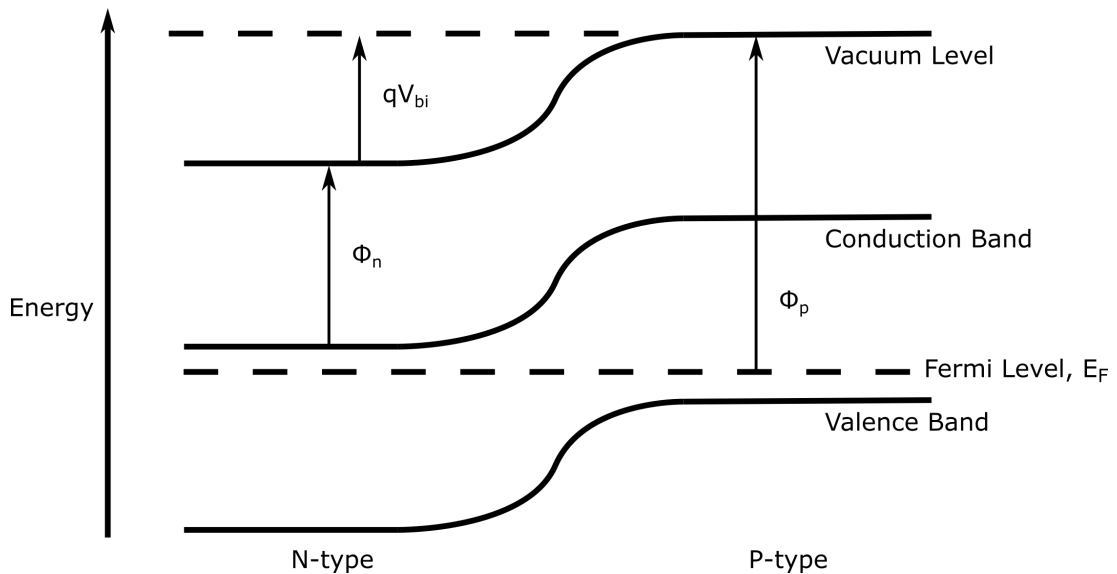


Figure 2-5: A schematic of a P-N junction showing the different band levels of the two separate materials, the vacuum level, the work functions of the two materials ($\theta_p$ and $\theta_n$) and the built in voltage bias $V_{bi}$.

A P-N junction in the dark with an applied voltage behaves like a diode. As the junction is forward biased more electrons and holes begin to diffuse across the depletion region and a net current flows. The current generated increases exponentially and can be calculated using equation 2.3.

$$I_d = I_0(e^{\frac{qV}{nKT}} - 1) \tag{2.3}$$

66
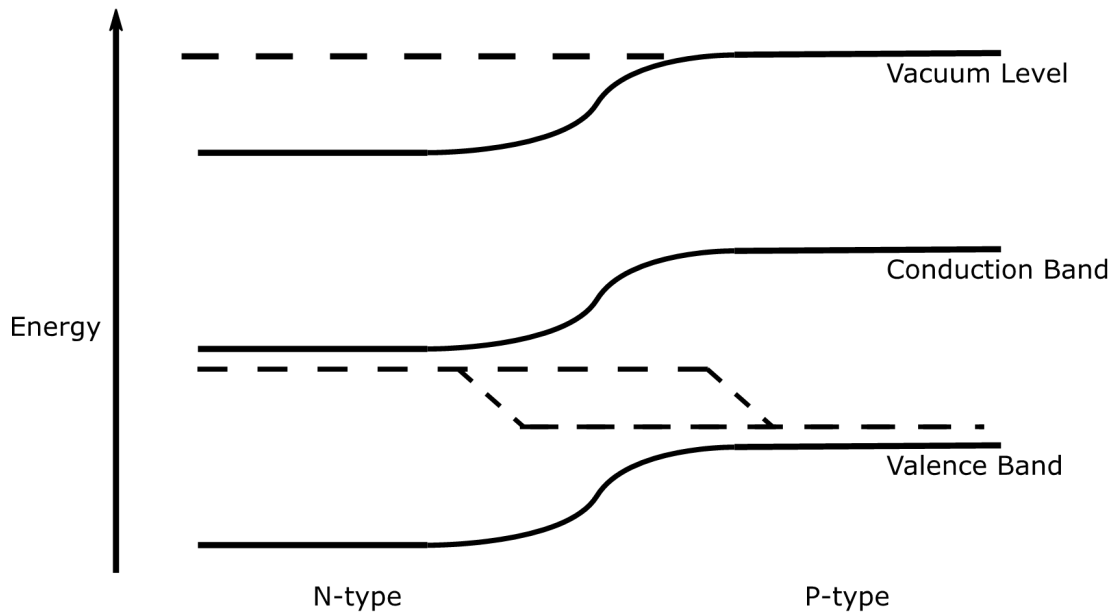
Figure 2-6: A schematic showing the formation of a quasi Fermi Level in a PN junction under illumination.

In this equation $I_d$ is equal to the net current flowing through the diode in the dark, $I_0$ is the dark saturation current, $q$ is the elementary charge of an electron, $V$ is the applied voltage across the diode, $n$ is the ideality factor and can be a number between 1 and 2, $K$ is Boltzmann's constant and $T$ is temperature.[11]

The situation changes under illumination as electron-hole pairs are created in the three different regions of the junction. This carrier generation causes a splitting of the Fermi level creating a quasi-Fermi level (Figure 2-6). The P-N junction then separates the electron hole pair as the minority carriers in either side are driven across the depletion region in a process called charge separation.[8] Also important is charge collection which is the probability of a generated carrier being collected by the PN junction and contributing to light generated current. Charge collection is governed by the diffusion length of charge carriers and the level of passivation of the device surface. As an electron and hole pair is generated further away from the P-N junction, its probability of collection decreases as it has further to diffuse before being taken across the junction. This increase in distance and therefore time taken increases the likelihood of recombination before the charges can be separated. The generation rate of carriers combined with the collection probability can be used to determine the light generated current ($I_L$).

The overall current of a PV device under illumination is equal to the light generated current minus the dark current (Equation 2.4).

$$I = I_L - I_d = I_L - I_0(e^{\frac{qV}{nKT}} - 1)$$ (2.4)

In perovskite devices charge separation is achieved using a P-I-N junction. In a perovskite P-I-N junction the P and N-type layers are provided by the hole transport layers and electron transport layers. The perovskite layer then behaves as an intrinsic semiconductor these three layers create the in build electric field needed to separate carriers.

**Solar Cell Parameters**

By sweeping across a voltage range and measuring the resultant current an IV curve can be produced. This is the standard method of analysing a PV device and produces a curve similar to that shown in Figure 2-7. The area of a solar cell is extremely important to the amount of current it can generate, therefore, to make it possible to easily compare devices it is common practice to report current density (J) making it a JV curve instead of an IV curve. From a JV curve it is possible to extract several important solar cell parameters: the open circuit voltage ($V_{OC}$), short circuit current density ($J_{SC}$), Fill Factor (FF) and power conversion efficiency (PCE). $J_{SC}$ is strongly dependent on the incident power of the light used for testing. To make comparison between studies possible there is an outlined standard that is used in device testing. The standardised system uses light at AM1.5 with an intensity of $1000 \, \text{W} \, \text{m}^{-1}$.

$J_{SC}$ is the point on a JV curve where the voltage is equal to zero. $J_{SC}$ is usually equal to light generated current $J_L$ and, when light intensity and spectrum are the same, is strongly dependent on charge generation rate and collection probability. $V_{OC}$ is the maximum voltage of a device and is at the point where the current is equal to zero. There are two different methods to calculate $V_{OC}$ one of these comes from rearranging Equation 2.4 and setting the current to zero to give Equation 2.5 (current has been replaced with current density).

$$V_{OC} = \frac{nKT}{q} \ln(\frac{J_L}{J_0} + 1)$$ (2.5)
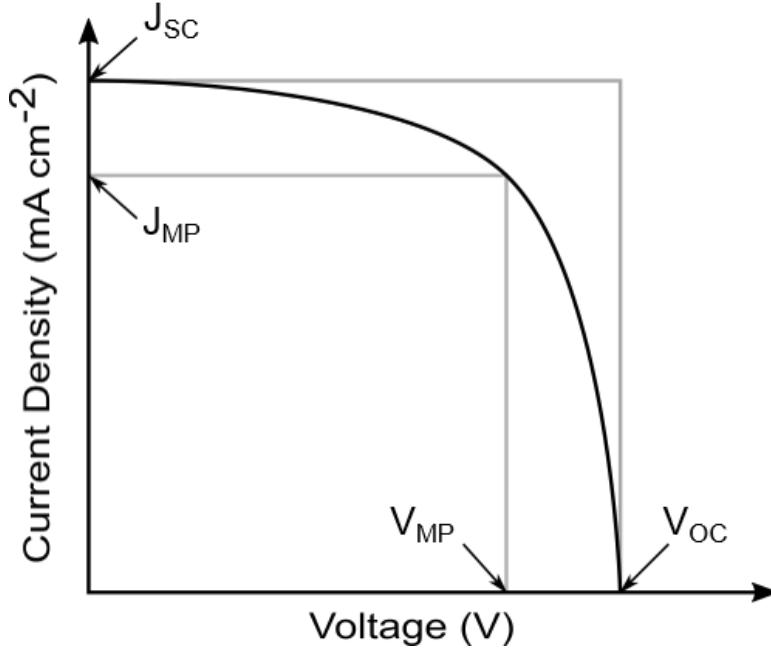
Figure 2-7: An example of a JV Curve

The other method uses carrier concentrations to calculate $V_{OC}$ as shown in Equation 2.6 where $N_A$ is the doping concentration, $\Delta n$ is excess carrier concentration and $n_i$ is the intrinsic carrier concentration.

$$V_{OC} = \frac{KT}{q} \ln\left[\frac{(N_A + \Delta n)\Delta n}{n_i^2}\right] \tag{2.6}$$

Fill factor is a measure of squareness of the JV curve and can be calculated using Equation 2.7 where $J_{MP}$ is the current density at maximum power and $V_{MP}$ is the voltage at maximum power. It is also equal to the area of the largest possible square beneath the JV curve divided by the area of square made using the $V_{OC}$ and $J_{SC}$ as corners (Figure 2-7).

$$FF = \frac{V_{MP}J_{MP}}{V_{OC}J_{SC}} \tag{2.7}$$

The final and most popular comparison value for solar cells is efficiency (PCE or $\eta$). The PCE can be calculated from $J_{SC}$, $V_{OC}$, FF and the power incident on the device, $P_{in}$, using Equation 2.8.

$$\eta = \frac{V_{OC}J_{SC}FF}{P_{in}} \tag{2.8}$$

With all the previously mentioned variables, if measurement conditions are kept the same, it is easy to compare results between different cells across different research groups.

## 2.4   Powder X-Ray Diffraction

Powder X-ray diffraction (pXRD) is a quick and inexpensive technique that can be used to determine several structural properties of a material. To perform pXRD, X-rays with a fixed wavelength are fired at a sample and X-rays that are diffracted from the sample are detected. The detector and X-ray source are moved around the sample varying the angle between the incident beam and the detector ($2\theta$) and a plot of intensity against $2\theta$ is produced. This intensity vs $2\theta$ plot can be used to compare with a database of diffraction patterns and can also give the distance between symmetry planes in the crystal. The relation between the diffraction angle ($\theta$) and the distance between symmetry planes ($d_{hkl}$) is given by Bragg's law (Equation 2.9), where $\lambda$ is the wavelength of the X-rays.[12]

$$\lambda = 2d_{hkl}sin\theta \tag{2.9}$$

When parallel atoms with an even $d_{hkl}$ space diffract X-rays they will constructively interfere with each other causing a diffraction peak. The different planes must be correctly aligned with the incident X-rays for a peak to be produced. A single crystal would produce a different diffraction pattern dependent on the orientation of the planes but for a bulk powder this orientation specific diffraction can be effectively ignored. It can be ignored because the crystals are randomly oriented so all of the planes would have some crystals aligned correctly to produce a diffraction peak.

Other useful information that can be gathered from pXRD is the average crystallite size. Using the full width at half maximum (FWHM)($\Delta$) and the Scherrer equation (Equation 2.10) the crystallite size ($\tau$) can be calculated.[13] In the below equation $\tau$ is the crystallite size, K is the shape factor, $\lambda$ is the wavelength of the incident X-rays, $\Delta$ is the FWHM and $\theta$ is the diffraction angle.

$$\tau = \frac{K\lambda}{\Delta cos\theta} \tag{2.10}$$

Based on the Scherrer formula narrower peaks mean bigger crystals, but there are other factors that impact peak width so the results of the Scherrer formula should be taken as an estimate.

## 2.5 UV-Vis Characterisation

In this work UV-Vis is used routinely to calculate the band gap of various perovskites. This is achieved using a Tauc plot. In 1966 the Tauc plot was first put forward as a method of calculating a material's band gap from UV-Vis measurements.[14] The use of a Tauc plot relies on the relation between the $E_g$ and absorbance shown in Equation 2.11 where $\alpha$ is the absorption coefficient, h is Planck's constant, $\nu$ is the wavelength of light and A is a proportionality constant.

$$(\alpha h\nu)^{\frac{1}{n}} = A(h\nu - E_g) \tag{2.11}$$

Transmittance and reflectance data was measured and converted to absorbance then subsequently converted to $(\alpha h\nu)$. The type of transition dictates the value of n that is used. For perovskites the transition is direct and allowed therefore $n = 1/2$. Plotting $(\alpha h\nu)^{\frac{1}{n}}$ against $h\nu$ gives a Tauc plot with the general form of Figure 2-8. The linear region of Figure 2-8 can be fitted and the X-intercept gives the band gap of the material.
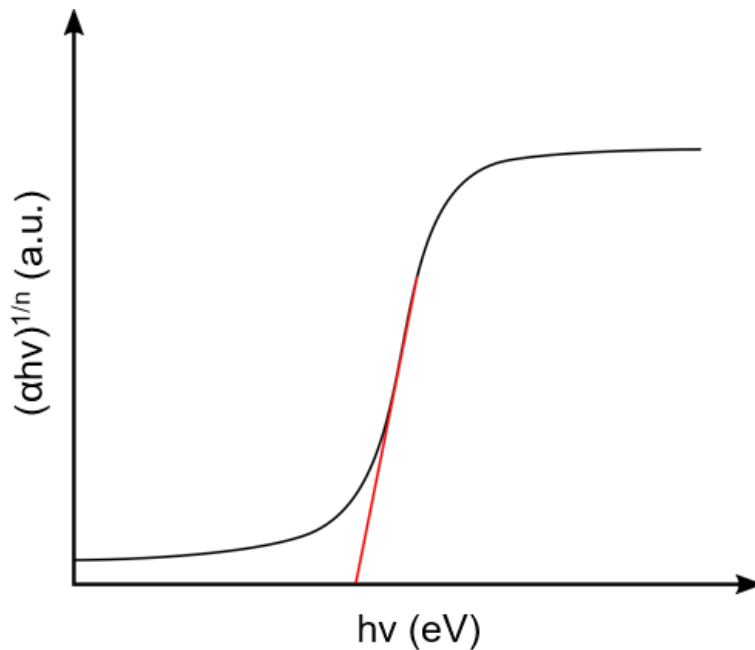


Figure 2-8: An example of a Tauc plot with the linear fit extrapolated to the X-axis in red

## 2.6 Electrochemical Impedance Spectroscopy

Electrochemical impedance spectroscopy (EIS) is a firmly established technique for the study of electrodes, corrosion and catalyst kinetics. More recently, EIS has been used to investigate the properties of dye sensitized solar cells and now perovskite solar cells. In this thesis EIS is used to study perovskite solar cells and to probe their internal dynamics. Presented here is a brief outline of the theory of EIS.

Impedance is similar to resistance that is defined by Ohm's law (Equation 2.12) except it is not limited to just ideal resistors.

$$R = \frac{V}{I} \tag{2.12}$$

Impedance can be defined as the ability of a material to resist the flow of electrons. To perform an EIS measurement an AC voltage is applied to the system and the AC current response as a function of frequency is measured. When plotted against time the sinusoidal voltage and current will be phase shifted (Figure 2-9). The voltage can be expressed as a function of time by Equation 2.13 where $V_t$ is potential at time t, $V_0$ is the signal amplitude and $\omega$ is the radial frequency.

$$V_t = V_0 cos(\omega t) \tag{2.13}$$

The measured current at time t ($I_t$) is phase shifted by ($\theta$) and is related to $I_0$ by Equation 2.14.

$$I_t = I_0 cos(\omega t + \theta) \tag{2.14}$$

EIS data is analysed by fitting it to an equivalent electrical circuit. These equivalent circuits are made up of various different electrical elements with the most common being resistors and capacitors. A resistor follows Ohm's law and therefore has an impedance that is equal to Equation 2.15.

$$Z = \frac{V}{I} \tag{2.15}$$

It is important to note that a resistor's impedance is not dependent on frequency therefore an ideal resistor would not produce a phase shift between the current and voltage. A capacitor's impedance is represented by Equation 2.16.

$$Z = \frac{1}{j\omega C} \tag{2.16}$$
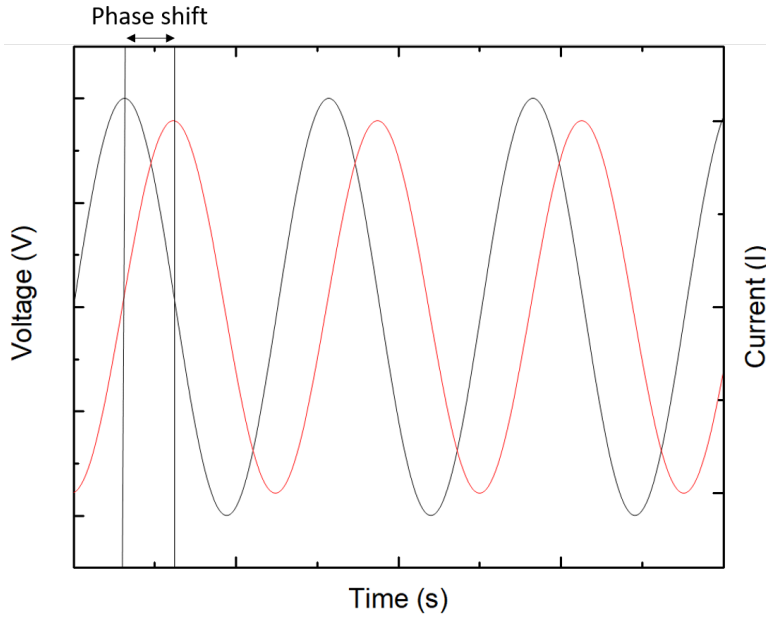
Figure 2-9: Sinusoidal voltage (black) and current response (red)

The origin of Equation 2.16 is explained by Equations 2.17-2.25. The charge stored in a capacitor is equal to the capacitance multiplied by the voltage (Equation 2.17) therefore the change in charge is equal to capacitance multiplied by change in voltage (Equation 2.18). The current is equal to the rate of change in charge with the time (Equation 2.19) and substituting in Equation 2.18 gives a current equal to capacitance multiplied by change in voltage with time (Equation 2.20). The change in voltage with time is sinusoidal therefore the phase shift of the capacitor is 90°.

$$Q = CV \tag{2.17}$$

$$dQ = CdV \tag{2.18}$$

$$I = \frac{dQ}{dt} \tag{2.19}$$

$$I = C\frac{dV}{dt} \tag{2.20}$$

Substituting Equation 2.20 into Ohm's law (Equation 2.15) gives Equation 2.21

$$Z = \frac{V}{C\frac{dV}{dt}} \tag{2.21}$$

73

Using Euler's notation (Equation 2.22), voltage (Equation 2.13) can be transformed to Equation 2.23. Using the complex voltage over real terms makes for a more simple representation of the total impedance of a capacitance.

$$e^{jx} = cos(x) + jsin(x) \tag{2.22}$$

$$V_t = V_0 e^{j\omega t} \tag{2.23}$$

Substituting Equation 2.23 and differentiating $dV/dt$ (Equation 2.24) gives Equation 2.25.

$$\frac{dV}{dt} = V_0 j\omega e^{j\omega t} \tag{2.24}$$

$$Z = \frac{V_0 e^{j\omega t}}{CV_0 j\omega e^{j\omega t}} \tag{2.25}$$

Finally, rearranging Equation 2.25 gives the final equation for the impedance of a capacitor (Equation 2.16). The impedance of a capacitor contains no real component and is phase shifted by 90°. The phase shift occurs because the current of a capacitor is related to voltage by integrating sine which gives cosine. This cosine, sine relationship causes the phase shift.

EIS is often presented in one of two different ways, a Nyquist or Bode plot. A Nyquist plot presents the imaginary impedance Z" on the Y-axis and the real component (Z') on the X-axis (Figure 2-10a). Each data point on the Nyquist plot represents a different frequency with high frequency data being further to the left and low frequency being further to the right. If a straight line is plotted from the origin to the data point the angle between the line and the axis is equal to the phase angle. The biggest weakness of the Nyquist plot is that it is not possible to know the frequency of the individual data point. The second type of graphs, the bode plots, have the phase shift or impedance on the Y-axis and the log of the frequency on the X-axis (Figure 2-10b and c). An important value that can be gathered from Nyquist and Bode plots is the RC time constant ($\tau$) for a process. $\tau$ is equal to the resistance multiplied by the capacitance (Equation 2.26) and is also equal to the inverse of the angular frequency ($\omega^{-1}$).

$$\tau = R \times C \tag{2.26}$$

74
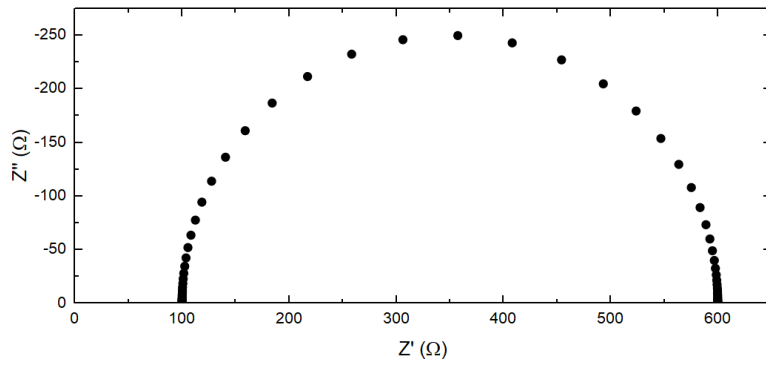
(a)
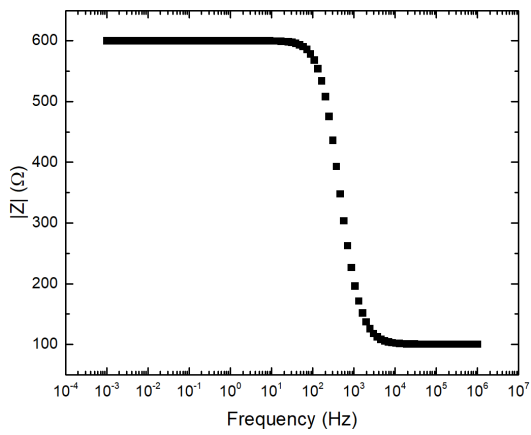


(b)
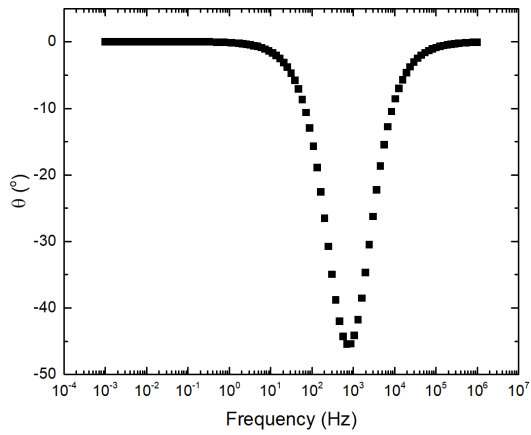


(c)

Figure 2-10: a) An example Nyquist plot and b/c) Bode plots of a simple circuit containing a series resistance and a parallel resistor and capacitor.

The apex of the semicircle in a Nyquist plot is equal to $\omega_{\text{max}}$ which is equal to the inverse of the time constant Equation 2.27.

$$\omega = \frac{1}{\tau} \tag{2.27}$$

The Nyquist plot in Figure 2-10 shows the impedance of a resistor and capacitor in parallel and represents one of the simplest possible circuits that can be modelled. As the system becomes more complex more elements would appear in the Nyquist plot, each represented by its own circuit elements. Multiple circuit elements can be connected either in series or in parallel, and summing the impedance is slightly different for each situation. For elements that are connected in series the total impedance can be calculated using Equation 2.28.

$$Z = Z_1 + Z_2 + Z_3 + ... + Z_n \tag{2.28}$$

If the elements are connected in parallel then the total impedance calculation changes to Equation 2.29.

$$\frac{1}{Z} = \frac{1}{Z_1} + \frac{1}{Z_2} + \frac{1}{Z_3} + ... + \frac{1}{Z_n} \tag{2.29}$$

All of the different elements present in an EIS response originate from a physical process. Choosing the correct way to model the data is crucial to correctly detecting changes in the physical processes present in the system. If the measurement and subsequent analysis are performed correctly EIS can be a powerful tool for investigating material properties. In perovskite research the most common uses of EIS are to investigate carrier recombination,[15] electron transportation[16] and ion migration.[17]

## 2.7  Muon Spin Relaxation ($\mu$SR)

### Muon Generation

Muons, a type of lepton, are the largest fraction of particles found in cosmic rays at sea level. The rate of muons incident on the earth from cosmic rays is $1\,\text{cm}^{-2}\,\text{min}^{-1}$. Muons are generated, alongside a muon neutrino, from charged pions in a two body decay.[18] The charge on the generated muon depends on the

charge of the initial pion (Equation 2.30 & 2.31).

$$\pi^+ \longrightarrow \mu^+ + \nu_\mu \tag{2.30}$$

$$\pi^- \longrightarrow \mu^- + \nu_\mu \tag{2.31}$$

Pions can either come from cosmic rays or be generated by an accelerator source. In an accelerator, a proton beam is fired at a target (graphene at ISIS) producing a pion, proton and neutron (Equation 2.32).

$$p + p \longrightarrow \pi^+ + p + n \tag{2.32}$$

To obey the basic laws of physics the decay products of the pion must conserve its momentum and spin therefore the muon and neutrino must have these parameters mirrored. A pion has zero spin and when at rest decays into a muon and neutrino. As it decays the two products are produced with opposite momenta away from the pion's location. A neutrino's spin is always aligned antiparallel to its momentum. Therefore, if the pion is at rest all of the neutrinos have the same spin and thus all of the muons have the same spin. This creates a 100 % spin polarized beam as long as the pions are at rest when they decay (Figure 2-11).[19]
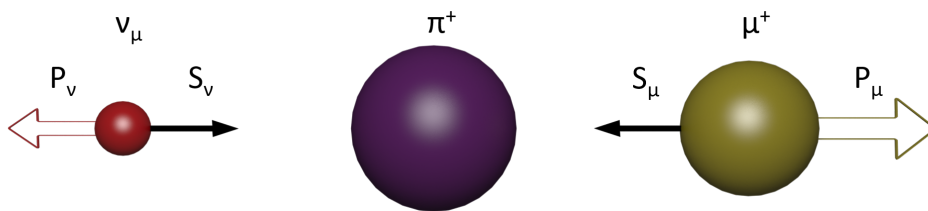


Figure 2-11: Schematic showing pion decay and the resulting muon and muon-neutrinos momentum and spin

**Muon Properties**

The properties of muons compared to protons and electrons are outlined in Table 2.1. While they have identical spins and magnitude of charge, they vary dramatically in mass and lifetime. The lifetimes of a proton and electron are infinite when compared to lifetime of a muon which is $2.2 \, \mu$s. Another difference is in

mass, a muon is 207 times heavier than an electron and approximately 9 times lighter than a proton. The differences in mass leads to muons sometimes being referred to as light protons or heavy electrons.[19]

Table 2.1: The properties of muons compared to electrons and protons

| Particle | Charge | Spin | Mass | Lifetime (µs) |
|---|---|---|---|---|
| Electron | $- e$ | 1/2 | $m_e$ | $\infty$ |
| Muon (µ) | $\pm e$ | 1/2 | $207\ m_e$ | 2.19 |
| Proton | $+ e$ | 1/2 | $1836\ m_e$ | $\infty$ |

Muon decay is a three body process into a positron, muon-antineutrino and an electron-neutrino (Equation 2.33 and Figure 2-12a).

$$\mu^+ \longrightarrow e^+ + \overline{\nu}_\mu + \nu_e \tag{2.33}$$

This decay happens via the weak interaction. The weak interaction is, one of the four fundamental interactions, the others being strong, gravity and electromagnetic. The weak interaction allows for the decay to violate parity. Parity conservation is the theory that an experiment will produce the same results as an exact mirror of the same experiment. By not conserving parity the decay into positrons is asymmetric in the direction of the muon spin. How the angular distribution of the positrons changes with muon spin direction is shown in Figure 2-12b.[20]

**Muons in Experiments**

When a muon is implanted into a sample it decays as outlined previously. The decay positron is detected and this gives information about the state of the muon at the moment of decay. Figure 2-13 shows a schematic of an experiment. At the moment of implantation the muon can decay and the positron will most likely be detected by the backwards detector. In a transverse magnetic field, after a small amount of time the muon will have rotated and then decay would be detected in the forward detector this process continues until all of the muons have decayed.

The number of positrons detected in the forward and backward detectors can then be plotted against time and the average of the two will be equal to the

(a)



(b)
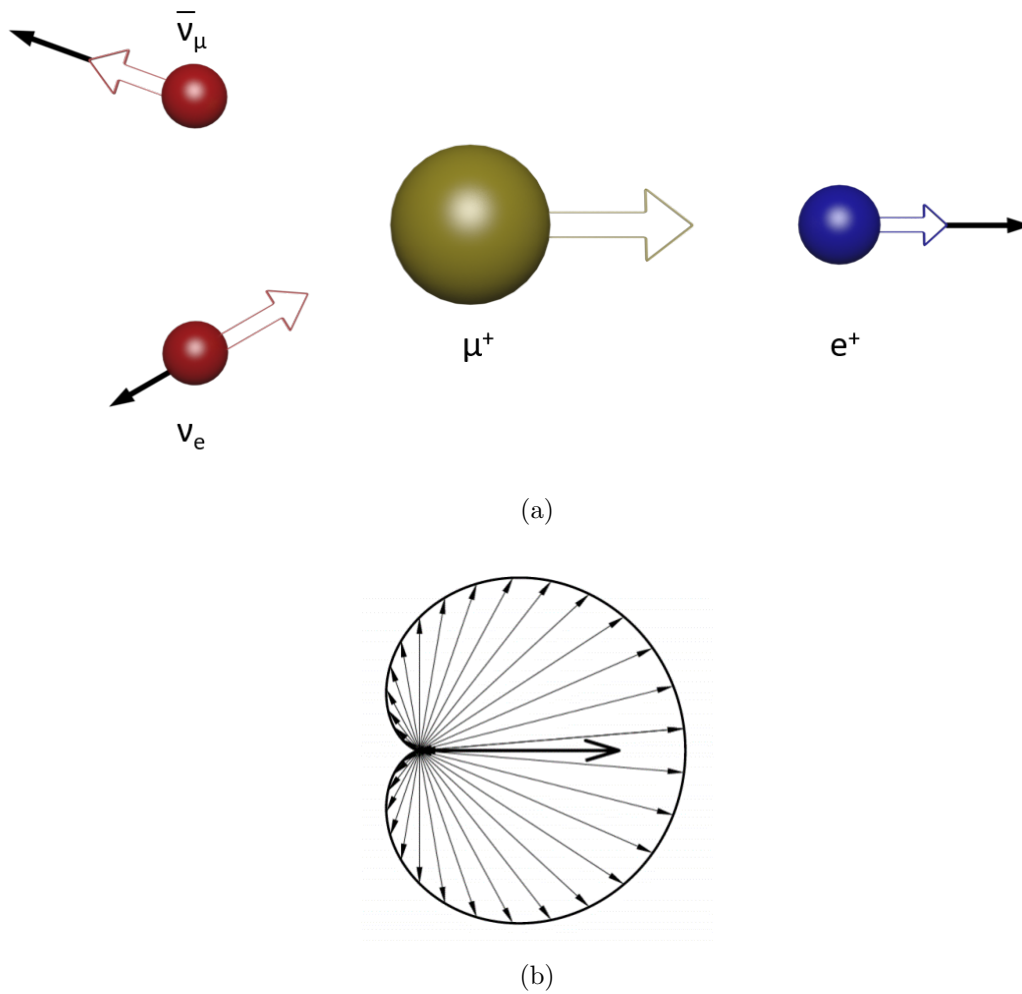
Figure 2-12: (a)Diagram depicting the decaying of a muon into a positron and two neutrinos. (b)Schematic showing the angular distribution of positrons with respect to muon spin direction adapted with permission from.[20] Copyright (2018) American Chemical Society

exponential rate of decay of muons (Figure 2-14a). The polarization of the muon with respect to time can then be produced by transforming the positron count in the forward and backward detector ($N_F$ and $N_B$) to asymmetry ($A_t$) using Equation 2.34. The transformation to asymmetry produces the graph shown in Figure 2-14b.

$$A(t) = \frac{N_B(t) - N_F(t)}{N_B(t) - N_F(t)} \qquad (2.34)$$

From the $A_t$ the time dependent spin polarisation ($P(t)$) can then be calculated by normalising the asymmetry data to the initial asymmetry (Equation

79
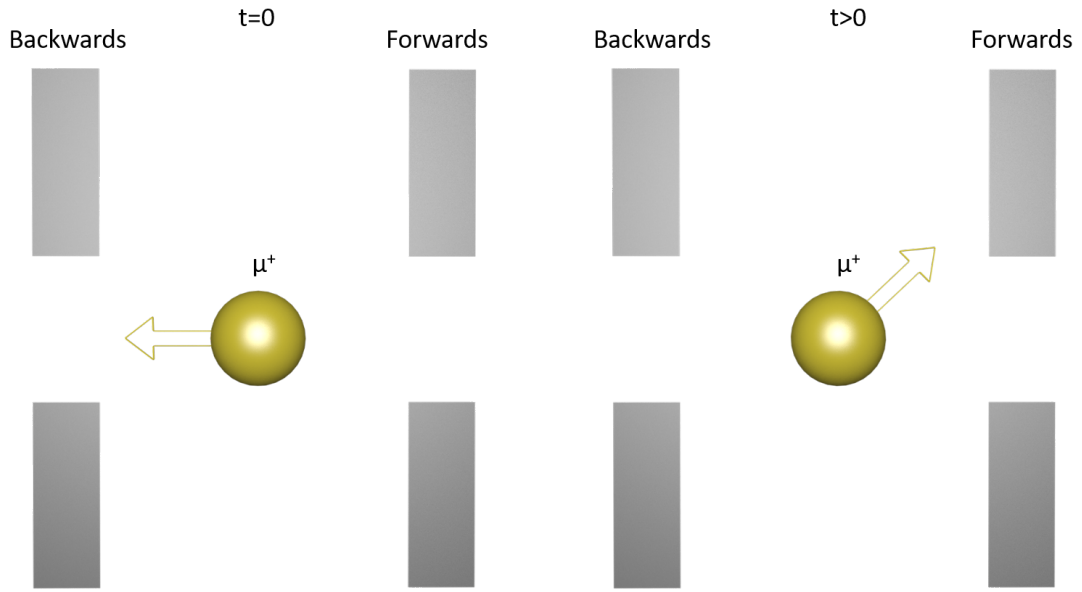
Figure 2-13: A diagram depicting a muon experiment at $t = 0$ and $t > 0$
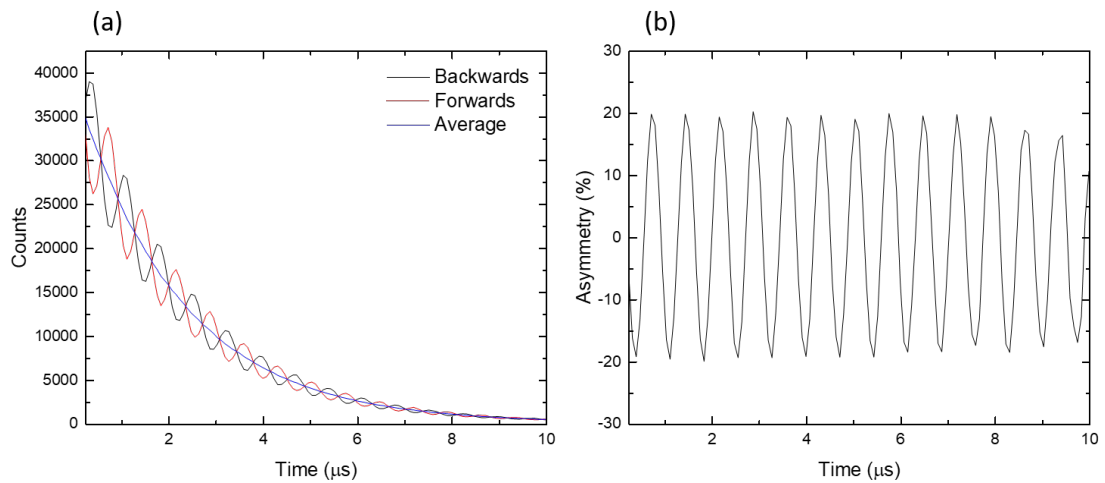


Figure 2-14: (a) The positron count in the backwards and forwards detectors and the average of the two (b) the changing of asymmetry with time calculated from the positron counts in (a).

2.35).

$$G(t) = \frac{A(t)}{A_o} \tag{2.35}$$

There are two different types of beam that can be used to insert muons into a sample, these are a continuous or pulsed beam. With a pulsed source, such as the one at ISIS, large numbers of muons arrive at the sample every 20 ms. Almost

all of these muons decay and a large number of resulting positrons are detected before the next pulse of muons arrive. With a continuous source, muons arrive at random time intervals. Continuous sources detect when a muon enters the sample and this creates a window of opportunity to detect a decay positron. If the positron is detected before a second muon enters the sample then the data would be accepted. If a second muon arrives before the positron is detected then the data from the decay positron of both muons would be rejected. This rejection is down to the fact that it is impossible to know which muon has produced which positron, meaning no information about either muons environment at the moment of decay can be gained. The discarding of events in a continuous source gives this method a lower resolution of data at longer time lengths as there are fewer events measured. This is not an issue with a pulsed source.

**Muon Relaxation Functions**

As previously discussed muons that enter the sample are 100 % spin polarised and upon entering a sample they will precess around any intrinsic or applied magnetic field (Figure 2-15a). In a static field the polarization in the Z axis is related to the magnetic field by Equation 2.36 where B is the magnetic field strength, $\gamma_\mu$ is the gyromagnetic ratio of the muon and t is time.

$$P_z(t) = cos^2\theta + sin^2\theta cos(\gamma_\mu Bt) \tag{2.36}$$

If the orientation of the static field is along the Z axis then the muons will not precess as $\theta = 0$. This would cause the muons to remain 100 % polarised. If a transverse field is applied $\theta = \pi/2$, this causes the muons to precess and the polarisation oscillates between 1 and -1. If the muon is in a sample where there is a random magnetic field in all directions then $\theta$ is averaged over all angles giving $cos^2\theta = 1/3$ and $sin^2\theta = 2/3$, this leads to Equation 2.37. If the angles of $\theta$ were to be averaged over just a 2D circle then $cos^2\theta$ and $sin^2\theta$ would both be equal to 0.5. When the averaging is performed over a 3D sphere the addition of an extra dimension increases the average of $sin^2\theta$ to 2/3 and decreases $cos^2\theta$ to 1/3 as there is a doubling of the impact from transverse magnetic fields. When in a magnetic field perpendicular to the initial polarisation, $cos^2\theta = 0$. With both the x and y component providing this value of 0 and the longitudinal field

81

providing 1 then the average becomes 1/3 the opposite situation is true for the sine component.

$$P_z(t) = \frac{1}{3} + \frac{2}{3}cos(\gamma_\mu Bt) \qquad (2.37)$$

The polarisation graph created from Equation 2.37 oscillates between 1 and -1/3. This is the type of response that is observed with a polycrystalline magnetic material which has a random magnetic field in all directions.[19]

Most systems are not as simple as a polycrystalline material and the magnetic fields have some form of distribution. In most cases, this distribution can be assumed to be Gaussian due to the central limit theorem which states that, given enough randomly occurring fields are combined they average out to a Gaussian distribution. In this Gaussian distribution case the polarization equation becomes equal to Equation 2.38.

$$P_z(t) = \frac{1}{3} + \frac{2}{3}e^{-\Delta^2 t^2/2}(1 - \Delta^2 t^2) \qquad (2.38)$$

This is the static Kubo-Toyabe (KT) function named after the researchers who derived it.[21] When plotted, this relaxation function takes the form shown in Figure 2-15b. The polarization drops to a minimum at approximately $1/\Delta$ and then rises back to a level at 1/3 of the maximum polarization. The tail at 1/3 is formed from destructive interference between all the muons that are experiencing slightly different magnetic fields.

In an experimental setting a longitudinal field (LF) can be applied to the experiment. The added LF causes the 1/3 tail of the Kubo-Toyabe relaxation to increase above 1/3 (Figure 2-15c). The reasons for applying a field are discussed below.

If the environment that the muon stops in is dynamic then the relaxation function has to be changed to include these dynamics. The different dynamics can arise from either muons moving between sites inside the crystal lattice or the field changing around a static muon. How different dynamic fields effect the polarization of muons is shown graphically in Figure 2-15d. At low fluctuation rates the tail of the KT function is depressed and at higher fluctuation rates it becomes an exponential decay. A combination of zero field and longitudinal field experiments, correctly fitted to the right relaxation function, makes it possible to
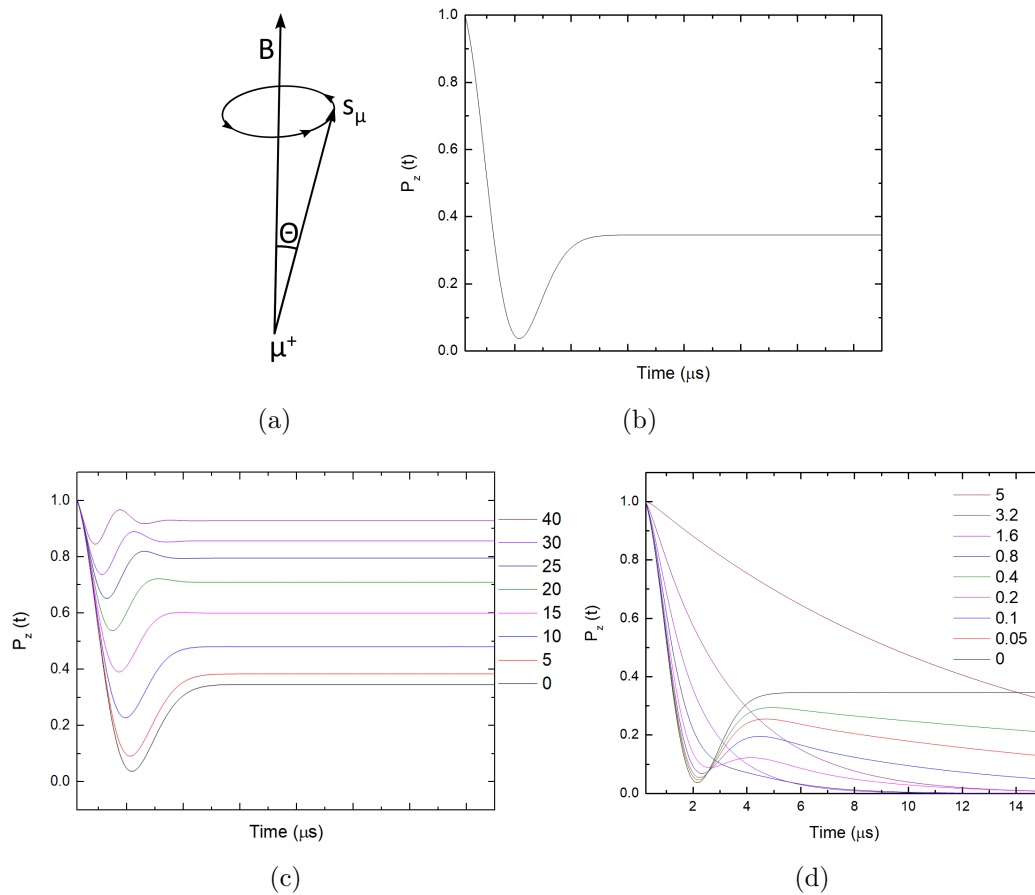
Figure 2-15: a) A diagram of muon precession around a magnetic field. b) A plot of the Kubo-Toyabe relaxation function. c) A graph showing the impact of changing longitudinal field (in Gauss) on the Kubo-Toyabe relaxation function. d) Graphic representation of the change in muon polarization with varying fluctuation rate in MHz.

elucidate information about the internal fields around the muon stopping sites in a sample.

# References

(1)   *Columbia Electronic Encyclopedia*, Columbia University Press, 6th, 2003.

(2)   C. C. Hu and R. M. White, *SOLAR CELLS: From Basics to Advanced Systems*, London, 1983.

(3)   A. Fraknoi, D. Morrison and S. Wolff, *Voyages Through the Universe*, Harcourt College Publishers, 2000.

(4)   J. C. Zwinkels, in *Encyclopedia of Color Science and Technology*, Springer Berlin Heidelberg, Berlin, Heidelberg, 2015, pp. 1–5.

(5)   P. Wurfel, *Physics of Solar Cells*, Wiley-Blackwell, 2008.

(6)   M. Grundmann, *The Physics of Semiconductors*, Springer Berlin Heidelberg, Berlin, Heidelberg, 2010.

(7)   W. Shockley and H. J. Queisser, *Journal of Applied Physics*, 1961, **32**, 510–519.

(8)   K. W. Böer, *Handbook of the Physics of Thin-Film Solar Cells*, Springer Berlin Heidelberg, Berlin, Heidelberg, 2013, pp. 625–627.

(9)   W. Shockley and W. T. Read, *Physical Review*, 1952, **87**, 835–842.

(10)  T. Markvart and L. Castañer, in *Practical Handbook of Photovoltaics*, Elsevier, 2012, pp. 33–62.

(11)  J. Nelson, *The Physics of Solar Cells*, 2003.

(12)  L. Bragg, *The crystalline state : a general survey*, Bell, London, 1933.

(13)  A. L. Patterson, *Physical Review*, 1939, **56**, 978–982.

(14)  J. Tauc, R. Grigorovici and A. Vancu, *Physica Status Solidi (b)*, 1966, **15**, 627–637.

(15)  A. Pockett, G. E. Eperon, T. Peltola, H. J. Snaith, A. Walker, L. M. Peter and P. J. Cameron, *The Journal of Physical Chemistry C*, 2015, **119**, 3456–3465.

(16)  E. Guillén, F. J. Ramos, J. A. Anta and S. Ahmad, *The Journal of Physical Chemistry C*, 2014, **118**, 22913–22922.

(17) L. Contreras, J. Idígoras, A. Todinova, M. Salado, S. Kazim, S. Ahmad and J. A. Anta, *Phys. Chem. Chem. Phys.*, 2016, **18**, 31033–31042.

(18) F. Jegerlehner, *The Anomalous Magnetic Moment of the Muon*, 2nd ed. 20, 2017.

(19) P. Carretta and A. Lascialfari, *NMR-MRI, μSR and Mössbauer Spectroscopies in Molecular Magnets*, Springer Milan, Milano, 2007, p. 294.

(20) S. J. Blundell, *Chemical Reviews*, 2004, **104**, 5717–5735.

(21) R. Kubo and T. Toyabe, *Magnetic Resonance and Relaxation*, ed. R. Blinc, Amsterdam, 1967, p. 810.

# Chapter 3

# Experimental

## 3.1 General

All solvents used in the experimental work in this thesis were from either VWR or Sigma and were not anhydrous unless otherwise stated. AFM imaging was performed using a Nanosurf easyScan 2 FlexAFM system. All NMR spectra were acquired using a Bruker 500 MHz instrument at 298 K unless otherwise stated. Optical absorption data was collected using a PerkinElmer Lambda 750s UV/Vis/NIR spectrometer with a 60 nm integrating sphere. X-ray diffraction patterns were obtained using a Bruker axs D8 advance powder X-ray diffractometer with Cu K$\alpha$ source and Ge monochromator.

## 3.2 Synthesis of d$_3$-MAI
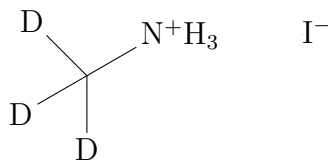


Under an inert atmosphere, d$_3$-methylamine (99 %, Sigma) (10 g) was slowly bubbled into ethanol (99.9 %(200 mL) at $-94\,°$C. To this solution was added 58 wt% hydroiodic acid in water (Sigma) (1 eq) and the reaction was allowed to heat to room temperature then left to stir for 16 hours. The ethanol was removed *in vacuo* and the resulting brown solid was washed with diethyl ether three times leading to the formation of a white powder.

Yield = 40.95 g (86 %)

$^1$H NMR, 500 MHz, $(CD_3)_2SO$, δ 7.40 (s)

$^{13}$C-{$^1$H} NMR, 500 MHz, $(CD_3)_2SO$, δ 23.4 (sept, $J = 43.3$ Hz)

$^2$H NMR, 500 MHz, $(CD_3)_2SO$, δ 2.18 (s)

## 3.3   Synthesis of $d_6$-MAI
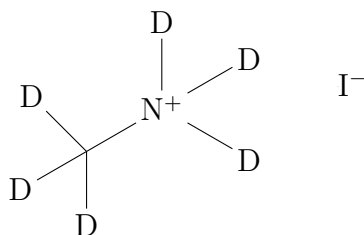


$d_3$-methylammonium iodide (20 g) was dissolved in $D_2O$ (99 %, Sigma) (25 eq, 55 mL) and stirred at room temperature for 16 hours. $D_2O$ was removed *in vacuo* and the procedure repeated twice to maximise proton exchange. The level of deuteration in the powder was confirmed to be 99 % using $^2$H NMR.

$^{13}$C-{$^1$H} NMR, 500 MHz, $(CD_3)_2SO$, δ 23.4 (sept, $J = 43.3$ Hz)

$^2$H NMR, 500 MHz, $(CH_3)_2SO$, δ 7.20 (s, 3H), 2.18 (s, 3H)

## 3.4   Synthesis of Other Organic Cations

Throughout this thesis a few different organic cations were used. Methylammonium iodide (purity unspecified by manufacturer, GreatCell), formamidinium iodide (purity unspecified by manufacturer, GreatCell) and caesium iodide (99.9 %, Alfa) were purchased and used as received. The following amines Phenyethylamine (99 %, Sigma), Propylamine (98 %, Sigma), 2,2,3,3,3-Pentafluoropropylamine (97 %, Fluorochem), Aniline (99 %, Sigma) and 4-Fluoroaniline (99 %, Fluorochem) were purchased and the iodide salts synthesised. The procedure used was the same for all the cations. A general synthesis is as follows, organic cation (1 eq) was diluted by half using EtOH and cooled down to 0 °C. Hydoriodic acid (1.5 eq) was added dropwise and the solution was left stirring for 2 hours. Depending on the organic cation, the solvent was removed *in vacuo* to produce the impure product or a solid precipitated out during reaction and the solution was filtered to give the

impure product. To purify, the solid was washed three times with ethyl acetate and then recrystallised with EtOH producing a white powder. NMR analysis was used to confirm the formation of the desired product. Finally, guanidinium iodide was synthesised by previous group member Adam Pockett using the same method as the other cations in this thesis.

## Phenylethylammonium Iodide
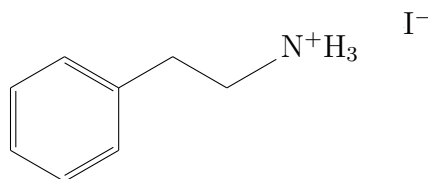


$^1$H NMR, 500 MHz, $(CD_3)_2SO$, δ 7.76 (s, 3H), 7.33 (t, 2H, $J = 7.34$ Hz), 7.25 (m, 3H), 3.05 (m, 2H), 2.86 (m, 2H)

$^{13}$C-{$^1$H} NMR, 500 MHz, $(CD_3)_2SO$, δ 137.14 (s), 125.5 (s), 131.8 (s), 126.71 (s), 36.23 (s), 30.73 (s)

## Propylammonium Iodide
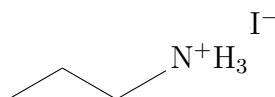


$^1$H NMR, 500 MHz, $(D_2O)$, δ 3.03 (t, 2H, $J = 7.5$ Hz), 2.74 (m, 2H, $J = 7.5$ Hz), 1.03 (t, 3H, $J = 7.5$ Hz)

$^{13}$C-{$^1$H} NMR, 500 MHz, $(CD_3)_2SO$, δ 40.42 (s), 20.34 (s), 10.81 (s)

## 2,2,3,3,3-Pentafluoropropylamonium Iodide
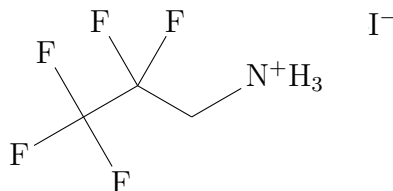


$^1$H NMR, 500 MHz, $(CD_3)_2SO$, δ 7.6 (s, 3H), 3.98 (t, 2H, $J = 17.3$ Hz)

$^{13}$C-{$^1$H} NMR, 500 MHz, $(CD_3)_2SO$, δ 118 (tq, $J = 32$ Hz and $J = 287$ Hz) 112.8 (qt, $J = 38$ Hz and $J = 260$ Hz), 37.8 (t, $J = 27$ Hz)

$^{19}$F NMR, 500 MHz, $(CD_3)_2SO$, δ -83.89 (s), -119.77 (t, $J = 17.3$ Hz)

**Anilinium Iodide**
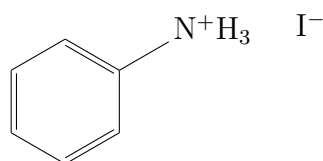


$^1$H NMR, 500 MHz, $(CD_3)_2$SO, δ 9.73 (broad s, 3H), 7.50 (tt, 2H, $J = 7.80$ Hz, 1.90 Hz, 7.40 (tt, 1H, $J = 7.40$ Hz, 1.1 Hz 7.50 (m, 2H)

$^{13}$C-$\{^1$H$\}$ NMR, 500 MHz, $(CD_3)_2$SO, δ 131.95 (s), 129.74 (s), 127.79 (s), 122.75 (s)

**4-Fluoroanilinium Iodide**
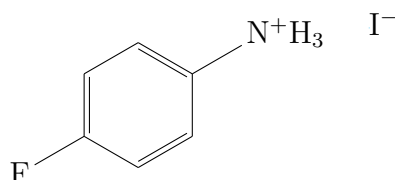


In an attempt to assign the aromatic peaks more easily, fluorine decoupled NMR was performed instead of a standard proton NMR. As well as this, hydrogen decoupled fluorine NMR was performed.

$^1$H NMR, 500 MHz, $(CD_3)_2$SO, δ 9.67 (broad s, 3H), 7.36 (m, 4H)

$^{13}$C-$\{^1$H$\}$ NMR, 500 MHz, $(CD_3)_2$SO, δ 161 (d, $J = 244$ Hz), 128 (s), 125 (d, $J = 8.8$ Hz), 117 (d, $J = 17.3$ Hz)

$^{19}$F-$\{^{19}$F$\}$ NMR, 500 MHz, $(CD_3)_2$SO, δ -114.2 (s)

## 3.5   Hotcasting Perovskite Powders

Unless otherwise stated, all perovskite powders were made by hotcasting. An example procedure for the synthesis of the MAPI powder is shown here. A $1.9\,\mathrm{mol\,dm^{-3}}$ $PbI_2$ (99.9 %, Sigma), $CH_3NH_3I$ and DMF (99.9 %, Anhydrous, Sigma) solution was prepared and stirred at 60 °C for an hour. The solution was cast onto a clean glass petri dish held at 110 °C and left for an hour to form a black film. The film was scratched from the petri dish to produce MAPI powder as confirmed by pXRD. When the deuterated analogue of MAPI ($d_6$-MAPI) was

synthesised the organic cation dissolved into the precursor solution was changed to $CD_3ND_3I$. The deuterium content of the $d_6$-MAPI powder was confirmed to be 83% by integrating the peaks in $^2$H NMR.

For the substituted perovskites, $5\,mol\%$ of the MA was replaced with the appropriate cation and the same synthesis procedure was followed. The stoichiometry of the final materials was determined using $^1$H NMR.

## 3.6 Cell Fabrication

Device fabrication was made up of six steps. The Figure 3-1 shows the appearance of the device after each step. The procedures involved in each step differ depending on the type of device (planar, inverted or mesoporous) being fabricated. In this thesis the devices used were all inverted devices containing the following order of layers: FTO/NiOx/Perovskite/PCBM/BCP/Ag. The individual deposition steps for these layers are outlined below.
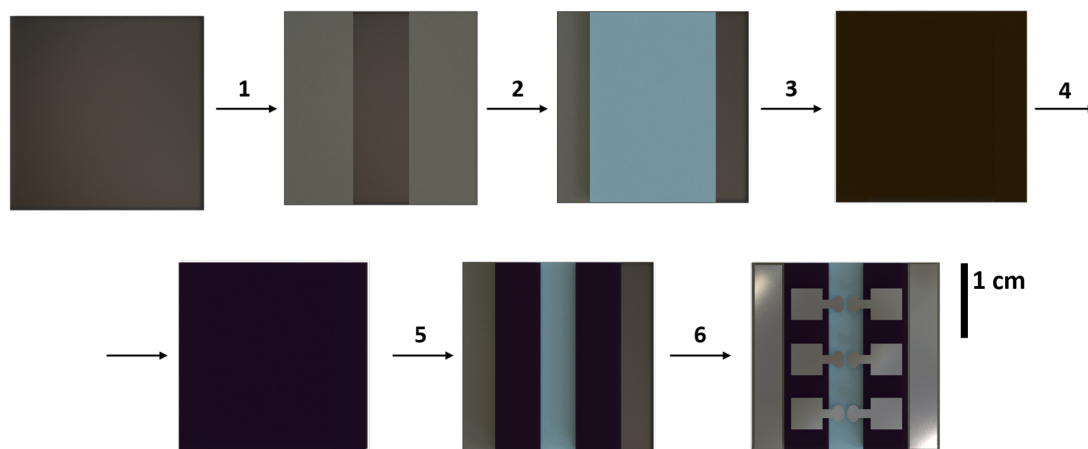


Figure 3-1: A diagram showing the individual steps in the device fabrication process. Steps 1-6 are outlined in the following sub sections.

### 3.6.1 Substrate Etching and Cleaning

First, the centre part of the Fluroine doped tin oxide (FTO) ($15\,\Omega$/sq, Solaronix or Sigma) substrates was etched away so as to remove the risk of short circuiting the device (Step **1** Figure 3-1). The etching was performed using $2\,mol\,dm^{-3}$ HCl and zinc powder. Subsequently, substrates were cleaned by five steps of sonicating

at 80 °C for 15 minutes in 2 % Helmanex detergent, water, acetone, propan-2-ol and ethanol, before finally being treated with UV/Ozone for 20 minutes. This procedure, apart from the etching step, is used for cleaning microscope slides which were used for UV/Vis analysis.

### 3.6.2 Nickel Oxide Hole Transport Layer

The first layer deposited on the etched FTO substrate can be either an electron transport layer, for planar cells, or a hole transport layer, for inverted cells (Figure 3-1 step **2**). For the inverted devices in this thesis the first layer was nickel oxide and was deposited as follows. A $0.2\,mol\,dm^{-3}$ solution of nickel acetate tetrahydrate (99.998 %, Sigma) in 2-methoxyethanol (99.8 %, Sigma, anhydrous) was prepared and once the solid was fully dissolved, $12\,\mu l\,ml^{-1}$ of ethanolamine (98 %, Sigma) was added to the solution. The solution was filtered through a (0.45 μm) PTFE syringe and 100 μl was spin coated onto the clean substrate at 3000 rpm for 30 seconds. The $NiO_2$ was cleaned from the edge of the substrate using a swab dipped in 2-methoxyethanol. The substrates were then annealed at 500 °C for 30 minutes. The FTO on the edge of the substrate was left exposed for the metal contact that is deposited in the last step.

### 3.6.3 Perovskite Layer

Perovskite layer deposition was achieved by spin coating 100 μl of precursor solution composed of 1.25 M $PbI_2$ and 1.25 M of cation dissolved in a 4:1 mix of DMF:DMSO (anhydrous). The precursor solution was manually spread over the substrate area then spin coated at 4000 rpm for 30 seconds. After 6 seconds 200 μl of ethyl acetate (99.8 %, Sigma, anhydrous) anti-solvent was dropped onto the substrate. After spin coating the device was annealed at 100 °C for 30 minutes.

### 3.6.4 PC$_{60}$BM and BCP Electron Transport Layer

The, electron transport layer deposited on top of the perovskite layer to make the inverted cells used in this thesis was actually two separate thin films of PC$_{60}$BM (95/5 %, Ossila) and BCP (96 %, Sigma). First the PC$_{60}$BM layer was made by

spin coating 100 µl of a 20 mg ml$^{-1}$ solution of PCBM in chlorobenzene (99.0 %, Sigma, anhydrous) at 3000 rpm for 30 seconds and then left to dry at room temperature. The BCP layer was subsequently deposited by spin coating 100 µl of a 0.5 mg ml$^{-1}$ solution of BCP in ethanol at 6000 rpm for 30 seconds and again left to dry at room temperature.

### 3.6.5  Finishing the Device

To finish the device (Figure 3-1 steps **5** and **6**) the perovskite and top contact layer are scratched away from the edge and centre to expose the FTO. This allows the metal to be deposited onto the substrate to avoid direct contact between the external circuit used during device testing and the perovskite layer. Finally, silver contacts were deposited by thermal evaporation of silver wire (99.9 % Alfa) under a vacuum of approximately $10^{-6}$ mbar.

## 3.7  PV Analysis

Current density-voltage curves were measured using a 2400 series Sourcemeter (Keithley Instruments), under simulated AM1.5 sunlight at 100 mW cm$^{-2}$ irradiance generated using a class AAA solar simulator (TS-Space Systems). The intensity was calibrated using a silicon reference cell (Fraunhofer). The active area of the pixels was 0.0625 cm$^2$.

## 3.8  µSR Experiments

### 3.8.1  MAPI, d$_6$-MAPI and Mixed Cations

The MAPI, d$_6$-MAPI and mixed cation studies were performed at the ISIS pulsed muon facility using the EMU instrument. Approximately 1 g of sample was packed into a 4 cm$^2$ packet made from silver foil which was subsequently attached to the sample stage. The temperature was controlled between 40 K and 410 K using a closed cycle refrigerator and a hot stage. Measurements at four different longitudinal fields (0, 5, 10 and 20 G) were taken for each temperature. To initially calibrate the instrument a transverse field of 100 G was applied.

### 3.8.2  Mixed Anion Study

The mixed anion perovskite study was performed at the ISIS pulsed muon facility using the HIFI instrument. The $MAPbBr_3$ experiment was done using the exact same procedure as the mixed cation and MAPI experiments. The $MAPb(I_{0.5}Br_{0.5})_3$ and $MAPb(I_{0.83}Br_{0.17})_3$ experiment used the same magnetic fields but the temperature range was only between $300\,K$ and $400\,K$.

# Chapter 4

# Investigation of Methyl Ammonium Lead Iodide Using Muon Spin Relaxation

## 4.1 Introduction

Methylammonium lead iodide (MAPI) was the first perovskite to be widely investigated for solar cells and it is still used as a component of the most efficient perovskite solar cells (PSC) (e.g. $Cs_x(MA_{0.17}FA_{0.83})_{100-x}Pb(I_{0.83}Br_{0.17})_3$).[1–5] While the improvement in efficiency of PSC has been rapid, the underlying physical properties of perovskite materials, such as molecular motion and ionic diffusion inside the material, are still not fully understood. The consensus is that both electronic and ionic motion occur within perovskite materials.[6,7] Ion movement has been proposed as a cause of JV curve hysteresis in perovskite devices.[8–10] This finding is sometimes disputed as changes in solar cell contacts can reduce hysteresis in PSC; however, some careful experimental studies have demonstrated that JV curve hysteresis is linked to both ion movement and interfacial recombination.[11,12]

There have been several computational and experimental studies on the movement of methyl ammonium ($[MA]^+$) and iodide ions in methyl ammonium lead iodide, producing a range of activation energies of 0.36 to 0.84 eV for $[MA]^+$ and 0.08 eV to 0.6 eV for iodide.[9,13–20] A summary of some iodide migration activation
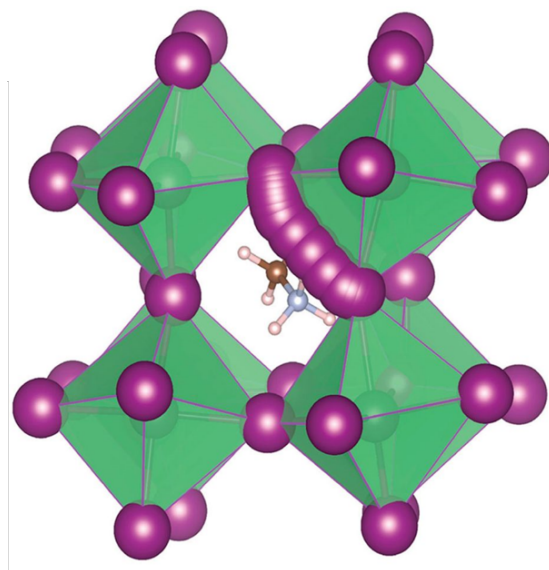
Figure 4-1: The predicted migration pathway for iodide diffusion in MAPI calculated by Eames *et al.*[13]

energies is shown in Table 4.1. Theoretical first principles calculations performed by Eames *et al.* derived activation energies ($E_a$)of $0.58\,\text{eV}$ and $0.84\,\text{eV}$ for iodide and $[\text{MA}]^+$ diffusion respectively.[13] In their work, they also performed current-voltage response analysis which produced similar activation energies. They suggested that the diffusion path for iodide diffusion is slightly bowed around the edge of the lead iodide octahedra which is important for correctly calculating diffusion coefficients (Figure 4-1). Other calculations using different computational methodologies and predicted diffusion paths have found activation energies for iodide diffusion as far apart as $0.08\,\text{eV}$[14] and $0.44\,\text{eV}$.[19]

Experimental measurements of iodide motion have also been carried out and activation energies ranging from $0.17\,\text{eV}$ measured by NMR[18] to $0.6\,\text{eV}$ measured by chronoamperometry have been reported.[13] A range of other techniques have been used; an activation energy of $0.45\,\text{eV}$ was found using capacitance measurements, $0.31\,\text{eV}$ from temperature dependant current analysis, $0.5\,\text{eV}$ from thermally stimulated current measurement and $0.55\,\text{eV}$ and $0.43\,\text{eV}$ using impedance spectroscopy.[9,15–18,21]

All of the previous experimental methods, except for the NMR study, involve applying a voltage to and/or drawing a current from a complete PSC. When a voltage is applied to a complete device, there is evidence that iodide (and

Table 4.1: Activation energy values taken from literature compared with this work.

| Method | $E_a$ eV | |
| --- | --- | --- |
| | Computational | Experimental |
| *Ab initio*/DFT& Chronoamperometry[13] | 0.58 | 0.6 |
| Intensity Modulated Voltage Spectroscopy[9] | - | 0.55 |
| Thermally Stimulated Current Measurement[21] | - | 0.5 |
| Capacitance[16] | - | 0.45 |
| *Ab initio*/DFT[19] | 0.44 | - |
| Impedance[17] | - | 0.43 |
| Temperature Dependant JV Curves[22] | - | 0.33 |
| Temperature Dependant Current[15] | - | 0.31 |
| NMR[18] | - | 0.17 |
| *Ab initio*/DFT[14] | 0.08 | - |
| **This work** | - | **0.174** |

possibly also methylammonium) ions migrate to create ionic double layers at the interfaces. However, it can be difficult to tell the difference between changes due to ionic movement, changes due to degradation of the perovskite and changes in the contacts as a current is drawn. Some measurements have focused on studying ion migration by applying a large voltage across a thin section of a perovskite film, however at these high voltages degradation could also occur quite rapidly.[23] It is clear from the literature that there is still disagreement on the activation energy of iodide diffusion in MAPI.

In this chapter, muon spin relaxation was used to directly probe ion movement in MAPI crystallites. The materials were measured in the dark and no current was drawn, the measurements allowed us to extract both an activation energy and a diffusion coefficient for the intrinsic movement of iodide inside the material.

### 4.1.1   Muon Spin Relaxation for Ion Diffusion

The positive muons used in this experiment are unstable subatomic particles with similar properties to a positron, except their mass is 207 times larger and their lifetime is 2.197 µs. Muons have been used to study many different properties such as magnetism and superconductivity in a range of different materials.[24] Muon spin relaxation (µSR) has, more recently, been used to investigate the diffusion of $Li^+$ and $Na^+$ in modern battery materials.[25–29] Muons are implanted into the sample and decay into a positron which is most likely to be emitted in the muon spin direction at the instant of decay.

The effect of local fields on the muon spins is detected by the change in the asymmetry of the positron counts in detectors around the sample. Using this technique activation energies and diffusion coefficients of ions with nuclear magnetic moments can be measured. Previous µSR studies have focused on diffusion of lithium and sodium ions but the similarity between the nuclear magnetic dipole moment of iodide ions ($2.81\,\mu_N$) and lithium ions ($3.26\,\mu_N$ where $\mu_N$ is the nuclear magneton) led us to the idea to investigate whether it would be possible to study iodide motion in MAPI using the same techniques that are applied to battery materials.[30] Iodide diffusion has not been widely studied by µSR previously. The ability of muons to act as discrete, non-destructive probes makes them ideal for studying the easily degraded perovskite material.

## 4.2   Synthesis & Characterisation of d$_6$-MAPI

To help to differentiate the impact of cations and anions on the µSR results, a deuterated analogue of MAPI was synthesised. Firstly, d$_3$-MAI was synthesised by bubbling d$_3$-methylamine gas into ethanol mixed with 1 equivalent of hydroiodic acid at $-94\,°C$. The low temperature synthesis was chosen to try to maximise yield by minimising loss of d$_3$-methylamine gas which is an expensive precursor. Once the product had been purified a combination of $^1H$, $^2H$ and $^{13}C$ NMR were used to confirm the correct product had been synthesised (Appendix Figures A-1 and A-2). As the sample used to acquire the $^{13}C$ NMR was the same as for the deuterated NMR, the solvent was non-deuterated giving rise to the

large peak at 40.5 ppm. The actual solvent peak was present at 30.5 ppm with the methyl carbon septet appearing at 23 ppm.
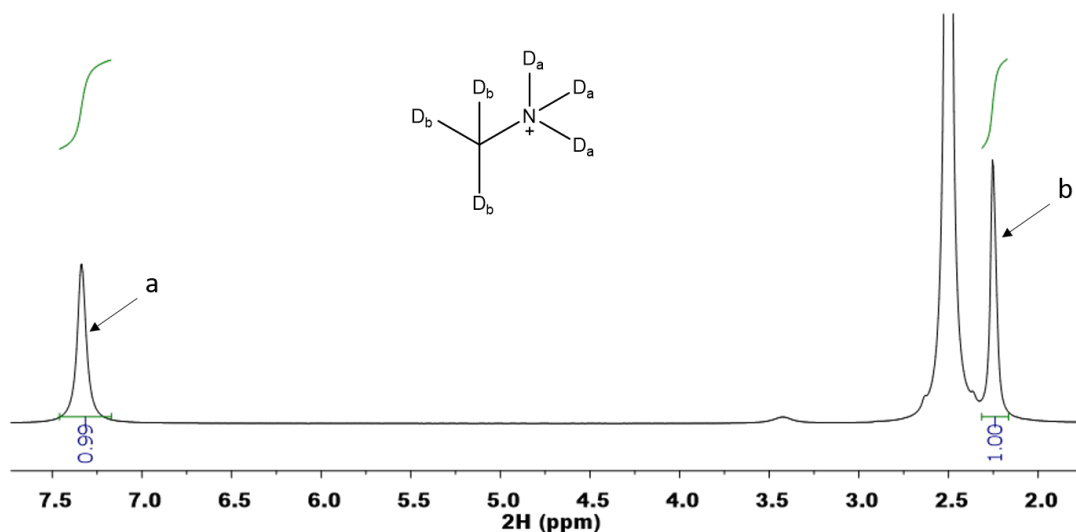


(a)
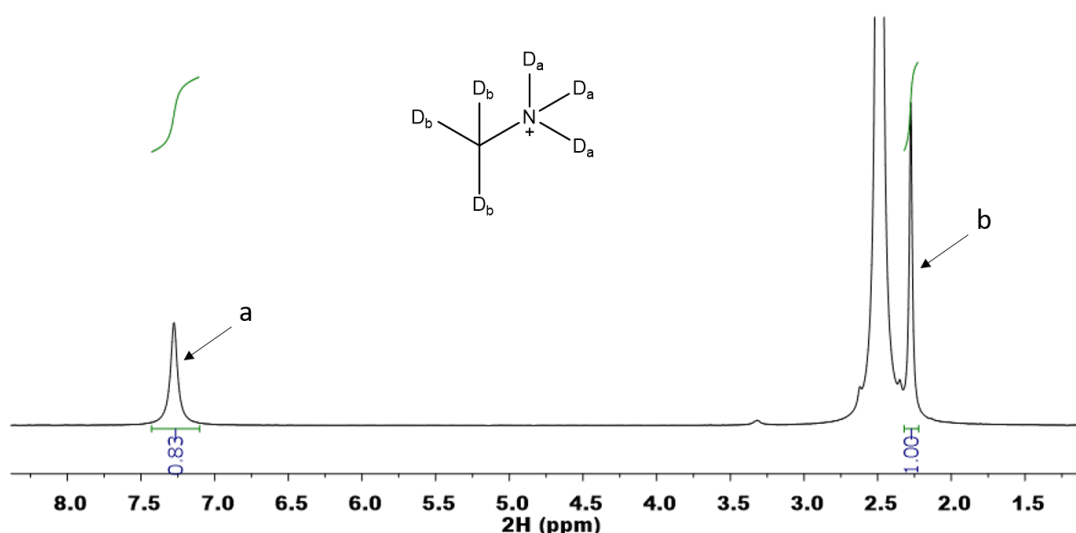


(b)

Figure 4-2: a) $^2$H NMR of $d_6$-MAI in DMSO. b) $^2$H NMR of $d_6$-MAPI in DMSO.

A proton exchange reaction was used to convert $d_3$-MAI to $d_6$-MAI. Amine protons are quite labile in solution so dissolving $d_3$-MAI in $D_2O$ led to the easy formation of $d_6$-MAI. The number of hydrogens that had been replaced by deuterium was measured by comparing the integrals of the 7.25 and 2.20 ppm peaks in the $^2$H NMR spectra (Figure 4-2a). The results of this integral comparison showed that 99 % of the hydrogens had been replaced with deuterium.

As proton exchange between the deuterated cation can occur with any labile

protons it comes into contact with, the number of methods that could be used to make $d_6$-MAPI powders was limited. The most common method used to form MAPI powders is an aqueous synthesis which would lead to hydrogenation of the cation and not work.[31] With the requirements of having no aqueous solvents, a hot casting method was used to fabricate the MAPI and deuterated MAPI. This process involved dissolving the precursors in anhydrous DMF and then spreading the solution over a hot glass petri dish forming black powders (Figure 4-3a).

The two black powders, $d_6$-MAPI and MAPI, were characterised using pXRD (Figure 4-3b). The peaks matched with pXRD patterns of MAPI in the literature.[32] The most important thing to note from the pXRD is the lack of $PbI_2$ peak at 12° indicating full conversion of the $PbI_2$ precursor to MAPI. The level of deuteration in the $d_6$-MAPI was measured using the same method as for the $d_3$-MAI precursor (Figure 4-2b) and was found to be 83%. The loss of deuteration was likely caused by the humidity of the processing environment; however, 83% deuteration should be sufficient to strongly affect the interaction of muons with the $d_6$-MAPI sample.



(a)  (b)
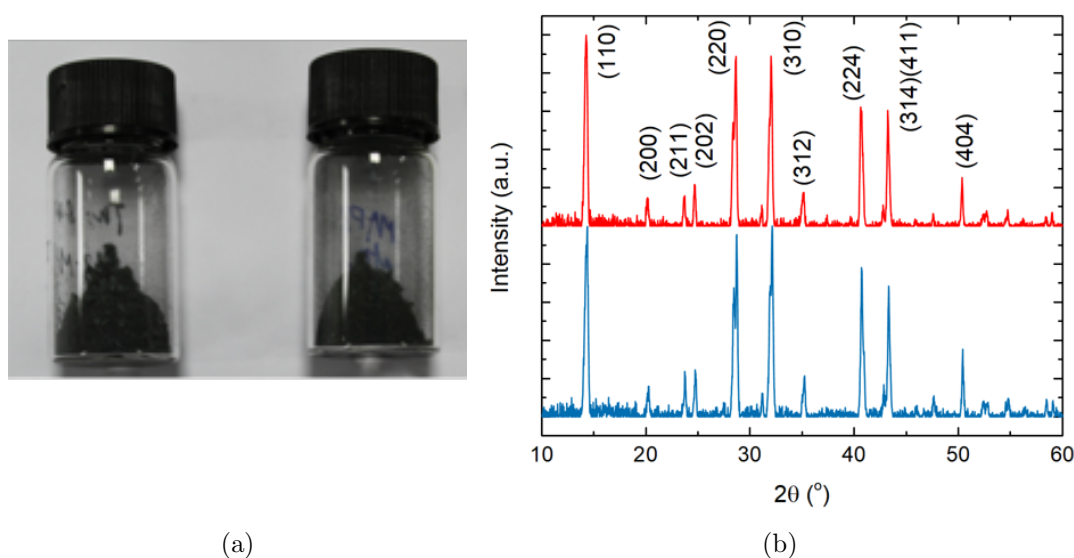
Figure 4-3: a) A picture of the two black perovskite powders made by hot casting. b) pXRD spectra of MAPI (blue) and $d_6$-MAPI (red) powders with the y-axis offset for clarity. The indices were taken from literature.[32]

## 4.3 Muon Spin Relaxation of MAPI

In this study μSR was carried out on powdered MAPI and $d_6$-MAPI. The two different cations were used so that it would be possible to observe if the cation had any effect on the muon spin relaxation data. Deuterating the MA has minimal effect on the crystal structure, as observed by Whitfield et al.[33] The minimal difference between deuterated and non-deuterated made this the best choice as it would have the least impact on the material properties. By comparing spectra taken with and without a $[d_6\text{-MA}]^+$ cation it was hoped that any features caused by cation motion would change and those caused by anion motion would not.
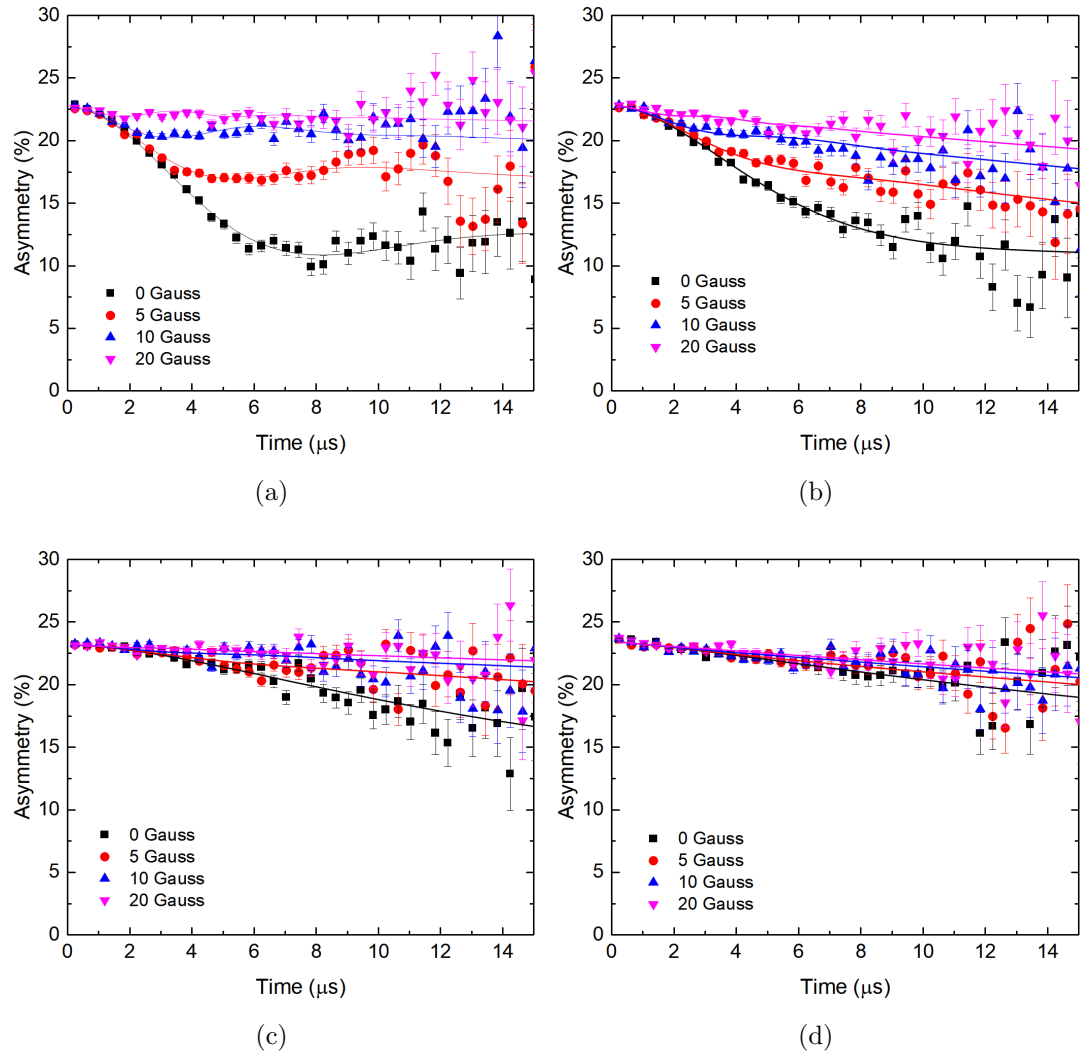


Figure 4-4: Raw muon data for MAPI at a) 50 K, b) 110 K, c) 350 K and d) 400 K. Also shown are the results of fitting the data to a dynamic Kubo-Toyabe function.
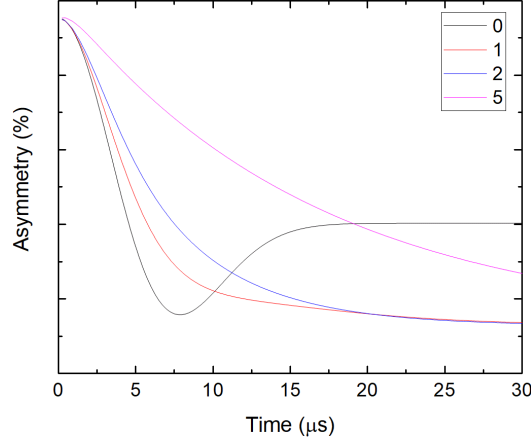
Figure 4-5: The change in μSR asymmetry response with different values of $\nu/\Delta$. The $\Delta$ for this example data was set at $0.22\,\text{MHz}$

μSR measurements were taken using a longitudinal field (LF) of 0, 5, 10 and 20 G between 50 and 410 K with fitted data at 50, 110, 350 and 400 K shown in Figure 4-4. Four different LFs were used to decouple the muon spin relaxation from the local magnetic fields to different extents, allowing for more reliable fits to the data at each temperature. The fluctuation rate ($\nu$) and the static width of the disordered local field distribution (coming from nuclear magnetic moments) at muon implantation sites ($\Delta$) were subsequently calculated by fitting the muon asymmetry data at each temperature to a dynamic Gaussian Kubo-Toyabe function multiplied by an exponential relaxation rate $exp(\lambda t)$ (Equation 4.1) using ISIS's bespoke muon fitting software, WIMDA.[34,35]

$$A_0 P_{LF}(t) = A_{KT} exp(-\lambda t) G^{DGKT}(\Delta, \nu, t, H_{HF}) + A_{BG} \qquad (4.1)$$

$A_0$ is the initial asymmetry, $A_{BG}$ and $A_{KT}$ are the asymmetries of the background and the sample, $\Delta$ and $\nu$ are the previously mentioned local field distribution and the fluctuation rate, respectively. The exponential function containing $\lambda$, where $\lambda$ is the relaxation rate, is used to account for the depolarization of muons by internal electronic fields caused by outer shell electrons on the metal and iodide ions. The electronic moments fluctuate rapidly and can therefore by modelled by a simple exponential. Finally, $t$ is time and $H_{LF}$ the applied longitudinal magnetic field.

The μSR response of a paramagnetic material with no dynamic fluctuations in the local field is modelled by the static Gaussian Kubo-Toyabe function (Figure

4-5). The origin of the specific features of the static Gaussian Kubo-Toyabe are discussed in more detail in Section 2.7. Briefly, the asymmetry initially decreases down to a minimum value and then the asymmetry returns to 1/3 of the initial asymmetry value. When there are fluctuations in the local field then the response is modelled by a dynamic Gaussian Kubo-Toyabe function. The μSR response then varies based on $\nu/\Delta$. Figure 4-5 shows how the asymmetry data would be changed with different values for $\nu/\Delta$. As the value of $\nu/\Delta$ increases then the response begins to take on the appearance of an exponential decay.

At 50 K (Figure 4-4a) the environment was mostly static with the asymmetry looking very similar to the static Gaussian Kubo-Toyabe function where it descends to a minimum before regaining a tail at 1/3 the maximum asymmetry. It is clear that the environment was still slightly dynamic as the tail does not fully return to 1/3. At 110 K (Figure 4-4b) the muon enviornment was more dynamic causing the relaxation to no longer decrease to a minimum or properly regain the 1/3 tail. At 350 K and above, an increase in the ratio of $\nu$ and $\Delta$ causes the μSR response to appear exponential (Figure 4-4c and d).
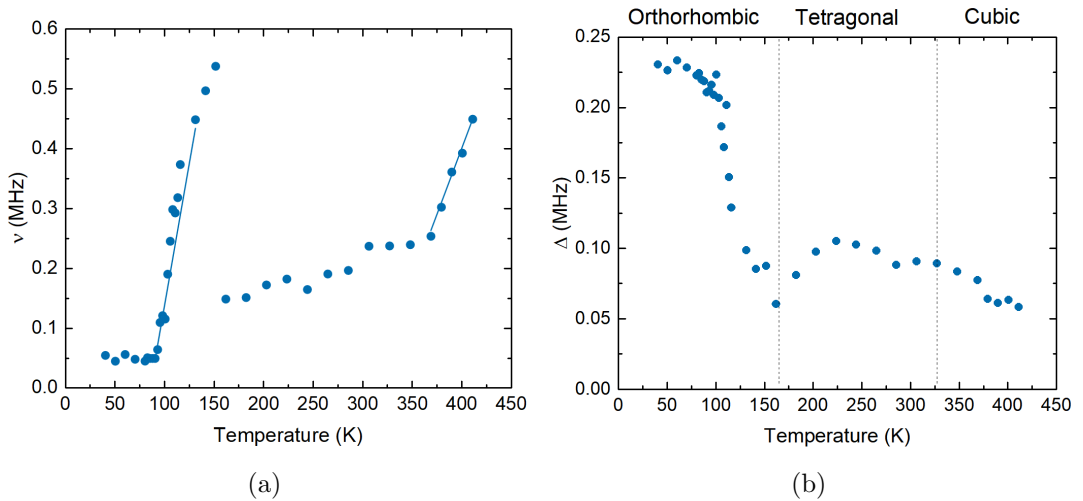


Figure 4-6: Temperature dependence of (a) $\nu$ with fit lines showing where the Arrhenius data was taken from and (b) $\Delta$ values for MAPI derived from fitting raw μSR data to a dynamic Gaussian Kubo-Toyabe function for measurements between 40 K and 410 K. The dashed lines in (b) indicate the phase transitions from orthorhombic to tetragonal and to cubic.

Once all of the different temperatures had been fitted to the same relaxation

function, the resulting $\nu$ and $\Delta$ data were plotted against temperature (Figure 4-6a,b). The value of $\Delta$ has the units of MHz as it represents the magnetic field width (in Tesla) divided by the constant gyromagnetic ratio of the muon (in MHz per Tesla) leaving a frequency. The $\nu$ initially plateaued between 50 K and 100 K as the muon experienced a static environment. At 100 K the fluctuation rate increased from 0.05 to 0.55 MHz at 150 K due to the muon environment becoming more dynamic. The fluctuation rate then abruptly dropped back down to a new minima that was slightly higher than the completely static system at 40 K. This abrupt drop aligns well with the phase transition (Figure 4-6b) of MAPI indicating that whatever process is occurring becomes far less pronounced or much faster and no longer seen on the µSR timescale in the tetragonal phase. The fluctuation rate then steadily increased until 350 K where there was a final steeper increase in $\nu$. There is a small increase of the fluctuation rate between 150 and 350 K. This process when fitted had an $E_a$ of 0.013 eV the origin of this process was not further explored as it didn't match with any currently known processes occurring in MAPI. Subsequent µSR data included in future chapters did not show any dramatic changes to this middle temperature process.

The dynamics of the methylammonium cation are strongly dependent on the perovskite phase. There are two types of cation dynamics that occur in perovskites, a wobbling along the C-N axis and a full rotation of the cation. In the orthorhombic phase the more energy intensive full rotation is restricted due to the lattice disorder.[36] Therefore, the only dynamic motion occurring in the orthorhombic is cation wobbling. When the perovskite transitions to a tetragonal phase the amount of full rotation increases. In the µSR results the fluctuation rate changes drops dramatically at the phase transition indicating that whatever process is occurring is strongly influenced by the phase similar to cation dynamics. Substituting the MA cation with a per deuterated analogue would make it possible to see if the low temperature process was related to cation dynamics.

The $\Delta$ data (Figure 4-6b) was initially flat at 0.22 MHz between 40 and 80 K and then the local field gradually decreased down to 0.05 MHz at 160 K. This decrease is caused by a phenomenon known as motional narrowing which is a common phenomena seen in both µSR and NMR.[37] As discussed in Section 2.7

the internal field in a sample is assumed to have a Gaussian distribution with a certain width equal to $\Delta/\gamma_\mu$ where $\Delta$ is the local field and $\gamma_\mu$ is the gyromagnetic ratio of a muon. As motion around the muon increases it begins to be influenced by a more average field which causes the Gaussian distribution to narrow. This narrowing caused by the increased motion is what is responsible for the decrease in local field observed in these experiments. The local field after 150 K increased slightly up to 0.1 MHz at 220 K before gradually decreasing down to 0.05 MHz.
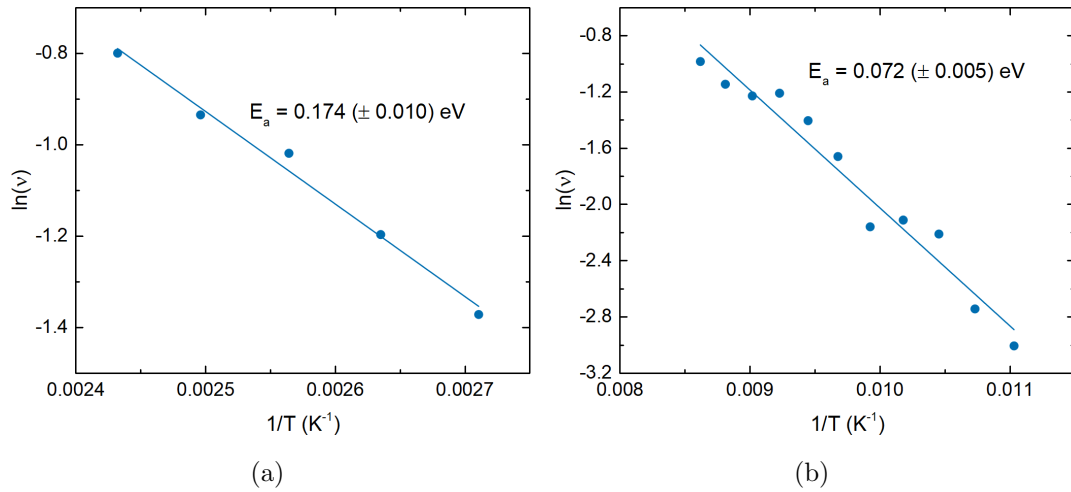


Figure 4-7: a) The Arrhenius plot for the high temperature region and b) the Arrhenius plot for the low temperature region of the fitted $\nu$ data.

The activation energies ($E_a$) of the high temperature and low temperature processes were calculated by plotting an Arrhenius fit of the linear regions (Figure 4-7a and b). The $E_a$ of the high temperature process was 0.174 eV and for the low temperature it was 0.072 eV. The high temperature $E_a$ and literature values for iodide transport are shown in Table 4.1. The technique most analogous to μSR is NMR spectroscopy as they both measure changes to local fields in the bulk material. It is promising that the $E_a$ from both techniques is almost identical. While the $E_a$ measured here is lower than several literature values, it has been shown that the processing method used to prepare the perovskite influences the activation energy for ion movement.[15] It is likely that small differences in activation energy between studies are due to changes in crystallinity and defect density resulting from the wide range of methods used to prepare perovskite thin films and powders.[38]

The low temperature $E_a$ is close to that observed for MA cation rotation (0.099 eV) by quasi elastic neutron scattering.[39] Despite the activation energies matching well with literature it was not possible to say exactly what was causing each process from just this data alone. With this in mind the μSR response of the per-deuterated analogue was also investigated.

## 4.4 Comparison with per-deuterated MAPI analogue

To see whether it was $[MA]^+$ or $I^-$ ions causing the fluctuation rate to change, μSR was also run on per-deuterated $d_6$-MAPI. The data was fitted to the same dynamic Gaussian Kubo-Toyabe function with an exponential relaxation as the MAPI data. Figure 4-8a-d shows raw muon data with fits at several different temperatures. As with MAPI the 50 K data showed the muon in an environment with a small amount of dynamics but it is mostly static. At 110 K, once again, the environment was more dynamic. At 350 K the raw data was similar to MAPI at the same temperature but with a much smaller difference between the different longitudinal fields indicating there was a difference in the ratio of fluctuation rate and local field for $d_6$-MAPI compared to MAPI. The muon environment at 400 K was similar to the same temperature data for MAPI.

Once all of the fits had been completed the $\nu$ and $\Delta$ were plotted. The overall trend of the change in fluctuation rate for $d_6$-MAPI (Figure 4-9a (red)) was similar to that for MAPI with both low and high temperature processes present. The $\Delta$ for $d_6$-MAPI (Figure 4-9c), while following a similar trend to MAPI, was approximately 0.04 MHz lower across the entire temperature range. The difference in the local field for the two perovskites will be addressed in section 4.4.1.

There are two main differences in the fluctuation rate data, at low temperature the increase in fluctuation is slightly steeper for $d_6$-MAPI than MAPI (Figure 4-9b). The second difference is at high temperature where initially the overall fluctuation rate of $d_6$-MAPI is lower than that of MAPI. The activation energies for the two processes occurring in $d_6$-MAPI were again calculated using Arrhenius
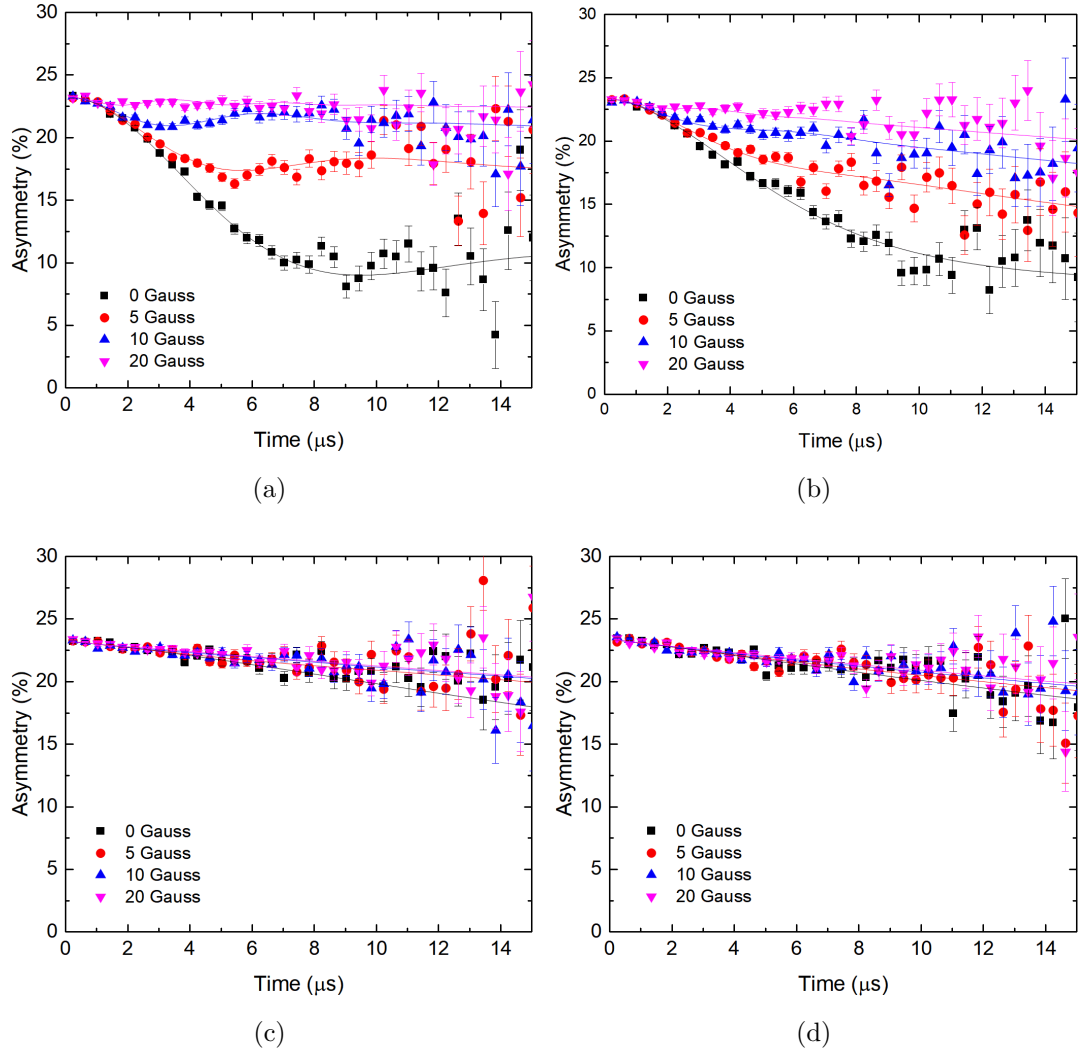
Figure 4-8: Raw muon data for $d_6$-MAPI at a) $50\,K$, b) $110\,K$, c) $350\,K$ and d) $400\,K$. Also shown are the results of fitting the data to a dynamic Kubo-Toyabe function.

plots (Figure 4-10a and b). This gave an $E_a$ of $0.082\,eV$ for the low temperature process and $0.174\,eV$ for the high temperature process.

A full comparison of the $E_a$ values is shown in Table 4.2. Deuteration slightly increased the low temperature activation energy compared to MAPI. For the high temperature process the $E_a$ was not affected by the lower initial fluctuation rate, while the two values of $E_a$ are different they remain within one standard deviation of each other.

The small increase in low temperature $E_a$ is caused by the added weight of the deuterium ions compared to protons. This increased mass would increase the
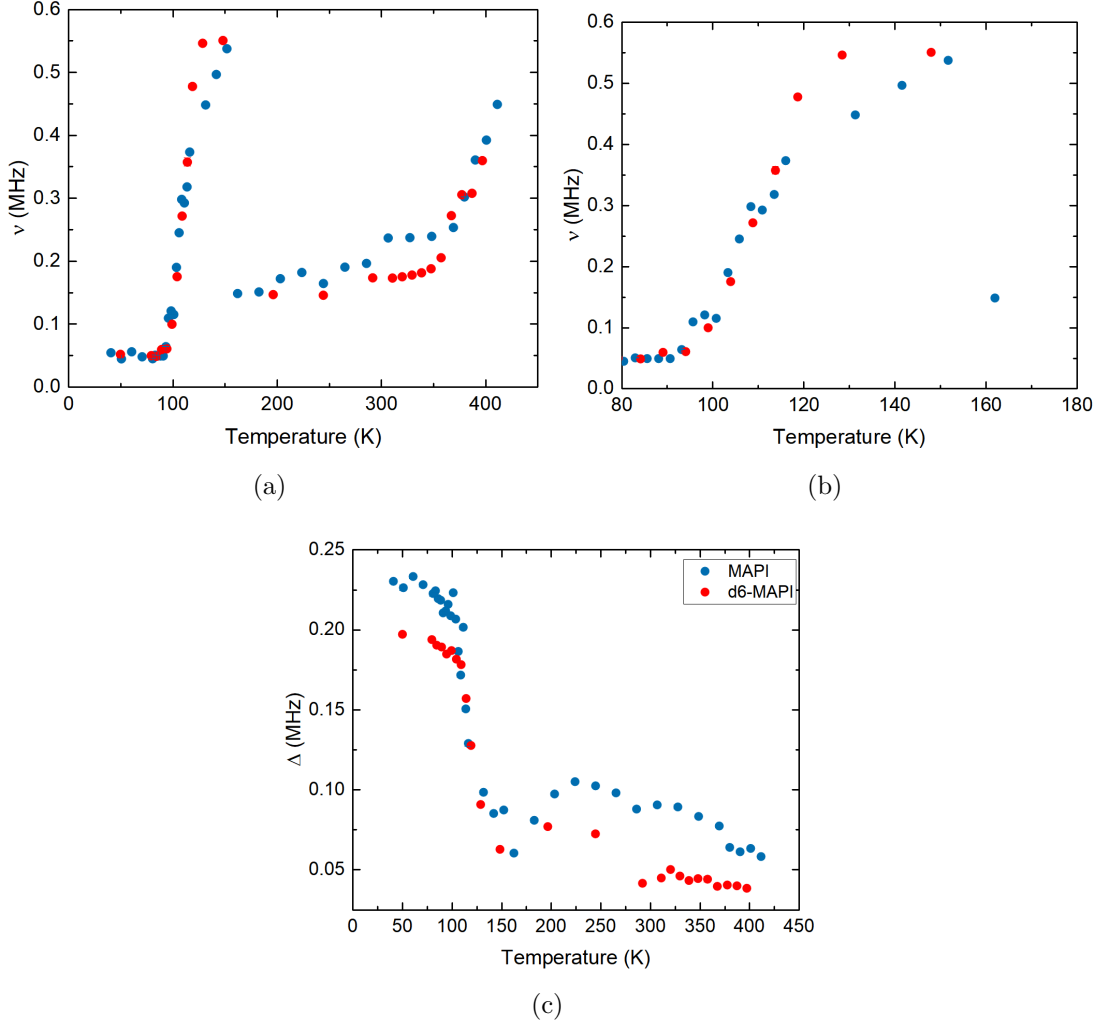
Figure 4-9: a) Comparison of the $\nu$ of $d_6$-MAPI (Red) and MAPI (Blue) between 40 K and 400 K. b) The same comparison with the temperature scale between 70 K and 180 K so as to more easily see the difference in the low temperature process. c)A plot showing the change in $\Delta$ with temperature for $d_6$-MAPI compared with MAPI.

Table 4.2: $E_a$ of mixed cation perovskites at high and low temperature as measured by muon spin relaxation.

| Perovskite | $E_a$ eV | |
| --- | --- | --- |
| | Low Temperature | High Temperature |
| $MAPbI_3$ | $0.072(\pm0.005)$ | $0.174(\pm0.010)$ |
| $d_6$-$MAPbI_3$ | $0.082(\pm0.003)$ | $0.158(\pm0.019)$ |
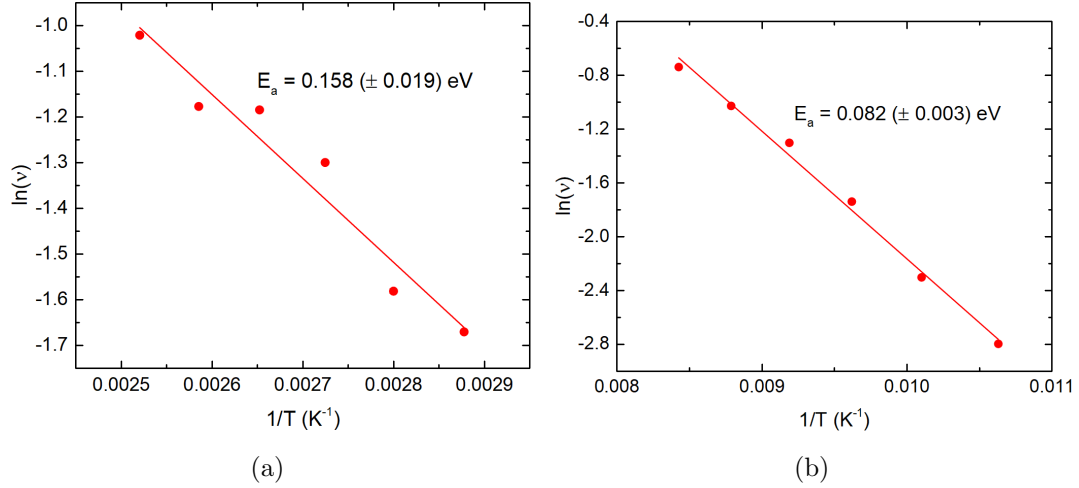
Figure 4-10: Arrhenius plots of the fluctuation rate for $d_6$-MAPI between (a) 340 K and 410 K (b) 100 K and 150 K

energy required for the amine group to rotate inside the lattice. The similarity in the values for activation of cation motion in lattice measured by Leguy *et al.* and the small difference in $E_a$ for the low temperature process following deuteration are both evidence for the low temperature process being related to cation dynamics.[39]

In contrast, the high temperature process has, within one standard deviation, the same $E_a$ for both deuterated and non-deuterated samples. This observation, along with the close agreement of the calculated activation with the NMR study for iodide diffusion (Table 4.1), makes it likely that the process being observed is that of iodide motion in the perovskite.

## 4.4.1 Muon Stopping Sites

An important part of μSR is where in the material the muon stops and whether it remains in that site until it decays. As discussed previously dynamics can be caused by mobile ions around a stationary muon or a mobile muon. To confirm that what is being studied here is movement of ions and not muons the stopping site and subsequent stability of the muon were investigated. A muon that is positively charged is most likely going to stop in the most electronegative location in the material due to the difference in charges. Computational modelling of the electrostatic potential map performed by Dibya Ghosh (Figure 4-11) gave an

indication of the most likely stopping sites in MAPI.
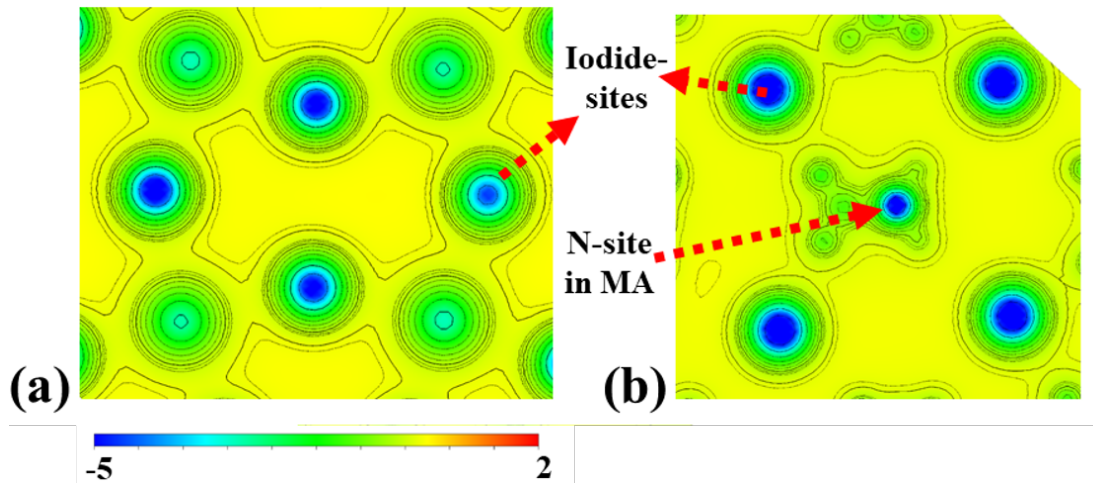


Figure 4-11: Two-dimensional electrostatic potential contour map for MAPI in the PbI$_2$ plane and the MAI plane. The colour scale is in eV

Unsurprisingly, the most electronegative areas of MAPI were the negatively charged iodides and the nitrogen on the MA cation. There is no literature precedence for muon stopping sites in materials with iodide. The most comparable situation are studies looking at muons implanted into fluoride materials as the fluoride muon interaction gives insight into fluoride bond lengths.[40,41] In these studies the muon interacts very strongly with the fluoride ion forming either an F$\mu$ or F-$\mu$-F bound state. It is possible to calculate an approximate value for $\Delta$ at different possible stopping sites using equation 4.2:[34]

$$\Delta^2 = \frac{2}{3}\mu_0^2\gamma_\mu^2\hbar^2 \sum_i \frac{I_i(I_i+1)\gamma_i^2}{r_i^6} \tag{4.2}$$

where $\gamma_{mu}$ is the gyromagnetic ratio of the muon, $I_i$ and $\gamma_i$ are the ratio of the $i$-th nucleus, and $r_i$ is the distance between the muon site and $i$-th nucleus. To get an accurate value, all the nuclei within a radius of ten-times the longest unit cell parameter were used in the calculations. Based on the electrostatic potential map the most likely location for the muons to stop is near the electronegative fluoride ions. The simplest possible situation in MAPI is the formation of a simple $\mu$-I bond. Calculating $\Delta$ in this scenario gives a value between 0.07 and 0.12 MHz. This value is similar to that observed in the tetragonal and cubic phase but not the orthorhombic phase. Another possible bonding mode would be a linear I-$\mu$-I site. $\Delta$ calculations using this site give values of 0.26 MHz,

0.11 MHz and 0.09 MHz for the orthorhombic, tetragonal and cubic state for MAPI. The same calculations for $d_6$-MAPI gave $\Delta$ values of 0.15 MHz, 0.07 MHz and 0.09 MHz for orthorhombic, tetragonal and cubic states. These values are in close agreement with the experimental data and even account for the difference between the deuterated and non-deuterated sample.

The strong correlation between the calculations of $\Delta$ and the experimental data indicate that the muon stopping site is a form of linear I-μ-I state analogous with those seen in previous fluoride studies.[41] It would be possible to get a more accurate stopping site using very complex and expensive computational analysis. Based on the electrostatic potential and the similarities between fluoride and iodide it is most likely that the muon is stopping near the iodide and the extra expense to find the exact stopping site is unnecessary.

## 4.5    Calculating the Iodide Diffusion Coefficient

With the fluctuation data and Equation 5.2 it is possible to calculate the diffusion coefficient of iodide ($D_I$). In Equation 5.2 $N_i$ is the number of accessible paths in the i-th path, $s_i$ the jump distance between iodide sites, $Z_{vi}$ is the vacancy fraction present and $\nu$ is the fluctuation rate taken from muon data.

$$D_I = \sum_{i=1}^{N} \frac{1}{N_i} Z_{vi} s_i^2 \nu \tag{4.3}$$

The diffusion coefficients (Figure 4-12) were calculated using the model for iodide diffusion presented by Eames $et\ al.$.[13] This assumes there is just one mechanism for diffusion but eight possible pathways. A jump distance of 4.49 Å, calculated from neutron diffraction data for the inter atomic distances was used.[42] A vacancy fraction of 0.4 %, as calculated by Walsh $et\ al.$ was used.[43] The calculated diffusion coefficient at 410 K was $2.5 \times 10^{-12}$ cm$^2$s$^{-1}$ and this decreased to $2.56 \times 10^{-13}$ cm$^2$s$^{-1}$ at 370 K.

Extrapolating Figure 4-12 to 300 K gave a diffusion coefficient of $7.38 \times 10^{-14}$ cm$^2$s$^{-1}$. Eames et al. predicted a diffusion coefficient of $10^{-12}$ cm$^2$s$^{-1}$ at 320 K which is approximately one order of magnitude greater than what was measured here at 320 K ($1.12 \times 10^{-13}$ cm$^2$s$^{-1}$).[13] At the time of writing there were
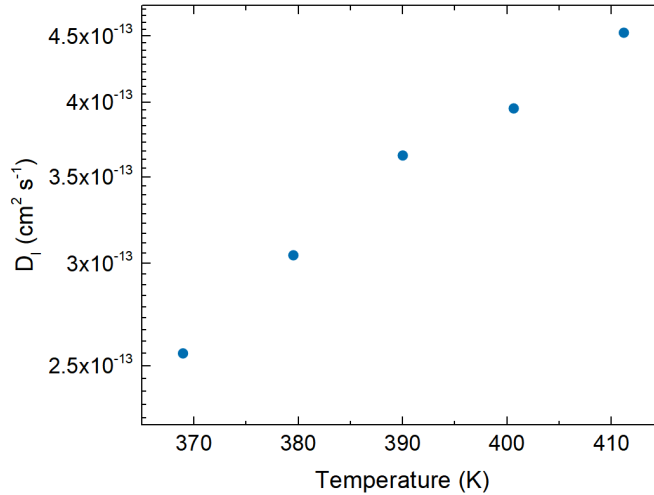
Figure 4-12: The change in $D_I$ between 370 and 400 K for MAPI with values calculated directly from the individually measured $\nu$ data

no other predictions or calculations of the diffusion coefficient for iodide motion to compare with. The value of the calculated diffusion coefficient is sensitive to the vacancy fraction used. Doubling the vacancy fraction from 0.4 % to 0.8 % gives a diffusion coefficient of $1.48 \times 10^{-13}\,\mathrm{cm^2 s^{-1}}$ at 300 K. In this experiment iodide transport is only observed above 360 K but that does not mean that it is not occurring at lower temperatures. The diffusion coefficients measured here are at the lower limit of what is observable using µSR. This means that, at lower temperatures, the iodide diffusion is likely still occurring but is unobservable because the movement of the ions is too slow to have an effect on the field that would impact the muon spin before decay.[44]

## 4.6 Material Stability

During the µSR measurements the temperature of both perovskite samples were raised to 410 K. Perovskites are known to degrade easily under a variety of conditions so it was important to prove that the material had not been damaged by the measurement. In an attempt to unequivocally rule out degradation as a cause of the high temperature change in the fluctuation data, three different methods were used to show that there had been no change to the material. Firstly, thermogravimetric analysis was performed on a MAPI sample between 300 K and 450 K. No obvious mass loss was observed in both the TGA trace(the 1$^{st}$

derivative is also presented).  The TGA data is in agreement with previously observed thermal analysis on MAPI (Figure 4-13a,b) where the first mass loss, apart from moisture from the sample, occured at $523\,\text{K}$. This is the loss of HI and is quickly followed by the loss of $CH_3NH_2$.[45]

Secondly, pXRD analysis was performed on the MAPI sample both before and after the μSR experiments.  There were some small changes in peak shape and intensity before and after the muon experiment, but the position of the peaks remained unchanged.  This indicates that there were some small changes to the crystal shape or size during the experiment.  This is likely to have occurred due to the large temperature range and long experimental time used but would be unlikely to have an impact on any observations made during the μSR experiment. The most important information from the pXRD is the absence of any peak at $2\theta = 12°$ associated with the presence of $PbI_2$, suggesting no degradation of the perovskite material had occurred (Figure 4-13c).  Thirdly, after the initial muon measurements were taken, one of the samples was cooled to $100\,\text{K}$ and repeat data were acquired at a few temperature points and there was no change in the resulting spectra compared to those collected during the first set of experiments.
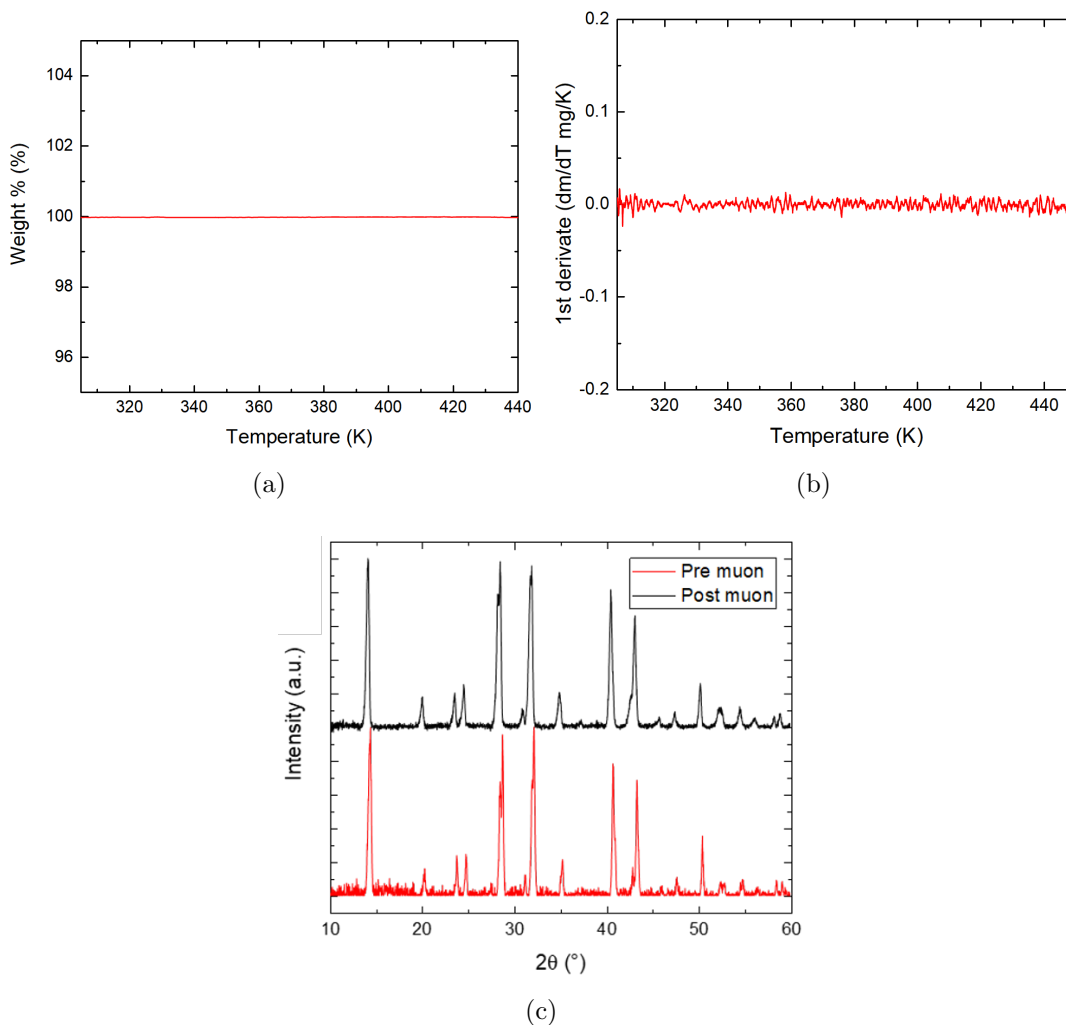
Figure 4-13: (a) Thermogravimetric analysis of MAPI between $300\,\mathrm{K}$ and $450\,\mathrm{K}$. (b) The 1ˢᵗ derivative of the TGA data. c) pXRD patterns of MAPI before (red) and after (black) the μSR experiment.

## 4.7    Deuterated Devices

To further compare the diffusion properties and to see if deuteration impacts performance, devices of MAPI and $d_6$-MAPI were fabricated. The performance and impedance response of the cells was then compared. To ensure there was no difference in properties of the thin films, XRD and UV-Vis analysis was performed. The Tauc plot of the two different films showed that there was an almost negligible difference in band gap between the two films (Figure 4-14a). The two different films also produced identical XRD patterns. (Figure 4-14b). The XRD patterns showed that the films were very crystalline. These two techniques showed that

the deuterated cation was not having an impact on the crystalline and electronic properties of the material.
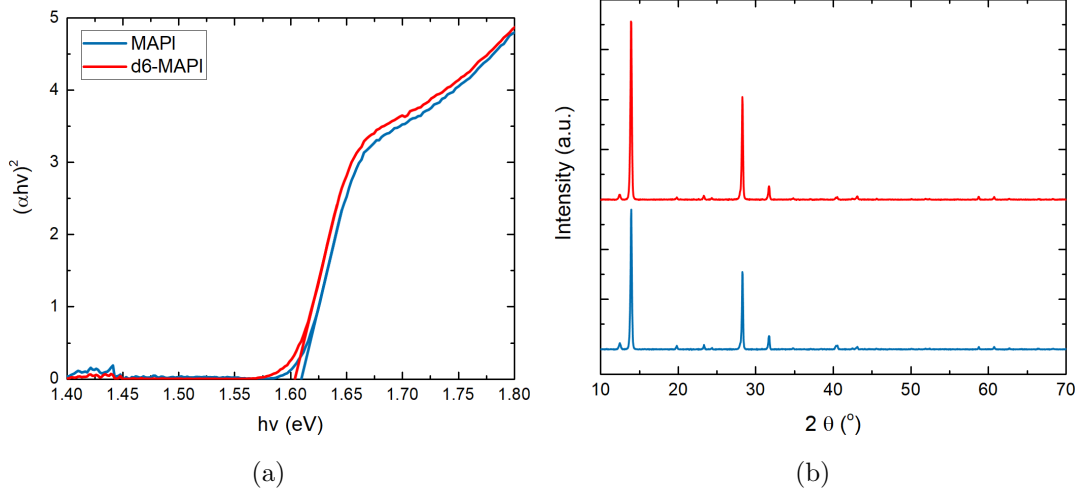


Figure 4-14: (a) Tauc and (b) XRD plots for thin films of MAPI (blue) and $d_6$-MAPI (red).

The JV response was compared for four cells of inverted NiO/Perovskite/PCBM/BCP/Ag cells made using an ethyl acetate anti-solvent drip. Some of the pixels produced no response due to short circuiting of the device during manufacturing and these data points were not included in the overall statistical analysis shown in Figure 4-15. The champion efficiencies were 10.65 % and 9.89 % for MAPI and $d_6$-MAPI respectively. The average efficiency for the $d_6$-MAPI cells was slightly lower than MAPI. This is unlikely to be a significant difference and would disappear if a larger sample size of devices was used. The other three important PV parameters, $V_{OC}$, $J_{SC}$ and Fill Factor, were unchanged with the deuterated cation.

The JV response of the two types of device is shown in Figure 4-16a. There was a small amount of hysteresis present in both types of cell. Differences in hysteresis between MAPI and $d_6$-MAPI was compared by calculating their hysteresis index. The hysteresis index was calculated using the equation from Kim and Park (Equation 4.4)

$$\text{hysteresis index} = \frac{J_{RS}(0.8V_{OC}) - J_{FS}(0.8V_{OC})}{J_{RS}(0.8V_{OC})} \tag{4.4}$$

where $J_{RS}(0.8V_{OC})$ and $J_{FS}(0.8V_{OC})$ are the current density of the forward and
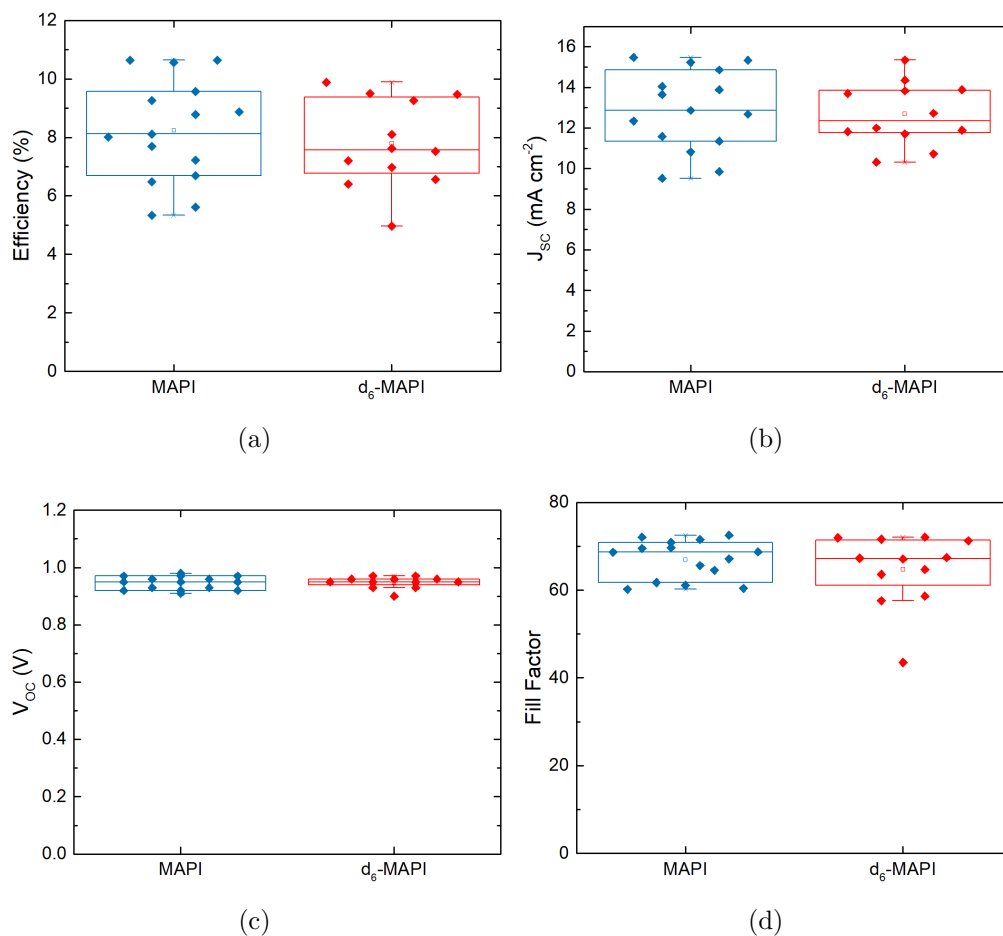
Figure 4-15: Efficiency, $J_{SC}$, $V_{OC}$ and Fill Factor data for MAPI and $d_6$-MAPI.

reverse scan at 80% of the $V_{OC}$.[46] The current at 80 % is used because this is the point where the largest degree of hysteresis is typically observed. The average hysteresis index for the two sets of cells shown in Figure 4-15 was $0.145 \pm (0.062)$ and $0.190 \pm (0.049)$ for MAPI and $d_6$-MAPI respectively (Figure 4-16b). The average difference in hysteresis between the two types of device is quite minimal with MAPI being slightly lower. The two averages are within one standard deviation of each other indicating that any difference could likely be attributed to difference in device performance and not a change to any internal dynamics of devices. It is also possible that the difference is being caused by the cation substitution.
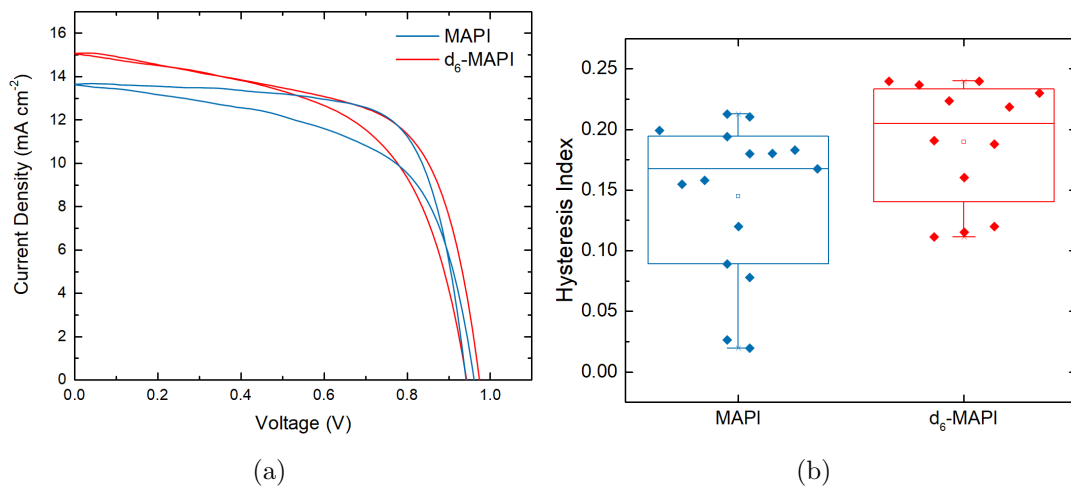
Figure 4-16: a) JV curves of pixels of MAPI and $d_6$-MAPI, both pixels were of cells with an overall efficiency of 9.3 %. b) A box plot of the hysteresis index for MAPI and $d_6$-MAPI cells.

## 4.8 Conclusions

In this chapter a muon spin relaxation study of MAPI and $d_6$-MAPI was presented. The initial study into MAPI showed that there were two distinct processes occurring in the material that were affecting the muons in the sample. Comparing the MAPI data with a per-deuterated MAPI analogue indicated that the lower temperature process was slightly impacted by the change in cation whereas the high temperature feature was mostly unchanged. The only minor change to the activation energy (from $0.172\,\mathrm{eV}$ to $0.154\,\mathrm{eV}$) at high temperature and its agreement with an analogous NMR study indicate that iodide diffusion was being observed at high temperature. Further experiments replacing the anion with bromide and altering the cation would help to further confirm that the high temperature process was iodide diffusion.

Using the fluctuation muon data, the diffusion coefficient of what was assumed to be iodide at various temperatures was calculated giving a room temperature value of $7.38 \times 10^{-14}\,\mathrm{cm^2 s^{-1}}$. This diffusion coefficient was the first experimentally measured value and was approximately one order of magnitude lower than the computationally predicted value at the same temperature. The impact of the deuterated cation on cell performance and EIS was also investigated, showing minimal difference to regular MAPI samples.

The stopping site of muons within MAPI and d$_6$-MAPI samples was also approximated using local field calculations. The $\Delta$ for both perovskites was calculated in each phase and the calculated values for muon stopping in between two iodide ions forming a linear I-μ-I state were similar to the experimental values. Therefore, it can be concluded that the most likely stopping site is in between two iodide ions forming a linear I-μ-I state.

This chapter has shown that μSR is a robust tool to probe iodide diffusion in perovskites without using external stimuli. The next chapter of this thesis will investigate the diffusion of iodide in three different mixed cation perovskites.

# References

(1) M. Saliba, T. Matsui, J.-Y. Seo, K. Domanski, J.-P. Correa-Baena, M. K. Nazeeruddin, S. M. Zakeeruddin, W. Tress, A. Abate, A. Hagfeldt, M. Grätzel, N. Mohammad K., S. M. Zakeeruddin, W. Tress, A. Abate, A. Hagfeldt and M. Grätzel, *Energy Environ. Sci.*, 2016, **9**, 1989–1997.

(2) G. Grancini, C. Roldán-Carmona, I. Zimmermann, E. Mosconi, X. Lee, D. Martineau, S. Narbey, F. Oswald, F. De Angelis, M. Graetzel and M. K. Nazeeruddin, *Nature Communications*, 2017, **8**, 15684.

(3) W. S. Yang, B.-W. Park, E. H. Jung, N. J. Jeon, Y. C. Kim, D. U. Lee, S. S. Shin, J. Seo, E. K. Kim, J. H. Noh and S. I. Seok, *Science*, 2017, **356**, 1376–1379.

(4) M. Zhang, J. S. Yun, Q. Ma, J. Zheng, C. F. J. Lau, X. Deng, J. Kim, D. Kim, J. Seidel, M. A. Green, S. Huang and A. W. Y. Ho-Baillie, *ACS Energy Letters*, 2017, **2**, 438–444.

(5) M. Saliba, T. Matsui, K. Domanski, J.-Y. Seo, A. Ummadisingu, S. M. Zakeeruddin, J.-P. Correa-Baena, W. R. Tress, A. Abate, A. Hagfeldt and M. Gratzel, *Science*, 2016, **354**, 206–209.

(6) J. M. Frost and A. Walsh, *Accounts of Chemical Research*, 2016, **49**, 528–535.

(7) O. Almora, C. Aranda, I. Zarazua, A. Guerrero and G. Garcia-Belmonte, *ACS Energy Letters*, 2016, **1**, 209–215.

(8) S. van Reenen, M. Kemerink and H. J. Snaith, *The Journal of Physical Chemistry Letters*, 2015, **6**, 3808–3814.

(9) A. Pockett, G. E. Eperon, N. Sakai, H. J. Snaith, L. M. Peter and P. J. Cameron, *Phys. Chem. Chem. Phys.*, 2017, **19**, 5959–5970.

(10) G. Richardson, S. E. J. O'Kane, R. G. Niemann, T. A. Peltola, J. M. Foster, P. J. Cameron and A. B. Walker, *Energy Environ. Sci.*, 2016, **9**, 1476–1485.

(11) H.-S. Kim, I.-H. Jang, N. Ahn, M. Choi, A. Guerrero, J. Bisquert and N.-G. Park, *The Journal of Physical Chemistry Letters*, 2015, **6**, 4633–4639.

(12) P. Calado, A. M. Telford, D. Bryant, X. Li, J. Nelson, B. C. O'Regan and P. R. Barnes, *Nature Communications*, 2016, **7**, 13831.

(13) C. Eames, J. M. Frost, P. R. F. Barnes, B. C. O'Regan, A. Walsh and M. S. Islam, *Nature Communications*, 2015, **6**, 7497.

(14) J. M. Azpiroz, E. Mosconi, J. Bisquert and F. De Angelis, *Energy Environ. Sci.*, 2015, **8**, 2118–2127.

(15) C. Li, S. Tscheuschner, F. Paulus, P. E. Hopkinson, J. Kießling, A. Köhler, Y. Vaynzof and S. Huettner, *Advanced Materials*, 2016, **28**, 2446–2454.

(16) O. Almora, I. Zarazua, E. Mas-Marza, I. Mora-Sero, J. Bisquert and G. Garcia-Belmonte, *Journal of Physical Chemistry Letters*, 2015, **6**, 1645–1652.

(17) T.-Y. Yang, G. Gregori, N. Pellet, M. Grätzel and J. Maier, *Angewandte Chemie International Edition*, 2015, **54**, 7905–7910.

(18) A. Senocrate, I. Moudrakovski, G. Y. Kim, T.-Y. Yang, G. Gregori, M. Grätzel and J. Maier, *Angewandte Chemie International Edition*, 2017, **56**, 7755–7759.

(19) J. Haruyama, K. Sodeyama, L. Han and Y. Tateyama, *Journal of the American Chemical Society*, 2015, **137**, 10048–10051.

(20) E. Mosconi and F. De Angelis, *ACS Energy Letters*, 2016, **1**, 182–188.

(21) A. Baumann, S. Väth, P. Rieder, M. C. Heiber, K. Tvingstedt and V. Dyakonov, *The Journal of Physical Chemistry Letters*, 2015, **6**, 2350–2354.

(22) S. Meloni, T. Moehl, W. Tress, M. Franckevičius, M. Saliba, Y. H. Lee, P. Gao, M. K. Nazeeruddin, S. M. Zakeeruddin, U. Rothlisberger and M. Graetzel, *Nature Communications*, 2016, **7**, 10334.

(23) S. Bae, S. Kim, S. W. Lee, K. J. Cho, S. Park, S. Lee, Y. Kang, H. S. Lee and D. Kim, *Journal of Physical Chemistry Letters*, 2016, **7**, 3091–3096.

(24) S. F. J. Cox, *Journal of Physics C: Solid State Physics*, 1987, **20**, 3187–3319.

(25) J. Sugiyama, K. Mukai, Y. Ikedo, H. Nozaki, M. Månsson and I. Watanabe, *Physical Review Letters*, 2009, **103**, 147601.

(26) J. Sugiyama, H. Nozaki, I. Umegaki, K. Mukai, K. Miwa, S. Shiraki, T. Hitosugi, A. Suter, T. Prokscha, Z. Salman, J. S. Lord and M. Månsson, *Physical Review B*, 2015, **92**, 014417.

(27) M. Månsson and J. Sugiyama, *Physica Scripta*, 2013, **88**, 068509.

(28) A. S. Powell, J. S. Lord, D. H. Gregory and J. J. Titman, *The Journal of Physical Chemistry C*, 2009, **113**, 20758–20763.

(29) T. E. Ashton, J. V. Laveda, D. A. MacLaren, P. J. Baker, A. Porch, M. O. Jones and S. A. Corr, *Journal of Materials Chemistry A*, 2014, **2**, 6238.

(30) N. Stone, *Atomic Data and Nuclear Data Tables*, 2005, **90**, 75–176.

(31) C. C. Stoumpos, C. D. Malliakas and M. G. Kanatzidis, *Inorganic Chemistry*, 2013, **52**, 9019–9038.

(32) B. Brunetti, C. Cavallo, A. Ciccioli, G. Gigli and A. Latini, *Scientific Reports*, 2016, **6**, 31896.

(33) P. S. Whitfield, N. Herron, W. E. Guise, K. Page, Y. Q. Cheng, I. Milas and M. K. Crawford, *Scientific Reports*, 2016, **6**, 35685.

(34) R. S. Hayano, Y. J. Uemura, J. Imazato, N. Nishida, T. Yamazaki and R. Kubo, *Physical Review B*, 1979, **20**, 850–859.

(35) F. L. Pratt, *Physica B: Condensed Matter*, 2000, **289-290**, 710–714.

(36) N. P. Gallop, O. Selig, G. Giubertoni, H. J. Bakker, Y. L. A. Rezus, J. M. Frost, T. L. C. Jansen, R. Lovrincic and A. A. Bakulin, *The Journal of Physical Chemistry Letters*, 2018, **9**, 5987–5997.

(37) R. Shakhovoy, M. Deschamps, A. Rakhmatullin, V. Sarou-Kanian, P. Florian and C. Bessada, *Solid State Nuclear Magnetic Resonance*, 2015, **71**, 80–86.

(38) J. Xing, Q. Wang, Q. Dong, Y. Yuan, Y. Fang and J. Huang, *Phys. Chem. Chem. Phys.*, 2016, **18**, 30484–30490.

(39) A. M. A. Leguy, J. M. Frost, A. P. McMahon, V. G. Sakai, W. Kochel-mann, C. Law, X. Li, F. Foglia, A. Walsh, B. C. O'Regan, J. Nelson, J. T. Cabral and P. R. F. Barnes, *Nature Communications*, 2015, **6**, 7124.

(40) J. H. Brewer, S. R. Kreitzman, D. R. Noakes, E. J. Ansaldo, D. R. Harsh-man and R. Keitel, *Physical Review B*, 1986, **33**, 7813–7816.

(41) T. Lancaster, S. J. Blundell, P. J. Baker, M. L. Brooks, W. Hayes, F. L. Pratt, J. L. Manson, M. M. Conner and J. A. Schlueter, *Physical Review Letters*, 2007, **99**, 1–4.

(42) M. T. Weller, O. J. Weber, P. F. Henry, A. M. D. Pumpo and T. C. Hansen, *Chem. Commun.*, 2015, **51**, 4180–4183.

(43) A. Walsh, D. O. Scanlon, S. Chen, X. G. Gong and S.-H. Wei, *Angewandte Chemie International Edition*, 2015, **54**, 1791–1794.

(44) J. Sugiyama, *Journal of the Physical Society of Japan*, 2013, **82**, SA023.

(45) A. Dualeh, N. Tétreault, T. Moehl, P. Gao, M. K. Nazeeruddin and M. Grätzel, *Advanced Functional Materials*, 2014, **24**, 3250–3258.

(46) H. S. Kim and N. G. Park, *Journal of Physical Chemistry Letters*, 2014, **5**, 2927–2934.

# Chapter 5
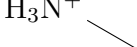
# Studying Partial Cation Substitution in Perovskites
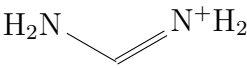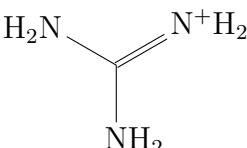
## 5.1 Introduction

Mixing of cations to improve the performance and stability of perovskites cells has become an essential part of perovskite research.[1–6] The initial mixing of 40 mol% formamidinium (FA) and methylammonium (MA) 60 mol% in 2014 by Pellet *et al.* showed the potential of mixed cation perovskites as device performance was improved comapared to single cation perovskite devices.[6] Since the initial MA/FA study, the top performing cells make use of a mixed cation formula with the current best performing cation stoichiometry being $Cs_{0.05}(FA_{0.83}MA_{0.17})_{0.95}$.[6,7]

As well as caesium and formamidinium, there have been several other cations of varying sizes from rubidium up to guanidinium (GA) that have been incorporated into perovskite solar cells.[1,3,8] Partial substitution of almost any appropriately sized cation appears to improve efficiency and stability.[2,9,10] For GA, 14% substitution into MAPI increased device stability and efficiency by 7%.[4] Early work with $Cs^+$ substitution showed that 10% substitution increased device efficiency by 40%.[11] FA substitution is well studied and initially 40% FA substitution gave the largest efficiency increase due to improved photon harvesting in the red region of the light spectrum.[6] This ability to increase efficiency and stability is invaluable in the pursuit of commercial relevance for perovskite solar cells.[12]

Mixing of cations in perovskites can lead to some phase separation or the

Table 5.1: The size and structure of MA and the three other cations covered in this study.

| Cation | Ionic Radius (pm) | Structure |
|--------|-------------------|-----------|
| MA | 217 | $H_3N^+$ |
| Cs | 174 | $Cs^+$ |
| FA | 253 | $H_2N$ $N^+H_2$ |
| GA | 278 | $H_2N$ $N^+H_2$ $NH_2$ |

formation of 2D perovskites. For FA/MA substitution, if the ratio of MA is below 20 % then the yellow δ-phase becomes prevalent as the MA is needed to stabilise the black α-phase.[13] It has also been reported that caesium lead iodide perovskites are polymorphic with an α and δ phase but thorough investigation of the impact of Cs/MA mixing on the phase stability has not yet been performed.[7] For GA/MA mixing the perovskite remains in phase pure in a 3D tetragonal perovskite up to 25 % substitution of GA after which the lattice becomes strongly distorted making a non tetragonal perovskite.[4]

What is unknown with cation substitution is the impact on the internal dynamics of the material. The diffusion of iodide in standard MAPI has been well covered using a variety of methods and we have studied it using the new technique μSR outlined in the previous chapter.[14–16] Meanwhile, there are almost no studies of ionic motion in other pure perovskites such as formamidinium lead iodide, caesium lead iodide and mixed cation perovskites. Understanding how cation substitution impacts ion dynamics is important for improving device stability and guiding the design of future materials.

In this chapter μSR was used to investigate iodide diffusion in partially substituted perovskites using the cations shown in Table 5.1. $Cs^+$, formamidinium and guanidinium were chosen for their size with one smaller, one larger and one substantially larger organic cation. The level of substitution selected was 5 mol% to minimise the changes to the overall perovskite structure so as best to compare with MAPI.

## 5.2 Powder Synthesis and Analysis

The three perovskite powder used in this study were synthesised using the same hot casting method from the previous muon study (Section 4.2). The same method was used to minimise the impact of fabrication method on the diffusion properties.[17] pXRD spectra (Figure 5-1) showed that the small amount of substitution did not have an impact on the crystal structure and the material was all in a single tetragoanl phase 3D perovskite. Crucially, there was no sign of the characteristic $PbI_2$ peak at $2\Theta = 12°$. This is similar to what other mixed cation studies on thin films have observed when investigating low substitution concentrations where they observed no change to the XRD pattern with $5\,mol\%$ cation substitution.[2,4,6,10]
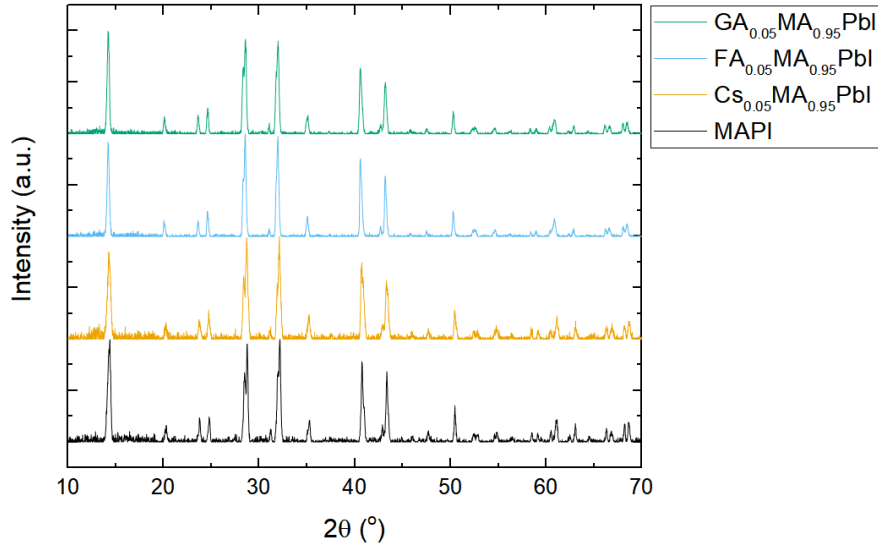


Figure 5-1: pXRD patterns for the three mixed cation perovskites studied in this chapter and MAPI for comparison.

NMR was used to confirm the amount of substitution in the perovskites; this is a quick and easy method that has been previously used in MA/FA studies.[18] In the case of GA and FA, the integrals of the peaks for MA and GA/FA were compared directly. For FA substitution, when the MA peak was set to 95 the corresponding FA peak was equal to 1.45 (Figure 5-2a). As the FA peak corresponds to only 1 proton and the MA corresponds to 3, the FA signal can be tripled giving a total substitution of 4.35 mol%. Using the same procedure for the GA substituted powder gave integrals of 95 for the MA and 10.27 for the GA. The GA peak

corresponds to 6 protons so halving the value gave a total substitution of 5.14 mol% (Figure 5-2b).

This technique does not work directly for $Cs^+$ susbtitution as there are no protons on $Cs^+$. Therefore, the method was adapted by mixing known quantities of acetonitrile (ACN) and $Cs_{0.05}MA_{0.95}PI_3$ in the NMR sample. The integral of the ACN and MA hydrogens was subsequently compared to calculate a quantitative value for the percentage of MA in the perovskite. The remaining percentage of cation was then attributed to $Cs^+$ (Figure 5-3) giving $4.3\,\mathrm{mol\%}$ substitution of $Cs^+$ into the perovskite. While only one of the powders contained exactly $5\,\%$ of the substituted cation the impact of the cations should still be observable and comparable. It was also important to prove that mixing ratios of cations in solution led to actual incorporation of the cations in the final perovskite.
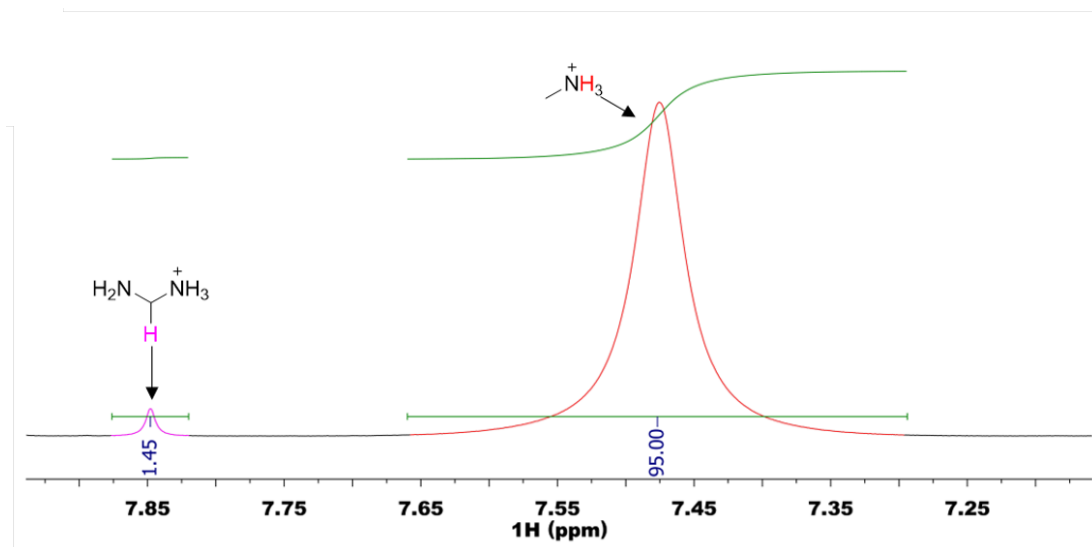
(a)
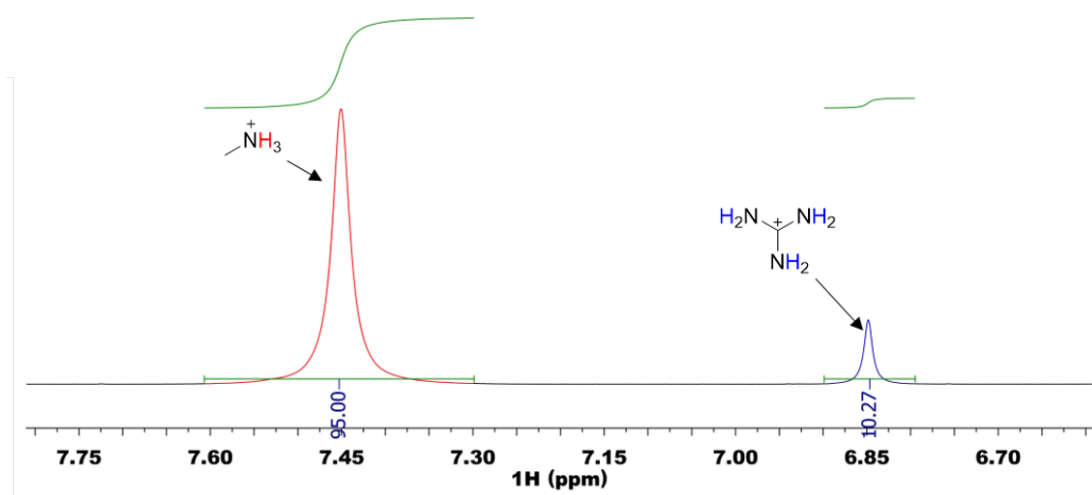


(b)

Figure 5-2: $^1$H NMR spectra of a) $FA_{0.05}MA_{0.95}PbI_3$ and b) $GA_{0.05}MA_{0.95}PbI_3$.
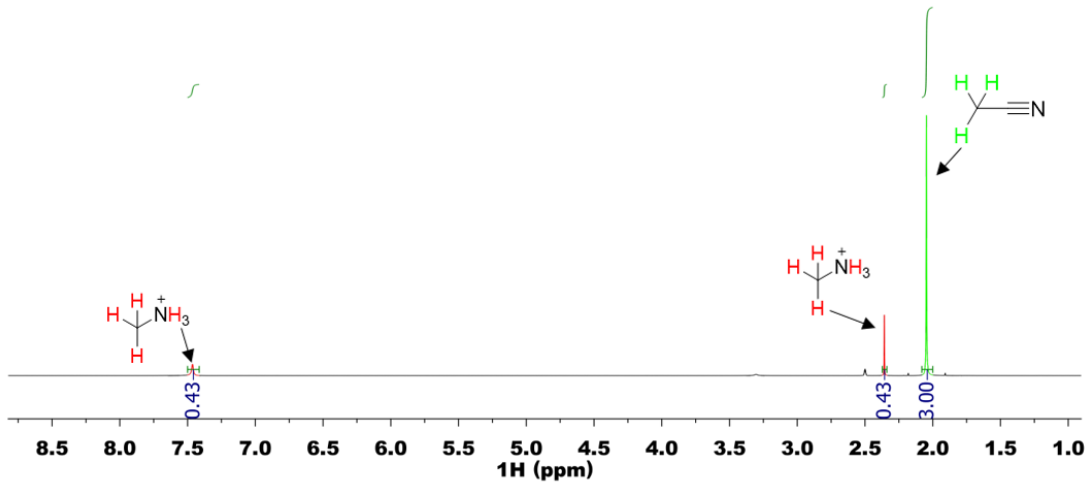
Figure 5-3: $^1$H NMR spectra of $Cs_{0.05}MA_{0.95}PbI_3$ with ACN as a comparison peak

## 5.3  µSR Analysis

The muon analysis performed here followed the same procedure as the MAPI/$d_6$-MAPI study where four different longitudinal fields are applied at each temperature over a range between 50 and 400 K. The temperature range used for each sample was intended to be the same as the MAPI experiment. However, the sample was not always perfectly heated so there are occasional differences between the applied temperature and the internally measured temperature. This minor difference explains the slightly larger range in the temperatures used for the mixed cations and why the temperature of measurements is not always the same between samples.

### 5.3.1  Guanidinium Substitution

Data for each cation substituted material is first presented, the results will then be discussed and compared in Section 5.3.4. Some examples of raw data for 5% GA subsitituted perovskite is shown in Figure (5-4). At 50 and 110 K the raw data was similar to that seen for MAPI in Section 4.3 where 50 K was a mostly static environment and 110 K was more dynamic (Figure 5-4a and b). The 350 K data was also the same as MAPI (Figure 5-4c). The biggest difference occurred when the temperature was increased to 400 K where the muon environment was unchanged in the GA substituted perovskite unlike MAPI where the muon envi-

ronment became more dynamic (Figure 5-4d).
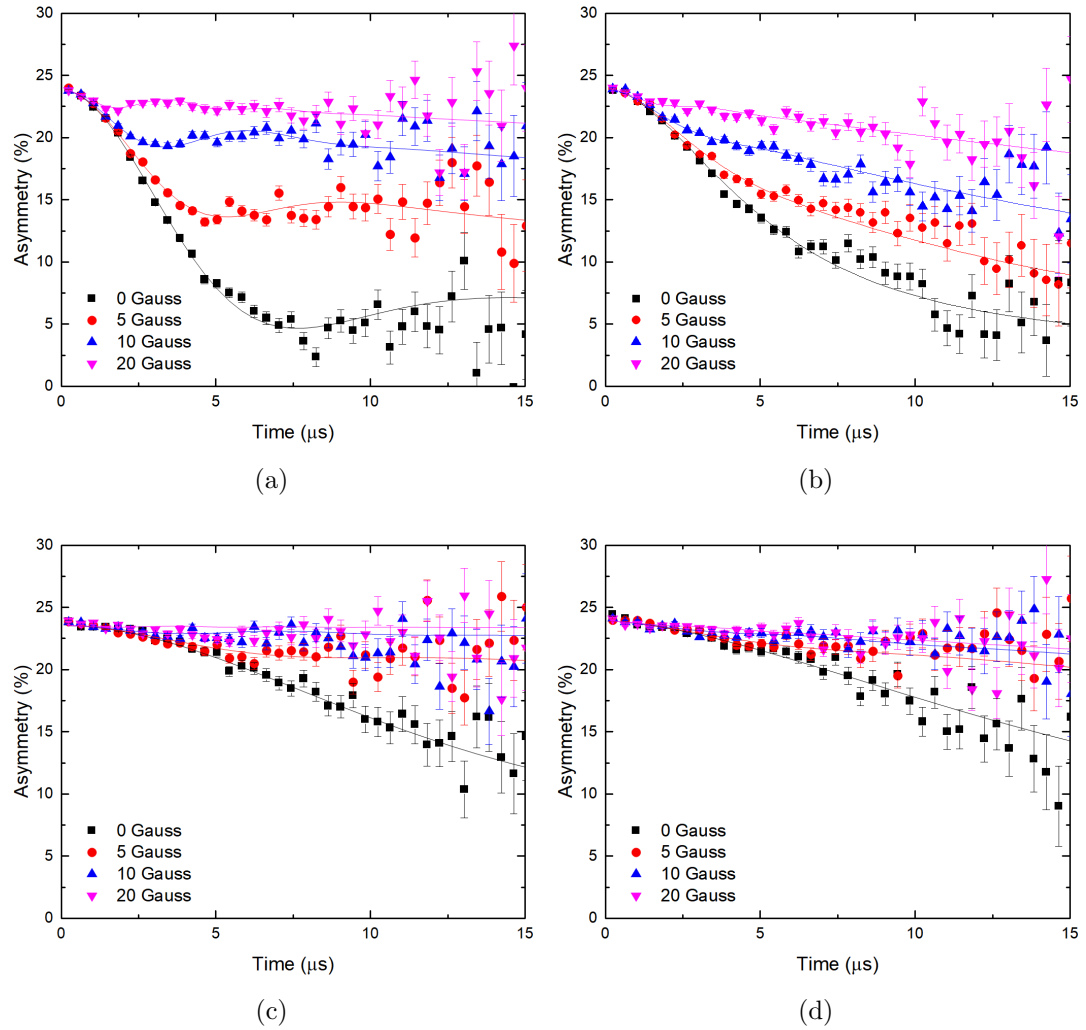


Figure 5-4: Raw muon data for $GA_{0.05}MA_{0.95}PI_3$ at a) $50\,K$, b) $110\,K$, c) $350\,K$ and d) $400\,K$. Also shown are the results of fitting the data to a dynamic Kubo-Toyabe function.

It is important to note that muon stopping sites are likely to be unaffected by the substitution of the cation. For GA substitution electrostatic potential calculations were performed by Dibya Ghosh and the resulting contour map is shown in Figure 5-5. It is clear that the most electronegative areas of the perovskite were still the iodide sites. The substitution of $5\,mol\%$ had minimal impact on the electronegativity meaning the stopping site were still be between two adjacent iodide ions.

The raw data for GAMAPI was fitted using the same dynamic Gaussian Kubo-Toyabe function multiplied by an exponential relaxation rate that was used for
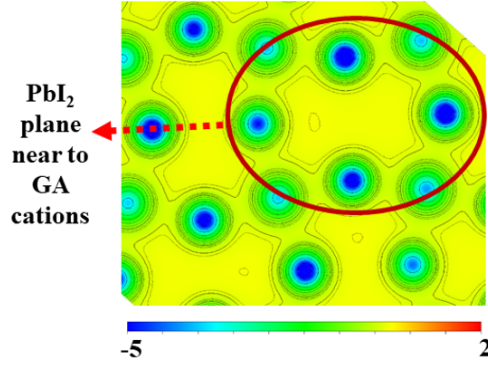
Figure 5-5: Electrostatic potential contour map of GA substituted perovskite with a scale in electronvolts.



(a)

(b)
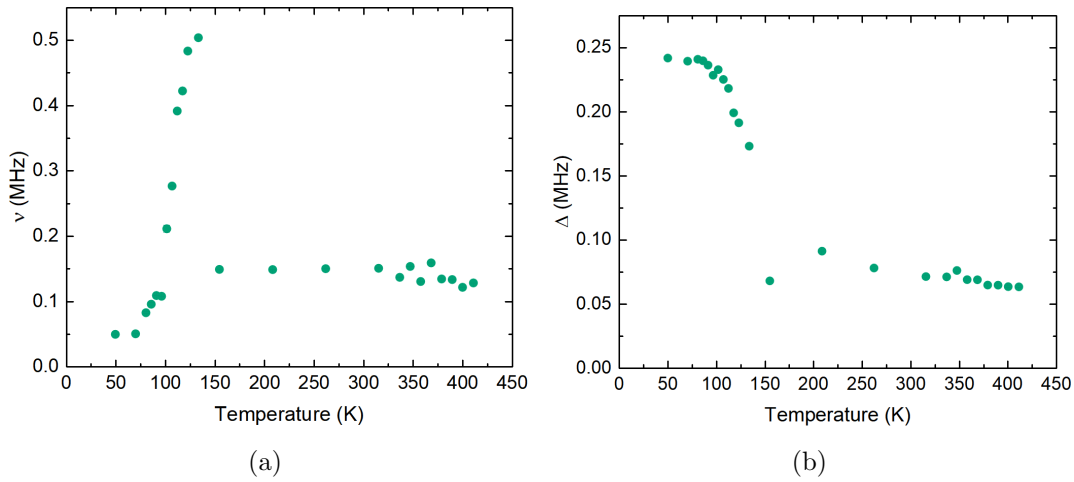
Figure 5-6: The temperature dependence of a) fluctuation rate and b) local field in $GA_{0.05}MA_{0.95}PI_3$.

MAPI (Equation 4.1). The change in local field distribution and fluctuation rates with temperature are shown in Figure 5-6. The fluctuation rate was constant until $80\,K$ where it increases from $0.05\,MHz$ to $0.5\,MHz$ at $140\,K$. After $140\,K$ $\nu$ drops down to $0.15\,MHz$ where it remains unchanged until the end of the temperature range of the experiment. The local field at $50\,K$ was $0.25\,MHz$ before decreasing to $0.07\,MHz$. This decreasing of the local field was caused by the same motional narrowing effect discussed in Section 4.3.

## 5.3.2 Caesium Substitution

The raw data for the smallest of the three cations used in this study, $Cs_{0.05}MA_{0.95}PI_3$ is shown in Figure 5-7. At $50\,K$ there was minimal dynamics with the data ap-

pearing similar to a static Kubo-Toyabe relaxation function with a minima and then a tail at 1/3. As the temperature increased to 110 K the environment became more dynamic reducing both the minima and the 1/3 tail of the asymmetry. At 350 K the raw data is visually similar to MAPI. Finally, at 400 K the environment was very dynamic and the asymmetry decreased exponentially as can be seen in Figure 5-7.
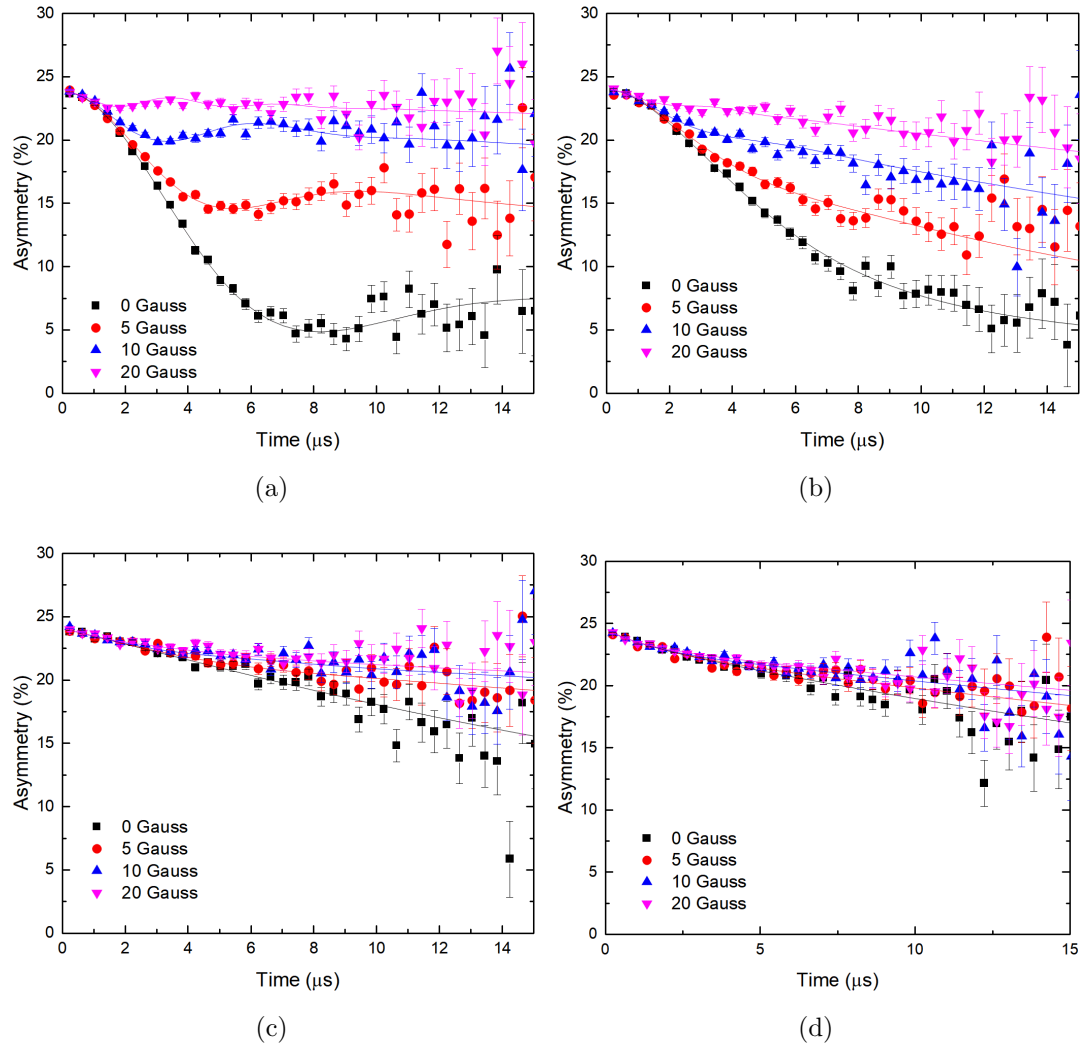


Figure 5-7: Raw muon data for $Cs_{0.05}MA_{0.95}PI_3$ at a) 50 K, b) 110 K, c) 350 K and d) 400 K. Also shown are the results of fitting the data to Equation 4.1 for a and b and Equation 5.1 for c and d.

The fitting of the CsMAPI data at temperatures up to 340 K used the same fitting equation as GAMAPI and MAPI (Equation 4.1). A change in the relaxation after 340 K meant the data had to be modelled using a different fitting equation.
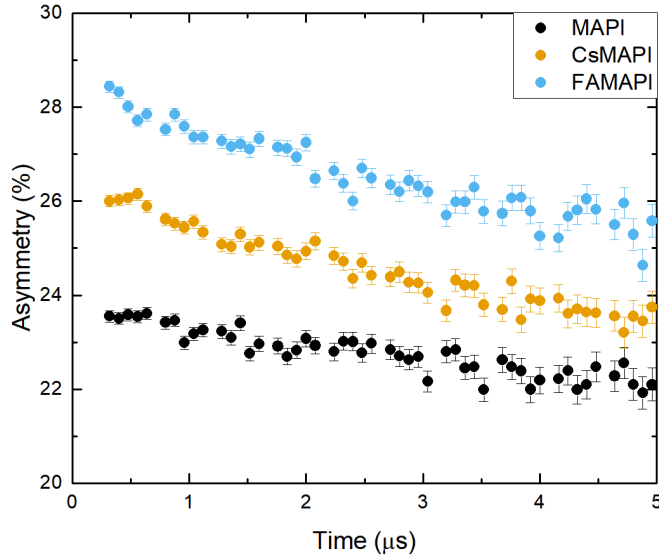
Figure 5-8: Raw muon data during the first five seconds of an experiment at 400 K for MAPI, $Cs_{0.05}MA_{0.95}PI_3$ and $FA_{0.05}MA_{0.95}PI_3$. The data is offset by 2% asymmetry so that it can be more easily visualised.

Initial attempts to fit with Equation 4.1 did not give the desired quality of fit due to a small decay in the asymmetry in the first 3 μs of the measurement. This slight difference can be seen in Figure 5-8a where the initial muon relaxation is different between the CsMAPI and FAMAPI samples when compared to MAPI.

An important point to note about the second exponential component is that it disappeared when the sample was cooled back down to 200 K. This disappearance indicates that the second exponential was not caused by degradation of the sample. The most likely origin of the extra relaxation component is the formation of muonium (Mu) in the sample. Muonium is formed when a muon picks up an electron to form a neutral species similar to atomic hydrogen.[19] The formation of a fraction of Mu would be clear in the transverse field (TF) measurements taken, to correct the asymmetry, as the overall asymmetry would be decreased. The Mu fraction would be depolarised and therefore would not decay, decreasing the total asymmetry for those samples.

Figure 5-9 shows the TF measurements for FA and Cs substituted perovskites as well as MAPI. These measurements were taken at room temperature with an applied field of 100 G. The overall asymmetry was not reduced between the three different perovskites showing that no Mu fraction was formed at this temperature.

131
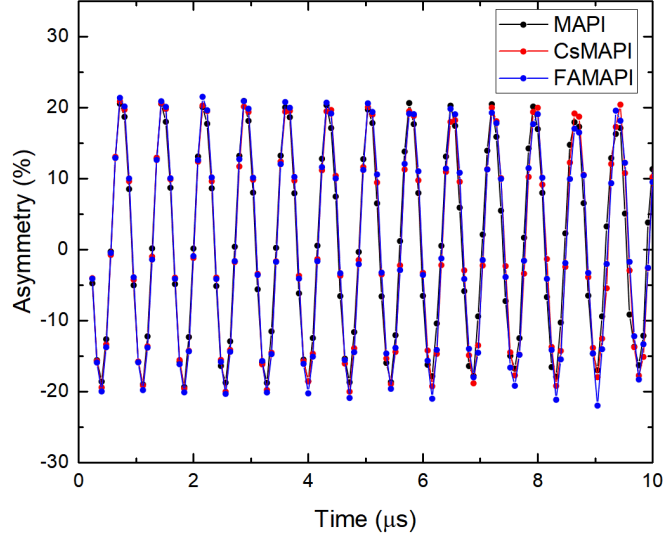
Figure 5-9: Comparison of the transverse field measurements of MAPI, $Cs_{0.05}MA_{0.95}PI_3$ and $FA_{0.05}MA_{0.95}PI_3$ at $300\,K$ with an applied field of $100\,G$.

Unfortunately the calibration measurements were only run at 300 and $50\,K$ as measuring the TF response at every temperature is not the standard methodology. A TF measurement for the three samples at greater than $350\,K$ would give the clearest indication of the formation of Mu in the FA and Cs perovskites. It is not clear why Mu is formed in FA and Cs perovskites but not the others. It is difficult to give a conclusive reason as there are not many differences between the samples that would give an obvious reason for it and there is not a lot of data. The most likely situation is that Mu would be formed in the other perovskites tested but only at higher temperatures.

To account for this change, a second component was added to the fitting equation.

$$A_0 P_{LF}(t) = A_{KT} exp(-\lambda t) G^{DGKT}(\Delta, \nu, t, H_{HF}) + A_2 exp(-\lambda_2 t) + A_{BG} \quad (5.1)$$

The new equation (Equation 5.1) contains a second exponential relaxation ($\lambda_2$) and a second asymmetry component ($A_2$) that relates to the asymmetry of the second component. The second exponential had an amplitude of about 1% asymmetry over the entire temperature range that it was required. The fact that the $2^{nd}$ component was so small meant that it did not have a noticeable impact on the fitted $\nu$ and $\Delta$ data.

The change in $\nu$ and $\Delta$ with respect to temperature is shown in Figure 5-
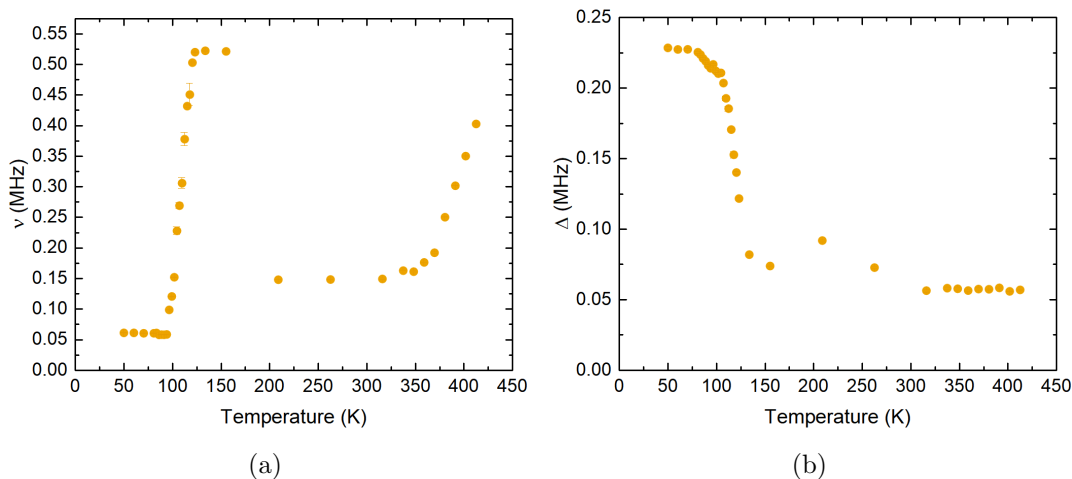
Figure 5-10: The temperature dependence of a) fluctuation rate and b) local field in $Cs_{0.05}MA_{0.95}PI_3$.

10. The change in $\nu$ with respect to temperature was similar to that observed for MAPI with an initial plateau followed by an increase at $100\,K$ followed by a decrease above $150\,K$. The temperature where the decrease in $\nu$ occurs corresponds to the perovskite's phase change (Figure 5-10a). The fluctuation rate then remained flat at $0.15\,MHz$ before a second increase at $350\,K$. The local field decreased with increasing temperatures (Figure 5-10b). This decrease was caused by motional narrowing associated with an increasingly dynamic environment.

### 5.3.3 Formamidinium Substitution

The raw FA substituted data (Figure 5-11) was very similar to the $Cs^+$ data. Once again, the $50\,K$ asymmetry showed a mostly static environment becoming more dynamic at $110\,K$. At $350\,K$ the data was similar to all of the previous samples with no real initial decrease in the asymmetry. The $400\,K$ asymmetry also showed a very dynamic environment.
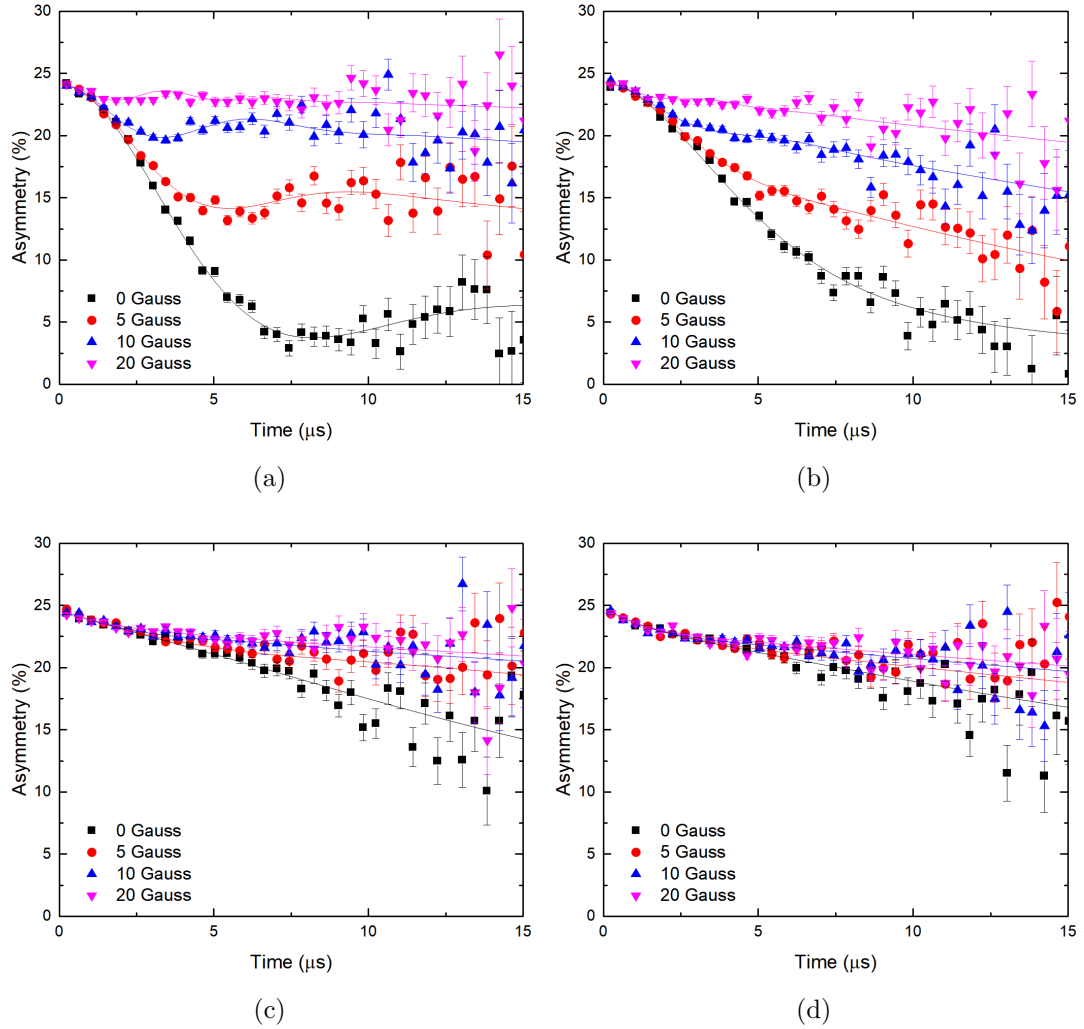
Figure 5-11: Raw muon data for $FA_{0.05}MA_{0.95}PI_3$ at a) 50 K, b) 110 K, c) 350 K and d) 400 K. Also shown are the results of fitting the data to Equation 4.1 for a and b and Equation 5.1 for c and d.

As with the CsMAPI data, the FAMAPI data was fit using Equation 4.1 at temperatures below 330 K and then Equation 5.1 above 330 K. The resulting change in $\nu$ and $\Delta$ with respect to temperature is shown in Figure 5-12. The fluctuation rate (Figure 5-12a) initially remained unchanged until 100 K where there was a sharp increase until 160 K where it decreased back down to 0.15 MHz. The fluctuation rate then remained unchanged until 350 K where it increased to 0.45 MHz. The local field (Figure 5-12b) started at 0.225 MHz before decreasing down to 0.07 MHz. This decrease in the local field can again be attributed to motional narrowing.
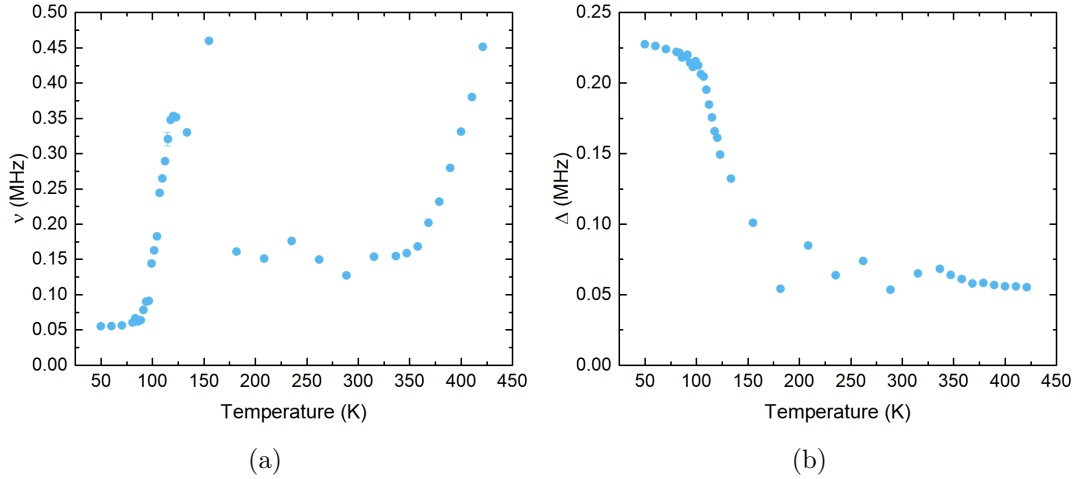
Figure 5-12: The temperature dependence of a) fluctuation rate and b) local field in $FA_{0.05}MA_{0.95}PI_3$.

## 5.3.4 Comparison of Muon Spin Relaxation Data

The change in $\nu$ with temperature for all the samples over the full temperature range is shown in Figure 5-13a along with MAPI for comparison. The partially $Cs^+$ and FA substituted perovskites followed a similar trend to the results for pure MAPI with two thermally activated processes occurring, one at low temperature and one at high temperature. The partially GA substituted perovskite, unlike MAPI, had only one thermally activated process which was at low temperature. Overall, the low temperature processes were all similar to MAPI as shown in Figure 5-13b. The FA substituted perovskite was the most unique with the total fluctuation rate at low temperature not reaching as high a level as the other three perovskites.

The activation energies for all of the processes were derived from Arrhenius plots (Figure 5-14) and the resulting values are listed in Table 5.2. At low temperature the $E_a$ of partially FA and GA substituted perovskites was approximately 0.02 eV lower than that of MAPI. The $E_a$ of $Cs^+$ substituted perovskites was the same as that calculated for MAPI. It is difficult to say what was causing the difference in activation for the low temperature process. It could be a slight expansion of the lattice caused by the larger cations making the rotation of the cation easier whereas the contraction from the smaller cation was not causing the dynamics to change. Without further studies into how partial cation substitu-
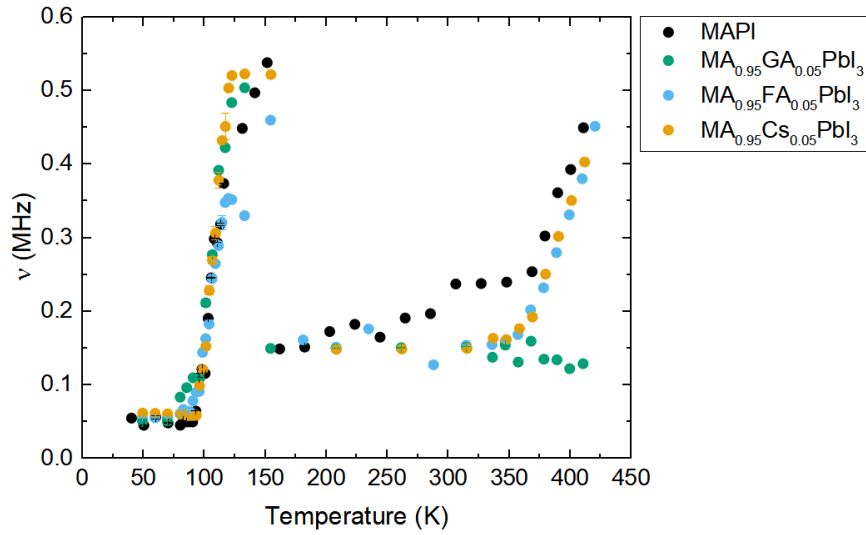
(a)
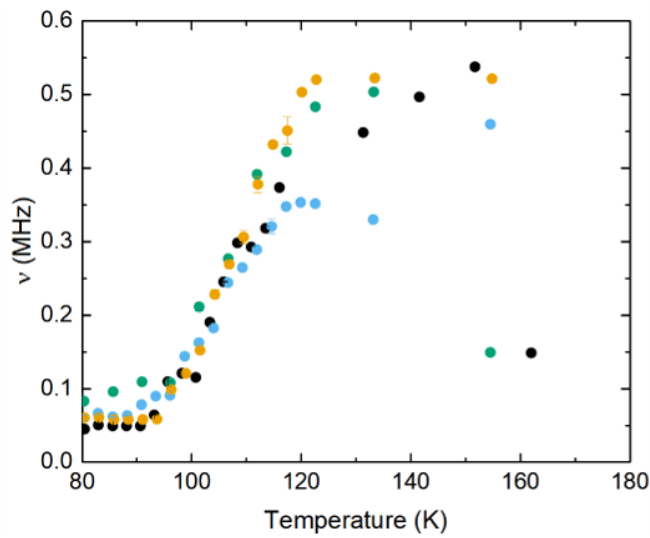


(b)

Figure 5-13: The resulting $\nu$ against temperature data for the three mixed cation perovskites acquired from fitting the raw muon data and MAPI for comparison a) is the full range of temperatures and b) shows the same data magnified between 70 and 140 K to show more clearly the low temperature region.

Table 5.2: $E_a$ of mixed cation perovskites at high and low temperature as measured by muon spin relaxation.

| | $E_a$ (eV) | |
| Perovskite | Low Temperature | High Temperature |
| --- | --- | --- |
| $Cs_{0.5}MA_{0.95}PbI_3$ | 0.074($\pm$0.004) | 0.187($\pm$0.014) |
| $FA_{0.5}MA_{0.95}PbI_3$ | 0.057($\pm$0.003) | 0.201($\pm$0.012) |
| $GA_{0.5}MA_{0.95}PbI_3$ | 0.051($\pm$0.005) | - |
| $MAPbI_3$ (Chapter 4) | 0.072($\pm$0.005) | 0.174($\pm$0.010) |

tion changes the low temperature structure, producing a definitive answer for the cause of the difference shown here would be difficult.

At high temperature the $E_a$ for $Cs^+$ and FA was marginally higher than that of MAPI (see Table 5.2). When the margin of experimental error is considered, it could be argued that the $E_a$ for $Cs^+$ is the same as MAPI as it is within one standard deviation. Further measurements to improve the accuracy of the results would help to determine if there is a statistically significant difference between the $E_a$ of the two materials. Meanwhile, the $E_a$ for partially FA substituted perovskite is outside of the error range and can therefore be considered to be higher. The $E_a$ of GA could not be calculated as there was no temperature dependent process to produce an Arrhenius plot from. The cause of this change in activation energy is discussed in section 5.3.7.

The change in local field with respect to temperature for the three partially substituted perovskites is shown in Figure 5-15 alongside MAPI for comparison. The change in $\Delta$ is similar to MAPI for all three of the partially substituted perovskites. All samples start with a local field of approximately 0.22 MHz which decreases to 0.07 MHz at around 160 K. The local field then fluctuates slightly before plateauing above 300 K. This early decrease is what would be expected due to motional narrowing of the local field as discussed in Section 4.3. A local field change with this appearance is standard for µSR studies into ion migration.[20,21]
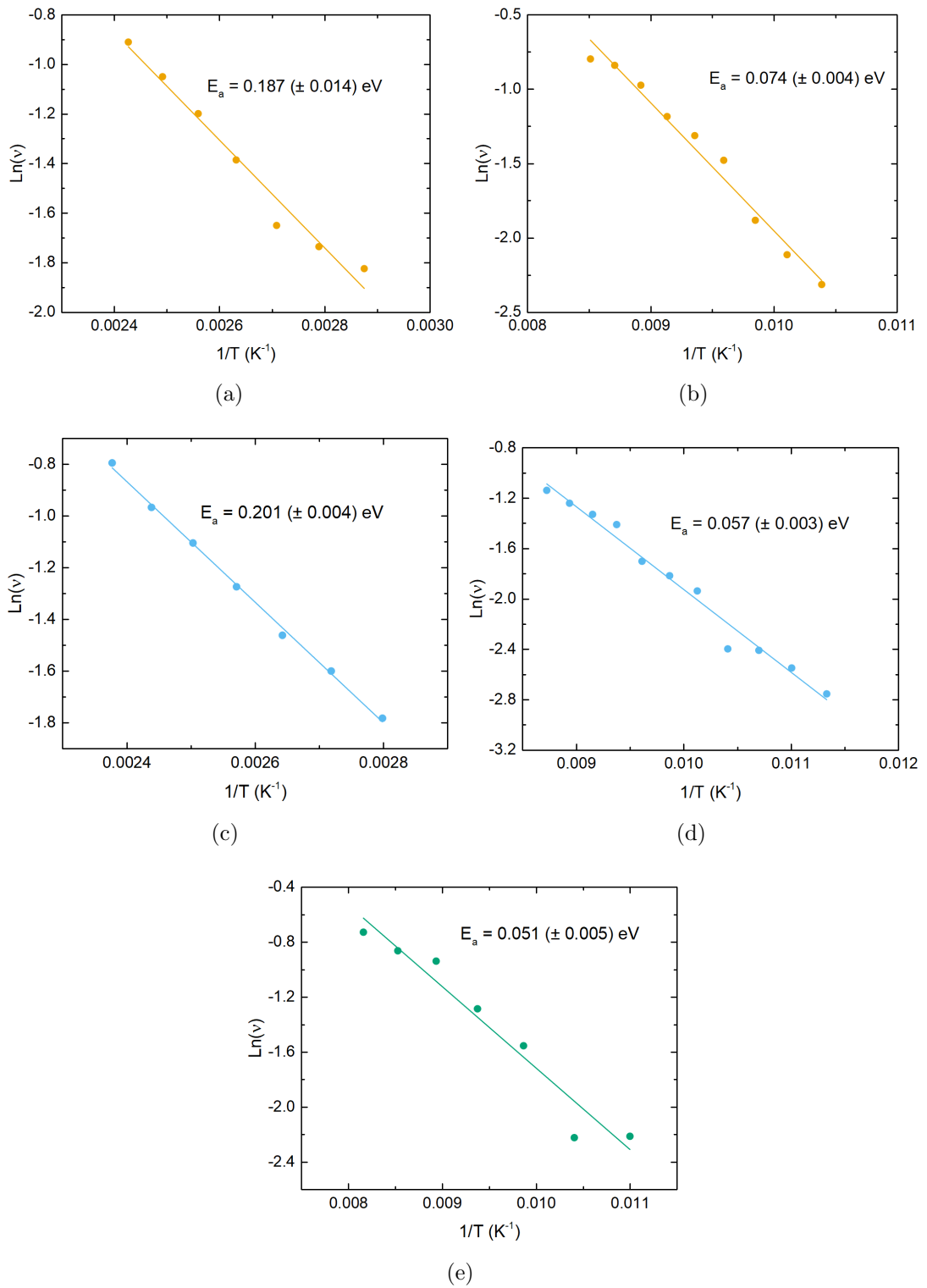
Figure 5-14: Arrhenius plots for $Cs_{0.05}MA_{0.95}PbI_3$ at a) high temperature and b) low temperature, $FA_{0.05}MA_{0.95}PbI_3$ at c) high temperature and d) temperature and $GA_{0.05}MA_{0.95}PbI_3$ at e) low temperature.
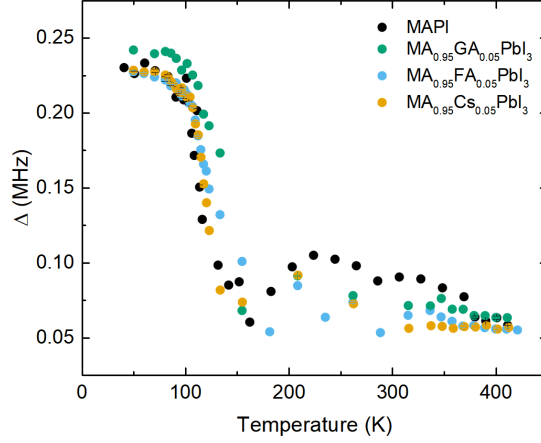
Figure 5-15: Change in $\Delta$ data with respect to temperature for all the mixed cations and MAPI for comparison.

### 5.3.5    Diffusion Coefficients

As in the previous chapter the diffusion coefficient at various temperature can be calculated using equation 5.2. The resulting $D_I$ values for $Cs_{0.05}$ and $FA_{0.05}$ are reported in Figure 5-16 with MAPI included for comparison.

$$D_I = \sum_{i=1}^{N} \frac{1}{N_i} Z_{vi} s_i^2 \nu \tag{5.2}$$

Despite the minimal change in the $E_a$, the $D_I$ for $Cs_{0.05}$ is decreased slightly compared to MAPI. The $D_I$ decreases from $7.92 \times 10^{-13} \, \mathrm{cm^2 s^{-1}}$ at $400 \, \mathrm{K}$ in MAPI to $3.53 \times 10^{-13} \, \mathrm{cm^2 s^{-1}}$ in CsMAPI. This change in diffusion coefficient is due to the shift of onset of the high temperature process in the $\nu$ data. The $D_I$ for $FA_{0.05}$ is also slightly lower than that of MAPI with a $D_I$ of $3.34 \times 10^{-13} \, \mathrm{cm^2 s^{-1}}$ at $400 \, \mathrm{K}$. As with the $E_a$, the lack of change in fluctuation at high temperature for $GA_{0.05}$ means there were no diffusion coefficients calculated.

### 5.3.6    Comparison with Impedance

This project was part of a wider study investigating partial cation substitution in perovskites. These three cations, as well as several others, were studied using electrochemical impedance spectroscopy (EIS) by Sam Pering. In these EIS experiments inverted perovskite device were manufactured and an external AC voltage with varying frequency was applied while the devices were illuminated. The resulting impedance of the devices were measured and presented as Nyquist
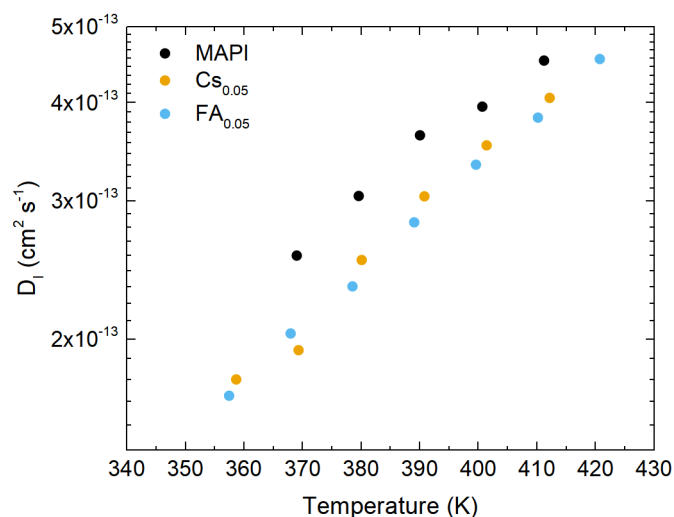
Figure 5-16: Calculated diffusion coefficients of $Cs^+$ and FA substituted perovskites compared with MAPI.
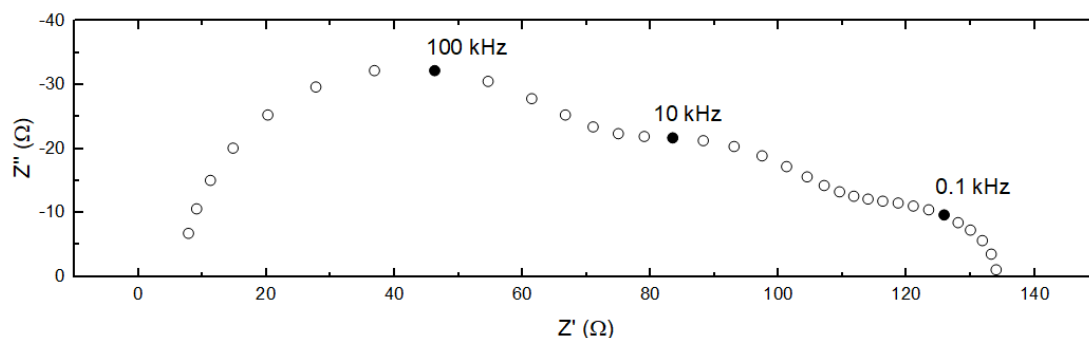


Figure 5-17: An example Nyquist plot that is produced from analysis of a MAPI device.

plots. An example Nyquist plot acquired from EIS analysis of a MAPI device is shown in Figure 5-17. The plot contains three distinct features, one at low frequency, one at middle frequency and one at high frequency. To calculate the activation energy of iodide diffusion for perovskite devices measurements are taken at a range of temperatures and the time constant for the low frequency feature is obtained by fitting the data to three simple semi circles.[14] An Arrhenius plot of the time constants then gives the $E_a$ of iodide migration. For this project, activation energies for iodide diffusion in complete devices made with the partially substituted perovskites were calculated and the results are shown in Table 5.3 next to the activation energies measured using μSR.

As with the μSR study, GA substitution of just 5% completely eliminated io-

Table 5.3: $E_A$ of iodide diffusion in mixed cation perovskites measured using EIS and μSR

| | $E_a$ (eV) | |
| --- | --- | --- |
| Perovskite | Impedance | μSR |
| $Cs_{0.05}MA_{0.95}PbI_3$ | $0.48(\pm0.02)$ | $0.187(\pm0.014)$ |
| $FA_{0.05}MA_{0.95}PbI_3$ | $0.54(\pm0.1)$ | $0.201(\pm0.012)$ |
| $GA_{0.05}MA_{0.95}PbI_3$ | - | - |
| $MAPbI_3$ | $0.40(\pm0.08)$ | $0.174(\pm0.010)$ |

dide diffusion therefore no activation energy could be calculated. The impedance data showed that either FA or $Cs^+$ substitution raised the $E_a$ of iodide diffusion. This follows a simialr trend to the μSR experiments where $Cs^+$ caused small increase in $E_a$ and FA caused a slightly larger shift. The overall $E_a$ for the EIS studies was just over double the value from μSR. It has been shown previously that different crystal sizes give different $E_a$ values so it is logical that a thin film would differ to powder sample.[17] It is also possible that the impedance study is measuring a combination of factors not just bulk iodide diffusion. As a full device is used there are activities occurring at the interface and also recombination factors as the process involves the generation of free carriers.

### 5.3.7 Computational Modelling

To compliment the experimental work, *ab initio* studies were performed by Dibya Ghosh to compare the activation energy results and investigate if there is a molecular explanation for the change to ion migration. The results of this modelling showed that when 20 % $Cs^+$ is substituted into the lattice the $E_a$ of increased from $0.44\,eV$ to $0.50\,eV$. The same trend is observed with the larger guanidinium cation but to a greater extent as the $E_a$ increased to $0.78\,eV$. The changes in $E_a$ also follow a similar trend to the μSR data where $Cs^+$ caused a small increase and GA caused a much larger change.

The *ab initio* results suggest a possible cause for the increased activation energy. When the differently sized cations are substituted into the perovskite lattice it caused disruption of the lattice structure. The distortion causes the

ion migration to take a more curved migration path out of the Pb/I plane. This distorted path causes the activation energy increase.

The diffusion coefficient of iodide diffusion was also modelled. The model demonstrated that for $Cs^+$ the $D_I$ was one order of magnitude larger and for GA it increased by five orders of magnitude. These modelling predictions agree well with the μSR and impedance data. The increase in diffusion is larger than that observed in the μSR experiment (Figure 5-16). This large change could be attributed to the fact that the *ab initio* study used 25% substitution of $Cs^+$. The very large change in $D_I$ for partial GA substituted perovskites gives an indication as to why no data from μSR can be observed in this sample. If the $D_I$ of MAPI is increased by five orders of magnitude it would be well outside of the observable diffusion rate range for μSR.

## 5.3.8   Muon Motion

It was shown in the Chapter 4 that the high temperature feature is not related to the cation, the final point to consider in the μSR experiments is whether it is the muon diffusing in an ionic environment or the ions diffusing around the muon. With the extra data from the mixed cation study it is possible to compare the results with other analogous muon studies on lithium ions, the impedance study carried out by Sam Pering and literature values for iodide migration activation energies to discount muon diffusion.

In previous muon studies on lithium performed by Sugiyama *et al.* a series of lithium transition metal oxides were studied.[22] In their work they looked at Li diffusion in $Li_xCoO_2$, $LiNiO_2$ and $LiCrO_2$ which are all structurally very similar. The cobalt and nickel based oxides both show diffusion of Li whereas the chromium sample does not. This is very similar to the experiment presented here where some of the samples show diffusion and the GA sample does not. pXRD showed that there was almost no structural change between the three samples studied here as was the case with the transition metal oxide studies.[22] In the lithium metal oxide studies muon diffusion was discounted due to the stability of muons around the $O_2^-$ sites up until high temperature. Based on the strength of the iodide muon interaction shown in Chapter 4 when compared to that of $O_2^-$

it is likely that the muons in this study are stable in their site up to 400 K. The activation energy results in this study were also similar to literature values and show the same trend with cation substitution as this study.[15] It is highly unlikely that the $E_a$ of muon diffusion, would match so well with literature values of iodide diffusion and also follow the same trend based on substitution.

## 5.4   Thermal Stability

The thermal stability of the perovskites was examined between room temperature and 450 K. The resulting TGA traces shown in Figure 5-18a shows that there was a mass loss of approximately 1.5 % and 1 % in the GA and FA perovskites respectively. This small mass loss occurred at around 100 °C and does not equate to any possible combination of by products being lost from the material. Small mass loses at 100 °C have been observed previously in MAPI and were attributed to water.[23] The previous literature observations and the inability to attribute the mass to anything in the perovskite make it likely that the small loss is residual water on the sample. This TGA data indicates that all three perovskites were stable beyond the temperature range used in the muon experiments.
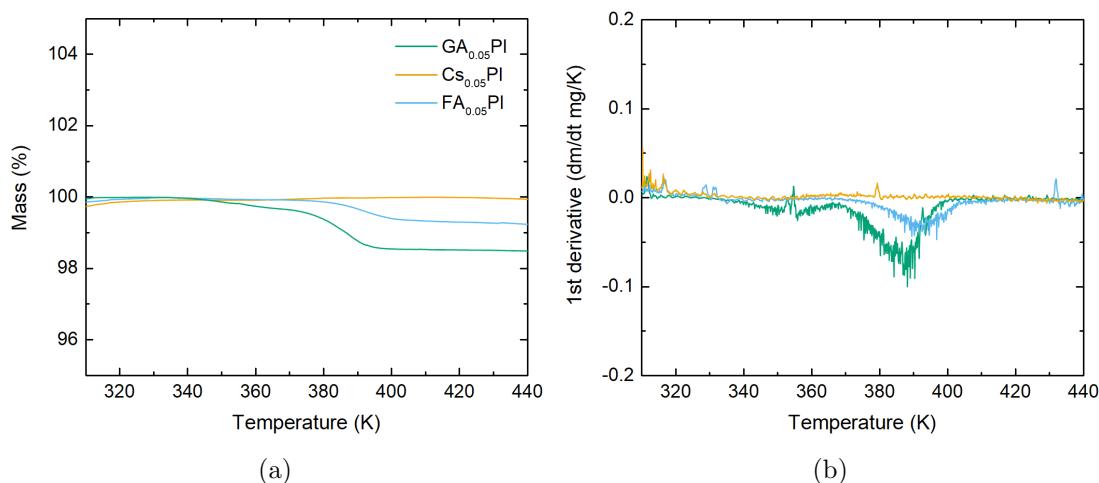
Figure 5-18: a) TGA of the three mixed cation perovskites between 300 and 450 K and b) the corresponding 1st derivative

## 5.5    Mixed Cation Devices

Full inverted architecture devices were fabricated to compare how the 5% substitution affects the performance and hysteresis. JV curves for the champion pixels are shown in Figure 5-20a. All three of the cells produced JV scans with some level of hysteresis. The average efficiency of the three cations compared with MAPI are shown in Figure 5-19a. The addition of just 5 mol% $Cs^+$ gave an average efficiency increase of almost 3%. As the $V_{OC}$ of the MAPI and CsMAPI were the same this increase was driven by a big increase in Fill Factor and a small increase in average $J_{SC}$ (Figure 5-19b,c and d).

Calculating the hysteresis index for the individual pixels showed that on average the $Cs^+$ substituted perovskites had the lowest hysteresis (Figure 5-20b). The FA and GA perovskites had similar average hysteresis to MAPI (Chapter 4). This difference in hysteresis was likely caused by differences in the device performance and not caused by any change in material properties as the average $Cs^+$ substituted device was better performing than the other three perovskite devices. As hysteresis has been linked to ion migration it would be expected that the substitution would cause a decrease in hysteresis as it decreases ion migration. Despite the increased barrier to ion migration, only devices using $Cs_{0.05}MA_{0.95}PbI_3$ showed decreased hysteresis. Several papers have shown that
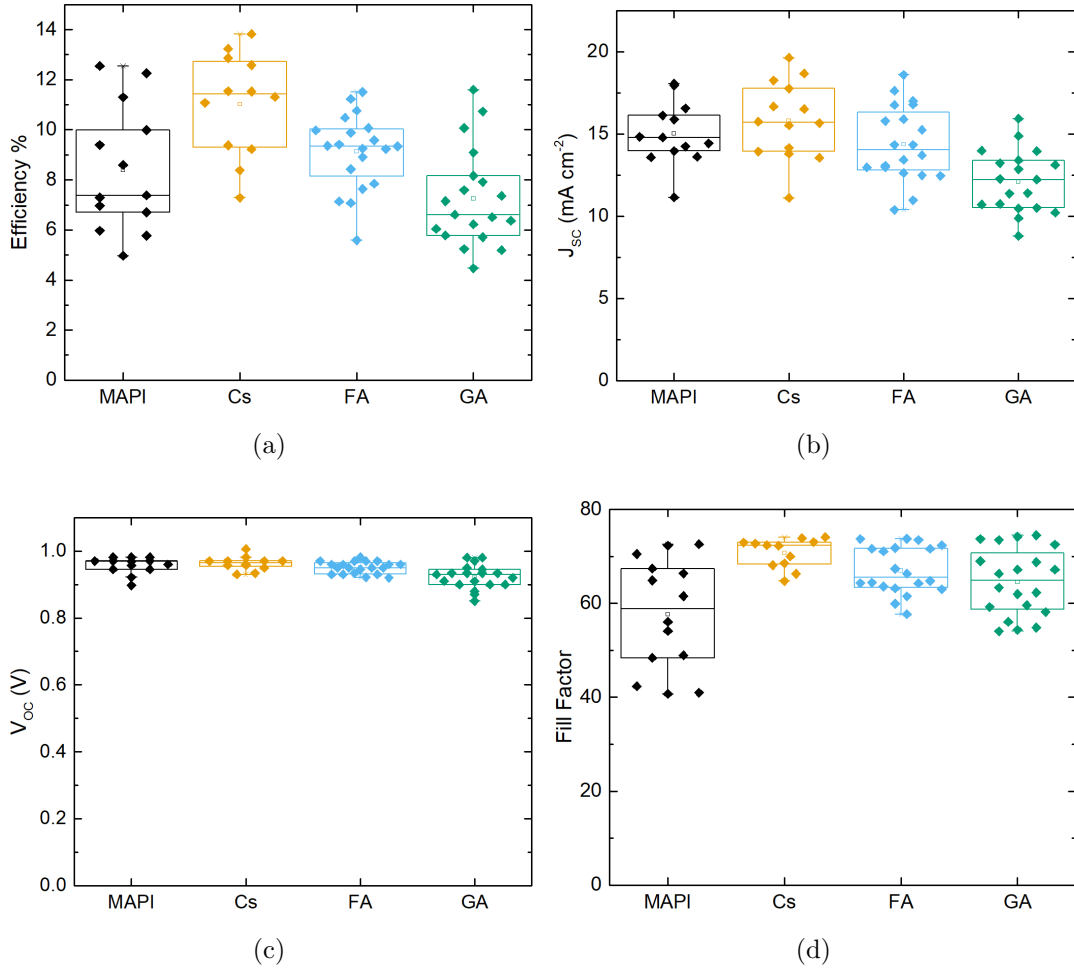
Figure 5-19: Box plots of a) %PCE, b) $J_{SC}$ c) $V_{OC}$ and d) Fill Factor for MAPI and the three mixed cation cells.

mixing FA and MA can decrease hysteresis but these papers involve substituting 40 mol% FA.[24] It is likely that the substitution is too small to observe any dramatic impact on device hysteresis.

The band gaps of the three different perovskites remained almost unchanged with only a few meV difference between them (Figure 5-21). This only minor change is unlikely to have been the cause of the improved device efficiency and hysteresis given that the best performing material had the slightly higher, therefore less optimal, $E_g$.

Atomic force microscopy (AFM) imaging of perovskite films on FTO/NiO$_x$ substrates showed minimal differences between the films (Figure 5-22). The average crystallite size of the three films was a few hundred microns as is often observed with anti-solvent deposition methods.[25] The films of FA$_{0.05}$ (Figure 5-
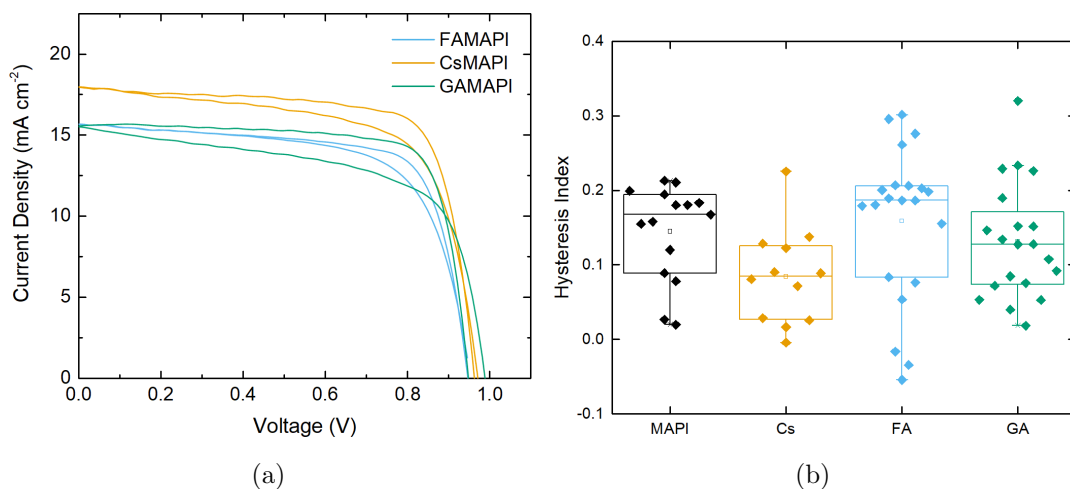
Figure 5-20: a) JV curves of the three mixed cation perovskites showing both the forwards and backwards scan and b) the range of hysteresis index values for devices made with the three mixed cation perovskites compared with MAPI.
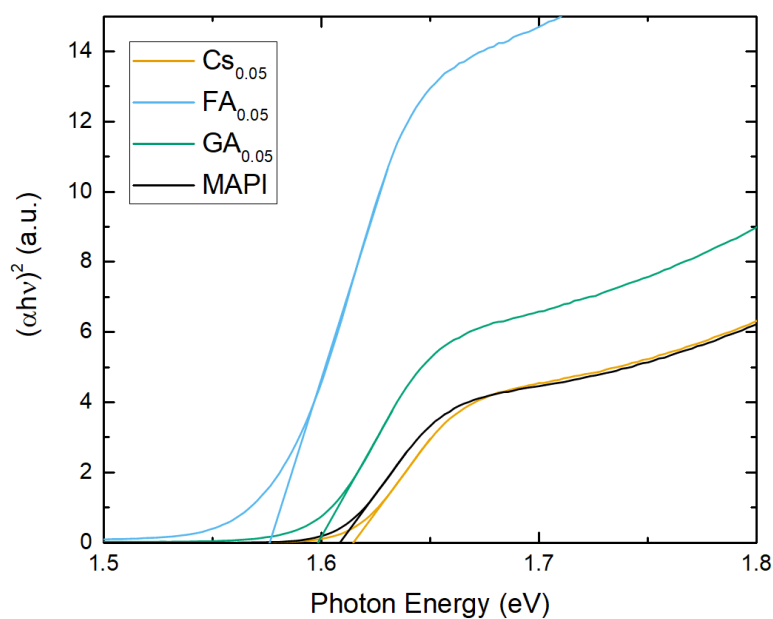


Figure 5-21: Calculated tauc plot data for $Cs_{0.5}MA_{0.95}PbI_3$, $FA_{0.5}MA_{0.95}PbI_3$ and $GA_{0.5}MA_{0.95}PbI_3$

22b) and $GA_{0.05}$ (Figure 5-22c) substituted perovskite contained more pinholes than $Cs_{0.05}$ (Figure 5-22a). This difference in film quality is the most likely cause for the improved performance of the $Cs^+$ substituted devices.
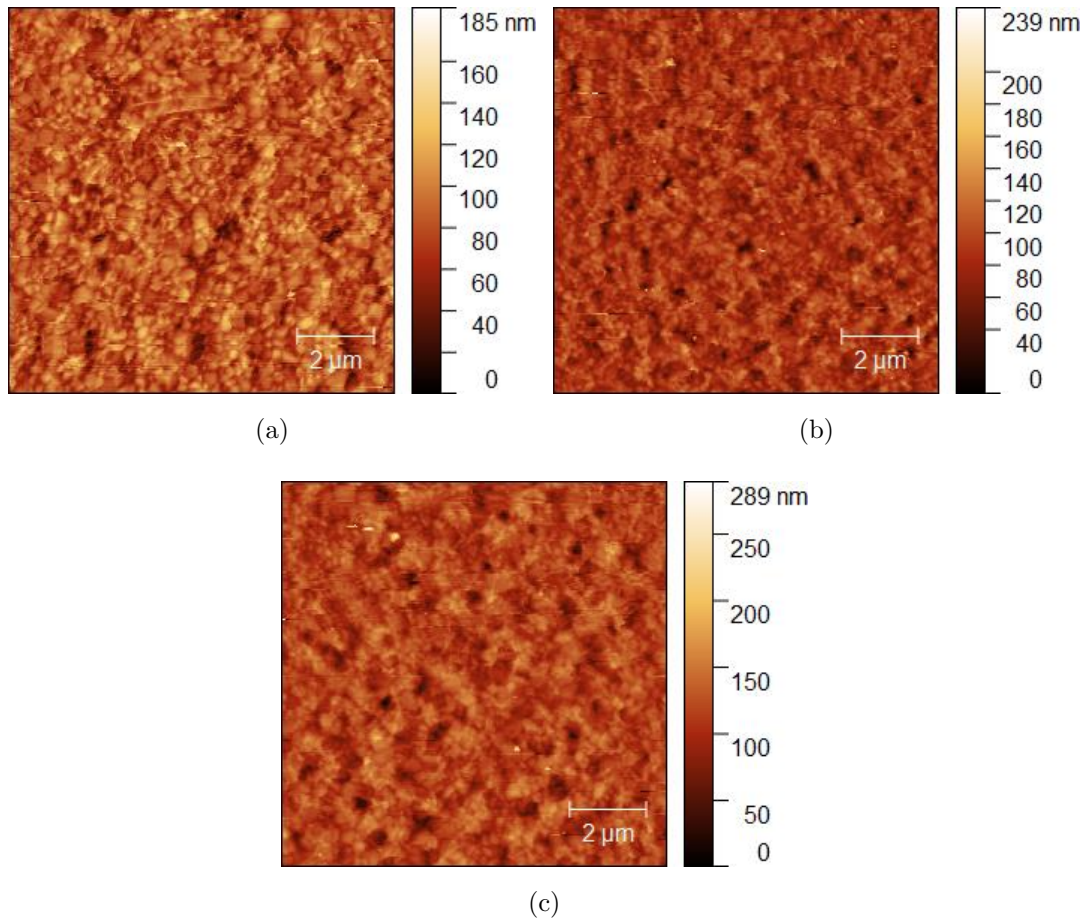
Figure 5-22: AFM images of films of a) $Cs_{0.5}MA_{0.95}PbI_3$, b) $FA_{0.5}MA_{0.95}PbI_3$ and c) $GA_{0.5}MA_{0.95}PbI_3$

## 5.6 Conclusions

This chapter sought to discover how small changes to the cation ratio of MAPI impacted the diffusion properties of iodide. The behaviour of implanted muons in perovskite samples was also investigated. First three different perovskite powders each with 5 % of MAPI changed to either formamidinium, guanidinium or cesium were synthesised and characterised by NMR and pXRD to confirm that the desired material was present. The three powders were subsequently studied using µSR and the same procedure as the previous chapters MAPI study to allow for easy comparison.

The results of the muon study showed that with all three perovskites just $5\,mol\%$ substitution caused the diffusion properties of the iodide in the material to change by varying amounts for the different cations. For $Cs^+$ the $E_a$ increased

slightly but the difference can not be confirmed to be statistically significant due to the error margins of the experiment. With FA substitution, the $E_a$ was increased slightly, whilst for GA the $E_a$ was unmeasurable as the diffusion had been altered so much that it was no longer detectable by μSR. These activation energy results were compared to impedance spectroscopy and a similar trend was observed.

The diffusion coefficients for iodide were calculated using the μSR fluctuation rate data. The results showed that the $D_I$ of the $Cs^+$ and FA substituted perovskites decreased slightly when compared to MAPI. A $D_I$ for the GA perovskite could not be calculated due to a lack of data from the μSR. These diffusion coefficients were compared with *ab initio* calculations. The *ab initio* results observed an order of magnitude decrease in $D_I$ for $Cs^+$ substitution and a five orders of magnitude decrease for GA substitution. The experimental results followed a similar trend and this large shift in diffusion is why the iodide diffusion in GA substituted perovskites was not observed. The likely cause of this shift in activation energy and diffusion was shown using the *ab initio* studies where distorting of the lattice and migration pathway when small amounts of cation substitution is present was observed.

The most important conclusion from this chapter is that the substitution of just 5 % guanidnium into the perovskite completely negated iodide diffusion in the measured temperature range. This kind of impact on ion migration from cation substitution has not previously been reported for perovskite solar cell materials.

# References

(1) L. K. Ono, E. J. Juarez-Perez and Y. Qi, *ACS Applied Materials and Interfaces*, 2017, **9**, 30197–30246.

(2) S. R. Pering, W. Deng, J. R. Troughton, P. S. Kubiak, D. Ghosh, R. G. Niemann, F. Brivio, F. E. Jeffrey, A. B. Walker, M. S. Islam, T. M. Watson, P. R. Raithby, A. L. Johnson, S. E. Lewis and P. J. Cameron, *J. Mater. Chem. A*, 2017, **5**, 20658–20665.

(3) G. Giorgi, J.-i. Fujisawa, H. Segawa and K. Yamashita, *The Journal of Physical Chemistry C*, 2015, **119**, 4694–4701.

(4) A. D. Jodlowski, C. Roldán-Carmona, G. Grancini, M. Salado, M. Ralaiarisoa, S. Ahmad, N. Koch, L. Camacho, G. De Miguel and M. K. Nazeeruddin, *Nature Energy*, 2017, **2**, 972–979.

(5) M. L. Petrus, J. Schlipf, C. Li, T. P. Gujar, N. Giesbrecht, P. Müller-Buschbaum, M. Thelakkat, T. Bein, S. Hüttner and P. Docampo, *Advanced Energy Materials*, 2017, **1700264**, 1–27.

(6) N. Pellet, P. Gao, G. Gregori, T. Y. Yang, M. K. Nazeeruddin, J. Maier and M. Graetzel, *Angewandte Chemie - International Edition*, 2014, **53**, 3151–3157.

(7) M. Saliba, T. Matsui, J.-Y. Seo, K. Domanski, J.-P. Correa-Baena, M. K. Nazeeruddin, S. M. Zakeeruddin, W. Tress, A. Abate, A. Hagfeldt, M. Grätzel, N. Mohammad K., S. M. Zakeeruddin, W. Tress, A. Abate, A. Hagfeldt and M. Grätzel, *Energy Environ. Sci.*, 2016, **9**, 1989–1997.

(8) M. Saliba, T. Matsui, K. Domanski, J.-Y. Seo, A. Ummadisingu, S. M. Zakeeruddin, J.-P. Correa-Baena, W. R. Tress, A. Abate, A. Hagfeldt and M. Gratzel, *Science*, 2016, **354**, 206–209.

(9) A. F. Akbulatov, L. A. Frolova, D. V. Anokhin, K. L. Gerasimov, N. N. Dremova and P. A. Troshin, *J. Mater. Chem. A*, 2016, **4**, 18378–18382.

(10) D. J. Kubicki, D. Prochowicz, A. Hofstetter, M. Saski, P. Yadav, D. Bi, N. Pellet, J. Lewiński, S. M. Zakeeruddin, M. Grätzel and L. Emsley, *Journal of the American Chemical Society*, 2018, **140**, 3345–3351.

(11) H. Choi, J. Jeong, H.-B. Kim, S. Kim, B. Walker, G.-H. Kim and J. Y. Kim, *Nano Energy*, 2014, **7**, 80–85.

(12) M. Grätzel, *Nature Materials*, 2014, **13**, 838–842.

(13) A. Binek, F. C. Hanusch, P. Docampo and T. Bein, *The Journal of Physical Chemistry Letters*, 2015, **6**, 1249–1253.

(14) A. Pockett, G. E. Eperon, N. Sakai, H. J. Snaith, L. M. Peter and P. J. Cameron, *Phys. Chem. Chem. Phys.*, 2017, **19**, 5959–5970.

(15) A. Senocrate, I. Moudrakovski, G. Y. Kim, T.-Y. Yang, G. Gregori, M. Grätzel and J. Maier, *Angewandte Chemie International Edition*, 2017, **56**, 7755–7759.

(16) J. M. Azpiroz, E. Mosconi, J. Bisquert and F. De Angelis, *Energy Environ. Sci.*, 2015, **8**, 2118–2127.

(17) J. Xing, Q. Wang, Q. Dong, Y. Yuan, Y. Fang and J. Huang, *Phys. Chem. Chem. Phys.*, 2016, **18**, 30484–30490.

(18) O. J. Weber, B. Charles and M. T. Weller, *J. Mater. Chem. A*, 2016, **4**, 15375–15382.

(19) S. J. Blundell, *Chemical Reviews*, 2004, **104**, 5717–5735.

(20) J. Sugiyama, K. Mukai, Y. Ikedo, H. Nozaki, M. Månsson and I. Watanabe, *Physical Review Letters*, 2009, **103**, 147601.

(21) M. Amores, T. E. Ashton, P. J. Baker, E. J. Cussen and S. A. Corr, *J. Mater. Chem. A*, 2016, **4**, 1729–1736.

(22) J. Sugiyama, K. Mukai, H. Nozaki, M. Harada, K. Kamazawa, Yutakaikedo, M. Månsson, O. Ofer, E. J. Ansaldo, J. H. Brewer, K. H. Chow, Isaowatanabe, Y. Miyake and T. Ohzuku, *Physics Procedia*, 2012, **30**, 105–108.

(23) A. Dualeh, P. Gao, S. I. Seok, M. K. Nazeeruddin and M. Grätzel, *Chemistry of Materials*, 2014, **26**, 6160–6164.

(24) Y. Yue, J. Liu, L. Han, X. Yang, W. Chen, A. Islam, Y. Wu and Y. Shirai, *Advanced Materials*, 2015, **27**, 4918–4923.

(25) M. Yin, F. Xie, H. Chen, X. Yang, F. Ye, E. Bi, Y. Wu, M. Cai and L. Han, *J. Mater. Chem. A*, 2016, **4**, 8548–8553.

# Chapter 6

# Ion Migration in Methylammonium Lead Bromide and Mixed Halide Perovskites

## 6.1 Introduction

Substitution at the X-site of MAPI can lead to increased stability, performance and the ability to tune the bandgap.[1–4] The most common form of X-site substitution in perovskite PV research is bromide substitution. The mixing of bromide at increasing concentrations can shift the band gap of the perovskite to higher energy and also increase the moisture stability.[1] Efficiencies of mixed iodide:bromide perovskites rose to 16 % by 2014.[5] More recently, mixing of anions produced some of the top efficiency devices that have enhanced stability and reduced hysteresis.[6,7]

There has been much less research into MAPbBr than into MAPI and mixed anion perovskties. The diffusion coefficient of bromide in pure MAPBr has been recently measured in single crystals as $1.8 \times 10^{-8}\,\mathrm{cm^2s^{-1}}$ using electrochemical impedance spectroscopy but this is the only study available.[8] The lack of research into MAPBr can be attributed to the fact that it does not have an ideal band gap for photovoltaic devices.[9] It has been shown that mixed halide perovskites present interesting photoluminescence properties due to re-ordering of a random array of bromide and iodide into an ordered structure via ion migration.[10,11] This process has only been observed under illumination and it is possible that bromide ions

only diffuse under illumination.[11] Due to the impact of ion migration on hysteresis and perovskite stability, it is important to understand how it changes when the halogen ratio in a system is changed.[12]

This chapter presents the first reported investigation of methylammonium lead bromide using muon spin relaxation. Also included, is an investigation into how the ion migration properties of two mixed anion perovskites, one containing a 50:50 mix of I:Br and the other a 83:17 mix, differ from those of the pure MAPI and MAPBr materials. Initially, the synthesis and characterisation results are presented, followed by the μSR data analysis. Finally, the results and their meaning are discussed.

## 6.2   Powder Characterisation

The three mixed anion powders used for this study were $MAPbBr_3$, $MAPb(I_{0.5}Br_{0.5})_3$ and $MAPb(I_{0.83}Br_{0.17})_3$. $MAPbBr_3$ was selected to investigate whether it was possible to observe bromide diffusion in perovskites using μSR. The two mixed anion powders were selected to probe the change to iodide diffusion caused by mixing with bromide. The powder with 17% bromide was chosen as, at the point of writing, that stoichiometry of anions was used to make the highest efficiency devices.[6] The choice of 50% mixing was hopefully to allow the diffusion of both anions to be observed in the material.

The powders were synthesied using the same hot casting method outlined previously (Section 4.2). Characterisation of the three powders was performed using pXRD and the resulting diffraction patterns are shown in Figure 6-1a. Methylammonium lead bromide (MAPBr), which was an orange powder, was a pure material with the same cubic structure that has been reported previously.[1,13] Importantly, there were no $PbBr_2$ peaks present in the pXRD pattern indicating the full conversion to $MAPbBr_3$.[14]

The mixed anion powders $MAPI_{0.5}Br_{0.5}$ and $MAPI_{0.83}Br_{0.17}$ were both black in appearance and produced the pXRD patterns shown in Figure 6-1. For both powders there was only one phase in the pXRD pattern. This was important as mixed anion powders have been shown to be prone to phase separation.[10,15]
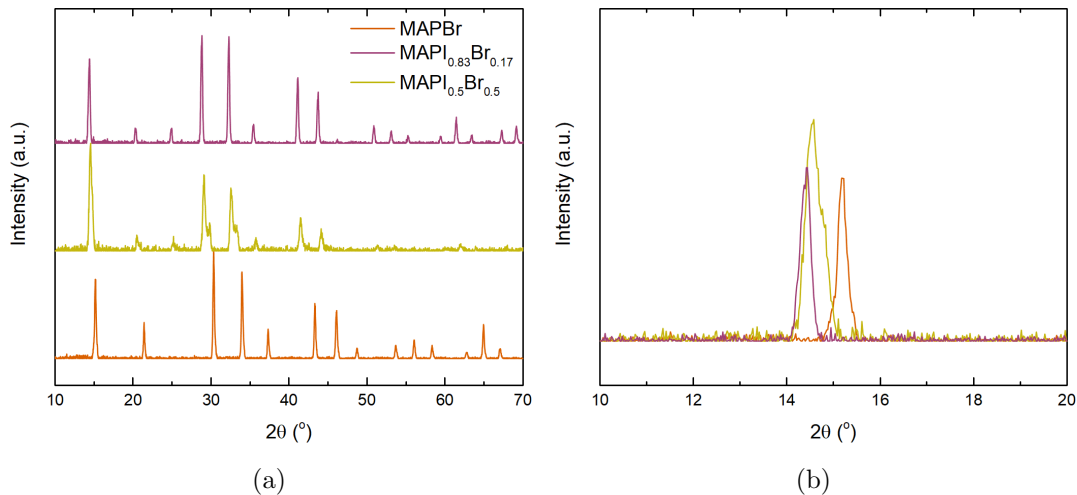
Figure 6-1: a) pXRD patterns of $MAPbBr_3$, $MAPb(I_{0.5}Br_{0.5})_3$ and $MAPb(I_{0.83}Br_{0.17})_3$ and b) the same diffraction patterns with the x-axis enhanced to show the 10 to 20 2θ range in more detail.

Importantly, there were no residual $PbBr_2$ peaks and no peak at $2\theta = 12°$ which is indicative of uncoverted $PbI_2$. Both of the pXRD patterns were shifted to lower angles indicating an expansion of the perovskite lattice with decreased bromide concentration, this is shown clearly for the peaks around 14° (Figure 6-1b). The results here match well with those previously observed by Noh *et al.* who showed the incremental shift of the 14° peak with decreasing concentration of bromide and how this increased the lattice parameters.[1] As there are very few simple ways to characterise the stoichiometry of mixed halide perovskites this shift in pXRD and lack of $PbI_2$ peak are the best indication that the desired perovskites had been formed.

## 6.3 µSR Study of Methyl Ammonium Lead Bromide

The three perovskite powders were studied at the ISIS pulsed muon facility using the HIFI instrument. Initially, the MAPBr powder was analysed to discover whether it was possible to detect bromide diffusion using µSR. As the previous methodology (Section 2-13) was successful in detecting iodide diffusion it was

replicated here. In brief, μSR measurements were taken over a temperature range between 50 and 400 K at varying intervals depending on the expected activity at the specific temperature range. Between 90 and 120 K measurements were taken every 5 K and between 330 and 400 K samples were taken every 10 K. At each temperature 4 individual measurements were taken at four different longitudinal fields 0, 5, 10 and 20 Gauss. Once all of the raw muon data had been acquired it was fitted using a dynamic Gaussian Kubo-Toyabe function multiplied by an exponential relaxation (Equation 4.1).
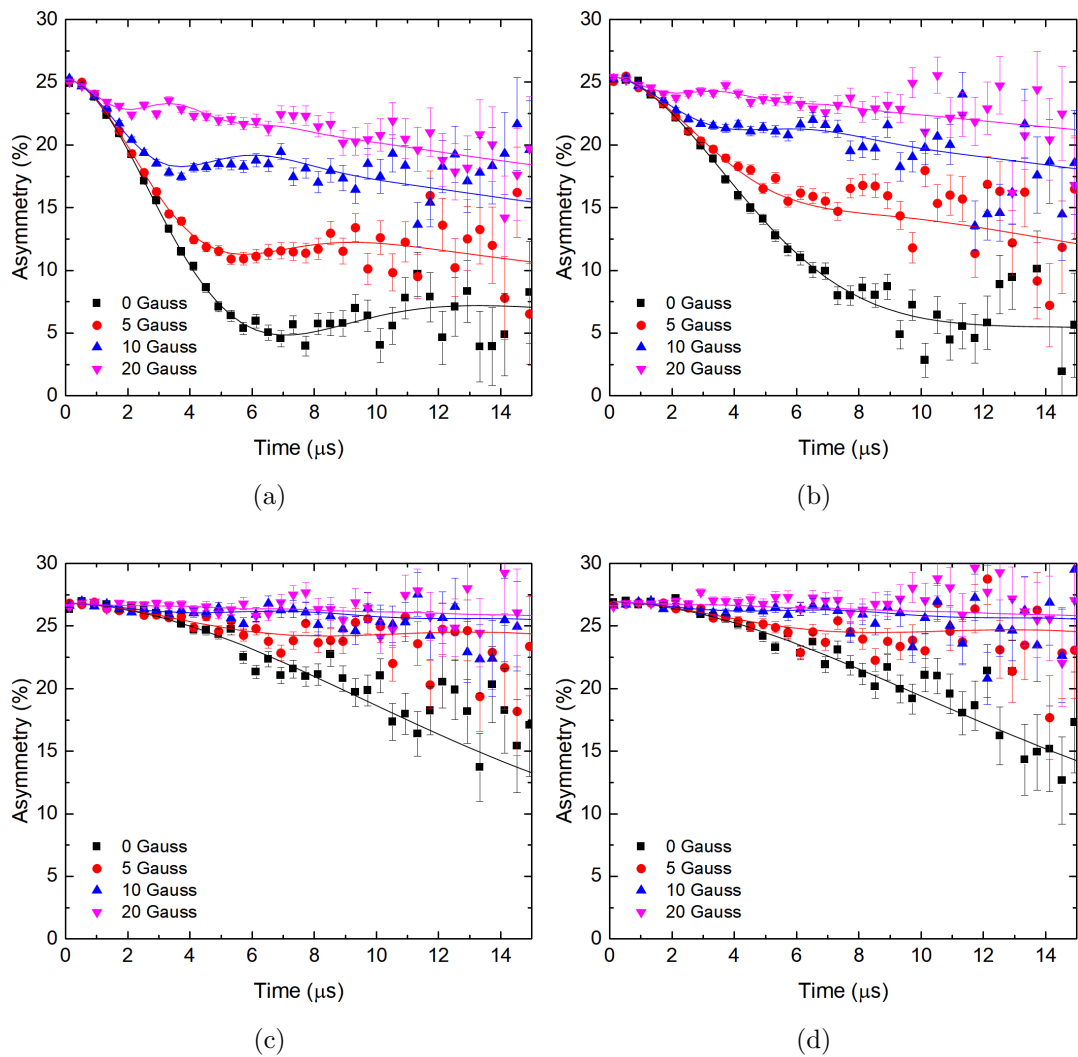


Figure 6-2: Raw muon data for MAPbBr$_3$ at a) 50 K, b) 110 K, c) 350 K and d) 400 K. Also shown are the results of fitting the data to a dynamic Kubo-Toyabe function multiplied by an exponential relaxation.

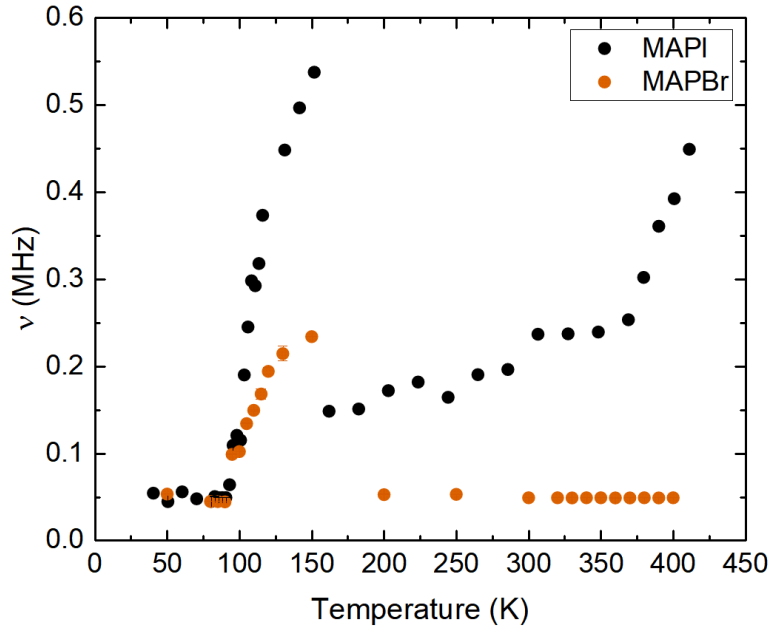An example of the resulting raw muon data with fits at temperatures of in-

Figure 6-3: The temperature dependence of $\nu$ for MAPI (red) and MAPBr (black)

terest is shown in Figure 6-2. Similar to MAPI, at 50 K (Figure 6-2a) the muon was experiencing a mostly static environment with a small amount of dynamic fluctuations depressing the 1/3 tail. Increasing the temperature to 110 K (Figure 6-2b) showed an increase in the dynamic component of the muon spectra with further loss of the tail and the minima increasing. When the temperature was further increased up to 350 K (Figure 6-2c) and up to 400 K (Figure 6-2d) the muon response was unchanged, this is different to MAPI where the dynamic fluctuations increased as the temperature increased up to 400 K.

The temperature dependence of fluctuation rate ($\nu$) for MAPBr is shown in Figure 6-3 along with the data for MAPI as comparison. At low temperature $\nu$ was unchanged until 100 K where there was small increase to 0.25 MHz. At 150 K the fluctuation rate decreased to 0.05 MHz where it remained unchanged until the end of the temperature range at 400 K. When comparing the response to MAPI there are some clear differences; at low temperature the fluctuation rate does not increase as much. After the intitial process the MAPBr$_3$ fluctuation rate also decreases to a lower level than MAPI. Finally, the biggest difference is at high temperature where MAPBr$_3$ shows no change in fluctuation rate whereas MAPI shows an increasing fluctuation rate.

The low temperature process in MAPBr$_3$ was thermally activated and an Ar-
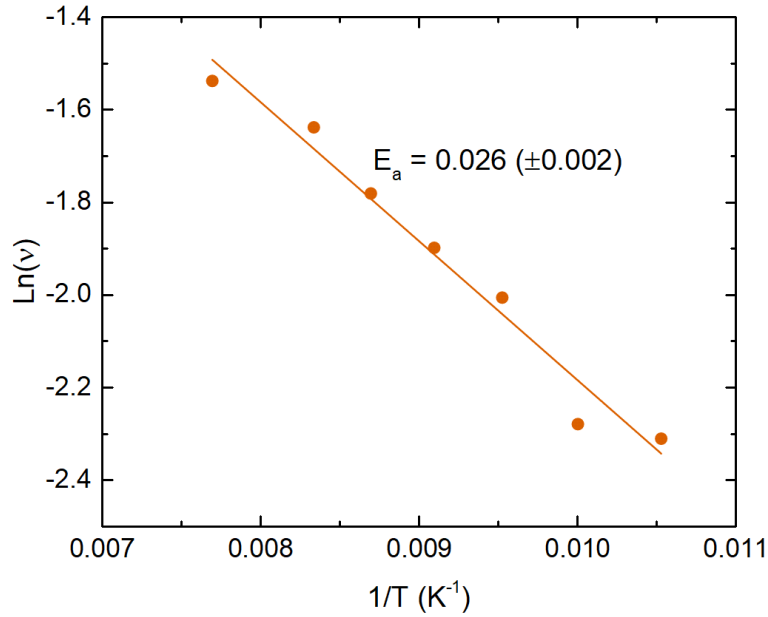
Figure 6-4: An Arrhenius plot of the low temperature process occurring in MAPBr$_3$

rhenius plot (Figure 6-4) produced an E$_a$ of 0.026 eV. This E$_a$ is a third of the value measured for MAPI (0.072 eV). The two different types of perovskite, bromide based and iodide based, do have different lattice parameters and therefore a different cage size for the cation to occupy. The size of the cage in the orthorhombic phase can be estimated from neutron diffraction data to be 261 Å$^3$ for MAPI and 211 Å$^3$ for MAPbBr$_3$.[16,17] Based on the simple size of the cation cage it would be expected that cation dynamics would be more difficult in MAPbBr$_3$. Computational modelling of cation migration in MAPI and MAPbBr$_3$ gave activation energies of 0.84 eV and 0.70 eV respectively.[18,19] These *ab initio* results show a small decrease in cation migration dynamics when changing the halogen from iodide to bromide. These results are not directly comparable to the experimental results presented here as they were modelled on perovskites in the cubic phase. They do however indicate that a lower cation activation energy for MAPbBr$_3$ compared to MAPI is not impossible.

A possible explanation for the lower activation energy is a difference in the hydrogen-halogen bonding interaction. Computational modelling of the interaction between the halide and protons on MA$^+$ has been carried out by El-Mellhoui *et al.*[20] In the modelling they showed that the hydrogen halogen interaction

strength increased from iodide to bromide to fluoride in the tetragonal phase. This would suggest that the activation energy should increase from MAPbBr$_3$ to MAPI but halide-halogen interactions could be different in the orthorhombic phase. It is possible that more complex interactions are occurring in the real MAPbBr$_3$ lattice. To make any definitive conclusions further studies into the low temperature interaction would need to be undertaken.

With the low temperature process once again being attributed to cation motion in the cage it is clear from the ν data that bromide diffusion was not observed using μSR in the temperature range selected in this experiment. There are four possible explanations for this; bromide as an ion is not observable, the diffusion is too fast, too slow or there is none. Bromide diffusion has been observed in CsPbBr$_3$ with an activation of 0.25 eV and also in MAPBr.[21] Perhaps surprisingly, given the prevalence of MAPI data there are no calculations or measurements of an $E_a$ for Br diffusion in MAPBr in the literature but the diffusion of bromide ions has been observed several times.[8,22] Given the activation energy for bromide diffusion in CsPbBr$_3$, and the fact that other studies have observed bromide diffusion, it is unlikely that it is not being observed in μSR because the ions are not mobile.

Given the window of observable diffusion rates in μSR, it is likely that bromide would appear in the window. The diffusion coefficients that are observable with muons are between approximately $10^{-13}$ cm$^2$s$^{-1}$ and $10^{-8}$ cm$^2$s$^{-1}$.[23] The only diffusion coefficient currently published for bromide in MAPBr is $1.8 \times 10^{-8}$ cm$^2$s$^{-1}$, this was measured using electrochemical impedance spectroscopy in the dark on a single crystal with an applied voltage.[8] This value is just inside the range of measurable rates using muons. With MAPI the activation energy varies depending on film synthesis conditions and crystallite size and this is likely mirrored in diffusion coefficient so it is hard to compare different measurement techniques.[24] This spread of diffusion coefficients is also likely to be seen in MAPBr meaning that it is very possible that the diffusion coefficient is outside of the measurable range.

The properties of bromide indicate that it should be possible to observe bromide diffusion using μSR. The properties of the nucleus compared with that of

Table 6.1: Spin and magnetic moment information for nuclei whose diffusion have been detected by μSR and bromine. All of this data was taken from the table of nuclear moments by N.J. Stone.[25]

| Nucleus | Spin | Nuclear Magnetic Moment ($\mu_N$) |
|---|---|---|
| $^{127}$I | 5/2 | +2.81 |
| $^{7}$Li | 3/2 | +3.26 |
| $^{23}$Na | 3/2 | +2.22 |
| $^{79}$Br | 3/2 | +2.12 |
| $^{81}$Br | 3/2 | +2.27 |

lithium, iodide and sodium are shown in Table 6.1. There are two prevalent isotopes of bromine so both have been included but their characteristics only differ slightly. It is clear from the table that the basic properties of a bromide anion make it amenable to detection using μSR. The spin is the same as that of sodium and lithium with a nuclear moment almost identical to sodium. These similarities make it plausible that diffusion of bromide could be detected using μSR but the data for MAPBr clearly shows that it is not.

Based on the previously outlined explanations for why bromide diffusion is not being detected, the most likely one is that the rate is to fast or slow to be detected, most likely fast. With only one comparable result currently published it is hard to say unequivocally that bromide diffusion rates would fall into the detectable range for μSR, whereas the other two theories can be more easily eliminated as possibilities based on current data. A higher temperature range could have been explored to see if bromide diffusion appeared, which would have indicated that it was too slow, but due to time constraints with the experiment and the risk of sample degradation this wasn't possible.

The local field data that was generated from the muon data fitting is shown in Figure 6-5 along with a comparison to MAPI. The change in local field with respect to temperature for MAPBr$_3$ follows a similar trend to MAPI. The local field started at 0.26 MHz then decreased to 0.06 MHz over the temperature range. This change in local field is attributed to motional narrowing due to the increasingly dynamic muon environment as the temperature is increased causing
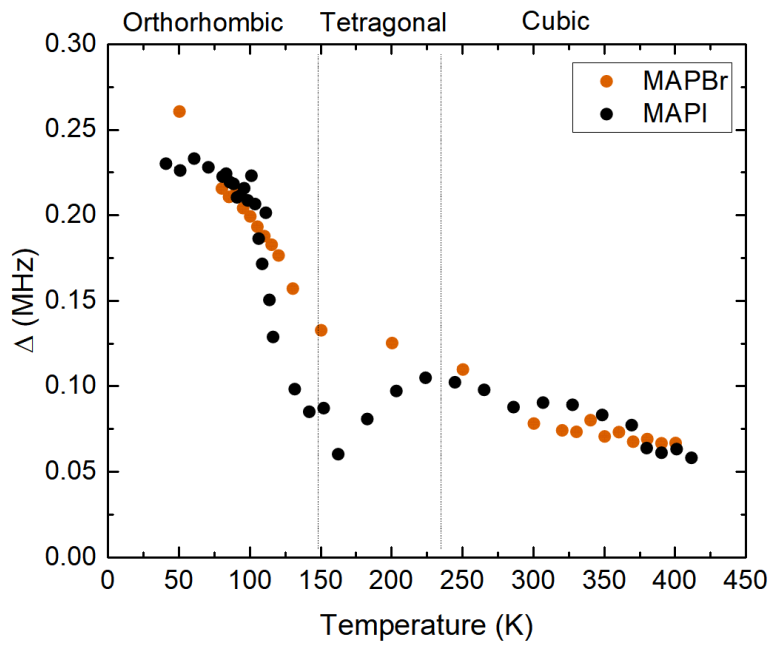
Figure 6-5: The change in $\Delta$ with temperature for MAPI and MAPBr. The dashed lines represent the two phase transitions that occur in MAPBr$_3$. The MAPI phase transitions occur at $160\,\mathrm{K}$ and $325\,\mathrm{K}$.

a narrowing of the field being observed by the muon.

## 6.4   μSR of Mixed Anion Perovskites

Despite not being able to detect bromide diffusion, the impact of halogen mixing on iodide diffusion was subsequently investigated. To do this two different mixed anion perovskites were studied, one with a 50:50 mix of I:Br and one with an 83:17 I:Br mix. The range of temperatures investigated here was limited to just the high temperature region between 250 and 400 K due to experimental time constraints.

During the experiment there were several problems with the magnets that were used to apply the longitudinal field (LF) to the sample. For the $MAPb(Br_{50}I_{50})_3$ experiment all of the magnetic fields were shifted by $-2.5$ G. This shift made the fields for 0 and 5 G appear to be the same. The 10 and 20 G fields were shifted to become 7.5 and 17.5 G respectively. With the $MAPb(Br_{17}I_{83})_3$ experiment, the 0 and 5 G fields were the same as the previous sample. In addition to the 2.5 G shift, the magnet providing the 10 G field was not functioning correctly and was actually providing a field of 17.5 G. This field ended up being the same as the 20 G field measurements which were shifted to 17.5 G by the previously mentioned problem with the magnet. These shifts in the LF fields were accounted for in the data fitting and are clearly visible in the raw data for both of the sample (Figure 6-7 and 6-6). The issue with the magnetic fields limited the amount of usable data collected for each sample. Having less data lead to slightly less reliable data fits but the overall results were not greatly affected.

As with previous studies a Gaussian dynamic Kubo-Toyabe function multiplied by an exponential relaxation was used to fit the data and two examples of raw data with fits for MAPBr50 is shown in Figure 6-6. The raw data remained almost unchanged between 350 K (Figure 6-6a) and 400 K (Figure 6-6b). This differs greatly from the previous μSR studies of MAPI where the muon response changes dramatically at higher temperatures.

Figure 6-7 shows the resulting raw muon data and fits for $MAPb(Br_{17}I_83)_3$ at two different temperatures. The first temperature shown is 350 K (Figure 6-7a) and the issue with the magnetic fields is quite apparent as there are two sets of identical raw data. As with the previous two mixed halide samples there is very minimal change between the 350 and 400 K raw data.
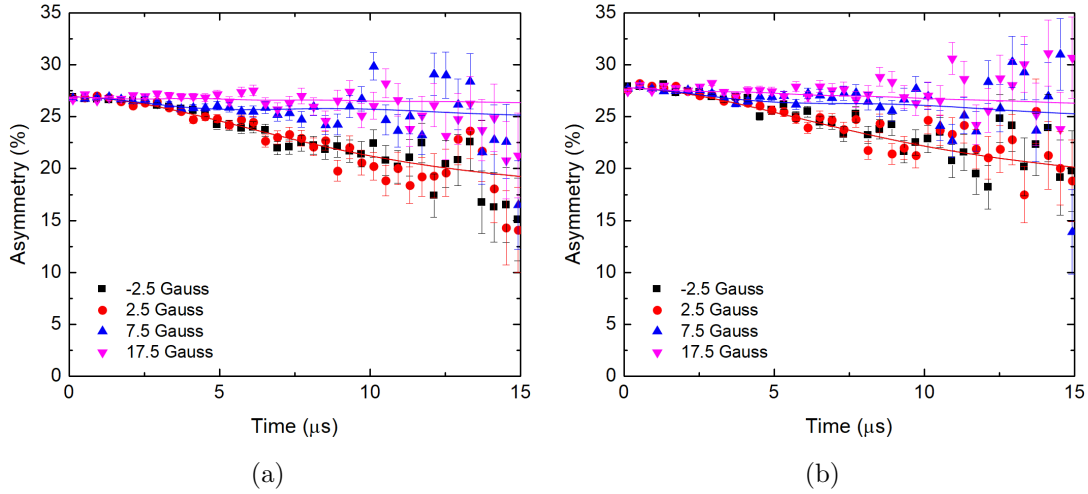
Figure 6-6: Raw muon data for MAPb(Br$_{50}$I$_{50}$)$_3$ at a) 350 K and b) 400 K. Also shown are the results of fitting the data to a dynamic Gaussian Kubo-Toyabe function with an exponential relaxation function.



Figure 6-7: Raw muon data for MAPb(Br$_{17}$I$_{83}$)$_3$ at a) 350 K and b) 400 K. Also shown are the results of fitting the data to a dynamic Gaussian Kubo-Toyabe function with an exponential relaxation function.
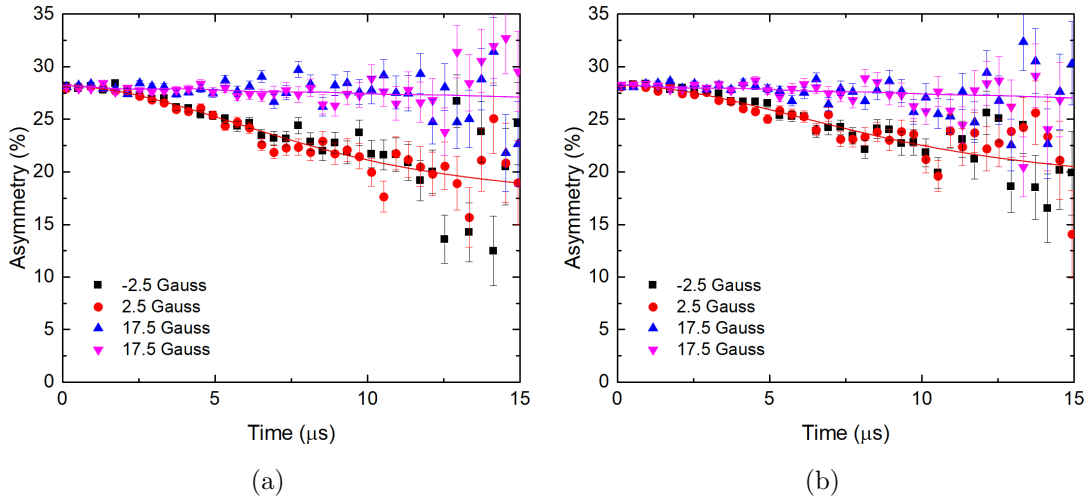
Once all of the raw muon data had been fitted the resulting changes in local field and dynamic fluctuation rates were compared with MAPBr and MAPI samples. Figure 6-8a shows the fluctuation rate changes for the two mixed anion perovskites with both showing a similar trend. Neither of the two mixed anion perovskites showed a thermally activated change in dynamic fluctuation rate between 250 and 400 K. The lack of response is the same as MAPBr$_3$ and
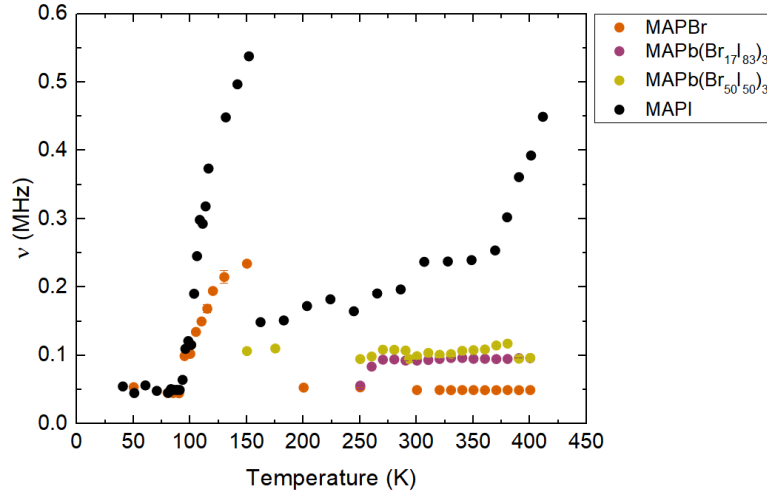
161

Figure 6-8: The change in $\nu$ with temperature for MAPBr, MAP$(I_{0.5}Br_{0.5})_3$ and MAP$(I_{0.83}Br_{0.17})_3$. b) The same data with MAPI included for comparison

significantly different to MAPI.

How the local field changed with respect to temperature for the two mixed anion perovskites is shown in Figure 6-9 along with MAPBr and MAPI for comparison. As the temperature increased $\Delta$ for both 50:50 and 83:17 I:Br perovskites decreased slightly. When the data is compared with MAPI and MAPBr$_3$ (Figure 6-9 it is clear that the there is no difference in the local fields of MAPI and the bromide based perovskites.

The muon results for the two mixed anion materials do not show any sign of a high temperature process occurring. This is surprising as, especially with the 83:17 mixture, there is a significant amount of iodide present in the material which has been previously shown to diffuse and be detectable by μSR. Based on the μSR results, it appears that the mixing of bromide and iodide restricts iodide diffusion in the perovskite.

When it comes to literature there is very little with respect to ion migration in bromide based perovskites and even less for mixed systems. Hoke *et al.* observed a photoactivated process of phase segregation that had an $E_a$ of $0.27\,\text{eV}$ in a mixed perovskite that was 40 % bromide.[10] They attributed this phenomena to reordering of the halide ions into iodide rich and bromide rich regions. It was also observed that the perovskite returns to disorder when left in the dark. As the μSR experiments were performed in the dark it is unlikely that this photoactive
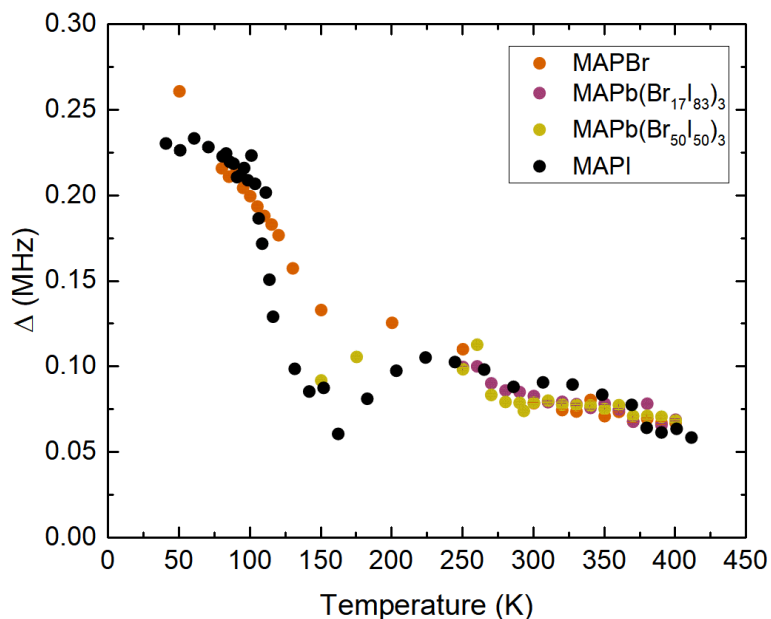
Figure 6-9: The change in $\Delta$ with temperature for MAPBr (Black), $MAP(I_{0.5}Br_{0.5})_3$, $MAP(I_{0.83}Br_{0.17})_3$ and MAPI

behaviour would be observed. Recent first principles calculations have shown that ion migration is greatly restricted by half mixing bromide and iodide.[26] It was also theorised that the cause of this decrease in migration is due to shortening of the Pb-I bond making it stronger thus inhibiting ion movement. These results agree strongly with what was observed here for 50-50 halide mixing. It is plausible that the same effect is the cause of ion migration loss in the 17 % Br perovskite.

To deduce how much of an impact the bromide is having further μSR studies with lower concentrations of bromide should be performed to see if there is a cut off point where diffusion ceases to occur or if it is a more gradual process. The diffusion properties could also be investigated using electrochemical impedance spectroscopy as well as computational modelling as was performed in the previous chapter.

## 6.5 Conclusions

In this chapter ion diffusion in methylammonium lead bromide and two mixed anion perovskites $MAPb(I_{0.5}Br_{0.5})_3$ and $MAPb(I_{0.83}Br_{0.17})_3$ was investigated. The three powders were initially synthesised and characterised using pXRD before being studied using μSR. The μSR study of the full bromide perovskite showed that detection of bromide diffusion was not possible between 40 and 400 K. The most likely reason for not observing bromide diffusion was that the rate of diffusion for bromide falls outside the measurable range for muons. There is no conclusive evidence for this conclusion but it is the most compatible with the current knowledge of μSR and of bromide diffusion in perovskites. The low temperature process was still present in $MAPBr_3$ and had an $E_a$ of 0.026 eV which was three times smaller than that of MAPI.

Next, two mixed anion perovskites were investigated to probe whether the bromide was having an impact on the diffusion rate of the iodide. This time, no iodide or bromide diffusion was observed between 250 and 400 K. As iodide diffusion had previously been observed it was clear that the mixing of anions was having an impact on the rate of diffusion for iodide. This altering of rate was likely caused by a changing of the lattice making the perovskite more rigid therefore increasing the activation energy for diffusion. In the future comparison with experimental and *in silico* techniques would help to elucidate the exact reason for the change in diffusion properties.

# References

(1) J. H. Noh, S. H. Im, J. H. Heo, T. N. Mandal and S. I. Seok, *Nano Letters*, 2013, **13**, 1764–1769.

(2) D. Luo, L. Yu, H. Wang, T. Zou, L. Luo, Z. Liu and Z. Lu, *RSC Adv.*, 2015, **5**, 85480–85485.

(3) S. Nagane, U. Bansode, O. Game, S. Chhatre and S. Ogale, *Chemical Communications*, 2014, **50**, 9741–9744.

(4) Y.-H. Chiang, M.-H. Li, H.-M. Cheng, P.-S. Shen and P. Chen, *ACS Applied Materials & Interfaces*, 2017, **9**, 2403–2409.

(5) N. J. Jeon, J. H. Noh, Y. C. Kim, W. S. Yang, S. Ryu and S. I. Seok, *Nature materials*, 2014, **13**, 1–7.

(6) M. Saliba, T. Matsui, J.-Y. Seo, K. Domanski, J.-P. Correa-Baena, M. K. Nazeeruddin, S. M. Zakeeruddin, W. Tress, A. Abate, A. Hagfeldt, M. Grätzel, N. Mohammad K., S. M. Zakeeruddin, W. Tress, A. Abate, A. Hagfeldt and M. Grätzel, *Energy Environ. Sci.*, 2016, **9**, 1989–1997.

(7) W. S. Yang, B.-W. Park, E. H. Jung, N. J. Jeon, Y. C. Kim, D. U. Lee, S. S. Shin, J. Seo, E. K. Kim, J. H. Noh and S. I. Seok, *Science*, 2017, **356**, 1376–1379.

(8) W. Peng, C. Aranda, O. M. Bakr, G. Garcia-Belmonte, J. Bisquert and A. Guerrero, *ACS Energy Letters*, 2018, **3**, 1477–1481.

(9) R. G. Niemann, A. G. Kontos, D. Palles, E. I. Kamitsos, A. Kaltzoglou, F. Brivio, P. Falaras and P. J. Cameron, *The Journal of Physical Chemistry C*, 2016, **120**, 2509–2519.

(10) E. T. Hoke, D. J. Slotcavage, E. R. Dohner, A. R. Bowring, H. I. Karunadasa and M. D. McGehee, *Chemical Science*, 2015, **6**, 613–617.

(11) R. K. Misra, L. Ciammaruchi, S. Aharon, D. Mogilyansky, L. Etgar, I. Visoly-Fisher and E. A. Katz, *ChemSusChem*, 2016, **9**, 2572–2577.

(12) P. Calado, A. M. Telford, D. Bryant, X. Li, J. Nelson, B. C. O'Regan and P. R. Barnes, *Nature Communications*, 2016, **7**, 13831.

(13)  A. Kojima, K. Teshima, Y. Shirai and T. Miyasaka, *Journal of the American Chemical Society*, 2009, **131**, 6050–1.

(14)  R. Sheng, A. Ho-Baillie, S. Huang, S. Chen, X. Wen, X. Hao and M. A. Green, *Journal of Physical Chemistry C*, 2015, **119**, 3545–3549.

(15)  M. C. Brennan, S. Draguta, P. V. Kamat and M. Kuno, *ACS Energy Letters*, 2018, **3**, 204–213.

(16)  M. T. Weller, O. J. Weber, P. F. Henry, A. M. Di Pumpo and T. C. Hansen, *Chem. Commun.*, 2015, **51**, 4180–4183.

(17)  I. P. Swainson, R. P. Hammond, C. Soullière, O. Knop and W. Massa, *Journal of Solid State Chemistry*, 2003, **176**, 97–104.

(18)  C. Eames, J. M. Frost, P. R. F. Barnes, B. C. O'Regan, A. Walsh and M. S. Islam, *Nature Communications*, 2015, **6**, 7497.

(19)  A. Oranskaia, J. Yin, O. M. Bakr, J. L. Brédas and O. F. Mohammed, *Journal of Physical Chemistry Letters*, 2018, **9**, 5474–5480.

(20)  F. El-Mellouhi, A. Marzouk, E. T. Bentria, S. N. Rashkeev, S. Kais and F. H. Alharbi, *ChemSusChem*, 2016, **9**, 2648–2655.

(21)  J. Mizusaki, K. Arai and K. Fueki, *Solid State Ionics*, 1983, **11**, 203–211.

(22)  M. C. Kim, B. J. Kim, D. Y. Son, N. G. Park, H. S. Jung and M. Choi, *Nano Letters*, 2016, **16**, 5756–5763.

(23)  M. Månsson and J. Sugiyama, *Physica Scripta*, 2013, **88**, 068509.

(24)  J. Xing, Q. Wang, Q. Dong, Y. Yuan, Y. Fang and J. Huang, *Phys. Chem. Chem. Phys.*, 2016, **18**, 30484–30490.

(25)  N. Stone, *Atomic Data and Nuclear Data Tables*, 2005, **90**, 75–176.

(26)  C. Lin, S. Li, W. Zhang, C. Shao and Z. Yang, *ACS Applied Energy Materials*, 2018, **1**, 1374–1380.

# Chapter 7

# Ion Migration in Reduced Dimensionality Perovskites

## 7.1 Introduction

Over the last few years, the range of cations that have been used to fabricate perovskite solar cells has increased from a handful of small molecules to include larger and more varied organic cations.[1–4] This includes several larger cations that do not lead to a traditional 3D perovskite structure, instead they form 2D Ruddlesden-Popper perovskite films.[5] Substituting 100 % of the A-site with larger cations leads to formation of a material with 2D sheets of $PbI_6$ octahedra with the larger cations separating these sheets.[6] 2D perovskites are a lot more stable but, due to poor charge transfer, have substantially lower device efficiency than their 3D counterparts.[7] It is possible, by mixing the 2D and 3D perovskite together, to improve the efficiency of cells while still retaining some of the improved stability, these are known as 2D/3D hybrid perovskites.[8]

A few of the most common larger A-site cations are shown in Figure 7-1. Amongst long alkyl chain cations, the most common is butylammonium (BA) (Figure 7-1a).[9] Substitution of up to 9 % BA can produce cells that retain the efficiency of unsubstituted MAPI while retaining 80 % of their efficiency for over 3000 hours.[10] Phenylethylammonium (PEA) has also been used to make 2D/3D hybrids, with a stabilised efficiency of 15 % over 1000 hours (Figure 7-1b).[3,11] The most recent success in 2D/3D hybrids was using 5-aminovaleric acid (AVA)
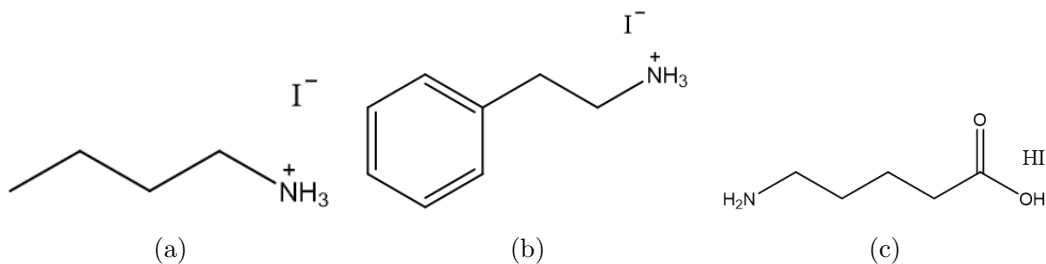
Figure 7-1: Three of the more common cations used to fabricate 2D/3D hybrid perovskites, a) Butylammonium iodide, b) Phenylethylammonium iodide and c) 5-aminovaleric acid hydroiodide.

(Figure 7-1c). Substitution of 5% AVA into the perovskite and the addition of carbon contacts has produced cells that have been stable for 10000 hours.[4,12,13]

Vertically aligning the lead iodide octahedra to overcome poor charge transfer in 2D/3D hybrid perovskites has recently become a method to improve stability with minimal performance loss. This method was first used by Tsai *et al.* when they deposited the 2D/3D hybrid perovskites at 150 °C creating a vertically aligned 2D/3D perovskite.[14] Since this discovery a few other methods using additives or precursor solvent engineering have been studied.[15–17] The use of 2D/3D hybrid perovskites in devices has led to important advances in long term stability. A full understanding of their properties would help to further tune devices leading to further performance advances.

In this chapter cells made with PEA substituted perovskites were investigated using electrochemical impedance spectroscopy (EIS). The results of this study were then compared to the impedance measurements on cells made with another 2D/3D hybrid perovskite made using propylammonium (PrA) iodide. Impedance was used to investigate how different cation substitution and size impact ion migration in the perovskite material. Finally, two new novel fluorinated organic cations were investigated with the goal of making the perovskite more hydrophobic and therefore improving stability.

## 7.2 The Impact of Phenylethylammonium on Ion Migration

### 7.2.1 PEAPI Synthesis and Characterisation

PEA (Figure 7-1b) has previously been shown to create 2D/3D hybrid perovskites and is an affordable, easy to synthesise A-site cation. PEA was therefore selected for this investigation into the properties of 2D/3D hybrids. First the organic cation was synthesised from the amine precursor using the method outlined in Section 3.4. The cation was then substituted at various mol% into the 3D perovskite by mixing two precursor solutions of 100% MAPI and 100% phenylethylammonium lead iodide (PEAPI) in the desired concentrations. Thin films were then fabricated on both FTO and microscope glass slides for XRD and UV/Vis respectively.
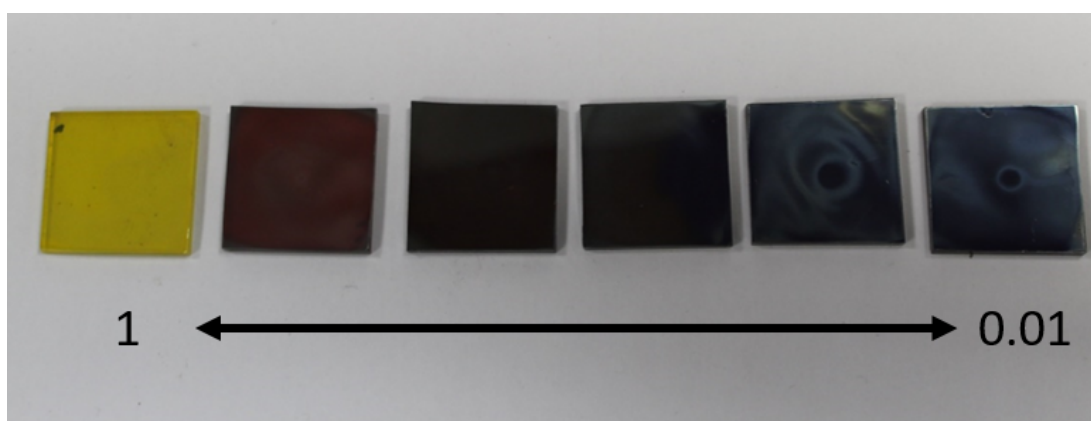


Figure 7-2: A photo of films with varying concentrations of PEA cation with 100 mol% PEA on the left down to 1 mol% PEA on the right

The colour of the resulting films is shown in Figure 7-2 with the colour changing from a bright yellow at 100% PEA, to a black film at 1 mol%. These colours are reflected in the change in the band gap (Figure 7-3a-d) as the onset of the ($E_g$) shifts from approximately 1.6 nm to 2.3 nm with composition. The band gaps were from Tauc plots presented in Figure 7-3.

The band gaps for concentrations between 0 and 10 % PEA substitution were between 1.61 and 1.63 eV, with small variations attributed to errors in the extrapolation process. The Tauc plot for 25 % PEA shows two possible band gaps,

one at 1.775 eV and one at 1.83 eV (Figure 7-3b). The same double band gap was observed for 50% PEAPI (Figure 7-3c) at 1.98 and 2.12 eV. Finally, the $E_g$ for 100 % PEAPI was calculated to be 2.3 eV which is what has been previously observed (Figure 7-3C).[3] The UV-Vis response of 25% and 50% PEAPI contained several absorbtions at different wavelengths. Multiple band gaps are caused by the material being formed from 2D/3D hybrids with varying n values, where n is the number of layers of PbI octahedra in between space layers, as was previously observed by Smith *et al.*[11] These varying n value materials produce multiple band gaps in the perovskite.
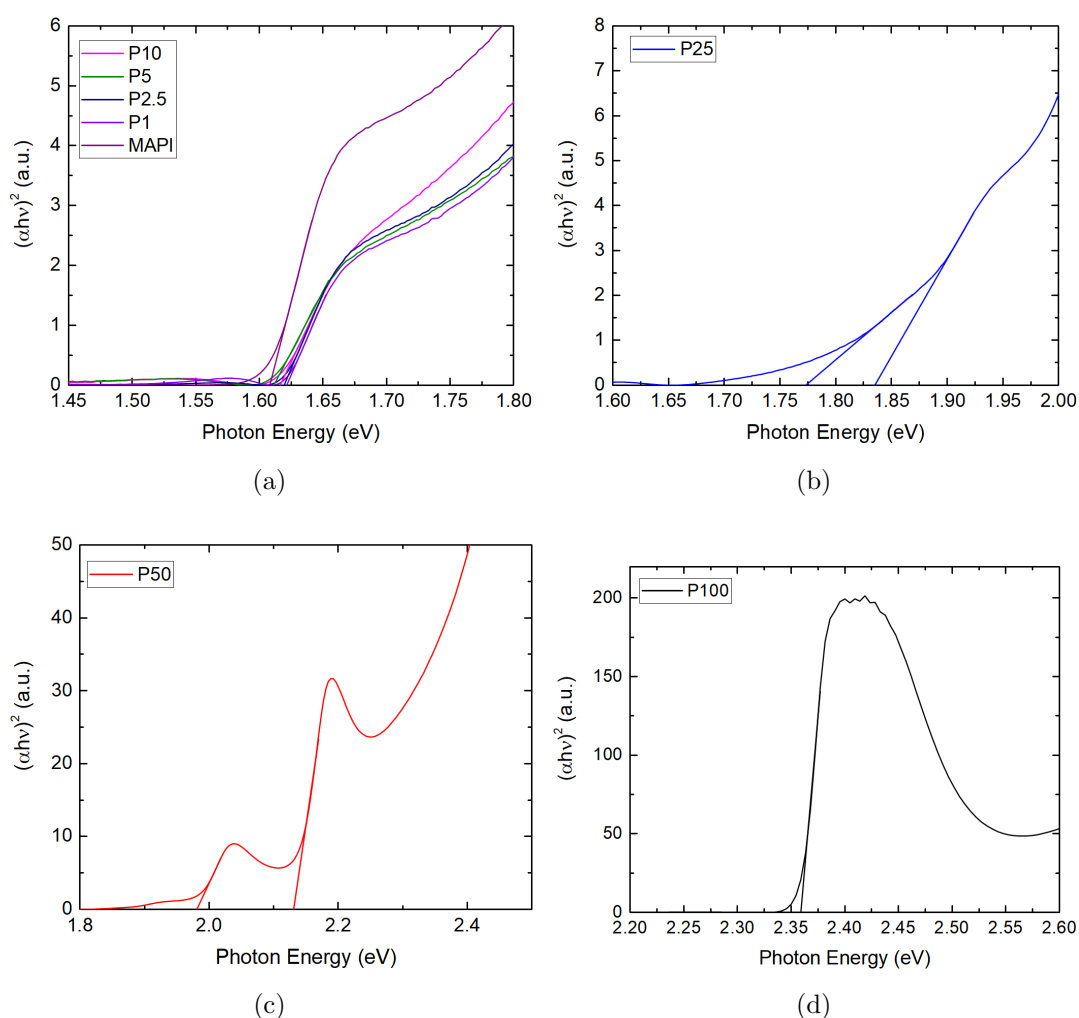


Figure 7-3: Tauc plots of a) 0 to 10-PEAPI b) 25-PEAPI c) 50-PEAPI and d) 100-PEAPI

Structural characterisation was performed on the materials using pXRD and the resulting patterns are shown in Figure 7-4. The pattern for 100 % PEAPI

(Figure 7-4a) contained a low angle peak at 6° that corresponds to the (002) plane that dissects the $PbI_6$ octahedra sheets and is indicative of a 2D perovskite.[3,18] The other labelled peaks present correspond to the (00l) plane, the lack of any other perovskite planes shows that the crystal growth was preferentially along the (110) plane and parallel to the substrate. There was also a substantial lead iodide peak (13°) showing that full conversion to perovskite was not achieved.
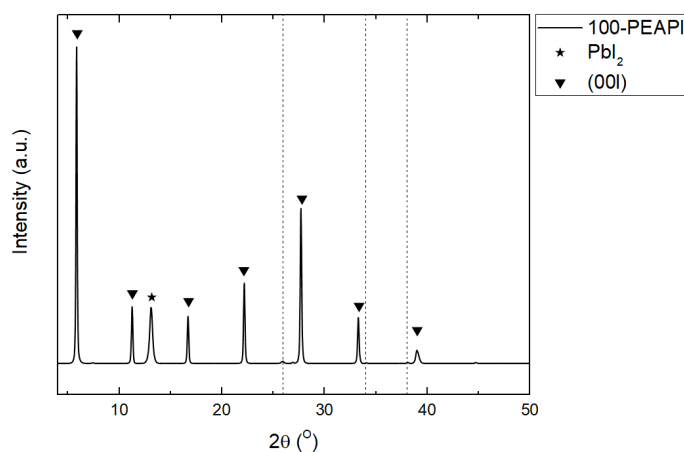


(a)
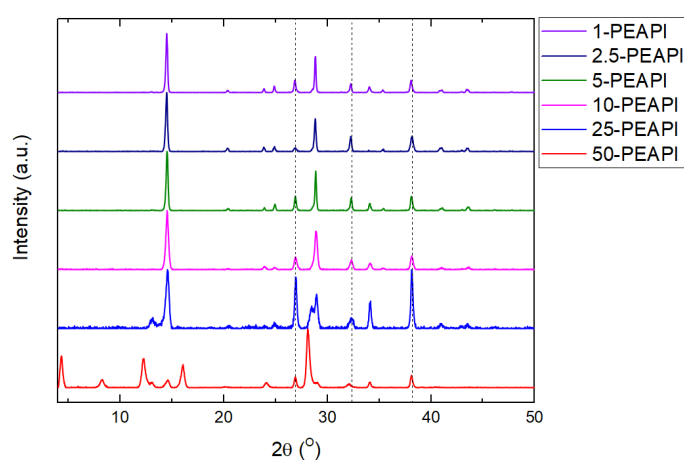


(b)

Figure 7-4: XRD data for films of a) 100-PEAPI and b) 1 to 50-PEAPI. The dashed lines are the location of the FTO peaks used to calibrate the data.

As the concentration of PEA was decreased to 50 % the pXRD pattern changed (Figure 7-4b). There was a very low angle peak at 4°, this has previously been attributed to the (020) plane.[3] The (020) plane goes through the bottom of a group of $PbI_6$ octahedra (see Figure 7-5). The peak shifts to lower angle as the unit cell size increases and the distance between the bottom of two

consecutive layers of octahedra is larger due to the fact that they are now grouped together. The changes in XRD patterns with cation concentration are similar to those observed by Cao *et al.* in BA based 2D/3D hybrid perovskites.[18] They observed a small $PbI_2$ peak at 13° but it is partly hidden by a peak due to the (060) plane at 12°.

Further lowering the concentration of PEA led to a pXRD pattern that looked more like that of MAPI with large peaks at 14° and 28° corresponding to the (110) and (220) planes.[19] At 25 % PEA there were still some remnants of the 2D perovskite peaks but at 10 % and lower only 3D perovskite was visible in the pXRD. The same patterns were observed by Quan *et al.* for low cation substitution 2D/3D perovskite films made using PEA.[3] These pXRD results agree with the UV-Vis observations where the higher concentrations cause changes to the structure and properties but up to 10 % there are no obvious changes.

### 7.2.2   Impedance Spectroscopy of PEAPI Cells

Inverted FTO/NiO/Perovskite/PCBM/BCP/Ag cells were made with perovskites with PEA concentrations of 1, 2.5, 5 and 10 mol%. The resulting cell data is shown in Figure 7-6. The impact of cation substitution on the efficiency of the devices (Figure 7-6a) is quite clear as the efficiency decreases with increasing PEA concentration. 10 mol% substitution lead to an average PCE of below 1 %. When compared to MAPI devices, the efficiency of some of the 1 mol% substituted devices is comparable. However devices showed a wide spread of efficiencies that pulled the average efficiency value to below that of MAPI.

The decrease in efficiency is mirrored in the fill factor (FF) where the 1-PEAPI cells have a similar FF to MAPI. The FF then decreases for 2.5-PEAPI, 5-PEAPI and 10-PEAPI. Interestingly, there is a very small increase in the mean $V_{OC}$ with the addition of 1 % PEA. There is a big drop in $J_{SC}$ with increasing PEA concentration with even 1-PEAPI having a $J_{SC}$ that is 75% of the MAPI control cells.

Electrochemical impedance spectroscopy (EIS) has previously been shown as an effective method to investigate the internal dynamics of perovskite devices such as ion migration, carrier mobility and recombination.[20–23] The standard EIS
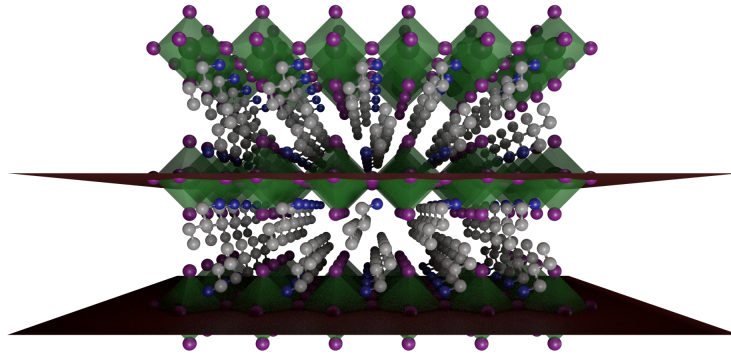
(a)
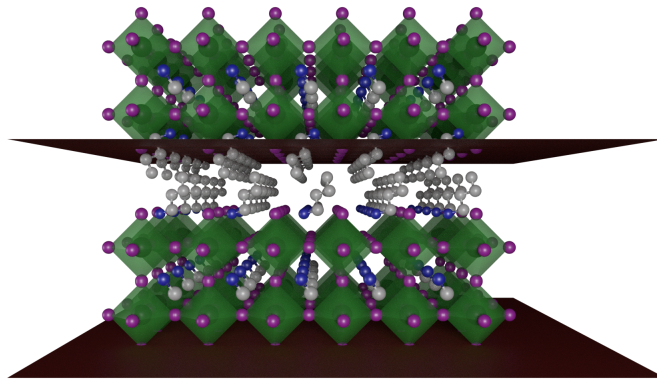


(b)

Figure 7-5: a) (002) plane in a fully 2D perovskite and b) (020) plane in a mixed 2D/3D hybrid perovskite

response of MAPI cells was shown in Section 5.3.6. In brief the response recorded at room temperature shows three semi-circles in the Nyquist plot. As previously discussed, these three semi-circles are labelled as high frequency (HF), mid frequency (MF) and low frequency (LF). To extract time constants ($\tau$) from the three features, they were fitted with a simple semi-circle as has been done in previous EIS studies performed in the group.[21] The feature of most interest in this work is the LF response as this is the feature that is linked to ion diffusion.[21,24,25] The HF response gives the geometric capacitance, $C_{geo}$, and recombination resistance, $R_{recomb}$.[26]

The temperature dependent Nyquist plots from EIS measurements taken between $-12\,°C$ and $45\,°C$ for 10-PEAPI cells are shown in Figure 7-7a. The pixel
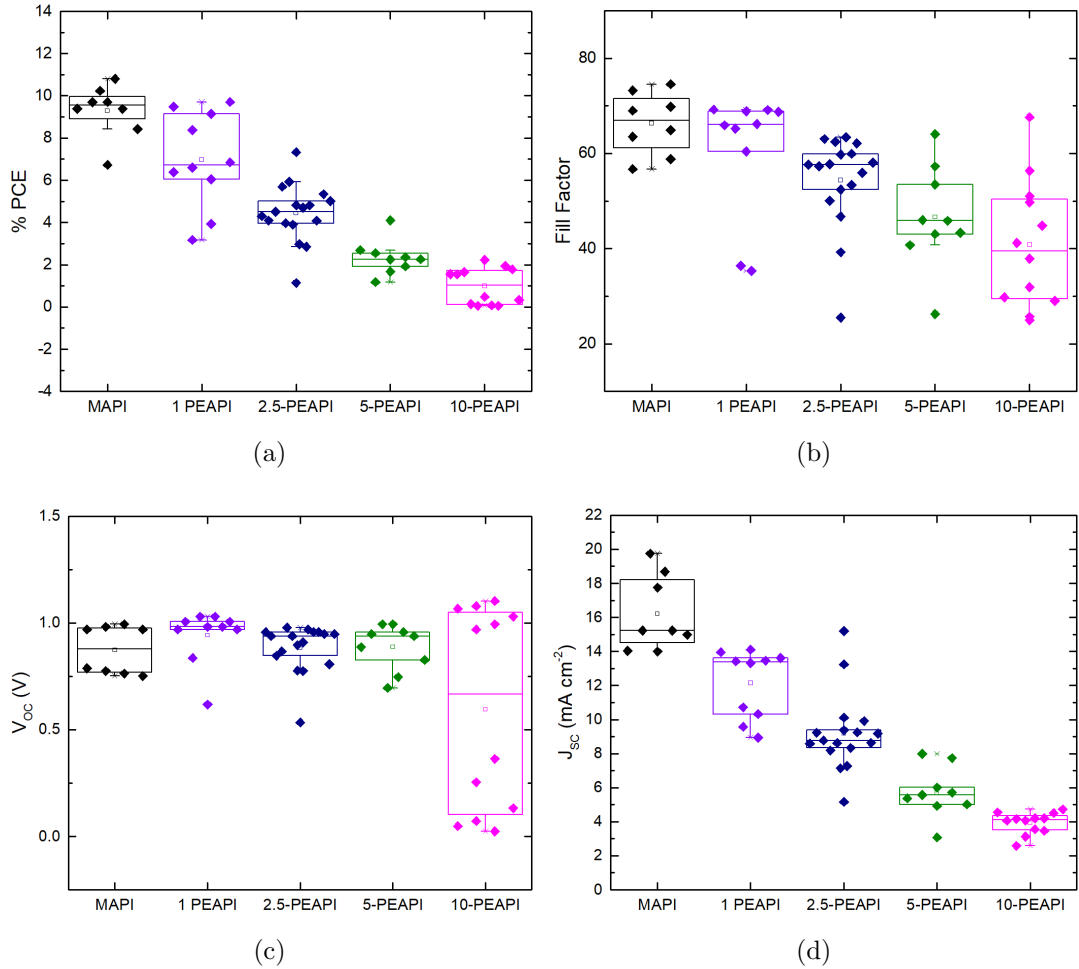
Figure 7-6: Solar cell data for several perovskites with varying concentration of PEA a) %PCE, b) Fill Factor, c) Open Circuit Voltage and d) Short Circuit Current Density

selected for this analysis was the best performing with an efficiency of 2 % and a $V_{OC}$ of over $1\,V$. The diameter of the HF semi-circles was very large compared to MAPI. The large HF semi-circle was caused by 10-PEAPI cells having a small current leading to a large recombination resistance.[27] The MF feature of 10-PEAPI has a strong, linear temperature dependence. An $E_a$ of $0.21\,eV$ was calculated for the MF feature using an Arrhenius plot (Figure 7-7b). The gradient of these Arrhenius plots is opposite of those shown in the µSR sections of this work. The reason that the gradient of the lines is opposite is that in µSR the value on the x-axis is a measure of frequency and in EIS the x-axis value is a time in seconds. As frequency and time are inversely related to each other the two different methods produce Arrhenius plots with opposite gradients.
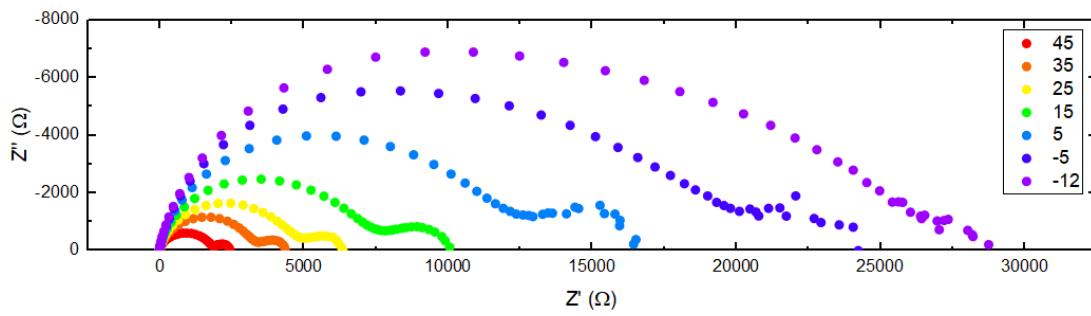
(a)
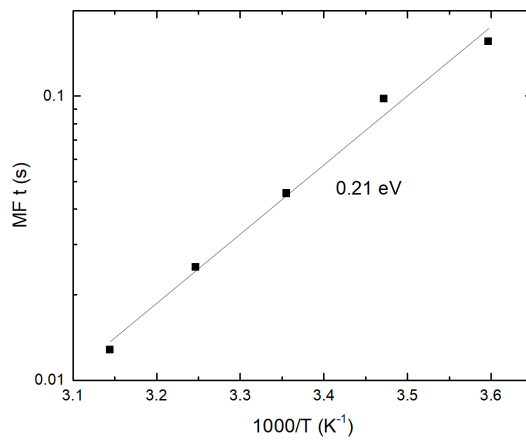


(b)

Figure 7-7: a) A nyquist plot of the impedance response for 10 PEAPI at various temperatures in °C, b) an Arrhenius plot of the mid frequency time constants.

The LF feature that is common in MAPI EIS, and is linked to ion diffusion, was not present in the response of 10-PEAPI. The lack of LF response indicates that iodide diffusion is too low to be measured in 10-PEAPI over the temperature range used in this experiment. It is quite clear that the addition of 10% PEA to the perovskite is having an impact on the ion diffusion. It should be noted that the performance of the cell can have an impact on the IS response. It is possible that some of the changes are related to the poor performance of the selected cell. With the possibility that cell performance was having a big impact on the 2D/3D EIS results the same investigation was performed with the a pixel from the higher efficiency 1-PEAPI cells. These cells have an efficiency comparable to MAPI so any changes are more likely to be caused by the material itself. The results of the temperature dependent EIS for 1-PEAPI are shown in Figure 7-8a.

The size of the HF semi-circles were reduced when compared to 10-PEAPI and were more similar to the usual response seen with MAPI. The change in HF response is due to the increased $J_{SC}$ of the 1-PEAPI devices causing a decrease in recombination resistance. The MF response was very similar to that of 10-PEAPI with an $E_a$ of $0.17\,eV$ (Figure 7-8c). As was observed with the 10-PEAPI there was no LF feature for 1-PEAPI.

It is clear from the EIS data that the addition of only 1% PEA can have a significant impact on iodide motion. With 99% of the material being 3D MAPI it is perhaps surprising that iodide diffusion appears to be completely eliminated at room temperature. A full discussion of the EIS results is included after the EIS results for vertically aligned 10-PEAPI and 10-PrAPI (Section 7.4).

### 7.2.3 Impedance Spectroscopy of Vertically Aligned PEAPI Cells

As mentioned earlier in the section, 2D perovskites often show poor charge transfer due to the preferential orientation of the iodide sheets parallel to the substrate making electron/hole transfer to the contacts difficult.[10] Some recent work by Tsai *et al.* to vertically orient the sheets showed that this could dramatically improve performance.[14] This then inspired several other groups to investigate methods of achieving vertical orientation. The issue with the method presented by Tsai is
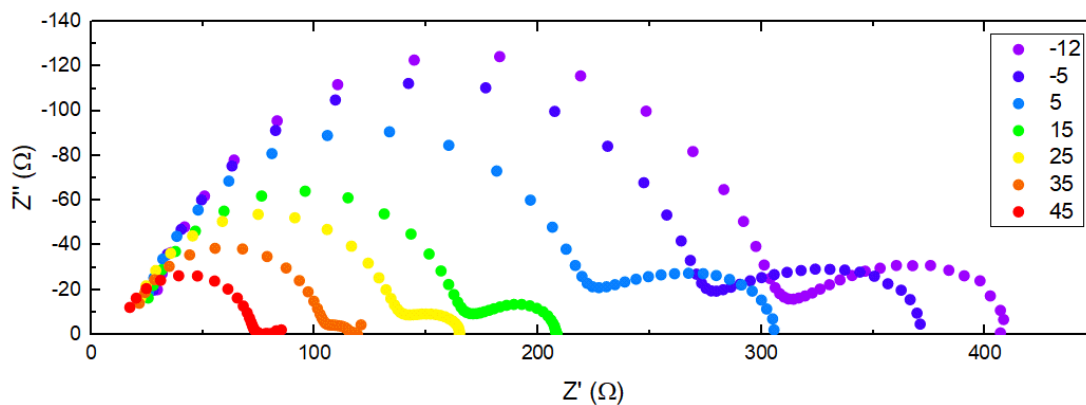
(a)
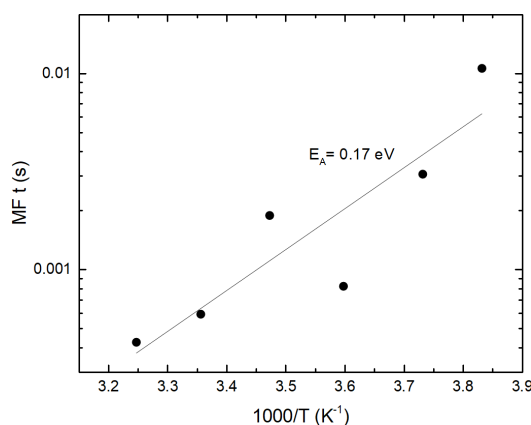


(b)

Figure 7-8: a) A nyquist plot of the impedance response for 1 PEAPI at various temperatures in °C, b) an Arrhenius plot of the mid frequency time constants.

the need to heat the substrate to over 150 °C during the spin coating process, requiring heat resistive spin coating equipment.

Since Tsai's work a couple of alternative methods for vertically orienting the growth have been discovered.[17,28] The method that was used here to make vertically oriented perovskites used an $NH_4SCN$ additive added into the precursor solution.[16] The method that first used the $NH_4SCN$ additive had a different solvent system, processing method and cell architecture to that used in the previous work in this chapter. With the often dramatic changes to film properties and device performance based on processing, the films were first investigated to ensure that the additive was still having the same effect using the cell fabrication methodology used in this work.

Films and devices were produced using the ethyl acetate anti-solvent method
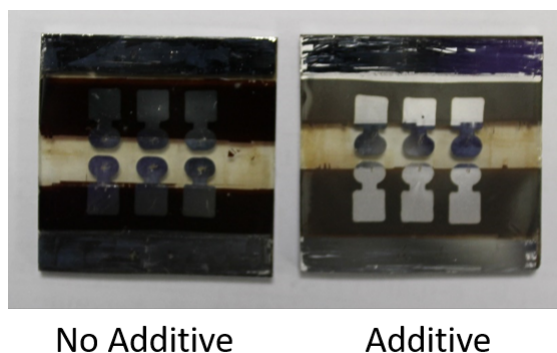
No Additive       Additive

Figure 7-9: Photo of a 10-PEAPI film and a 10-PEAPI film made with $NH_4SCN$ additive.

outlined in previous chapters (Section 3.6). The precursor solutions were made using the same methodology as the non vertically-aligned 10-PEAPI. The only difference between films is how much $NH_4SCN$ additive was added to each solution. The different concentration corresponds to the labelling of the samples for example 0.125 M refers to a 10-PEAPI perovskite with 0.125 M additive.

The first and most obvious difference between films without and with additive was in the visual quality of the films (Figure 7-9). Films made with additive were greyer than those made without and were not as specular as films made without the additive. Lower film quality is most commonly caused by the size and shape of the crystallites and pinholes in the film. AFM was used to examine the nature of the crystals formed during deposition (Figure 7-9). The film without additive had few pinholes and was a compact film made up of many small crystallites. The addition of additive caused the film to have more pinholes and larger crystallites. It is clear from looking at the two films that the additive is having an impact on how the perovskite crystallises.

The changes to the band gap of 10-PEAPI with varying concentrations of $NH_4SCN$ was investigated. A band gap of 1.61 eV for the different concentration of additives was derived from Tauc plots (Figure 7-11). There is an extremely small difference between the three films with additives and the film without additive. The difference can be attributed to small variations in film thickness and extrapolation error.

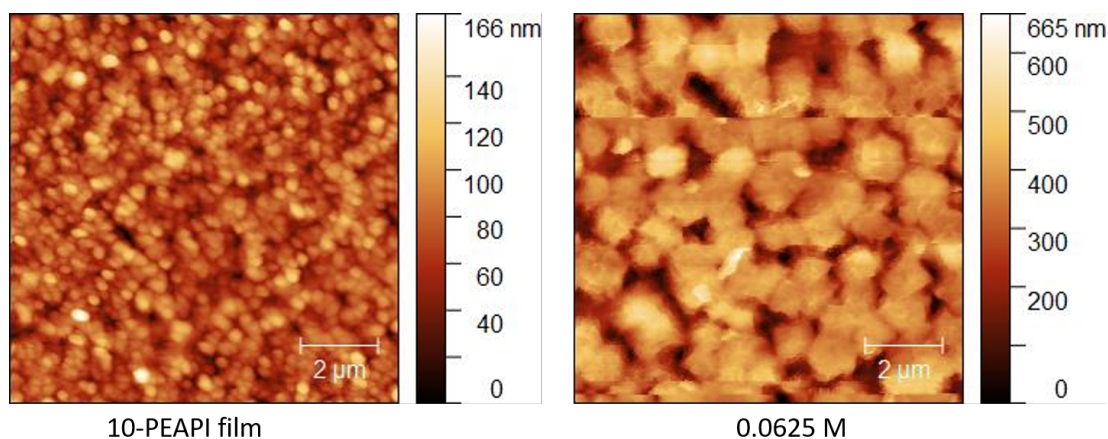The pXRD data for 10-PEAPI with three different additive concentrations

Figure 7-10: AFM of a 10-PEAPI film and a 10-PEAPI film made with $0.0625\,M$ of $NH_4SCN$.
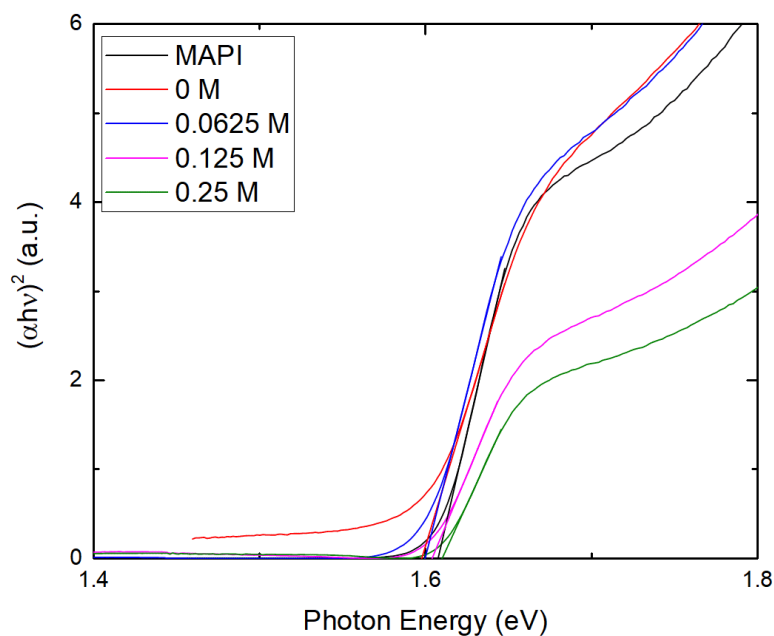


Figure 7-11: Tauc plot derived from absorbance data and band gaps calculated using linear fits for 10-PEAPI films with three different concentrations of $NH_4SCN$ additive, no additive and a standard MAPI film.

and no additive are shown in Figure 7-12a (along with MAPI for comparison). The first thing to note from the pXRD is that there were no peaks below 10° that usually indicate the presence of 2D perovskite. With an increasing concentration of additive there appeared to be some formation of lead iodide as shown by the presence of the peak at 13°. The addition of $NH_4SCN$ to the precursor solution caused the peaks at 24° and 43° to increase significantly. The increase in these

peaks can be explained by an increase in the order of the films. When the material is randomly oriented this peak is restricted but the addition of $NH_4SCN$ helps to orient the film making this peak appear far more intense.
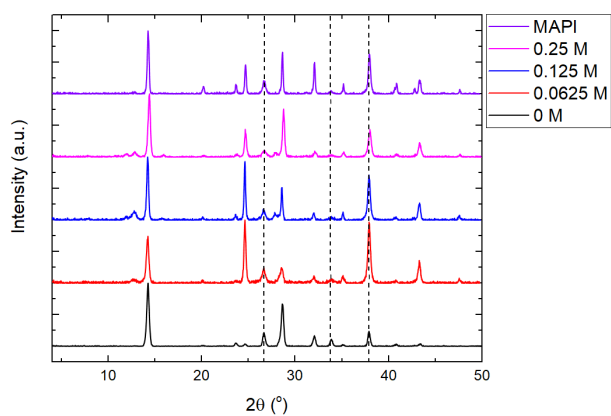


(a)
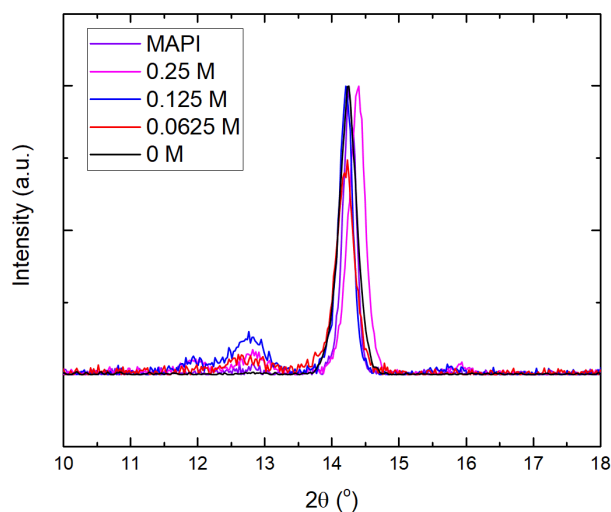


(b)

Figure 7-12: a) XRD of thin films of MAPI, 10-PEAPI and 10-PEAPI made with three different concentrations of $NH_4SCN$. The dashed lines show the FTO peaks used for calibrating the data. b) The same XRD patterns zoomed into the peak at $2\theta = 14°$

Interestingly, there was a shift in $2\theta$ for the perovskite with the addition of $0.25\,M$ of $NH_4SCN$ (Figure 7-12b). This shift was present in all of the peaks indicating that there was a contraction in the lattice of the perovskite. This is surprising as there is no obvious reason for this to occur given that it does not take place for the other additive concentrations. It could indicate that some $NH_4^+$ is being incorporated into the perovskite at these concentrations causing
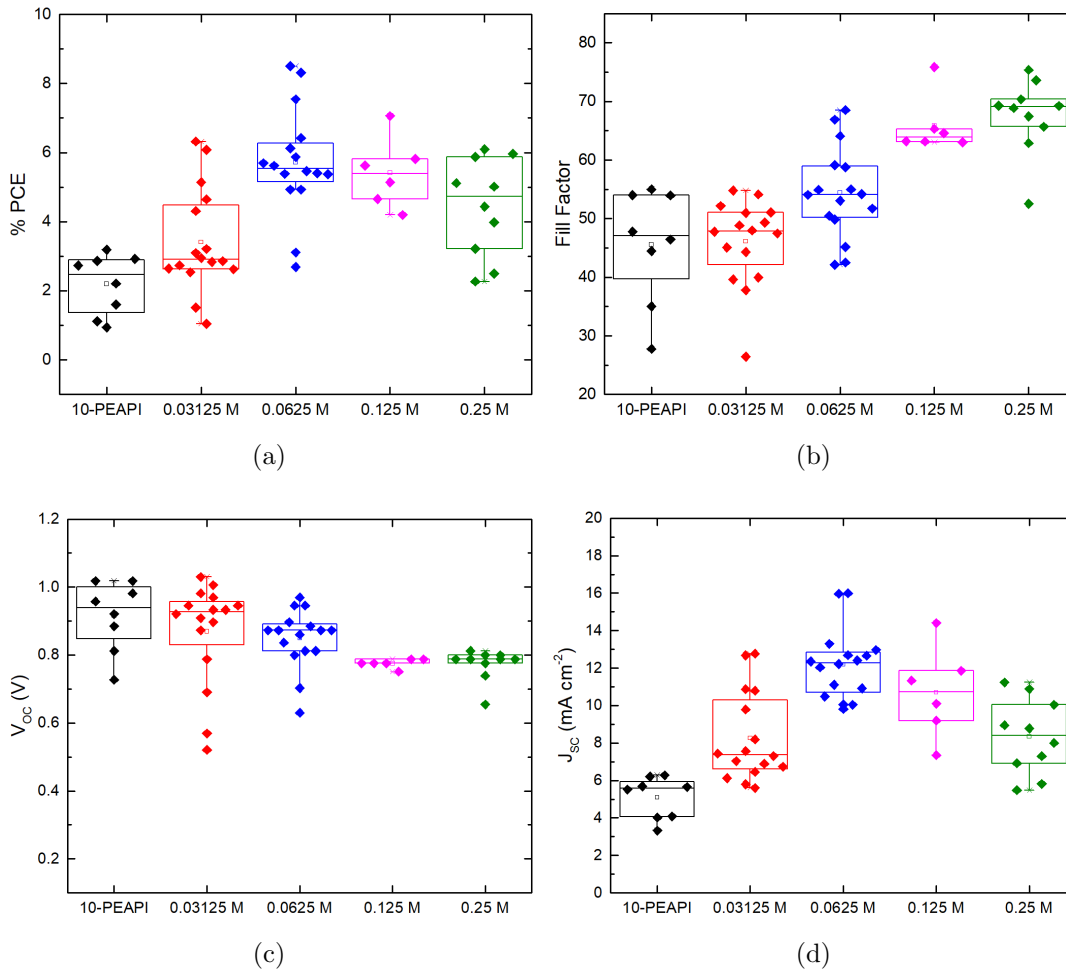
the lattice to contract slightly.



Figure 7-13: Cell data for 10-PEAPI with varying concentrations of $NH_4SCN$ additive a) %PCE, b) Fill Factor, c) Open Circuit Voltage and d) Short Circuit Current Density

Devices were made with precursor solutions containing 0, 0.03125, 0.0625, 0.125 and 0.25 M $NH_4SCN$ and the resulting JV data is shown in Figure 7-13. There was a clear trend in the %PCE data (Figure 7-13a) with 0.0625 M being the best concentration of additive with an average efficiency of 6 % and champion pixels nearing 9 %. Increasing the concentration above 0.0625 M caused a small drop in average performance and decreasing the concentration produced a substantial drop.

The other JV metrics were also changed by the addition of additive, Fill Factor increased, $V_{OC}$ decreased and $J_{SC}$ increased until 0.0625 M then decreased (Figure 7-13b-d). The main factor that caused the improved efficiency for the

additive based perovskites was the large change in $J_{SC}$. The large increase in $J_{SC}$ indicates that the poor charge transfer that reduces efficiency in 2D perovskites is not as dramatic after the addition of $NH_4SCN$. These results agree with those of Zhang *et al.* who first used $NH_4SCN$ as an additive.[16]

To fully confirm the orientation of the perovskite, grazing incidence wide angle X-ray scattering (GIWAXS) would need to be performed and due to time constraints it was not possible to perform the required experiments. The improvement to device performance and the pXRD data indicate that there is at least some orientation of the 2D/3D hybrid perovskite with the additive. The agreement with the literature data also helps to further show that the oriented perovskite was formed.
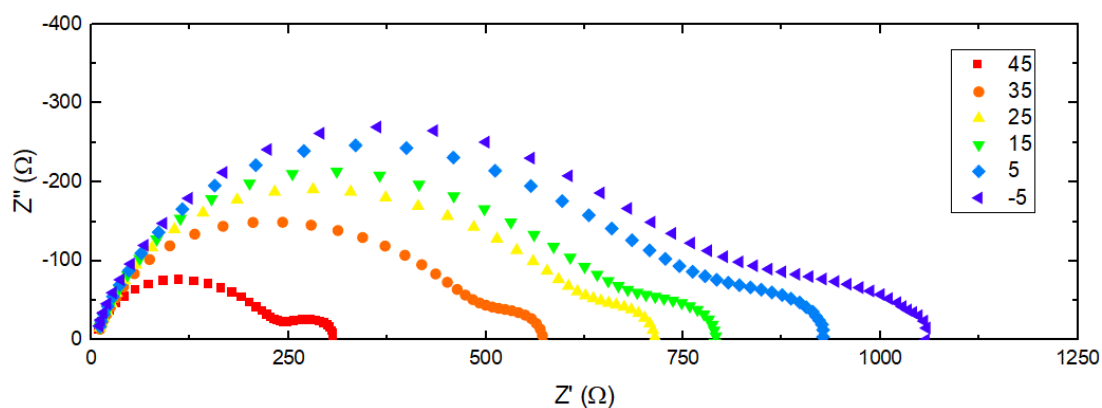


(a)
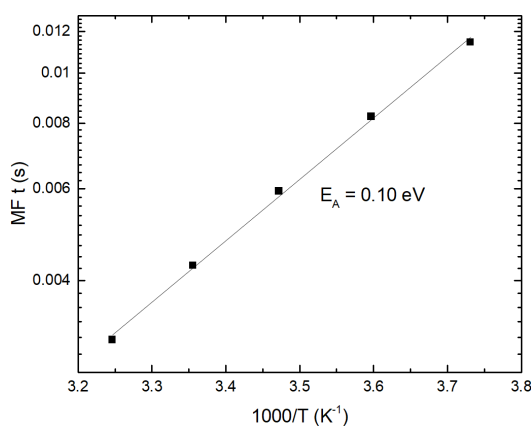


(b)

Figure 7-14: a) A nyquist plot for the EIS response of 10 PEAPI containing 0.0625 M $NH_4SCN$ at various temperatures in °C and b) an Arrhenius plot of the mid frequency time constants.

EIS of the oriented 2D film was measured to investigate how the response changed upon orientation. The results (Figure 7-14) showed some clear changes when compared to the response of both non-oriented 10-PEAPI and regular MAPI. The HF semi-circle in the Nyquist plot (Figure 7-14a) was reduced substantially when compared to the previous non-oriented 10-PEAPI due to the increased current of the vertically aligned device. The MF element varied linearly with changing temperature (Figure 7-14c) giving an activation energy of 0.10 eV. This activation energy is half of that observed for the non-oriented perovskite.

There was no third semi-circle observed in the EIS response of vertically aligned 10-PEAPI. As previously mentioned in this chapter, the LF semi-circle is due to a frequency dependent increase in recombination resistance as ions move to reduce recombination under the influence of the applied voltage. The time constants can be used to calculate the $E_a$ for ion motion. The lack of third semi-circle shows that the diffusion of iodide in vertically aligned 2D/3D perovskites is not occurring in the same temperature range as it does in MAPI. A full discussion of the ion migration properties of PEAPI, vertically aligned PEAPI and PrAPI is included at the end of the PrAPI section of this chapter (Section 7.4).

## 7.3 Propylammonium Iodide as an A-Site Cation

As previously discussed, there are a wide variety of possible large A-site cations that can be introduced into the perovskite to form 2D perovskites. The simplest cation is a long chain alkyl with an amine head group. When it comes to alkyl amines, butylamine has been extensively investigated but other chain lengths are far less prevelent in the literature. Propylammonium (PrA) has not been investigated in great detail with only a few studies ever using it.[15] Previously it was seen as an additive to improve the crystallisation of perovskite films instead of an A-site cation.[29] In this section the use of PrA as an A-site cation in 2D/3D perovskites is investigated. Films of $PrA_xMA_{1-x}PI_3$ with varying x values were characterised by UV-Vis, XRD and AFM. Cell performance, stability and impedance of devices using various stoichiometric ratios was also studied. When 100 % of MA is substituted with 100 % PrA then the material is labelled as

100-PrAPI. If the cation substitution was at 5 % then the label used is 5-PrAPI and the varying numbers indicate the varying percentage substitution.
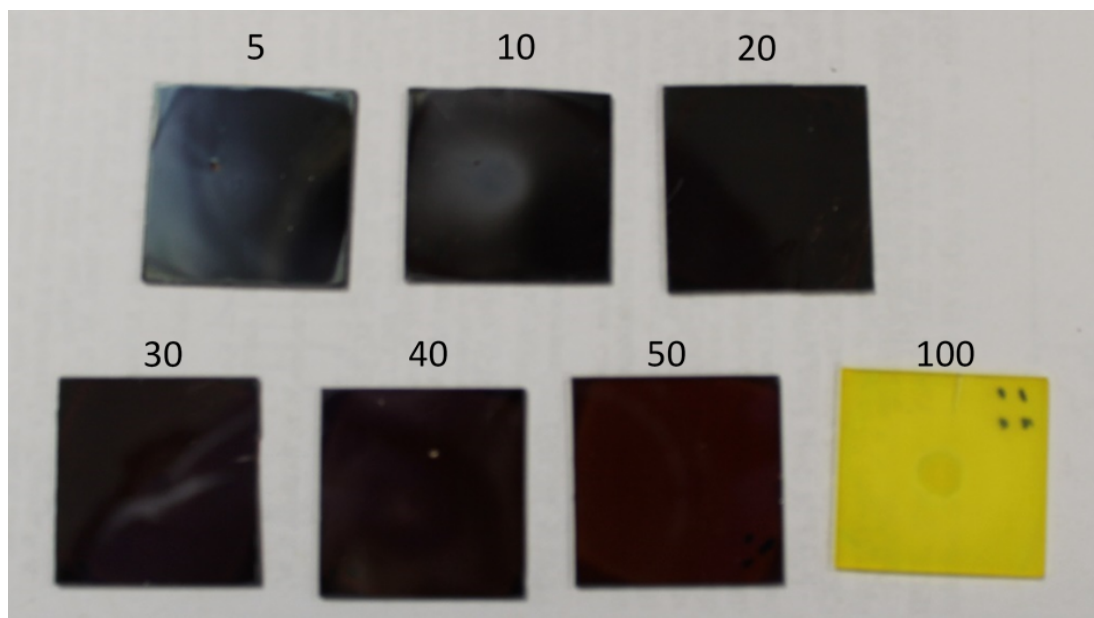
## 7.3.1 PrAPI Film Characterisation



Figure 7-15: PRAPI film photo.

Films of PrAMAPI with PrA concentrations of 5, 10, 20, 30, 40, 50 and 100 mol% were all made using the same ethyl acetate anti-solvent deposition method used in previous sections of this thesis (Section 3.6). Figure 7-15 shows the changing colour of the films with different mol% of PrA. As with other 2D/3D perovskites, the colour changed from black at low PrA concentrations to yellow at higher concentrations with 50 mol% being a deep red colour.[3] For the films of 5 and 10 mol% PrA the films were dark brown. There was some clouding of the low percentage films, this occurs with the ethyl acetate anti-solvent deposition method. If the anti-solvent is added too late then the films take on a cloudy nature.[30]

The films were analysed using UV-Vis and pXRD. The resulting UV-Vis showed a steady increase in the band gap between 5 and 20 mol% PrA (Figure 7-16a). As the concentration of PrA increased to 30, 40 and 50 mol% the band gap became less sharp due to the increased presence of 2D perovskite creating mixed n value perovskite as previously discussed (Figure 7-16b). The changes
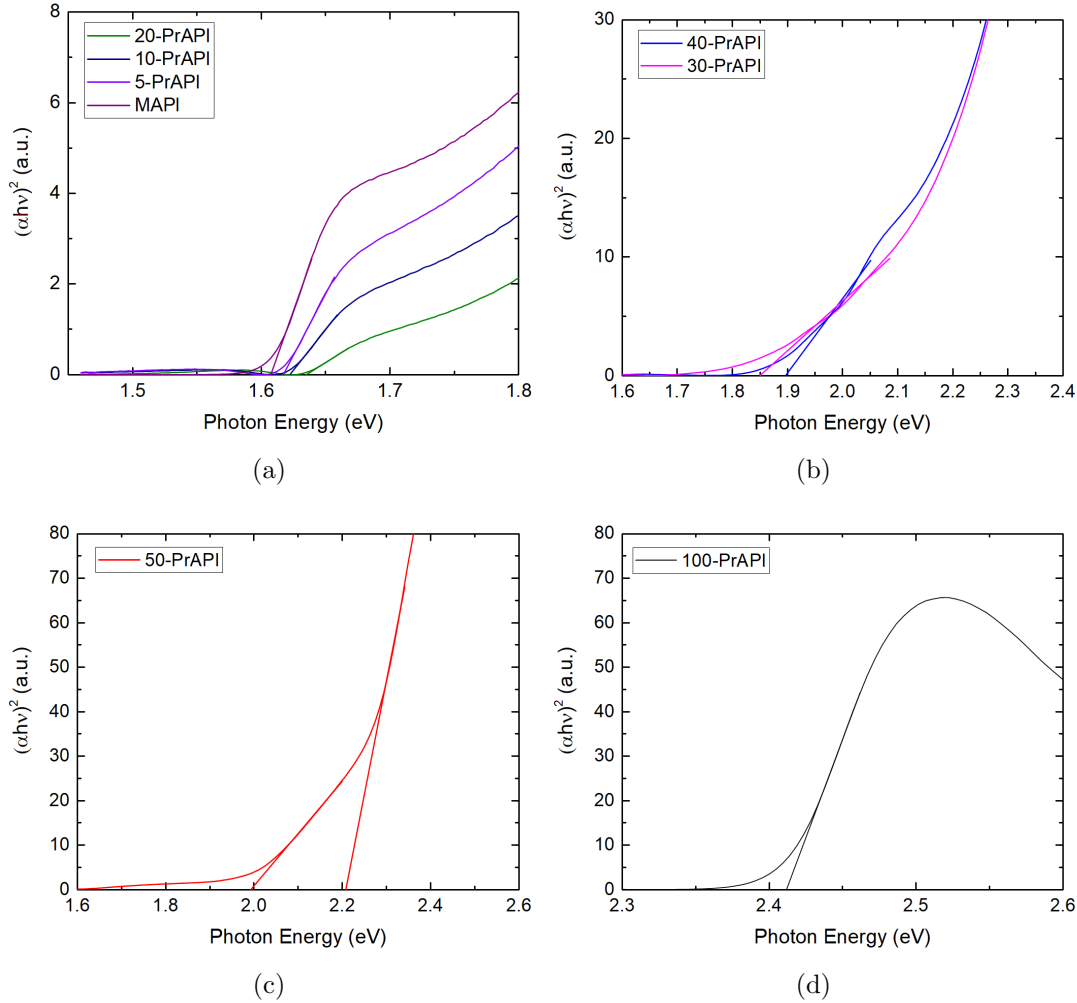
Figure 7-16: Tauc plots of $PrA_xMA_{100-x}PbI_3$. a) Shows the perovskites up to 20 mol% PrA, b) shows the 30 and 40 mol% perovskites, c) shows the Tauc plot of 5-PrAPI clearly showing the multiple band gaps present in the material and d) shows the 100 mol% PrAPI perovskite.

here followed the same trend as those observed in previous 2D/3D hybrid studies in this chapter as well as in the literature.[3,31] When the perovskite was made with 100 mol% of PrA the $E_g$ was 2.4 eV (Figure 7-16c). This band gap is similar to that of fully 2D PEAPI from earlier in the chapter.

The band gap of the 100 mol% PrA perovskite is similar to that of $PbI_2$ so to prove that the material is actually a 2D perovskite XRD analysis was performed. As well as looking at the 100 mol% PrA perovskite the other stoichiometric ratio perovskites were also investigated with XRD (Figure 7-17). The XRD response of 100-PrAPI had a low angle peak below 10° that is characteristic of 2D perovskites.

The 50-PrAPI diffraction pattern had a peak at 10° that again indicates the presence of 2D perovskite. It was expected that there would be an even lower angle peak that corresponds to the (002) plane as seen for 50-PEAPI in the previous section. This predicted lower angle peak is likely would be occur below the lowest angle measured here as the d spacing of the plane would be very small. The low angle peak in 50-PEAPI was at 5°. PEA is a much larger cation than PrA therefore the unit cell size for 50-PrAPI is smaller making the d spacing smaller and pushing the angle of the peak to below 5°. The pXRD pattern for 40 mol% PrA showed the same peaks as 50 mol% except with a slight shift to the right for the lowest angle peak.
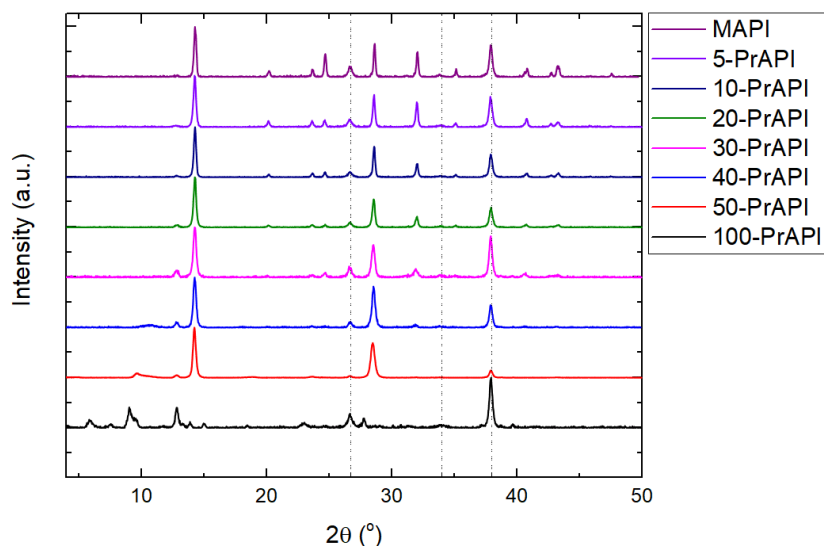


Figure 7-17: XRD response for perovskites made with various concentration ratios of PRA and MAI. The dashed line shows the FTO peaks that were used to align the patterns.

The diffraction pattern for 30-PrAPI begins to look very similar to MAPI except with a much lower intensity peak at 25°. This trend continues as the concentration of PrA decreases. Overall, the pXRD confirms that at 100 mol% PrA a 2D perovskite is formed and as the concentration of PrA is decreased the overall material becomes more and more similar to MAPI.

## 7.3.2   Impedance Spectroscopy of PrAPI Cells

Inverted NiO/Perovskites/PCBM/BCP/Ag devices were made with 5, 10, 20, 30 mol% substitution of PrA. A few control MAPI cells were also made for comparison. The resulting device parameters shown in Figure 7-18 were surprising when compared to previous 2D/3D hybrid cells made here and also compared to other reported work. The PCE (Figure 7-18a) dropped by approximately 50 % with the substitution of 5 mol% PrA which is similar to the reduction in efficiency with 50 mol% PEAPI shown earlier, this loss of efficiency can be related to the large reduction in $J_{SC}$ (Figure 7-18d). The FF and $V_{OC}$ of the 5 mol% PrAPI increased slightly when compared to MAPI (Figure 7-18b,c).
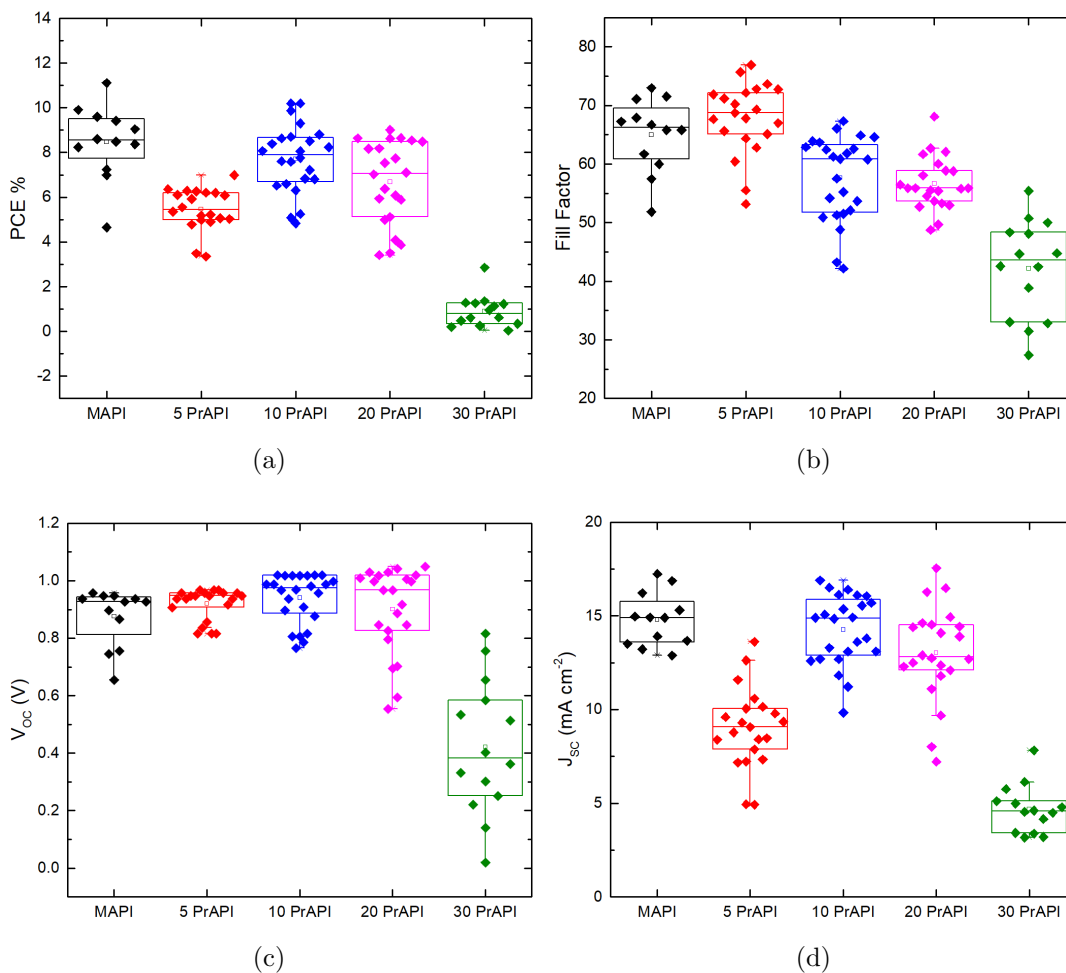


Figure 7-18: Solar cell data for several perovskites with varying concentration of PrA a) %PCE, b) Fill Factor, c) Open Circuit Voltage and d) Short Circuit Current Density

In the case of PEAPI, as the percentage of large cation increased the efficiency decreased. For PrAPI the efficiency increased when the amount of cation increased from 5 mol% to 10 mol%. The PCE of the 10 PrAPI cells was on average 8 % this is only marginally lower than the MAPI control cells. The champion pixel had an efficiency of 10.2 %. The FF was, on average, about 5 % lower than control cells while the $V_{OC}$ increased slightly and the $J_{SC}$ was the same (Figure 7-18b-d). Doubling the PrA percentage to 20 mol% caused a small drop in PCE, FF and $J_{SC}$ while the $V_{OC}$ remained about the same. Finally, for 30 mol% PrA the PCE and $J_{SC}$ dropped to nearly zero, the fill factor and $V_{OC}$ decreased to an average of 40 % and 0.4 V, respectively.

### 7.3.3   PrAPI Impedance

EIS analysis was performed on 10-PrAPI perovskite devices, Nyquist plots are shown in Figure 7-19a. As the range of interest in previous EIS studies was between 15 and 45 °C, these cells were only measured between 15 and 45 °C and the step size was decreased to 5 °C to collect more data points.

As with the 10-PEAPI devices, the HF time constant increased with decreasing temperature. The HF semi-circle was much smaller than that of 10-PEAPI due to the 10-PrAPI having a larger $J_{SC}$. The MF feature produced time constants that gave an Arrhenius response between 15 and 30 °C. This response had an $E_a$ of 0.13 eV (Figure 7-19c). As with the previous 2D based EIS results the LF response was not present in the Nyquist plot of 10-PrAPI.
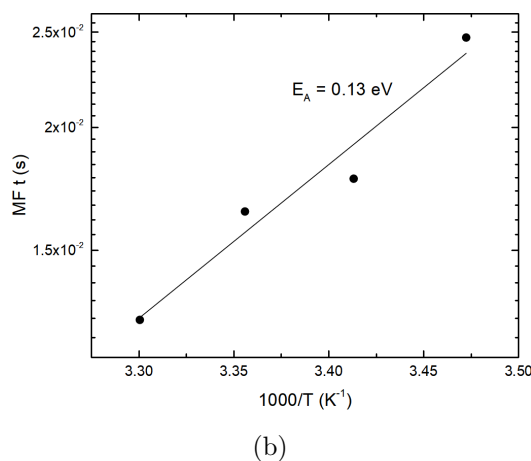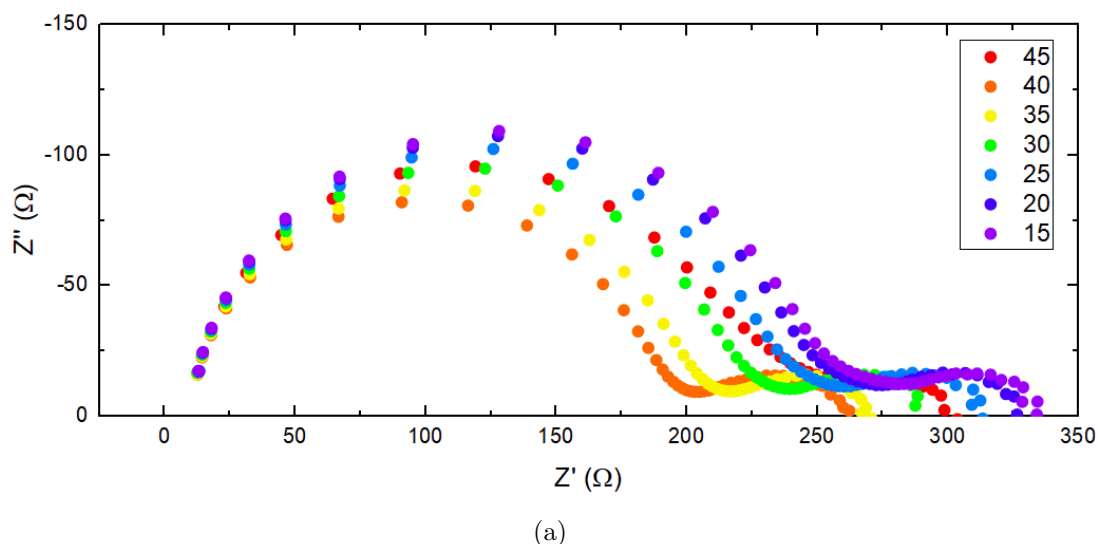
(a)



(b)

Figure 7-19: a) A nyquist plot for the impedance response of 10 PrAPI at various temperatures in °C, b) an Arrhenius plot of the high frequency time constants and c) an Arrhenius plot of the mid frequency time constants.

## 7.4 Impedance Discussion

The $E_a$ of all the MF impedance responses are summarised in Table 7.1. There were some small differences in the MF response for the 4 different 2D/3D hybrids. When the 10-PEAPI perovskite was vertically aligned the $E_a$ dropped by about half compared to a randomly oriented perovskite. Reducing the percentage of PEA from 10 to 1 only caused a small reduction in $E_a$. Changing the cation to the smaller PrA also caused a reduction in $E_a$. All of the 2D/3D hybrids have a lower MF activation energy than that of regular MAPI.

It is, at present, unknown for certain what causes the MF response in per-

Table 7.1: A summary of the MF activation energies of several 2D/3D perovskites compared with MAPI.*v10-PEAPI is vertically aligned 10-PEAPI.

| Perovskite | $E_a$ MF (eV) |
|---|---|
| 10-PEAPI | 0.21($\pm$0.011) |
| 1-PEAPI | 0.17($\pm$0.045) |
| 10-PrAPI | 0.13($\pm$0.021) |
| v10-PEAPI* | 0.10($\pm$0.002) |
| MAPI | 0.29($\pm$0.027) |

ovskite EIS. As part of the previous mixed cation study a wider range of smaller organic cations that form 3D perovskites were studied by Sam Pering using EIS. The MF response remained mostly unaffected by 5% substitution of cations, apart from Cs substitution which caused the activation energy to increase. The current theory for the origin of the mid frequency AC response is that it is caused by changes to recombination rates due to field induced diffusion of iodide along the surface of perovskite grains. At present, there is not enough evidence to confirm this theory and further studies into surface passivation would help to elucidate the true origin of the mid-frequency response.

For all of the EIS results, bar those for MAPI, there was no LF response detected. The LF semi-circle has previously been related to diffusion of iodide in the bulk of the 3D material. These results show that non-aligned 2D/3D hybrid materials restrict iodide diffusion even at only 1% substitution. Similar results were observed in 2017 by Lin *et al.*. They showed, using temperature dependent conductivity measurements, that with 40% BA substitution that ion migration was suppressed.[32] This is what would likely be expected given that the large spacer groups in between the layers would most likely block migration of ions across the spacer layers. It is perhaps surprising that just 1 mol% causes the same kind of effect as there is far less blocking of charges. It is possible that the reduction in ion migration is again being caused by small structural changes similar to that observed with GA substitution. Further investigation using computational modelling could help to elucidate the cause of reduction in ion migration in low percentage 2D/3D perovskites.

The vertically aligned perovskites made it possible to see how the large cations could affect ion migration along the planes of the 2D devices. Unlike the non-aligned perovskite, the aligned materials allow for easy charge transfer between electrodes along the octahedra sheets, therefore it would be expected that long range ion migration would be possible as well. The lack of low frequency response in the vertically aligned 10-PEAPI cells shows that this is not the case. Despite there being large sections of aligned material that is effectively MAPI, ion migration is too slow to be detected. This phenomena was observed to occur in single crystal perovskites with 50 % butylammonium.[33] In the single crystal work the loss of migration was attributed to an increase in the energy required to form vacancies leading to less vacancies and therefore reduced diffusion.

## 7.5 Fluorinated A-Site Cations

It is well known that 2D perovskites are more stable than their 3D counterparts and the possibility to use almost any size cation opens up a wide range of possible cations to investigate.[7] As previously discussed, moisture stability is a big issue for commercialisation of perovskites.[34] Fluorine containing compounds have long been known to have hydrophobic properties.[35] With respect to perovskites there have been some attempts to incorporate the fluorinated anions $BF_4^-$ and $PF_6^-$ into the lattice leading to improved stability.[36,37] There have also been a couple of reports of fluorinated ionic liquids being used in the manufacturing process of perovskite devices and this was also shown to be an effective way of improving device stability.[38,39]

The final section of this chapter focuses on the use of fluorinated ammonium cations in an attempt to improve long term stability of perovskites. More specifically, the incorporation of the fluorinated analogues of propylammonium iodide, 2,2,3,3,3-pentafluoropropylammonium iodide (F-PrA) and 4-fluoroanilinium iodide (F-An), were studied to improve moisture stability with minimal sacrifice of performance.
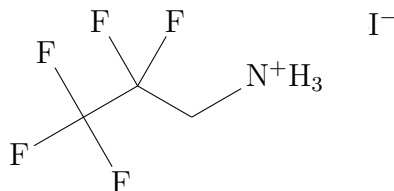
Figure 7-20: Structure of F-PrA

## 7.5.1 Fluorinated Propylammonium Iodide

The synthesis of F-PrA (Figure 7-20) was achieved by addition of hydroiodic acid to 2,2,3,3,3-pentafluoroamine using the method outlined previously in Section 1-10 and the resulting salt was characterised using $^{19}$F, $^{1}$H and $^{13}$C NMR (Appendix Figure A-5). The $^{19}$F NMR contained two peaks, a singlet at -80 ppm which corresponds to the 3 fluorines on the last carbon and a triplet at -120 ppm corresponding to the 2 fluorines on the second carbon coupled to the adjacent hydrogens. As the measurement decouples the fluorines from each other there is no splitting caused by them. As expected, the proton NMR contained a broad singlet at 8.8 ppm for the amine protons and a triplet at 4 ppm for the protons on the carbon adjacent to the amine group, the triplet is caused by coupling to the two adjacent fluorines.
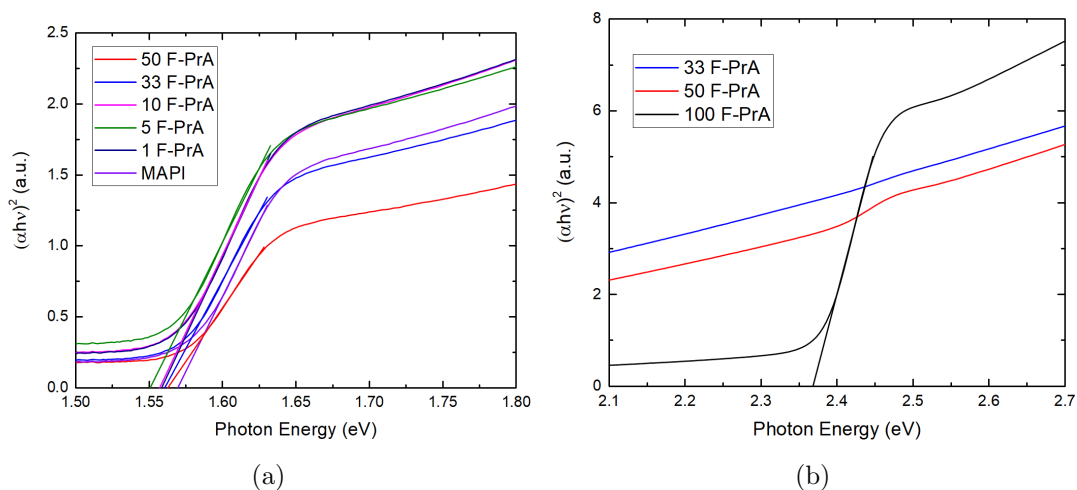


Figure 7-21: Tauc plots of a)0-50 F-PrAPI and b) 33-100 F-PrAPI

Thin films of $F-PrA_xMA_{1-x}PbI_3$ were made with x being equal to 100, 50, 33, 10, 5 and 1. UV-Vis analysis of the various films deposited on glass was performed and the resulting Tauc plots are shown in Figure 7-21a and b. The

band gap for all the concentrations, except 100 mol%, was approximately 1.57 eV which is similar to MAPI. The $E_g$ of 100 mol% F-PrA perovskite was at 2.4 eV and the 50 mol% F-PrA perovskite also appeared to have a small peak at the same position.

To study the structure of the mixed cation perovskites XRD was performed on films of the same concentration ratio as used in the UV-Vis experiments (Figure 7-22). The diffraction pattern of 100 mol% F-PrA had four distinct peaks (not including the FTO peaks) at 12, 26, 38 and 39°. These peaks matched with the expected peak positions of a film made of pure $PbI_2$ (marked as triangles in the XRD). At the opposite end of the F-PrA:MA ratio, the 1 mol% diffraction pattern had peaks that aligned almost perfectly with MAPI with the presence of small amount of $PbI_2$ as shown by the peak at 12°. All of the stoichiometry ratios in between 1 and 100 mol% showed a mixture of the pure $PbI_2$ and MAPI patterns.
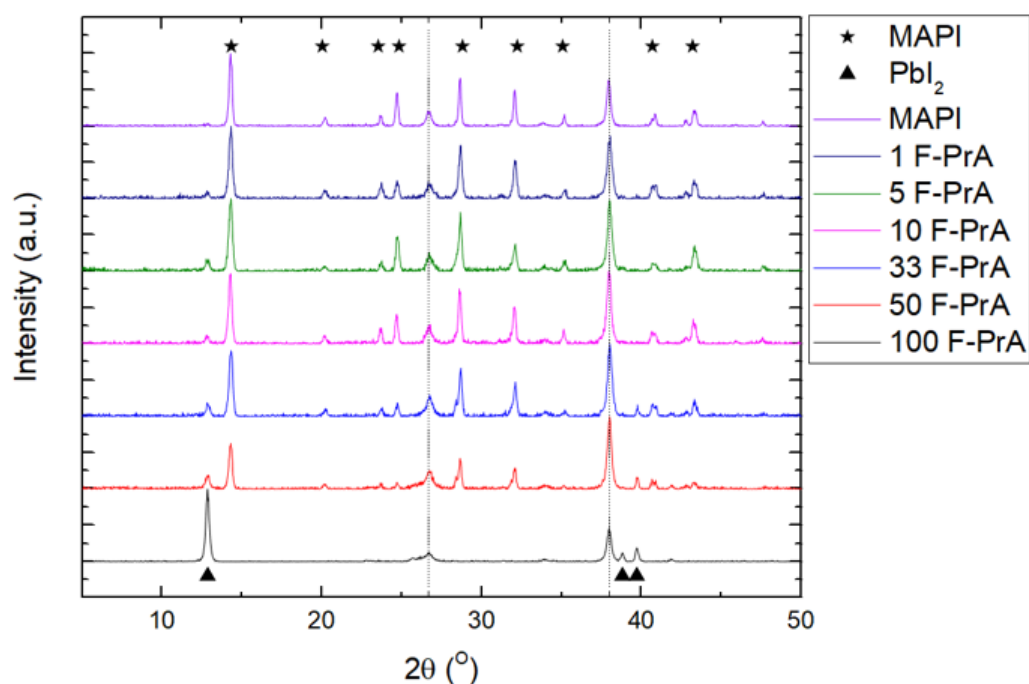


Figure 7-22: XRD patterns of thin films of 0-100 F-PrAPI

Based on a combination of the pXRD and UV-Vis data it is clear that at 100 mol% F-PrA there was no cation incorporation into the film leaving behind just $PbI_2$. It is also the case that at 50 mol% what is formed is a two phase film of MAPI and $PbI_2$. This is based on the lack of 2D peak, the mixture of MAPI

and PbI$_2$ peaks in the XRD, and the presence of the second band gap at 2.4 eV in the UV-Vis spectrum. Based on this evidence, it is likely that even down to lower concentrations the F-PrA is not being incorporated into the perovskite and all that is formed is varying amounts of MAPI and PbI$_2$ based on the ratio of cations involved. The size of the cation is unlikely to be the cause of this lack of cation uptake as bigger cations have been used to fabricate 2D lead iodide perovskites before.[40,41] The most likely explanation, is that the large amount of fluorination causes the the cation to be too electronegative and therefore not able to pack close enough to each other. The inability to pack closely would make it impossible to form a 2D perovskite.

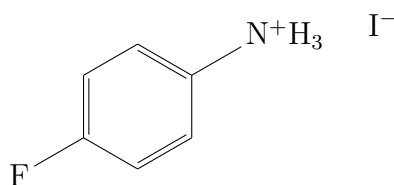### 7.5.2   Fluorinated Anilinium Iodide



Figure 7-23: Structure of 4-fluoroanilinium iodide

A second possible fluorinatd cation that was investigated was 4-fluoroanilinium iodide (Figure 7-23). This was synthesised in the same way as the previous fluorinated cation by adding hydroiodic acid to a solution containing the desired amine precursor. Once again the product was characterised using several NMR techniques (Appendix Figure A-7). Proton decoupled fluorine NMR and fluorine decoupled proton NMR were used instead of standard methods to make assignment easier. The NMR contained a broad singlet at 9.7 ppm corresponding to the three amine protons. The spectrum also contained a multiplet at 7.4 ppm that was assigned to the aromatic protons. Despite the decoupling of the fluorine the aromatic proton peaks were still complex and could not be assigned individually. The fluorine NMR contained just a singlet at -114 ppm for the fluorine at the 4 position on the aromatic ring.

Finally, the carbon NMR had three separate doublets at 161 ($J = 244$ Hz), 125 ($J = 8.8$ Hz) and 117 ($J = 17.3$ Hz)ppm and a singlet at 125 ppm. The doublets

were all coupled to the fluorine with the coupling constant getting smaller as the carbon gets further away from the fluorine therefore the peaks were assigned as follow: 161 was the 4-carbon, 117 the 3-carbon and 125 the 2-carbon. The final carbon at the 1 position with the amine functional group is the remaining singlet at 125 ppm. More time consuming NMR techniques, such as PENDANT, COSY, HMBC and HMQC, could have been performed to attempt to fully assign the peaks in the proton NMR. Due to the simplicity of the reaction and the evidence presented by the peak integrals and the other NMR techniques it was deemed unnecessary.



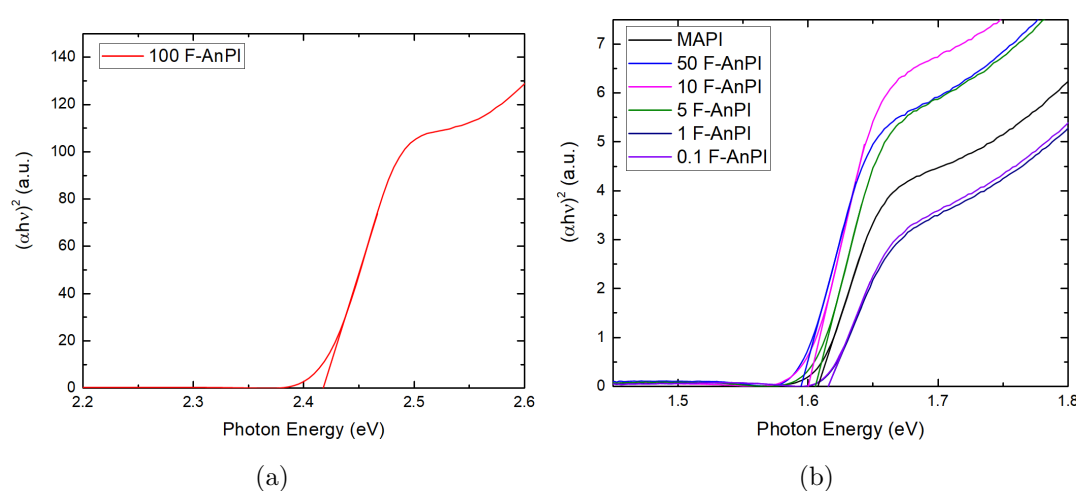(a)                                                        (b)

Figure 7-24: Tauc plots of a) 100 F-AnMAPI and b) 0-50 F-AnMAPI.

Thin films of F-AnMAPI with varying cation ratios were made and characterised using UV-Vis and XRD. The UV-Vis spectra and resulting Tauc plots are shown in Figure 7-24. The $E_g$ for all of the film concentrations except 100 F-AnMAPI were 1.60 eV. The $E_g$ of 100 F-AnMAPI was observed at 2.4 eV (Figure 7-24a), this is in line with the measured $E_g$ of $PbI_2$.

X-ray diffraction of the various powders was performed and the resulting patterns are shown in Figure 7-25. The patterns observed for F-AnMAPI show a similar trend to those of F-PrAPI. At 100 F-AnMAPI the produced pattern matches exactly with a thin film of $PbI_2$. When the concentration of F-An is only 0.1 % the pattern is effectively identical to MAPI. As the cation concentrations are mixed the amount of $PbI_2$ increases relative to the MAPI peaks.

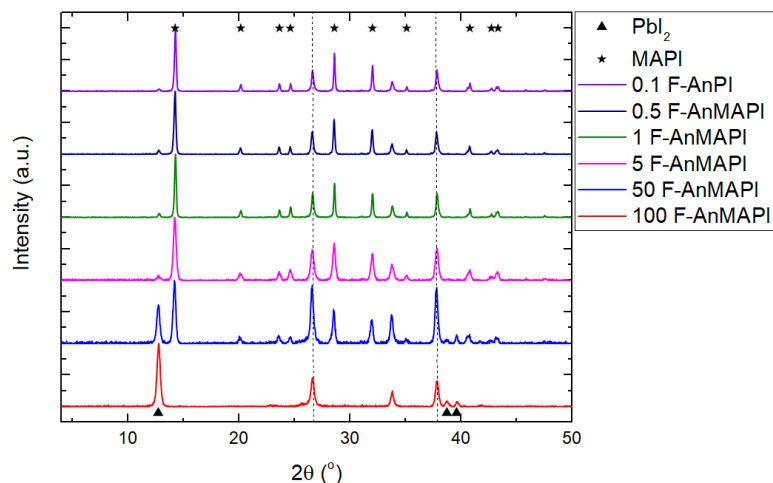The combination of XRD and UV-Vis data indicates, as was observed for

Figure 7-25: XRD patterns of F-AnMAPI perovskite films with varying concentrations of F-An

F-PrAPI, that the F-An is not being incorporated into the perovskite lattice causing a mixed film of $PbI_2$ and MAPI depending on the cation concentration. There are a few possible causes for the failure to incorporate the fluorinated cation, the size of the cation, the electro negativity of the cation or the amine groups ability to coordinated with the octahedra. Once again, size can be ruled out as larger cations have been used before. The use of anilinium in 2D/3D perovskites has been previously reported but the processing method was the high temperature vertically oriented method outlined previously.[14,42] To see if the change in method had an impact, perovskites using non-fluorinated anilinium in varying concentration were also fabricated.

The AnMAPI XRD and UV-Vis gave very similar results as those for F-AnMAPI. Once again the 100 % AnMAPI produced an XRD pattern showing the presence of only $PbI_2$ and as the concentration of MA was increased the XRD pattern began to be a mixture of $PbI_2$ and MAPI (Figure 7-26). The Tauc plots for the various samples showed an $E_g$ of 2.4 eV for 100 AnMAPI and 1.6 eV for all of the other concentrations. These findings show that An is not an appropriate A-site cation when the perovskite is fabricated using ethyl acetate anti-solvent. These findings indicate that the reason F-An does not form a perovskites as an A-site cation is because of a lack of flexibility in the amine group.
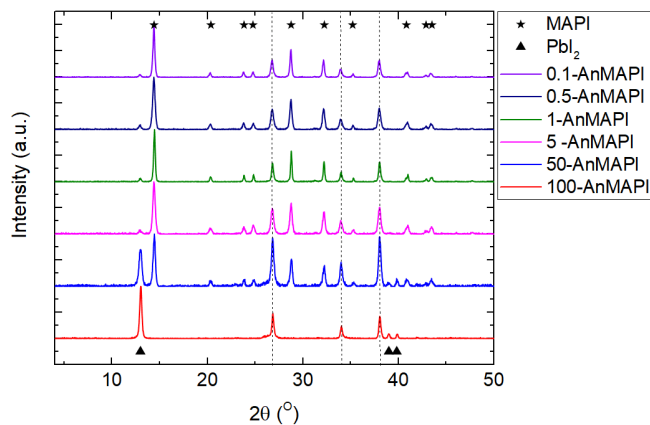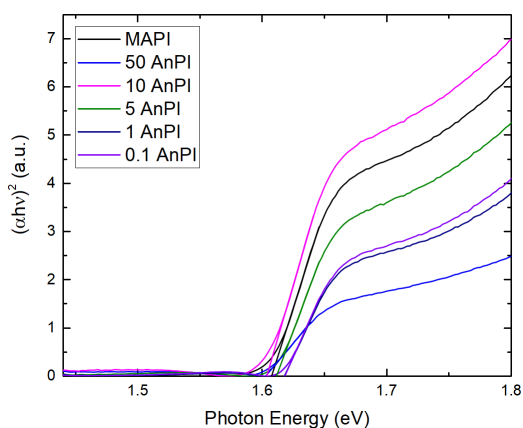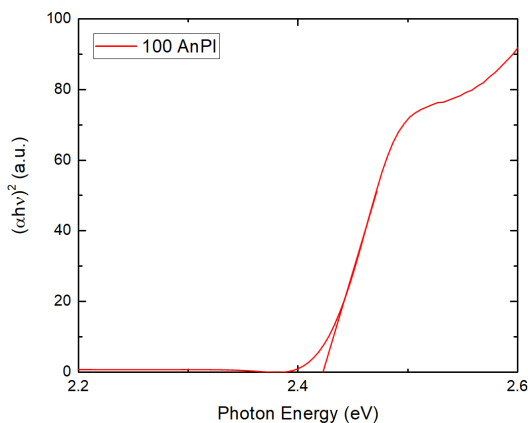
Figure 7-26: a) XRD patterns for various percentage substitutions of An into MAPI. b) and c) shows Tauc plots for the same mixed cation perovskites.

## 7.6 Conclusions and Outlook

In this chapter, the iodide diffusion in 2D/3D hybrid perovskites was investigated using EIS. Two novel fluorinated cations were also investigated. First, phenylethylammonium was incorporated into methylammonium lead iodide perovskites and the structure of films was confirmed using pXRD and UV/Vis. The performance of devices made using a mix of phenylethylammonium and methylammonium cations decreased dramatically after $1\,\text{mol}\%$ substitution. Electrochemical impedance spectroscopy analysis of 10-PEAPI and 1-PEAPI devices showed that iodide diffusion was completely inhibited by the substitution of the large cation. The loss of iodide diffusion was also observed in devices made with propylammonium as the large organic cation. With 10 mol% substitution there

was no evidence of iodide diffusion.

To investigate diffusion along vertically aligned iodide octahedra sheets, 10-PEAPI films were fabricated using $NH_4SCN$ as an additive. The orientation of these films was supported by pXRD analysis but GIWAXS is required to fully confirm this. The performance of the vertically aligned devices was three times greater than non-oriented devices. EIS analysis of the vertically aligned 10-PEAPI devices showed that iodide diffusion was not measurable. The lack of diffusion shows the orientation of the lead iodide octahedra does not influence iodide diffusion. The addition of the larger cations is the cause of the diffusion loss and not the orientation.

Finally, the use of 4-fluoroanilinium and 2,2,3,3,3-pentafluoropropylammonium was investigated. Neither of these cations could be successfully incorporated into the perovskite lattice and led to the formation of lead iodide phases in the film. For 4-fluoroanilinium the lack of incorporation was likely caused by the rigidity of the amine group and for 2,2,3,3,3-pentafluoropropylammonium it was likely caused by the cations being too electronegative and therefore unable to pack closely to other cations.

# References

(1) A. Kojima, K. Teshima, Y. Shirai and T. Miyasaka, *Journal of the American Chemical Society*, 2009, **131**, 6050–6051.

(2) G. E. Eperon, S. D. Stranks, C. Menelaou, M. B. Johnston, L. M. Herz and H. J. Snaith, *Energy Environ. Sci.*, 2014, **7**, 982.

(3) L. N. Quan, M. Yuan, R. Comin, O. Voznyy, E. M. Beauregard, S. Hoogland, A. Buin, A. R. Kirmani, K. Zhao, A. Amassian, D. H. Kim and E. H. Sargent, *Journal of the American Chemical Society*, 2016, **138**, 2649–2655.

(4) G. Grancini, C. Roldán-Carmona, I. Zimmermann, E. Mosconi, X. Lee, D. Martineau, S. Narbey, F. Oswald, F. De Angelis, M. Graetzel and M. K. Nazeeruddin, *Nature Communications*, 2017, **8**, 15684.

(5) Y. Chen, Y. Sun, J. Peng, J. Tang, K. Zheng and Z. Liang, *Advanced Materials*, 2018, **30**, 1703487.

(6) C. C. Stoumpos, D. H. Cao, D. J. Clark, J. Young, J. M. Rondinelli, J. I. Jang, J. T. Hupp and M. G. Kanatzidis, *Chemistry of Materials*, 2016, **28**, 2852–2867.

(7) J. Yan, W. Qiu, G. Wu, P. Heremans and H. Chen, *J. Mater. Chem. A*, 2018, 11063–11077.

(8) A. Krishna, S. Gottis and M. K. Nazeeruddin, 2018, **1806482**, 1–20.

(9) C. C. Stoumpos, C. D. Malliakas and M. G. Kanatzidis, *Inorganic Chemistry*, 2013, **52**, 9019–9038.

(10) Z. Wang, Q. Lin, F. P. Chmiel, N. Sakai, L. M. Herz and H. J. Snaith, *Nature Energy*, 2017, **2**, 1–10.

(11) I. C. Smith, E. T. Hoke, D. Solis-Ibarra, M. D. McGehee and H. I. Karunadasa, *Angewandte Chemie-International Edition*, 2014, **53**, 11232–11235.

(12) M. Hu, L. Liu, A. Mei, Y. Yang, T. Liu and H. Han, *J. Mater. Chem. A*, 2014, **2**, 17115–17121.

(13) D. Wang, M. Wright, N. K. Elumalai and A. Uddin, *Solar Energy Materials and Solar Cells*, 2016, **147**, 255–275.

(14)    H. Tsai, W. Nie, J.-C. Blancon, C. C. Stoumpos, R. Asadpour, B. Harutyunyan, A. J. Neukirch, R. Verduzco, J. J. Crochet, S. Tretiak, L. Pedesseau, J. Even, M. A. Alam, G. Gupta, J. Lou, P. M. Ajayan, M. J. Bedzyk, M. G. Kanatzidis and A. D. Mohite, *Nature*, 2016, **536**, 312–316.

(15)    P. Cheng, Z. Xu, J. Li, Y. Liu, Y. Fan, L. Yu, D.-M. Smilgies, C. Müller, K. Zhao and S. F. Liu, *ACS Energy Letters*, 2018, **3**, 1975–1982.

(16)    X. Zhang, G. Wu, W. Fu, M. Qin, W. Yang, J. Yan, Z. Zhang, X. Lu and H. Chen, *Advanced Energy Materials*, 2018, **8**, 1–9.

(17)    J. Qing, X. K. Liu, M. Li, F. Liu, Z. Yuan, E. Tiukalova, Z. Yan, M. Duchamp, S. Chen, Y. Wang, S. Bai, J. M. Liu, H. J. Snaith, C. S. Lee, T. C. Sum and F. Gao, *Advanced Energy Materials*, 2018, **1800185**, 1–8.

(18)    D. H. Cao, C. C. Stoumpos, O. K. Farha, J. T. Hupp and M. G. Kanatzidis, *Journal of the American Chemical Society*, 2015, **137**, 7843–7850.

(19)    S. Casaluci, L. Cinà, A. Pockett, P. S. Kubiak, R. G. Niemann, A. Reale, A. Di Carlo and P. Cameron, *Journal of Power Sources*, 2015, **297**, 504–510.

(20)    A. Pockett, G. E. Eperon, T. Peltola, H. J. Snaith, A. Walker, L. M. Peter and P. J. Cameron, *The Journal of Physical Chemistry C*, 2015, **119**, 3456–3465.

(21)    A. Pockett, G. E. Eperon, N. Sakai, H. J. Snaith, L. M. Peter and P. J. Cameron, *Phys. Chem. Chem. Phys.*, 2017, **19**, 5959–5970.

(22)    E. Guillén, F. J. Ramos, J. A. Anta and S. Ahmad, *The Journal of Physical Chemistry C*, 2014, **118**, 22913–22922.

(23)    A. Dualeh, T. Moehl, N. Tetreault, J. Teuscher, P. Gao, M. K. Nazeeruddin and M. Gratzel, *Acs Nano*, 2014, **8**, 362–373.

(24)    M. Bag, L. A. Renna, R. Y. Adhikari, S. Karak, F. Liu, P. M. Lahti, T. P. Russell, M. T. Tuominen and D. Venkataraman, *Journal of the American Chemical Society*, 2015, **137**, 13130–13137.

(25)    L. Contreras, J. Idígoras, A. Todinova, M. Salado, S. Kazim, S. Ahmad and J. A. Anta, *Phys. Chem. Chem. Phys.*, 2016, **18**, 31033–31042.

(26) A. Todinova, L. Contreras-Bernal, M. Salado, S. Ahmad, N. Morillo, J. Idígoras and J. A. Anta, *ChemElectroChem*, 2017, **4**, 2891–2901.

(27) L. Gan, J. Li, Z. Fang, H. He and Z. Ye, *Journal of Physical Chemistry Letters*, 2017, **8**, 5177–5183.

(28) C. M. M. Soe, W. Nie, C. C. Stoumpos, H. Tsai, J. C. Blancon, F. Liu, J. Even, T. J. Marks, A. D. Mohite and M. G. Kanatzidis, *Advanced Energy Materials*, 2018, **8**, 2–11.

(29) C.-M. Hsieh, Y.-L. Yu, C.-P. Chen and S.-C. Chuang, *RSC Adv.*, 2017, **7**, 55986–55992.

(30) Q. Niu, W. Huang, H. Lv, Y. Hu, H. Zhang, C. Zhang, S. Ren, W. Zeng, R. Xia and Y. Min, *Journal of Physics D: Applied Physics*, 2018, **51**, 295105.

(31) T. Zhang, L. Xie, L. Chen, N. Guo, G. Li, Z. Tian, B. Mao and Y. Zhao, *Advanced Functional Materials*, 2017, **27**, 1–8.

(32) Y. Lin, Y. Bai, Y. Fang, Q. Wang, Y. Deng and J. Huang, *ACS Energy Letters*, 2017, **2**, 1571–1572.

(33) X. Xiao, J. Dai, Y. Fang, J. Zhao, X. Zheng, S. Tang, P. N. Rudd, X. C. Zeng and J. Huang, *ACS Energy Letters*, 2018, **3**, 684–688.

(34) M. Grätzel, *Nature Materials*, 2014, **13**, 838–842.

(35) M. Pagliaro and R. Ciriminna, *J. Mater. Chem. A*, 2005, **15**, 4981–4991.

(36) S. Nagane, U. Bansode, O. Game, S. Chhatre and S. Ogale, *Chemical Communications*, 2014, **50**, 9741–9744.

(37) C. H. Hendon, R. X. Yang, L. A. Burton and A. Walsh, *J. Mater. Chem. A*, 2015, **3**, 9067–9070.

(38) M. Li, C. Zhao, Z.-K. Wang, C.-C. Zhang, H. K. H. Lee, A. Pockett, J. Barbé, W. C. Tsoi, Y.-G. Yang, M. J. Carnie, X.-Y. Gao, W.-X. Yang, J. R. Durrant, L.-S. Liao and S. M. Jain, *Advanced Energy Materials*, 2018, **8**, 1801509.

(39) M. Salado, F. J. Ramos, V. M. Manzanares, P. Gao, M. K. Nazeeruddin, P. J. Dyson and S. Ahmad, *ChemSusChem*, 2016, **9**, 2708–2714.

(40)  T. M. Koh, V. Shanmugam, X. Guo, S. S. Lim, O. Filonik, E. M. Herzig, P. Müller-Buschbaum, V. Swamy, S. T. Chien, S. G. Mhaisalkar and N. Mathews, *Journal of Materials Chemistry A*, 2018, **6**, 2122–2128.

(41)  D. B. Mitzi, K. Chondroudis and C. R. Kagan, *Inorganic Chemistry*, 1999, **38**, 6246–6256.

(42)  J. Rodríguez-Romero, B. C. Hames, I. Mora-Seró and E. M. Barea, *ACS Energy Letters*, 2017, **2**, 1969–1970.

# Chapter 8

# Final Conclusions and Outlook

## 8.1 Conclusions

This thesis presents four studies on ion migration and the impact of perovskite stoichiometry upon it. It has introduced muon spin relaxation as a novel non-destructive probe for iodide migration in perovskites.

The first study includes a muon spin relaxation (μSR) study of methyl ammonium lead iodide (MAPI) and the deuterated analogue d6-MAPI. It was discovered that it is possible to detect the diffusion of iodide ions in MAPI using μSR. The muon response of both materials was measured and compared and at temperatures above $350\,\mathrm{K}$ the fluctuation rate of the local nuclear magnetic field in the perovskite increased with increasing temperature. This high temperature process had an activation energy of $0.17\,\mathrm{eV}$. This activation energy agreed with the value presented by NMR which, as a technique, is analogous to μSR. Also present in the μSR fluctuation rate response of MAPI was a low temperature process occurring at $100\,\mathrm{K}$ with an $E_a$ of $0.072\,\mathrm{eV}$. When the deuterated analogue was subsequently studied it showed the same two features but a small shift in the low temperature activation energy. The small shift in activation energy between the non-deuterated and deuterated analogue, along with similar $E_a$ values to a previous QENS study, lead to this process being attributed to cation dynamics.

The μSR data for MAPI was also used to calculate an experimental diffusion coefficient for iodide. A value of $7.38 \times 10^{-14}\,\mathrm{cm^2 s^{-1}}$ was calculated at room temperature. It was also shown that the muon stopping site in MAPI is in between

two iodide ions forming a linear I-μ-I state. This state is highly electronegative making the muon stable in this environment up to high temperatures. Finally, it was shown that solar cells made using the deuterated perovskite analogue have the same performance as those made with standard MAPI. This study was the first time that iodide diffusion in any material had been measured using μSR and showed that μSR is a useful and novel technique that can probe perovskite ion diffusion without external stimuli.

With μSR proving to be a sound method to investigate iodide diffusion, the range of studied perovskites was expanded. This follow up study invovled substituting 5 mol% of methylammonium with either caesium, formamidinium (FA) or guanidinium (GA). Substituting with FA and $Cs^+$ led to the formation of a small muonium fraction which had a negligible impact on the overall iodide diffusion study. Addition of all three cations caused the diffusion of iodide to be impacted by varying degrees.

FA and $Cs^+$ changed the activation energies for iodide diffusion from $0.17\,eV$ to $0.201\,eV$ and $0.187\,eV$ respectively. In the case of GA substitution it was not possible to measure the diffusion of iodide in the temperature range of the experiment. The GA substitution caused a disruption of the perovskite lattice lengthening the migration pathway for iodide diffusion, therefore increasing the activation energy. Diffusion coefficients were also shown to decrease slightly for $5\,mol\%$ FA and $Cs^+$ substitution when compared to MAPI. The diffusion coefficient of iodide in the material substituted with $5\,mol\%$ GA was too low to be measured using μSR and *ab initio* results showed that it would be approximately 5 orders of magnitude smaller than the diffusion coefficient of MAPI. This large change takes the diffusion coefficient of ions in GA substituted MAPI outside of μSR's detection range. The other trends in activation energy and diffusion coefficient were further backed up by *ab initio* and electrochemical impedance spectroscopy studies. Mixed cation perovskite devices were shown to produce similar efficiencies to MAPI devices, with $Cs^+$ substitution improving the cells slightly due to improved crystallinity of the perovskite film.

The diffusion of bromide and the impact of halide mixing on ion diffusion in perovskites has also been studied using μSR. Initially, methylammonium lead

bromide (MAPBr) was studied with μSR to investigate bromide diffusion. There was no clear bromide diffusion present in the μSR results for MAPBr. It was concluded that Br diffusion was too fast to be detectable by μSR. A response due to cation dynamics was still observed at low temperature. The low temperature μSR response of $MAPbBr_3$ was shown to have a different activation energy than the same response by MAPI. The reason behind this can not, with the current amount of data, be explained. Further investigations into low temperature cation dynamics of $MAPbBr_3$ would help to deduce what the cause of the change in response is.

The mixed halide perovskites $MAPb(Br_{0.5}I_{0.5})_3$ and $MAPb(Br_{0.17}I_{0.83})_3$ were shown to produce no detectable iodide or bromide diffusion. The results clearly showed that substitution of bromide restricts diffusion of iodide, as even at $83\,mol\%$ the iodide motion was not measurable. The loss of iodide diffusion in the two mixed halide perovskites was likely caused by disruption of the perovskite lattice. Shortening of the Pb-I bond increases its strength and thus makes ion migration more difficult. It is also possible that the lattice disruption alters the diffusion pathway in the same way as GA substitution did. Further *ab initio* studies would be required to confirm this theory.

The final study presented in this thesis is into ion migration in 2D/3D perovskites. It was shown in this work that 2D/3D hybrid perovskites have substantially different iodide diffusion properties to their fully 3D counterparts. The difference in iodide diffusion is also shown to be independent of the orientation of the 2D/3D hybrid perovskites. Non-aligned devices made with 10 mol% substitution of phenylethylammonium showed a complete loss of iodide diffusion as measured by electrochemical impedance spectroscopy. The same results were also observed for vertically aligned perovskites of the same stoichiometry. The loss of iodide diffusion was also observed to be independent of the cation substituted as 10 mol% substitution of propylammonium had the same impact. Finally, even down to 1 mol% substitution, iodide diffusion is still mitigated. The exact cause of the loss of migration is unknown but could be caused by lattice distortion as seen for the mixed cation perovskite study, or a loss of iodide diffusion pathways caused by the 2D spacer layers blocking diffusion.

## 8.2 Outlook

This work has shown the possibilities of using μSR as an iodide diffusion probe on perovskite powders. To develop this work further there are several different possible avenues of investigation. The study into mixed anion hybrid perovskites could be developed to fully study the impact of bromde: iodide mixing by probing a wider range of stoichiometric ratios. To try and elucidate the point at which iodide diffusion becomes visible in μSR lower percentages of bromide should be investigated. This would show if there was a gradual change to the material properties or if it is a more abrupt switching on off the iodide diffusion process. The μSR work could also be compared with electrochemical impedance results and the impact of the bromide mixing on the perovskite structure could be investigated using *ab initio* studies. This combination of studies would help to elucidate the mechanism of diffusion inhibition and how much bromide mixing is required to get the maximum benefits of ion migration inhibition.

The studies into 2D/3D hybrid perovskites could be expanded in two directions either to cover a wider range of perovskite materials or a more focused study into just one material. These two different approaches would yield a better understanding of the overall impact of different larger organic cations on ion diffusion. When looking at a wider range of materials initially, the known materials, for example 5-amino valeric acid, would be studied using EIS and then *ab initio* studies could help to guide research into novel cations that can provide interesting material properties.

Another possible avenue of investigation with μSR is into thin films. Investigation of iodide motion in thin films has already been extensively investigated but usually involves external stimuli such as light or voltage. Using low energy muons to probe thin films, especially of 2D/3D perovskites, is a promising avenue to help further understand the impact of stoichiometry on the internal dynamics of perovskites.

As perovskite device performance reaches higher levels, every increase in efficiency is hard gained. Continuing investigation of the internal material properties is essential to help continue pushing performance and stability to the point where perovskites can compete with, or be used in tandem with, silicon solar cells.

# Appendix: NMR Spectra

## Deuterated Perovskites
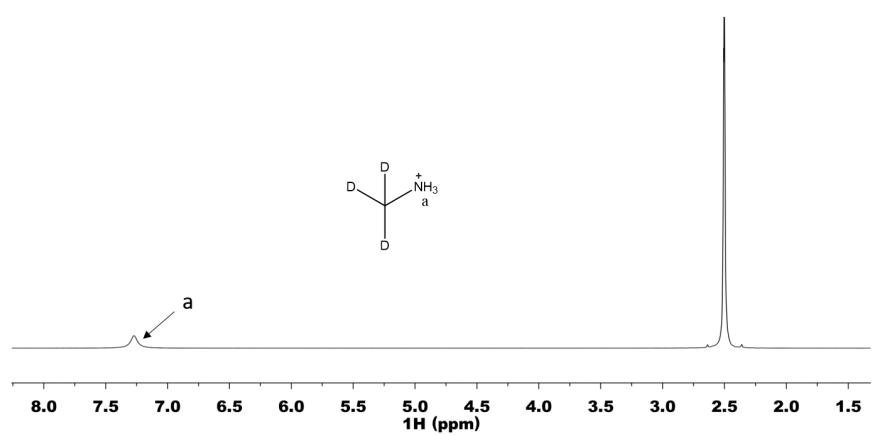


(a)
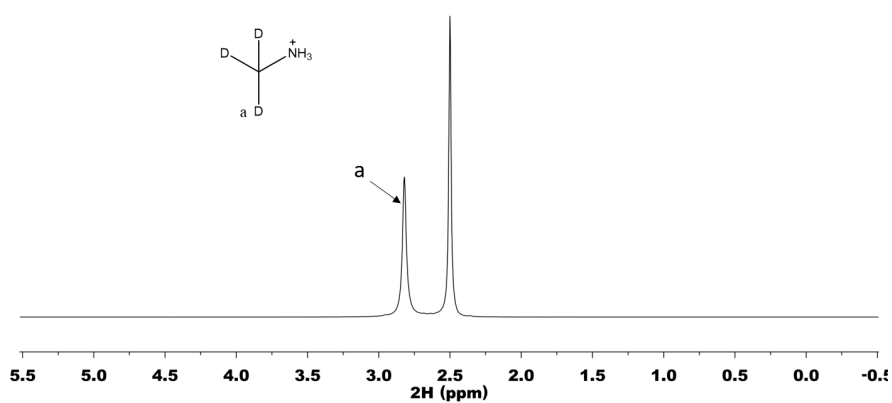


(b)

Figure A-1: a) $^1$H NMR of d$_3$-MAI in d$_6$-DMSO. b) $^2$H NMR of d$_3$-MAI in DMSO.
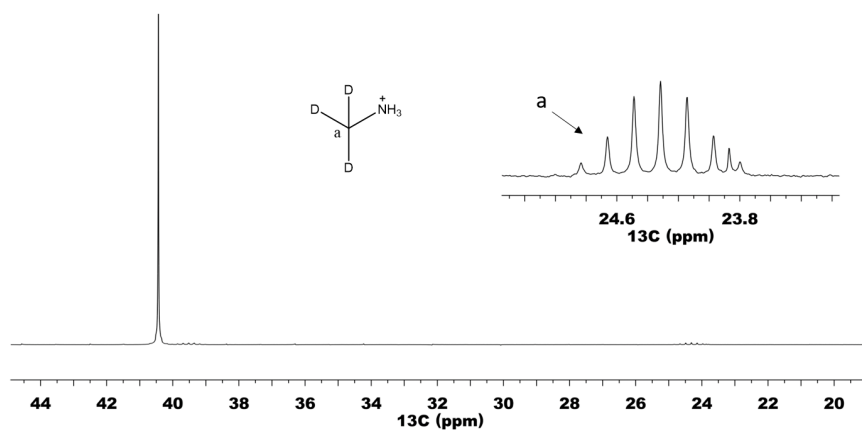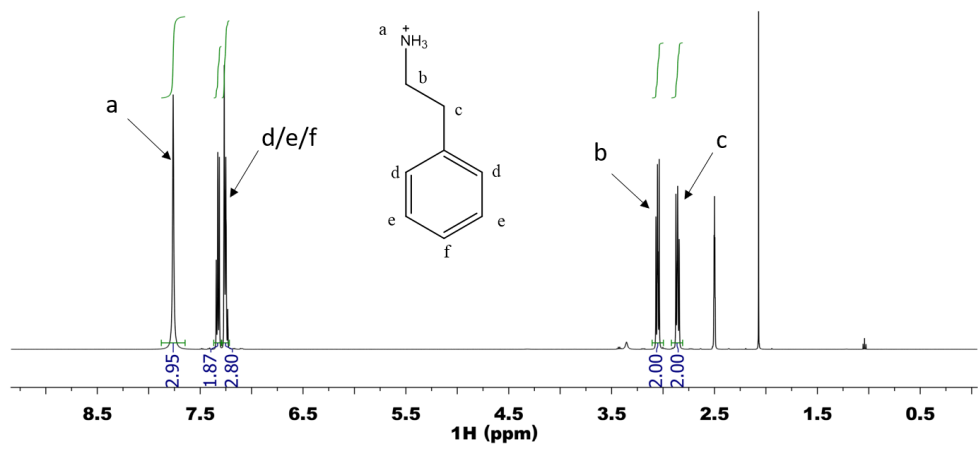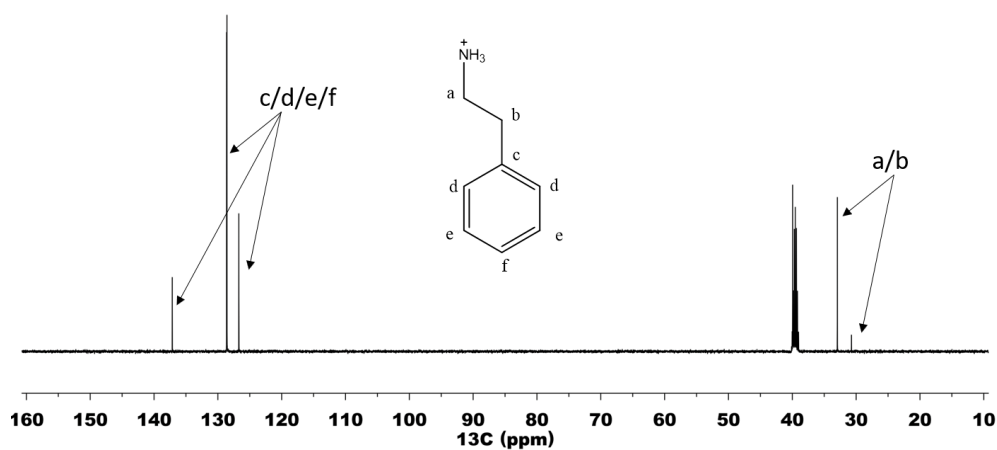
Figure A-2: $^{13}$C NMR of d$_3$-MAI in DMSO.

# 2D Perovskites

## Phenylethylammonium Iodide

(a)



(b)

Figure A-3: a) $^1$H NMR and b)$^{13}$C NMR spectra of phenylethylammonium iodide in d$_6$-DMSO
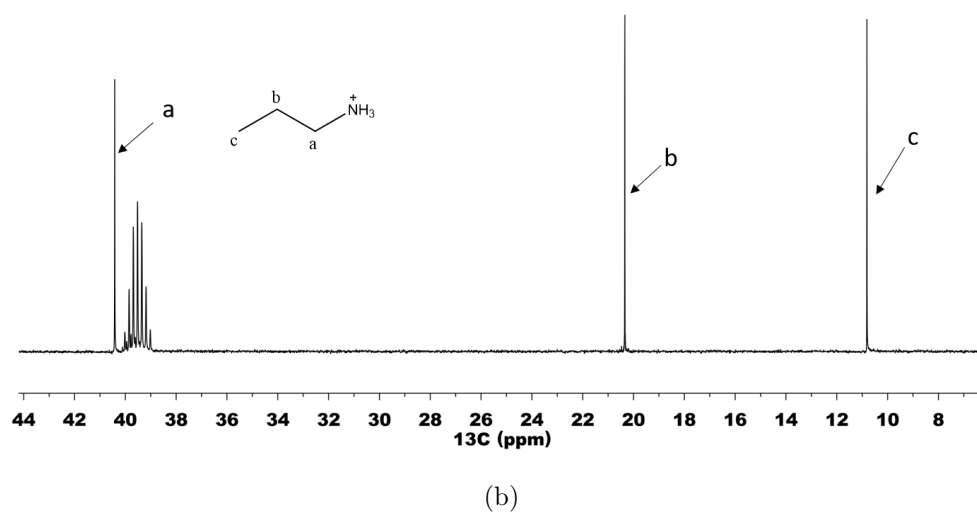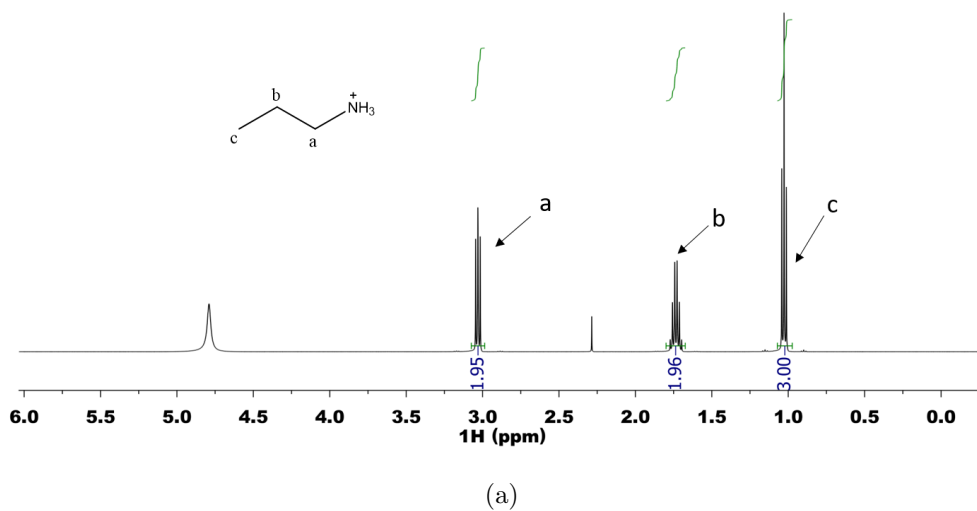
## Propylammonium Iodide

(a)



(b)

Figure A-4: a) $^1$H NMR spectra of propylammonium iodide in $D_2O$ and b) $^{13}$C NMR in $d_6$-DMSO

## 2,2,3,3,3-Pentafluoropropylammonium Iodide

(a)



(b)



(c)
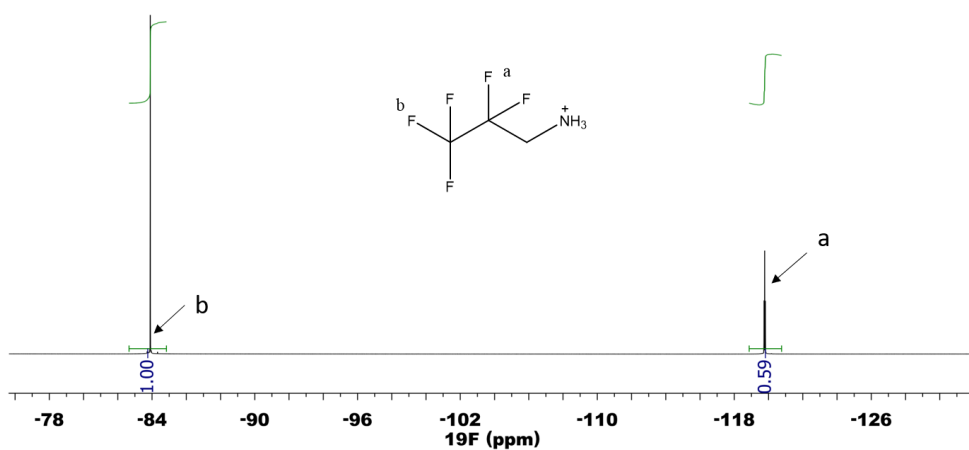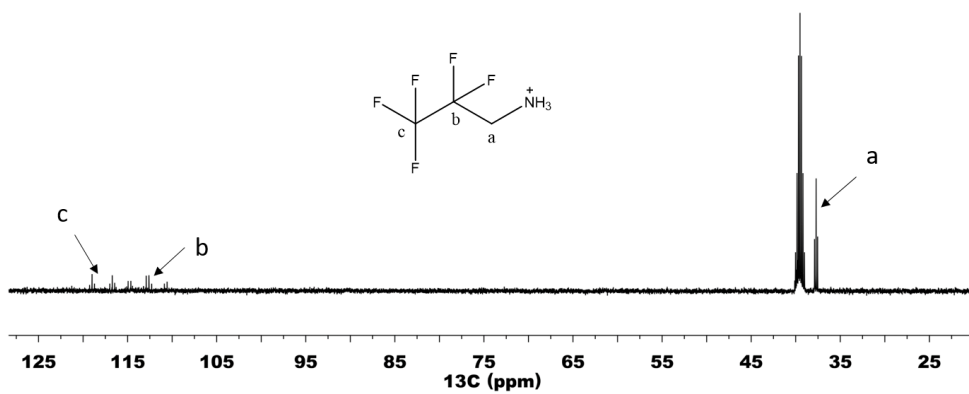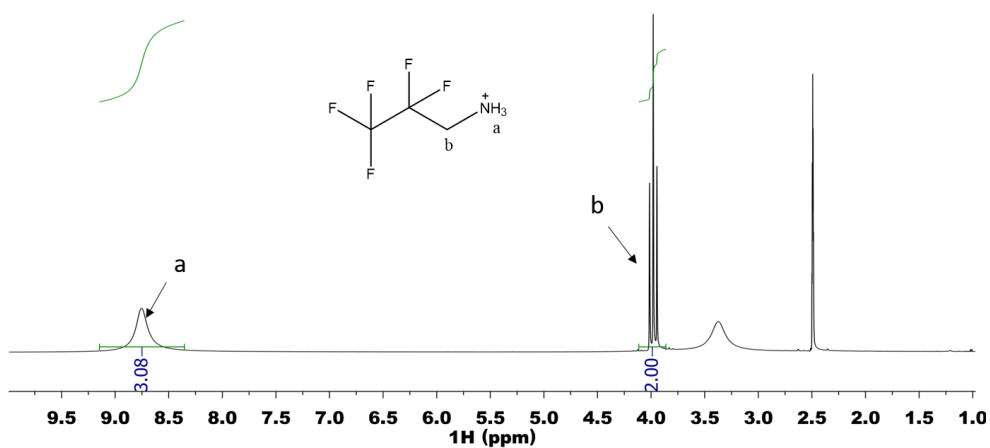
Figure A-5: a)$^1$H, b)$^{13}$C and c)$^{19}$F NMR of 2,2,3,3,3-pentafluoropropylammonium iodide in d$_6$-DMSO
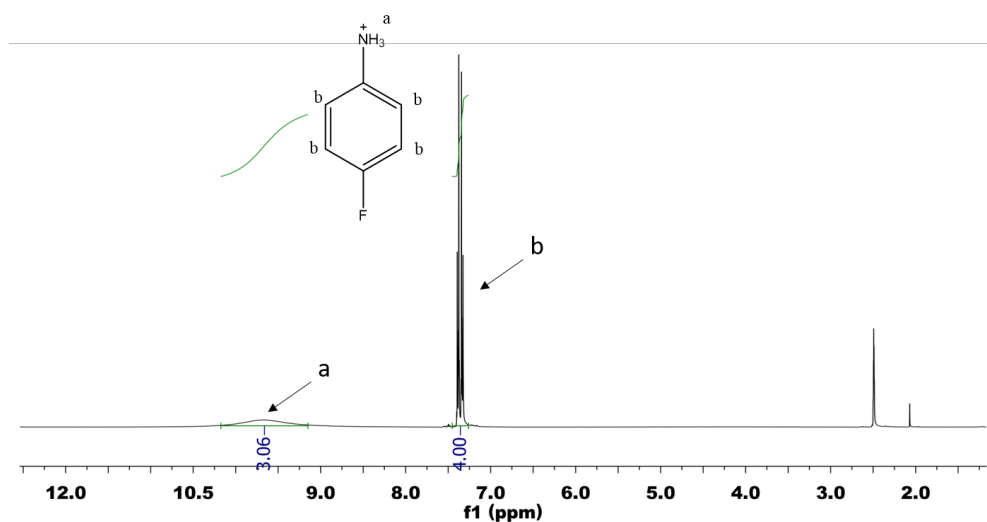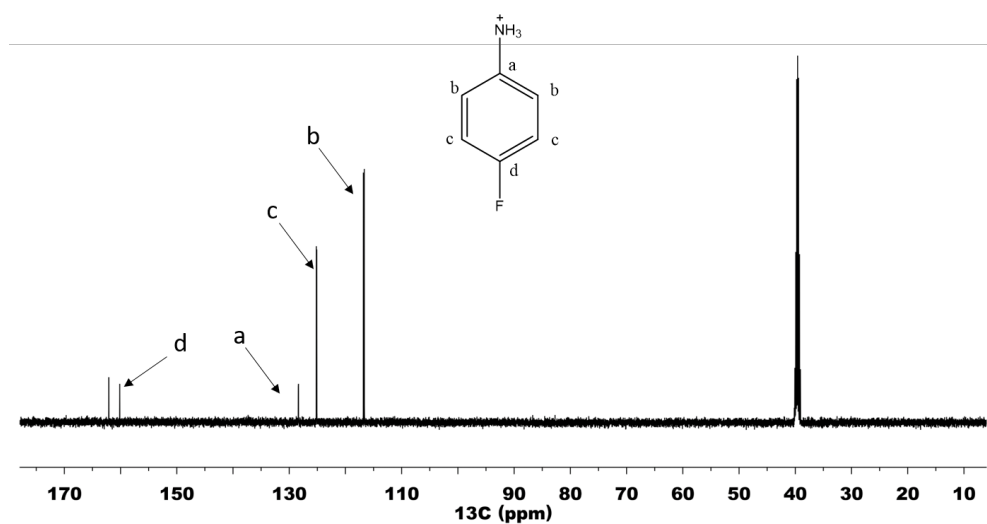
# Anilinium Iodide



(a)



(b)
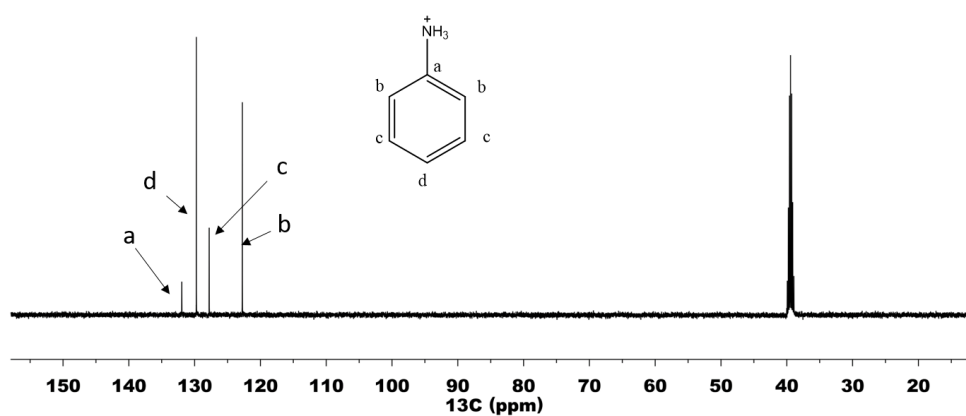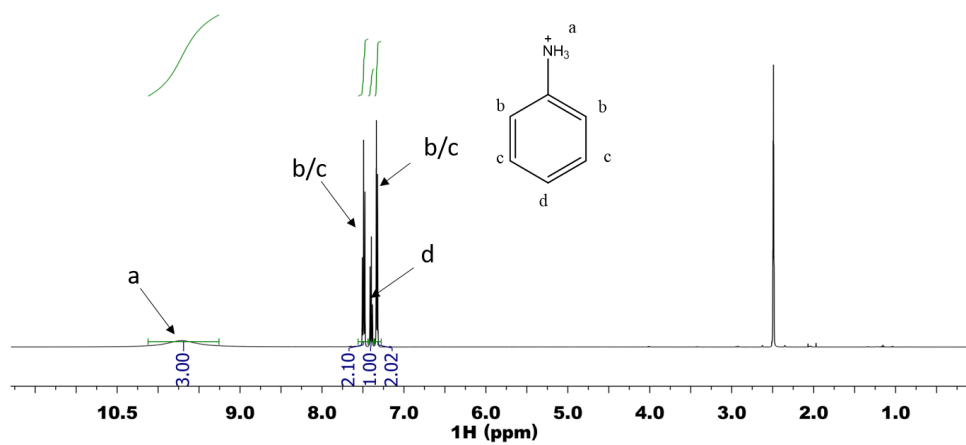
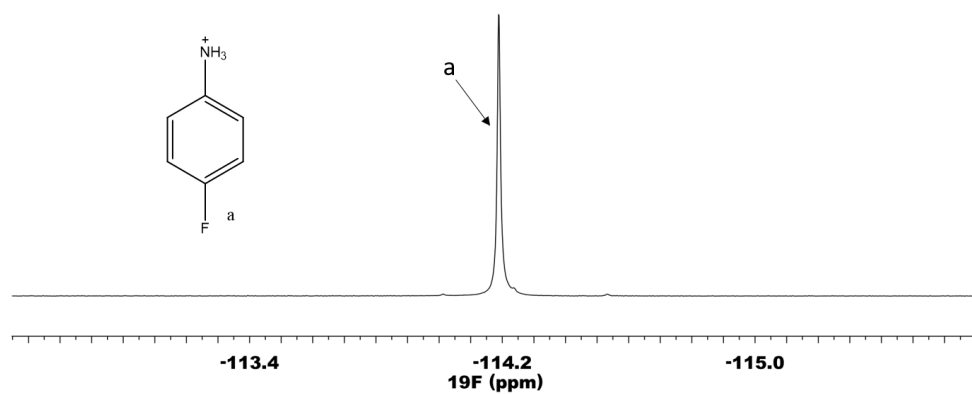Figure A-6: a) $^1$H and b) $^{13}$C NMR spectra of anilinium iodide in d$_6$-DMSO

# 4-fluoroanilinium Iodide

(a)



(b)



(c)

Figure A-7: a)$^1$H, b) $^{13}$C and c) $^{19}$F NMR spectra of 4-fluoroanilinium iodide in d$_6$-DMSO

213